

This copy of the thesis has been supplied on condition that anyone who consults it is understood to recognise that its copyright rests with its author and that no quotation from the thesis and no information derived from it may be published without the author's prior consent.



**UNIVERSITY OF  
PLYMOUTH**

**WaveCat Wave Energy  
Converter: Performance and  
Wave Field Interaction**

by  
James ALLEN

A thesis submitted to University of Plymouth in  
partial fulfilment for the degree of

**DOCTOR OF PHILOSOPHY**

School of Engineering, Computing and Mathematics

May 2022



# Acknowledgements

Firstly, I would like to thank my supervisory team, Dr Jon Miles, Professor Deborah Greaves and Professor Gregorio Iglesias for supporting me throughout this project. Their guidance has been invaluable.

Secondly, I would like to thank the technical staff in the COAST Laboratory for their tireless work and patience during the experimental testing.

I would also like to thank my wife Sarah, without whom I certainly would not have completed this work. And Luna for letting me explain things to her even though she just wanted to sleep.

Finally, I would like to thank my parents who always supported me from my first days in higher education.

# Author's Declaration

At no time during the registration for the degree of Doctor of Philosophy has the author been registered for any other University award without prior agreement of the Doctoral College Quality Sub-Committee.

Work submitted for this research degree at the University of Plymouth has not formed part of any other degree either at the University of Plymouth or at another establishment.

Word count of the main body of the thesis: **34,579**

Signed:

A handwritten signature in dark ink, appearing to read 'Z. Allen', is written above a horizontal line.

Date: 13th May 2022

---

**Publications:**

J. Allen et al. (2016). ‘Laboratory tests in the development of WaveCat’. In: *Sustainability (Switzerland)* 8.12. ISSN: 20711050. DOI: 10.3390/su8121339

R. Bergillos et al. (2019b). ‘Wave energy converter geometry for coastal flooding mitigation’. In: *Science of The Total Environment*. ISSN: 0048-9697. DOI: <https://doi.org/10.1016/j.scitotenv.2019.03.022>. URL: <http://www.sciencedirect.com/science/article/pii/S0048969719310009>

R. Bergillos et al. (2019a). ‘Wave energy converter configuration in dual wave farms’. In: *Ocean Engineering* 178, pp. 204–214. ISSN: 0029-8018. DOI: <https://doi.org/10.1016/j.oceaneng.2019.03.001>. URL: <http://www.sciencedirect.com/science/article/pii/S0029801819300939>

J. Allen et al. (2021). ‘Physical Modelling of the Effect on the Wave Field of the WaveCat Wave Energy Converter’. In: *Journal of Marine Science and Engineering* 9.3. DOI: 10.3390/jmse9030309

**Presentations at conferences:**

J. Allen et al. (2017). ‘Laboratory tests and numerical modelling in the development of WaveCat’. In: *Proceedings of the Twelfth European Wave and Tidal Energy Conference*

J. Allen et al. (2020). ‘Physical modelling of the effect on the wave field of the WaveCat WEC’. in: *7th PRIMaRE Conference*. Plymouth, UK

# Abstract

## WaveCat Wave Energy Converter: Performance and Wave Field Interaction

by

James ALLEN

Wave Energy Converters (WECs) have been shown to offer a promising option for power generation. The WaveCat is a moored WEC design which uses wave overtopping discharge into a variable v-shaped hull, to generate electricity through low head turbines. Physical model tests of the WaveCat WEC were carried out at the University of Plymouth COAST Laboratory to determine the device reflection, transmission and absorption coefficients.  $60^\circ$  and  $30^\circ$  wedge angles were tested, where wedge angle is the angle between the two hulls. Motion response of the WaveCat model was also quantified. The device heave and pitch motions were simulated using the CFD package STAR-CCM+.

The results show the WaveCat absorption coefficient and expected power generation is highest during the largest  $H_s$  and smallest  $T_p$  conditions tested for both wedge angle cases. During the wave conditions that exhibit highest amount of power captured, the device has the lowest motion responses. When at a  $60^\circ$  wedge angle the device generated the highest power (0.4 W) during tests of  $H_s = 0.12$  m and  $T_p = 1.09$  s. When at a  $30^\circ$  wedge angle the device generated the highest power (1.8 W) during tests of  $H_s = 0.15$  m and  $T_p = 1.46$  s which would be normal operating conditions.

The  $60^\circ$  and  $30^\circ$  configurations showed the highest surge Response Amplitude Operator (RAO) (0.68 and 0.79 respectively), pitch RAO (1.9 and 2.2 respectively) and heave RAO (0.97 and 0.92 respectively) values during tests where the wavelength

is larger than the model length. Experimental responses were shown to be well predicted by the numerical model.

The  $60^\circ$  configuration Capture Width Ratio (CWR) peaked at 1.5% during tests indicating greatest efficiency. This occurred at  $H_s$  of 0.08 m and  $T_p$  of 1.09 s. The  $30^\circ$  configuration CWR peaked at 5.4% during tests indicating greatest efficiency. This occurred at tests with  $H_s$  of 0.15 m and  $T_p$  of 1.46 s. At full scale the  $60^\circ$  configuration produced the equivalent of 64.6 kW in conditions of  $H_s = 3.5$  m and  $T_p = 6$  s. At full scale the  $30^\circ$  configuration produced the equivalent of 269.2 kW in conditions of  $H_s = 4.5$  m and  $T_p = 8$  s. These values show the device successfully captures and generates power and is suitable for further development.

The findings presented in this thesis have increased understanding of behaviour of the WaveCat in a wide range of wave conditions and across two wedge angles.

# Contents

<b>List of Figures</b>	<b>xii</b>
<b>List of Tables</b>	<b>xviii</b>
<b>List of Acronyms</b>	<b>xix</b>
<b>List of Symbols</b>	<b>xxi</b>
<b>1 Introduction to Wave Energy</b>	<b>1</b>
1.1 Wave Energy Converters . . . . .	5
1.2 The WaveCat Device . . . . .	8
1.3 Aims and Objectives . . . . .	9
1.4 Thesis Structure . . . . .	10
<b>2 Background to Wave Energy Extraction</b>	<b>12</b>
2.1 Introduction . . . . .	12
2.2 Review of Current Technologies . . . . .	13
2.2.1 WaveCat . . . . .	13
2.2.2 Wave Dragon . . . . .	14
2.2.3 Sea Slot-Cone Generator . . . . .	16
2.2.4 Pelamis . . . . .	17
2.2.5 M4 . . . . .	19
2.2.6 AquaBuOY . . . . .	19
2.2.7 Oyster . . . . .	21
2.2.8 WaveRoller . . . . .	22
2.2.9 Limpet . . . . .	23
2.2.10 Pico Power Plant . . . . .	24
2.2.11 OE Buoy . . . . .	25
2.3 Wave Energy Theory . . . . .	26
2.3.1 Wave Reflections . . . . .	32
2.3.2 Overtopping Flow Rate . . . . .	32
2.3.3 Hydraulic Pipe Friction . . . . .	34
2.3.4 Turbine Selection . . . . .	35
2.4 Physical Model Testing . . . . .	37
2.5 Numerical Modelling . . . . .	39

2.6	Wave Field Coefficients . . . . .	41
2.7	Motion and Response Amplitude Operators . . . . .	43
2.8	Summary . . . . .	45
<b>3</b>	<b>Modelling Methodology</b>	<b>47</b>
3.1	The COAST Laboratory Ocean Basin . . . . .	47
3.2	The WaveCat Model . . . . .	48
3.3	Testing Objectives . . . . .	54
3.4	Instrumentation . . . . .	55
3.4.1	Wave Gauges . . . . .	55
3.4.2	Qualisys Motion Capture System . . . . .	55
3.4.3	Mounted Video Cameras . . . . .	57
3.4.4	Onboard Controls . . . . .	57
3.4.5	Level Sensors . . . . .	59
3.4.6	Flowmeters . . . . .	60
3.5	Physical Modelling Experimental Configurations . . . . .	61
3.5.1	60° Tests - Scoping . . . . .	62
3.5.2	30° Tests . . . . .	62
3.5.3	Numerical Modelling Verification Tests Model Configuration . . . . .	63
3.5.4	60° Tests . . . . .	63
3.6	Physical Modelling Test Conditions . . . . .	64
3.6.1	Preliminary Test Results - 60° Scoping Tests . . . . .	65
3.6.2	30° Tests . . . . .	65
3.6.3	30° Numerical Model Verification Tests . . . . .	67
3.6.4	60° Tests . . . . .	69
3.7	Ocean Basin Characteristics . . . . .	69
3.7.1	Beach Reflection . . . . .	70
3.7.2	Wave Repeatability . . . . .	71
3.8	Numerical Modelling . . . . .	71
3.9	Conclusion . . . . .	76
<b>4</b>	<b>Data Analysis Methodology</b>	<b>77</b>
4.1	Analysis Setup and Core Concepts . . . . .	78
4.2	Reflection and Transmission Analysis . . . . .	84
4.3	Interpolated Test . . . . .	85
4.4	Spectral Analysis . . . . .	88
4.5	Calculation of Wave Field Coefficients . . . . .	92
4.6	Calculation of Power Captured by the Device . . . . .	96
4.7	Response Analysis to Regular Waves . . . . .	98
4.8	Response Analysis to Random Waves . . . . .	107
<b>5</b>	<b>Wave Field Coefficient Results</b>	<b>108</b>
5.1	Results for $\theta_w = 60^\circ$ . . . . .	108
5.1.1	Wave Field Spectral Analysis . . . . .	108

5.1.2	Energy Coefficients . . . . .	113
5.1.3	Generalised Coefficients . . . . .	119
5.2	Results for $\theta_w = 30^\circ$ . . . . .	123
5.2.1	Wave Field Spectral Analysis . . . . .	124
5.2.2	Energy Coefficients . . . . .	127
5.2.3	Generalised Coefficients . . . . .	133
5.3	Comparison of $\theta_w$ . . . . .	137
5.4	Comparison with Other Devices . . . . .	142
5.4.1	Device Coefficients . . . . .	142
5.4.2	Power Generation . . . . .	145
5.5	Full Scale WaveCat . . . . .	148
<b>6</b>	<b>Responses in Regular and Random Waves</b>	<b>152</b>
6.1	60° Wedge Angle . . . . .	152
6.1.1	Response Amplitude Operators . . . . .	152
6.1.2	Responses to Random Waves . . . . .	157
6.2	30° Wedge Angle . . . . .	163
6.2.1	Response Amplitude Operators . . . . .	163
6.2.2	Responses to Random Waves . . . . .	168
6.3	Comparison of $\theta_w$ . . . . .	172
6.4	Comparison to Other Devices . . . . .	180
<b>7</b>	<b>Numerical Modelling Results</b>	<b>182</b>
7.1	Introduction . . . . .	182
7.2	Results . . . . .	183
7.3	Discussion . . . . .	189
<b>8</b>	<b>Summary, Conclusions and Recommendations</b>	<b>191</b>
8.1	Summary . . . . .	191
8.2	Conclusions . . . . .	196
8.3	Recommendations . . . . .	200
	<b>References</b>	<b>204</b>
<b>Appendix A</b>	<b>Modelling Setup</b>	<b>226</b>
A.1	Basin Repeatability . . . . .	226
A.2	Wave Synthesis Software . . . . .	227
A.3	60° Initial Regular Tests . . . . .	231
A.4	60° Initial Random Tests . . . . .	231
A.5	30° Regular Wave Tests . . . . .	232
A.6	30° Random Wave Tests . . . . .	232
A.7	60° Regular Wave Tests . . . . .	234
A.8	60° Random Wave Tests . . . . .	237



---

A.9	WG Locations . . . . .	239
A.9.1	Initial 60° Tests . . . . .	239
A.9.2	30° Tests . . . . .	240
A.9.3	60° Tests . . . . .	240
A.10	Experimental Constants . . . . .	241
A.11	Repeat Tests . . . . .	242
A.11.1	30° Regular Wave Repeat Tests . . . . .	242
A.11.2	30° Random Wave Repeat Tests . . . . .	242
A.11.3	60° Regular Wave Repeat Tests . . . . .	242
A.11.4	60° Random Wave Repeat Tests . . . . .	243
A.12	Numerical Modelling Test Case Run Times . . . . .	243
<b>Appendix B Alternatively Displayed Results Graphs</b>		<b>244</b>
B.1	Reflected, Transmitted and Absorbed Energy . . . . .	244
B.1.1	60° . . . . .	244
B.1.2	30° . . . . .	247
B.2	Responses and RAOs . . . . .	252
B.2.1	60° . . . . .	252
B.2.2	30° . . . . .	256

# List of Figures

1.1	Worldwide annual mean power density of Wave energy also showing prominent direction of swell . . . . .	3
1.2	United Kingdom annual mean power density in United Kingdom territorial sea limits . . . . .	4
1.3	WEC types by mode of operation . . . . .	6
1.4	The WaveCat concept design, a twin-hulled device with a variable opening angle . . . . .	8
2.1	The Wave Dragon in Nissum Bredning (Tedd et al., 2006) . . . . .	14
2.2	Power matrix (kW) of the Wave Dragon against $H_s$ on the vertical axis and $T_p$ on the horizontal axis (Silva et al., 2013; Kofoed et al., 2006) . . . . .	16
2.3	The SSG design (Vicinanza and Frigaard, 2008) . . . . .	16
2.4	Power matrix (kW) of the SSG against $H_s$ on the vertical axis and $T_e$ on the horizontal axis (Silva et al., 2013; Vicinanza et al., 2012) . . . .	17
2.5	The Pelamis attenuator in Portugal (Yemm et al., 2012) . . . . .	18
2.6	Power matrix (kW) of Pelamis against $H_s$ on the vertical axis and $T_e$ on the horizontal axis (Silva et al., 2013; Henderson, 2006) . . . . .	18
2.7	The M4 device in experimental tests (Stansby et al., 2017) . . . . .	19
2.8	a) The AquaBuOY device, b) section view (Munteanu, 2015) . . . . .	20
2.9	Power matrix (kW) of the AquaBuOY against $H_s$ on the vertical axis and $T_p$ on the horizontal axis (Silva et al., 2013; Weinstein et al., 2004) . . . . .	20
2.10	The Oyster device (Whittaker and Folley, 2012) . . . . .	21
2.11	Power matrix (kW) of the Oyster against $H_s$ on the vertical axis and $T_e$ on the horizontal axis (Silva et al., 2013; Whittaker et al., 2007) . . . . .	22
2.12	The WaveRoller device (AW-Energy, 2020) . . . . .	22
2.13	The WaveRoller normalised power matrix (adapted from Mäki et al. (2014)) . . . . .	23
2.14	The LIMPET device (Boake et al., 2002) . . . . .	24
2.15	The Pico device (Falcão et al., 2020) . . . . .	25
2.16	Power matrix of the Pico power plant (Monk et al., 2013) . . . . .	25
2.17	The OE Buoy device (OceanEnergy, 2020) . . . . .	26
2.18	Power matrix of the OE Buoy with power in Watts (Lavelle and Kofoed, 2011) . . . . .	27
2.19	Orbital motion displacement direction under wave action . . . . .	28

2.20	Ratio of energy available to a device of draught $d_r$ in water depth $d$ for a range of $kd$ values . . . . .	34
2.21	Comparison of operating regions for different turbines relative to head and flow, from Greaves and Iglesias (2018) . . . . .	36
2.22	Translational and rotational degrees of freedom . . . . .	44
3.1	WaveCat 1:30 model with 30° wedge angle diagram. Dimensions are in mm . . . . .	49
3.2	The exploded CAD model of the WaveCat from SolidWorks . . . . .	50
3.3	The WaveCat model construction . . . . .	51
3.4	The WaveCat overtopping chambers onboard the model . . . . .	51
3.5	The WaveCat wave deflector mounted on the model . . . . .	52
3.6	WaveCat 1:30 model with 30° wedge angle in the Ocean Basin . . . . .	53
3.7	Mooring plan showing (a) above view and (b) lateral view . . . . .	54
3.8	Reflective Qualisys markers mounted on the WaveCat, with infra-red cameras visible in the background . . . . .	56
3.9	The body co-ordinate systems and locations of Qualisys markers . . . . .	57
3.10	Flowchart showing the decision process controlling the overtopping chambers . . . . .	58
3.11	Level sensor mounted in WaveCat overtopping tank within an open pipe . . . . .	59
3.12	Example calibration of level sensor . . . . .	60
3.13	Flowmeter mounted in WaveCat . . . . .	61
3.14	Ocean Basin layout for 60° single device tests . . . . .	62
3.15	Ocean Basin layout for 30° single device tests . . . . .	63
3.16	Ocean Basin layout for second set of tests with WaveCat at 60° . . . . .	64
3.17	Targeted conditions for regular waves and random spectra tested for $\theta_w = 30^\circ$ . . . . .	66
3.18	Targeted conditions for regular waves and random spectra tested for $\theta_w = 60^\circ$ . . . . .	68
3.19	The SolidWorks mesh of the WaveCat with tanks covered . . . . .	72
3.20	A plane section of the computational domain with the WaveCat model. Refined sections are seen around the model and free surface . . . . .	73
3.21	Mesh convergence results compared to the experimental and theoretical waves. Case 3 was chosen as a balance between reproduction of the regular wave and computational time . . . . .	74
3.22	The free surface of the VOF wave during simulation. The overset mesh can be observed around the WaveCat device, where the cells change from cubic to polyhedral . . . . .	75
3.23	A comparison between a regular wave after the same time period with and without a damping zone active . . . . .	75
4.1	Example time series of raw WG data showing (a), a complete test and (b), a segment of a complete test of the front three WG . . . . .	86
4.2	Windowed and mean-adjusted raw WG data of the front three WG . . . . .	86

4.3	Example complete, (a), and segment of time series of incident, reflected and transmitted wave trains reconstructed from the reflection analysis on the WaveCat, (b)	87
4.4	An example of the location of windowed data compared to a complete test series and how the windows of $m$ length overlap to reduce information loss	88
4.5	Spectral peak multiplication factor, y-axis, against NDF, x-axis, for 99%, 95% and 80% confidence intervals (Jenkins and Watts, 1968)	90
4.6	Example of differing overlapping window length, $m$ , on the spectra resolution and confidence intervals	91
4.7	Example incident spectrum	94
4.8	Example reflected spectrum	95
4.9	Example transmitted spectrum	95
4.10	Example pulse output from a flowmeter for (a), a complete test and (b), a subsection of the test	97
4.11	Levels in starboard tanks during example test	98
4.12	Test parameters against predicted values for a) wave period and b) wave height, for $\theta_w = 60^\circ$	100
4.13	Test parameters against predicted values for a) wave period and b) wave height, for $\theta_w = 30^\circ$	101
4.14	The WaveCat model coordinate origin comparison when level and when ballasted	102
4.15	An example of the raw WG surface elevation data for WG 3 and WG 8 during a test with $T = 1.83$ s and $H = 0.1$ m	104
4.16	An example of peak identification within a test window of regular wave data during a test with $T = 1.83$ s and $H = 0.1$ m	104
4.17	An example of the raw Qualisys data showing large trends in surge, sway and yaw during a test with $T = 1.83$ s and $H = 0.1$ m	105
4.18	Qualisys data once large scale trends are removed and pitch correction applied during a test with $T = 1.83$ s and $H = 0.1$ m	106
5.1	Spectral analysis of $H_s = 0.12$ m, $T_p = 1.28$ s, $\theta_w = 60^\circ$	109
5.2	Spectral analysis of $H_s = 0.12$ m, $T_p = 0.91$ s, $\theta_w = 60^\circ$	110
5.3	Spectral analysis of $H_s = 0.12$ m, $T_p = 2.37$ s, $\theta_w = 60^\circ$	111
5.4	Spectral analysis of $H_s = 0.08$ m, $T_p = 0.91$ s, $\theta_w = 60^\circ$	112
5.5	Spectral analysis of $H_s = 0.08$ m, $T_p = 2.37$ s, $\theta_w = 60^\circ$	112
5.6	a) $k_r$ as a function of $T_p$ , and b) $k_r$ as a contour plot against $H_s$ and $T_p$ , for $\theta_w = 60^\circ$	114
5.7	a) $k_t$ as a function of $T_p$ , and b) $k_t$ as a contour plot against $H_s$ and $T_p$ , for $\theta_w = 60^\circ$	115
5.8	a) $k_a$ as a function of $T_p$ , and b) $k_a$ as a contour plot against $H_s$ and $T_p$ , for $\theta_w = 60^\circ$	117
5.9	Measured energy captured from flowmeters against $H_s$ and $T_p$ for $\theta_w = 60^\circ$	118
5.10	CWR against $H_s$ and $T_p$ for $\theta_w = 60^\circ$	118

5.11	Equations to reconstruct $k_r$ for $\theta_w = 60^\circ$ , showing (a) generalised coefficient against $T_p$ , and (b) normalisation coefficient against $H_s$ . .	120
5.12	Equations to reconstruct $k_t$ for $\theta_w = 60^\circ$ , showing (a) generalised coefficient against $T_p$ , and (b) normalisation coefficient against $H_s$ . .	121
5.13	Equations to reconstruct $k_a$ for $\theta_w = 60^\circ$ , showing (a) generalised coefficient against $T_p$ , and (b) normalisation coefficient against $H_s$ . .	122
5.14	Spectral analysis of $H_s = 0.15$ m, $T_p = 1.46$ s, $\theta_w = 30^\circ$ . . . . .	123
5.15	Spectral analysis of $H_s = 0.15$ m, $T_p = 1.28$ s, $\theta_w = 30^\circ$ . . . . .	124
5.16	Spectral analysis of $H_s = 0.15$ m, $T_p = 2.56$ s, $\theta_w = 30^\circ$ . . . . .	125
5.17	Spectral analysis of $H_s = 0.07$ m, $T_p = 1.28$ s, $\theta_w = 30^\circ$ . . . . .	126
5.18	Spectral analysis of $H_s = 0.07$ m, $T_p = 2.56$ s, $\theta_w = 30^\circ$ . . . . .	127
5.19	$k_r$ as a function of $T_p$ , (a), and as a contour plot against $H_s$ and $T_p$ , (b) for $\theta_w = 30^\circ$ . . . . .	128
5.20	$k_t$ as a function of $T_p$ , (a), and as a contour plot against $H_s$ and $T_p$ , (b) for $\theta_w = 30^\circ$ . . . . .	129
5.21	$k_a$ as a function of $T_p$ , (a), and as a contour plot against $H_s$ and $T_p$ , (b) for $\theta_w = 30^\circ$ . . . . .	131
5.22	Energy captured against $H_s$ and $T_p$ for $\theta_w = 30^\circ$ . . . . .	132
5.23	Contour plot of Capture Width Ratio (CWR) against $H_s$ and $T_p$ . . .	132
5.24	Equations to reconstruct $k_r$ for $\theta_w = 30^\circ$ , showing (a) generalised coefficient against $T_p$ , and (b) normalisation coefficient against $H_s$ . .	134
5.25	Equations to reconstruct $k_t$ for $\theta_w = 30^\circ$ , showing (a) generalised coefficient against $T_p$ , and (b) normalisation coefficient against $H_s$ . .	135
5.26	Equations to reconstruct $k_a$ for $\theta_w = 30^\circ$ , showing (a) generalised coefficient against $T_p$ , and (b) normalisation coefficient against $H_s$ . .	136
5.27	Comparison of $k_r$ for $\theta_w = 60^\circ$ and $\theta_w = 30^\circ$ . . . . .	137
5.28	Comparison of $k_t$ for $\theta_w = 60^\circ$ and $\theta_w = 30^\circ$ . . . . .	138
5.29	Comparison of $k_a$ for $\theta_w = 60^\circ$ and $\theta_w = 30^\circ$ . . . . .	139
5.30	Anticipated WaveCat response to variations of wave steepness and amplitude . . . . .	141
5.31	Wave ray trace of the $60^\circ$ model configuration . . . . .	142
5.32	Wave ray trace of the $30^\circ$ model configuration . . . . .	143
5.33	Power output of $60^\circ$ and $30^\circ$ configurations scaled up to full scale . .	149
6.1	Surge RAO against wave period, wavelength and model length for $\theta_w = 60^\circ$ . . . . .	153
6.2	Heave RAO against wave period, wavelength and model length for $\theta_w = 60^\circ$ . . . . .	154
6.3	Pitch RAO against wave period, wavelength and model length for $\theta_w = 60^\circ$ . . . . .	156
6.4	Spectral analysis of responses to random waves of $H_s = 0.12$ m, $T_p = 1.28$ s, $\theta_w = 60^\circ$ . . . . .	157
6.5	Spectral analysis of responses to random waves of $H_s = 0.12$ m, $T_p = 0.91$ s, $\theta_w = 60^\circ$ . . . . .	158

6.6	Spectral analysis of responses to random waves of $H_s = 0.12$ m, $T_p = 2.37$ s, $\theta_w = 60^\circ$ . . . . .	159
6.7	Spectral analysis of responses to random waves of $H_s = 0.08$ m, $T_p = 0.91$ s, $\theta_w = 60^\circ$ . . . . .	159
6.8	Spectral analysis of responses to random waves of $H_s = 0.08$ m, $T_p = 2.37$ s, $\theta_w = 60^\circ$ . . . . .	160
6.9	Scatter plot of normalised surge response against random wave conditions for $\theta_w = 60^\circ$ model configuration . . . . .	161
6.10	Scatter plot of normalised pitch response against random wave conditions for $\theta_w = 60^\circ$ model configuration . . . . .	162
6.11	Scatter plot of normalised heave response against random wave conditions for $\theta_w = 60^\circ$ model configuration . . . . .	162
6.12	Surge RAO against wave period, wavelength and model length for $\theta_w = 30^\circ$ . . . . .	164
6.13	Heave RAO against wave period, wavelength and model length for $\theta_w = 30^\circ$ . . . . .	165
6.14	Pitch response against wave period, wavelength and model length for $\theta_w = 30^\circ$ . . . . .	166
6.15	Pitch RAO against wave period, wavelength and model length for $\theta_w = 30^\circ$ . . . . .	167
6.16	Spectral analysis of responses to random waves of $H_s = 0.15$ m, $T_p = 1.46$ s, $\theta_w = 30^\circ$ . . . . .	168
6.17	Spectral analysis of responses to random waves of $H_s = 0.15$ m, $T_p = 1.28$ s, $\theta_w = 30^\circ$ . . . . .	169
6.18	Spectral analysis of responses to random waves of $H_s = 0.15$ m, $T_p = 2.56$ s, $\theta_w = 30^\circ$ . . . . .	170
6.19	Spectral analysis of responses to random waves of $H_s = 0.07$ m, $T_p = 1.28$ s, $\theta_w = 30^\circ$ . . . . .	170
6.20	Spectral analysis of responses to random waves of $H_s = 0.07$ m, $T_p = 2.56$ s, $\theta_w = 30^\circ$ . . . . .	171
6.21	Scatter plot of normalised surge response against random wave conditions for $\theta_w = 30^\circ$ model configuration . . . . .	172
6.22	Scatter plot of normalised pitch response against random wave conditions for $\theta_w = 30^\circ$ model configuration . . . . .	173
6.23	Scatter plot of normalised heave response against random wave conditions for $\theta_w = 30^\circ$ model configuration . . . . .	173
6.24	Comparison of surge RAOs for $60^\circ$ and $30^\circ$ conditions . . . . .	174
6.25	Comparison of Pitch responses for $60^\circ$ and $30^\circ$ conditions . . . . .	175
6.26	Comparison of heave RAOs for $60^\circ$ and $30^\circ$ conditions . . . . .	175
6.27	Scatter plots of normalised surge responses to random waves of $60^\circ$ configuration, above, and $30^\circ$ configuration, below . . . . .	177
6.28	Scatter plots of normalised pitch responses to random waves of $60^\circ$ configuration, above, and $30^\circ$ configuration, below . . . . .	178

6.29	Scatter plots of normalised heave responses to random waves of $60^\circ$ configuration, above, and $30^\circ$ configuration, below . . . . .	179
7.1	Experimental and numerical responses for test case 1 . . . . .	183
7.2	Experimental and numerical responses for test case 2 . . . . .	184
7.3	Experimental and numerical responses for test case 3 . . . . .	184
7.4	Experimental and numerical responses for test case 4 . . . . .	185
7.5	Experimental and numerical responses for test case 5 . . . . .	186
7.6	Experimental and numerical responses for test case 6 . . . . .	186
7.7	Experimental and numerical responses for test case 7 . . . . .	187
7.8	Experimental and numerical responses for test case 8 . . . . .	188
7.9	Experimental and numerical responses for test case 9 . . . . .	188
A.1	Regular wave repeatability tests . . . . .	227
A.2	Random wave repeatability tests . . . . .	228
A.3	Njörðr Wave Synthesis interfaces showing both regular and random example tests. 1 shows the test list, 2 shows the test specification, 3 shows the test parameters, 4 shows a summary of test conditions, 5 shows the expected surface elevation and 6 shows the expected power spectrum. . . . .	229
B.1	Reflected energy shown as functions of (a) $H_s$ and (b) $T_p$ for $\theta_w = 60^\circ$	245
B.2	Transmitted energy shown as functions of (a) $H_s$ and (b) $T_p$ for $\theta_w = 60^\circ$ . . . . .	246
B.3	Absorbed energy shown as functions of (a) $H_s$ and (b) $T_p$ for $\theta_w = 60^\circ$	248
B.4	Reflected energy shown as functions of $H_s$ and $T_p$ for $\theta_w = 30^\circ$ . . . .	249
B.5	Transmitted energy shown as functions of $H_s$ and $T_p$ for $\theta_w = 30^\circ$ . .	250
B.6	Absorbed energy shown as functions of $H_s$ and $T_p$ for $\theta_w = 30^\circ$ . . . .	251
B.7	Surge response against wave period, wavelength and model length for $\theta_w = 60^\circ$ . . . . .	253
B.8	Heave response against wave period, wavelength and model length for $\theta_w = 60^\circ$ . . . . .	254
B.9	Pitch response against wave period, wavelength and model length for $\theta_w = 60^\circ$ . . . . .	255
B.10	Surge response against wave period, wavelength and model length for $\theta_w = 30^\circ$ . . . . .	257
B.11	Heave response against wave period, wavelength and model length for $\theta_w = 30^\circ$ . . . . .	258

# List of Tables

3.1	Froude scaling factors to convert from model scale to full scale, where S is the scaling factor . . . . .	48
3.2	Test conditions of regular waves for numerical modelling verification experiments . . . . .	67
3.3	Reflection coefficient of the Ocean Basin beach for regular waves in an empty tank . . . . .	70
3.4	Summary of repeated wave conditions tested . . . . .	71
3.5	The cell dimensions and runtime for each convergence case . . . . .	74
4.1	Constants used during experimental campaigns . . . . .	79
4.2	Wave period to wavelength conversion in 2 m water depth . . . . .	80
5.1	Properties of the WaveCat scaled from 1:30 to 1:1 . . . . .	148
7.1	$R^2$ errors for heave and pitch for tested numerical cases . . . . .	189
A.1	Initial regular wave tests showing model and full scale conditions . . .	231
A.2	Initial random wave tests showing model and full scale conditions . .	231
A.3	$\theta_w = 30^\circ$ regular wave tests showing model and full scale conditions .	232
A.4	$\theta_w = 30^\circ$ random wave tests showing model and full scale conditions .	232
A.5	$\theta_w = 60^\circ$ regular wave tests showing model and full scale conditions .	234
A.6	$\theta_w = 60^\circ$ random wave tests showing model and full scale conditions .	237
A.7	Wave gauge locations for $60^\circ$ single device tests . . . . .	239
A.8	Wave gauge locations for $30^\circ$ single device tests . . . . .	240
A.9	Wave gauge locations for the second set of $\theta_w = 60^\circ$ tests . . . . .	240
A.10	Experimental setup comparison between experimental sessions . . . .	241
A.11	$\theta_w = 30^\circ$ regular wave repeat tests showing model and full scale conditions . . . . .	242
A.12	$\theta_w = 30^\circ$ random wave repeat tests showing model and full scale conditions . . . . .	242
A.13	$\theta_w = 60^\circ$ regular wave repeat tests showing model and full scale conditions . . . . .	242
A.14	$\theta_w = 60^\circ$ random wave repeat tests showing model and full scale conditions . . . . .	243
A.15	Numerical case runtimes and hardware specifications . . . . .	243



# List of Acronyms

The following acronyms are used within the document

**6DOF** 6 Degrees of Freedom.

**BEM** Boundary Element Method.

**CAD** Computer Aided Design.

**CALM** Catenary Anchor Leg Mooring.

**CCTV** Closed-Circuit Television.

**CFD** Computational Fluid Dynamics.

**COAST** Coastal, Ocean and Sediment Transport.

**CW** Capture Width.

**CWR** Capture Width Ratio.

**FFT** Fast Fourier Transform.

**GPE** Gravitational Potential Energy.

**ITTC** International Towing Tank Conference.

**LIMPET** Land Installed Marine Powered Energy Transformer.

**NDF** Number of Degrees of Freedom.

**OWC** Oscillating Water Column.

**OWEC** Overtopping Wave Energy Converter.

**OWSC** Oscillating Wave Surge Converter.

**PTO** Power Take-Off.

**RANS** Reynolds-Averaged Navier Stokes.

**RAO** Response Amplitude Operator.

**RMS** Root Mean Squared.

**SDF** Spectral Density Function.

**SSG** Sea Slot-Cone Generator.

**TRL** Technology Readiness Level.

**VOF** Volume Of Fluid.

**WEC** Wave Energy Converter.

**WG** Wave Gauge.

# List of Symbols

The following symbols and constants are used within the document

## Constants

$\rho_w$	Density of fresh water at 21°C	997.5 kgm <sup>-3</sup>
$g$	Acceleration due to gravity	9.81 ms <sup>-2</sup>
Mtoe	Million tons of oil equivalent	11.63 MWh

## Greek Symbols

$\Delta f$	Bandwidth	Hz
$\eta$	Surface elevation of water surface	m
$\eta_i$	Surface elevation of incident wave water surface	m
$\eta_r$	Surface elevation of reflected wave water surface	m
$\eta_t$	Surface elevation of transmitted wave water surface	m
$\eta_T$	Efficiency of turbine	-
$\gamma_\beta$	Influence factor - oblique angle of attack	-
$\gamma_\mu$	Influence factor - vertical wall	-
$\gamma_b$	Influence factor - berm influence	-
$\gamma_f$	Influence factor - roughness	-

---

$\lambda$	Wavelength	m
$\lambda_F$	Friction coefficient	-
$\Lambda_m$	Overtopping discharge modifier - ramp and guiding wall shape	-
$\Lambda_\alpha$	Overtopping discharge modifier - ramp slope	-
$\Lambda_{dr}$	Overtopping discharge modifier - draft	-
$\Lambda_s$	Overtopping discharge modifier - low crest freeboards	-
$\omega$	Angular velocity	$^\circ\text{s}^{-1}$
$\rho$	Density of medium	$\text{kgm}^{-3}$
$\sigma$	Variance	$\text{unit}^2$
$\sigma_\eta$	Variance of $\eta$	$\text{m}^2$
$\theta_w$	Wedge angle of WaveCat	$^\circ$

**Roman Symbols**

$\overline{Q}$	Average overtopping per metre of crest width	$\text{m}^3\text{s}^{-1}$
$\text{RAO}_{\text{heave}}$	Heave RAO	-
$\text{RAO}_{\text{pitch}}$	Pitch RAO	-
$\text{RAO}_{\text{roll}}$	Roll RAO	-
$\text{RAO}_{\text{surge}}$	Surge RAO	-
$\text{RAO}_{\text{sway}}$	Sway RAO	-
$\text{RAO}_{\text{yaw}}$	Yaw RAO	-
$A$	Wave Amplitude	m
$B$	Characteristic dimension of device	m
$c$	Phase velocity	$\text{ms}^{-1}$

---

$c_g$	Group velocity	$\text{ms}^{-1}$
$D$	Pipe diameter	m
$d$	Water depth	m
$d_r$	Device draft	m
$E$	Energy per unit area of wave	$\text{Jm}^{-2}$
$f$	Frequency	Hz
$f_N$	Nyquist frequency	Hz
$f_L$	Frequency associated with model length	Hz
$f_s$	Sampling frequency	Hz
$f_{sf}$	Sampling frequency of flowmeter	Hz
$H$	Wave height of regular waves	m
$h$	Head height	m
$h$	Hydraulic head	m
$h_f$	head loss due to friction	m
$H_m$	Wave height at model scale	m
$H_{1/3}$	Average wave height of highest 1/3 waves	m
$H_{sa}$	Significant wave height of absorbed waves	m
$H_{si}$	Significant wave height of incident waves	m
$H_{sr}$	Significant wave height of reflected waves	m
$H_{st}$	Significant wave height of transmitted waves	m
$H_s$	Significant wave height of random waves	m
$H_{pr}$	Wave height at prototype scale	m

---

$i$	Imaginary unit	-
$K$	Flowmeter “K-Factor”	-
$k_a$	Absorption coefficient	-
$k_p$	Wavenumber of peak period wave	$\text{m}^{-1}$
$k_r$	Reflection coefficient	-
$k_t$	Transmission coefficient	-
$L$	Surface elevation of water in overtopping tank	m
$l$	Characteristic length of device	m
$L_e$	Length of the inner edge of the model	m
$L_i$	Initial surface elevation in overtopping tank	m
$L_m$	Effective model length	m
$L_P$	Length of pipe	m
$L_{max}$	Surface elevation of water in overtopping tank at which the valves open	m
$L_{min}$	Surface elevation of water in overtopping tank at which the valves close	m
$m$	Mass	kg
$m_0$	Zeroth-order moment (of surface elevation)	$\text{m}^2$
$N_p$	Number of flowmeter pulses	-
$P$	Power per unit of wave front	$\text{Wm}^{-1}$
$P_{in}$	Power input	W
$P_{out}$	Power generated	W
$Q_N$	Non-dimensional overtopping discharge	-
$Q_T$	Flow rate through turbine	$\text{m}^3\text{s}^{-1}$

---

$R_c$	Relative crest	-
$S(f)$	Spectral density	$\text{m}^2\text{s}^{-1}$
$T$	Wave period of regular waves	s
$t$	Time	s
$T_e$	Wave energy period	s
$T_p$	Peak wave period	s
$V$	Voltage	V
$V_p$	Flow velocity	$\text{ms}^{-1}$
$W$	Wave crest width	m
$x$	Surface position in $x$ dimension	m
$S$	Scaling factor	-

# Chapter 1

## Introduction to Wave Energy

As world population and manufacturing increases, energy usage has never been higher. Human activity has contributed to an increase in greenhouse gas emissions, particularly CO<sub>2</sub>, such that the average global temperature has risen 2°C above pre-industrial level (NOAA, 2019). In 2018, total worldwide energy use was calculated at 14,282 Mtoe, where one Mtoe is the equivalent energy of one million tons of oil, approximately 11.63 MWh (IEA, 2020a). This was an increase from 5,523 Mtoe in 1976, with the majority generated from non-renewable means such as oil, coal and natural gas. Of the 2018 energy consumption totals, approximately 13.5% was generated from renewable sources, further split into 9.0% supplied by biofuels, 2.5% by hydro power and the remaining 2% by solar, wind, geothermal and tidal combined (IEA, 2020b).

In order to reduce the impact of fossil fuels on our environment, alternative means of energy generation must be considered. Originally the European Union set out energy generation targets in which member countries were to achieve a percentage of their energy generation from renewable sources by 2020 (European Parliament and Council, 2009), however since then a new agreement has come into force revising the date to 2030 (European Parliament and Council, 2018). After the United Kingdom left the EU, the UK government introduced the Environment Bill House of



Commons, 2020 outlining targets towards cutting fossil fuel emissions, which is currently before Parliament (UK Parliament, 2021). One alternative source of energy is marine renewable energy.

To achieve the proposals set out in the above legislation, the United Kingdom must increase the amount of energy generation from renewable energy sources. The primary use of energy is in the form of electricity (Department for Business Energy & Industrial Strategy, 2018), of which the United Kingdom provided 29.3% from renewable sources in 2017, representing 99.3 TWh of electricity. Of the 2017 generation total, onshore wind accounted for 29.1 TWh, offshore wind 20.9 TWh and solar responsible for 11.5 TWh. Bioenergy sources contributed a further 32.1 TWh of electricity leaving 6 TWh of electricity generated by hydro power. Of this 6 TWh, 4 GWh was generated from wave and tidal sources combined.

By the end of 2019, this share of electricity generation had grown to 37.1% (Digest of UK Energy Statistics, 2020), particularly in offshore wind, whose generation rose 20% in 2019 alone. Recently, with the global COVID-19 pandemic, demand for electricity dropped (IEA, 2021) when nations were placed into lockdowns. This is an ongoing factor with effects that are unknown thus far.

Wave energy is recognised as a potential renewable energy source (Falnes and Løvseth, 1991; Jeffrey et al., 2013; Bahaj, 2011), with studies performed into the economic viability of wave energy conversion (Sandberg et al., 2016; Astariz and Iglesias, 2015).

Due to the variable nature of solar heating, temperature gradients are formed, creating winds. The winds act over a body of water and friction, caused by shear stresses between air and water particles, create waves. While the initial energy transfer may be small, on the order of  $0.01$  to  $0.1 \text{ Wm}^{-2}$ , compared to the average solar energy density at the ocean surface of  $1 \text{ kWm}^{-2}$  on a clear day (Barstow et al., 2008), the energy is transferred over a large area and can continue to grow as the wave propagates. Wave energy may be thought of as a concentrated form of solar energy, expressed in the form of wind and surface gravity waves. The amount of energy

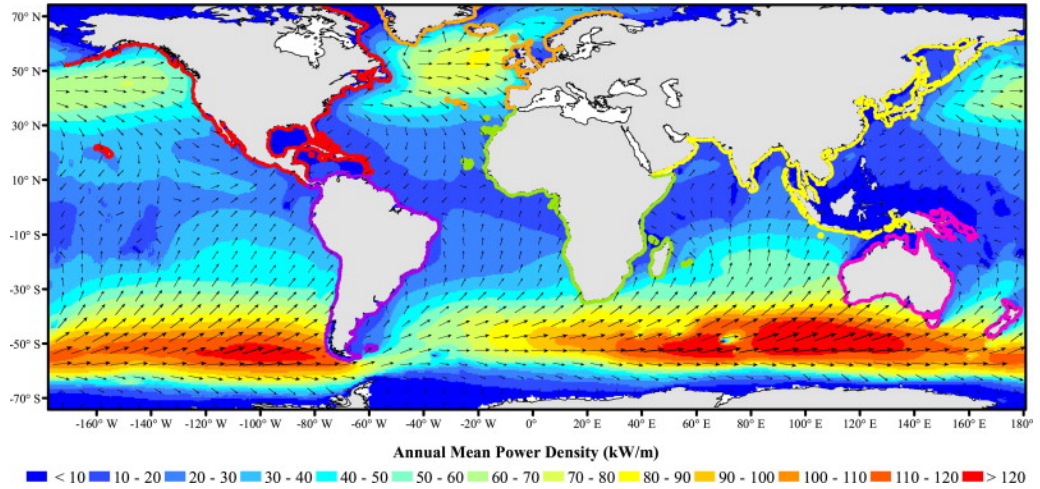


FIGURE 1.1: Worldwide annual mean power density of Wave energy also showing prominent direction of swell (Gunn and Stock-Williams, 2012)

transferred depends on three factors: the wind speed, or rate of energy transfer; the wind duration, or time of energy transfer; and fetch, the distance over which the wind is blowing. With these three factors working in concert, the energy density of ocean wave fronts can reach  $100 \text{ kWm}^{-1}$  (Barstow et al., 2008).

Figure 1.1 (Gunn and Stock-Williams, 2012) shows the worldwide distribution of wave energy. The highest concentrations of energy are located in the most open parts of the ocean, typically between  $40^\circ$  and  $60^\circ$  latitude in both hemispheres, highlighting the importance of having a large fetch distance for the wind to act upon. The United Kingdom is ideally situated to exploit wave energy from both the Atlantic Ocean and North Sea. Of particular interest is the Atlantic due to the long fetch. Figure 1.2 shows the resource around the United Kingdom up to territorial sea limits, with higher concentrations of energy towards Scotland and Cornwall, away from the shadow of Ireland. The concentration of energy extends around Scotland and the Shetland Isles into the North Sea (ABPmer, 2019).

It follows, therefore, that with the abundance of energy available in wave energy, that efforts should be made to harness the power of the sea, through wave energy converters. A further advantage of harnessing energy from the ocean comes in that there is less interference with human populations, who typically spend the majority of their time onshore. This allows for larger structures to be built and in bigger

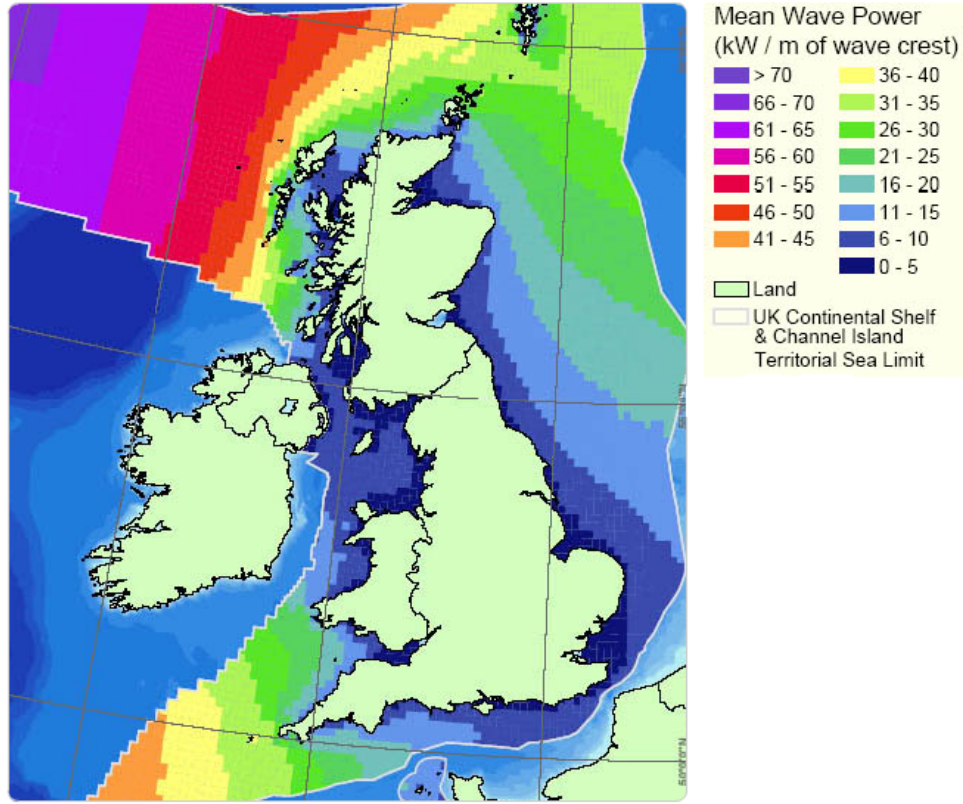


FIGURE 1.2: United Kingdom annual mean power density in United Kingdom territorial sea limits (ABPmer, 2019)

numbers. This phenomenon is already seen when comparing offshore wind turbines to onshore wind turbines, where the largest offshore wind turbines rotor diameter is 220 m (GE Renewable Energy, 2021) compared to onshore wind turbines largest rotor diameter of 170 m (Siemens Gamesa Renewable Energy, 2021). Studies show support for offshore projects among local populations (Wiersma, 2016; Hattam et al., 2015b; Hattam et al., 2015a).

A device used to extract energy from waves is called a Wave Energy Converter (WEC). Energy extraction from waves has been performed for centuries, with the earliest known patent filed in 1799 (Ross, 1995) to directly drive agricultural machinery.

One of the earliest developed concepts was the Oscillating Water Column (OWC) type WEC; originally used as fog horns on harbour buoys, it converted the moving column of water to audio energy rather than electrical energy by forcing air through

channels designed to make a whistling noise as long as the air column was moving. In the 1940s, Japanese naval commander Yoshio Masuda designed a Power Take-Off (PTO) to attach to a navigational buoy, based on an OWC, which was used to charge the buoys batteries. These buoys were later commercialised, primarily in Japan (Masuda, 1971).

In the oil crisis of the 1970s wave energy devices were developed in response to the energy shortage. One such device was the Edinburgh Duck, also known as Salter's Duck after the inventor, Stephen Salter (Salter, 1974). An eccentric float housed gyroscopes which converted rotation of the float to electricity through a generator.

OWCs can be mounted on existing breakwaters. On Islay, Scotland, the Land Installed Marine Powered Energy Transformer (LIMPET) was built in 1991. It began as a 75 kW prototype before a grid-connected 500 kW unit was built in 2000 (Boake et al., 2002; Whittaker et al., 2003). The device also had the facilities to test turbines (Heath, 2003). In a similar vein the Mutriku power plant (Torre-Enciso et al., 2009) in Spain contained multiple turbines with 296 kW of capacity to power nearby houses (Schroeder, 2011). The Pico Power Plant (Falcão et al., 2020) in the Azores, operational between 1999 and 2018, contained a 400 kW turbine and supplied electricity to the local island grid. All of these plants had the advantage of being shore based, and hence easier to access for operations and maintenance.

## 1.1 Wave Energy Converters

Unlike wind turbines, which in the majority have converged to a three blade horizontal axis design, WECs have a multitude of different designs and operation methods. Examples of common types are shown in Figure 1.3, where the Types are as follows:

- Type 1 a point absorber
- Type 2 an attenuator

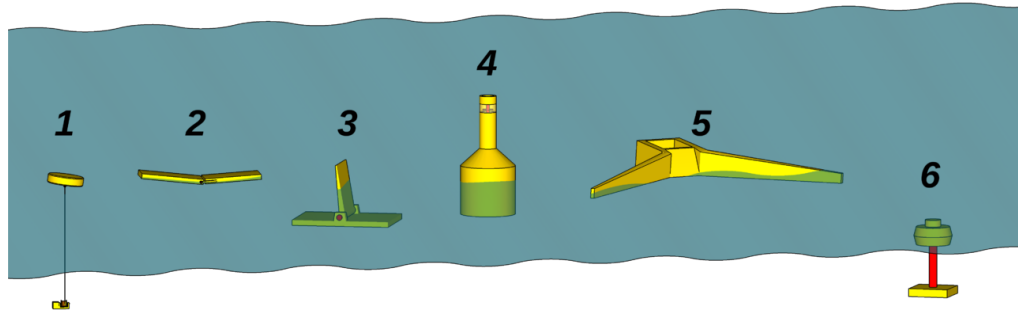


FIGURE 1.3: WEC types by mode of operation. Type 1 corresponds to a point absorber, type 2 an attenuator, type 3 an oscillating wave surge converter, type 4 an OWC, type 5 an OWEC and type 6 a submerged pressure differential device (Straume, 2010)

- Type 3 an Oscillating Wave Surge Converter (OWSC)
- Type 4 an OWC
- Type 5 an Overtopping Wave Energy Converter (OWEC)
- Type 6 a submerged pressure differential device.

A further mode of operation that has been used is the rotating mass, such as the Wello Oy Penguin (Wello Oy, 2021) and the aforementioned Salter's Duck (Salter, 1974), use an eccentric mass rotating about multiple axes. The mass is typically contained within a floating buoy so wave motion in any direction will cause the mass to rotate driving a PTO.

Point absorbers, such as the Ocean Power Technology PowerBuoy (Hart, 2012; Rij et al., 2017a) and Carnegie CETO (Carnegie Clean Energy, 2021; Rafiee and Fiévez, 2015), are devices which utilise the heave motion of the waves to move a body relative to static anchor points. The heave movement drives various PTOs (Göteman et al., 2015a), mechanical, electrical or hydraulic, to generate electrical energy.

Attenuators, such as Pelamis (Retzler, 2006) and M4 (Stansby et al., 2015b; Carpintero Moreno and Stansby, 2019), use the relative motion of individual waves in the wave field at different points along a segmented body to produce relative motion

between the segments. Devices are long compared to the wavelength such that multiple waves are acting on the device along its length, with the PTO located at hinges or couplings between adjoining segments.

Oscillating Wave Surge Converters, such as Oyster (Whittaker et al., 2007; Whittaker and Folley, 2012) and WaveRoller (Mäki et al., 2014; Tan Loh et al., 2016), use the surge of the wave to move a section of the device, typically a flap, about a rotating hinge. The flap is submerged and the wave action causes it to oscillate about a rotating hinge, powering a PTO.

OWCs use the motion of the water surface contained within a chamber to push air through a turbine. These devices can be shore mounted, such as LIMPET (Heath et al., 2001), Pico (Falcão, 2000) and Mutriku Wave Power Plant (Torre-Enciso et al., 2009), or floating, such as Spar Buoy (Collins et al., 2017) and OE Buoy (Lavelle and Kofoed, 2011). The turbine can be bi-directional, thus generating electricity on the rise and fall of the water surface, however using a system of valves to redirect the air flow through a uni-directional turbine increases efficiency.

Submerged pressure differential devices, such as Bombora's mWave (Bombora, 2020) and Anaconda (Mendes et al., 2017), use the hydrostatic pressure of passing waves to generate electricity. This can be in the form of pumping a fluid, for example air or hydraulics, through flexible areas of the device.

Finally, OWECs, such as the subject of this thesis, the WaveCat, as well as Wave Dragon (Kofoed et al., 1998) and Sea Slot-Cone Generator (SSG) (Margheritini, 2009), utilise the increase in surface elevation due to wave action to capture water in a collection reservoir in the device. The water is then released through low-head turbines back to the sea.

Other notable OWECs include the Wave Dragon and the SSG. The Wave Dragon is a floating OWEC that has been tested in sea conditions in Nisum Bredning, Denmark (Frigaard et al., 2004). The SSG is a shore mounted OWEC intended for deployment in breakwaters and other coastal structures, and tested around the Isle

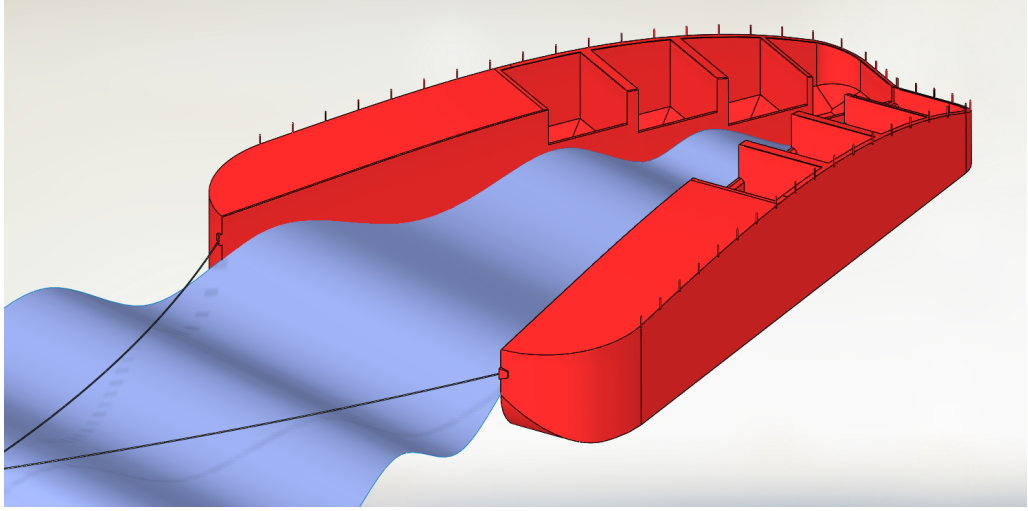


FIGURE 1.4: The WaveCat concept design, a twin-hulled device with a variable opening angle. It has four chambers in each hull which collect water from the wave field

of Kvitsøy (Vicinanza et al., 2015). Both devices utilise reservoirs and low head turbines to capture overtopping waves and generate electricity. The WaveCat shares principles of wave energy conversion with the Wave Dragon and SSG in that it captures overtopping water from waves and drains it through low head turbines to generate electricity. It differs in that it relies instead on the principle of oblique overtopping compared to a frontal overtopping method employed by the Wave Dragon and SSG.

## 1.2 The WaveCat Device

The WaveCat device is a floating OWEC (Fernández et al., 2012a) and was the main focus of the experimental campaign presented in this thesis.

The WaveCat is based on the principle of oblique overtopping and wave concentration, which has several advantages over devices that use frontal overtopping to generate electricity. Firstly, the overtopping occurs at an angle to the device, rather than directly on to a frontal ramp, reducing structural loads by spreading the wave action over a larger point of contact. Secondly, variations in wave height and device positioning merely changes the point at which overtopping occurs along the device,

whereas pitch and heave motion in particular may negatively impact overtopping over a frontal ramp if at an unfavourable angle. Lastly, the freeboard of the inner edge of the WaveCat decreases along the device towards the stern. As waves decrease in height due to overtopping the resulting decrease in freeboard allows overtopping to continue along the device and spread into multiple overtopping chambers.

At full scale the WaveCat is intended to be approximately 90 m in length, chosen to be longer than short period wind-wave wavelengths but of the order of longer period swell wavelengths. There are four overtopping chambers in each hull, for a total of eight chambers on the whole device. At the base of each chamber the collected water is released through a low-head turbine and exhausted through the keel of the device. The hulls are able to move relative to each other about a fixed hinge point at the stern of the device to control the distance between bows and therefore the size of the aperture into which waves propagate. The device is intended to be moored in deep water.

The trim and freeboard of the device can be controlled by pumping water to and from a series of ballast tanks underneath the overtopping chambers. Combined with the variable angle of the hulls the device can regulate the point at which waves begin overtopping along the inner edge.

When in operation the device is moored with a Catenary Anchor Leg Mooring (CALM) which allows it to passively orient itself with the predominant wave field (Harris et al., 2004). As a survival measure the WaveCat can bring the two hulls together, i.e. a wedge angle of  $0^\circ$ , to act as a monohull vessel and ride extreme conditions out as a ship at anchor would.

### 1.3 Aims and Objectives

Given the capabilities of the WaveCat, the stage of development it is currently at, and the research opportunities available to it, the overall aim of the research



programme is to advance the knowledge of the WaveCat and form a better understanding of the behaviour of the device. As such the research aims of the thesis are:

- Establish experimentally how characteristics and behaviour of the device, namely the wedge angle and motions, affect the wave field under a range of monochromatic and random waves and develop generalised equations for them.
- Investigate numerically modelling the devices motions under wave action and validate with physical results.

The specific objectives to achieve these research aims are:

- Design and build an updated scale model of the WaveCat for physical model testing in the Ocean Basin in the University of Plymouth COAST Laboratory.
- Perform tests using a wide range of wave conditions for monochromatic and random wave states, using two different wedge angles of the device.
- Investigate the nature of the reflection of the device, the transmission past the device and the absorption of the device and how this impacts the estimated power production of the device.
- Investigate how the motion response of the device impacts the reflection, transmission and absorption of the device, as well as the estimated power production.
- Develop and validate a numerical model of WaveCat device motions to incident wave conditions in absence of overtopping.

## 1.4 Thesis Structure

The thesis is structured as follows. Chapter 2 explores the current state-of-the-art and identifies research opportunities. Chapter 3 shows the WaveCat model that

was built for this thesis, identifies the test cases performed and the experimental method of the physical modelling. Chapter 4 describes the analysis methods used to analyse the experimental data, provides examples of test cases and shows the numerical modelling development of the WaveCat model. Chapter 5 describes the results of the experiments focussed on wave field coefficients and power generation, then compares the two wedge angle configurations tested and discusses the results. Chapter 6 describes the results of the experiments focussed on the WaveCat responses and Response Amplitude Operators (RAOs) to regular and random waves, with comparison between the two wedge angle configurations tested and discusses the results. Chapter 7 describes the results of numerical modelling during regular waves with respect to device motion and discusses the results. Finally, Chapter 8 summarises the methods and findings of the thesis in the context of the wider community, highlights recommendations and suggests future work.

## Chapter 2

# Background to Wave Energy Extraction

### 2.1 Introduction

This thesis is focussed on the WaveCat, shown in Figure 1.4, a floating OWEC in the early stages of development that uses overtopping to generate power. The WaveCat was chosen for two reasons: (i) the author's familiarity with the device from past studies, and (ii) the flexibility afforded in the design to make operational changes quickly and efficiently between and during testing periods.

Within this Chapter the key principles of wave energy theory and wave energy extraction that the WaveCat is based on are introduced. A summary of devices in the field provide a dataset with which to conduct benchmarking comparisons. Techniques for physical modelling of WECs at scale are also presented. Numerical studies are investigated and suitable numerical modelling software chosen to achieve the research aims. Finally, research gaps and key findings are highlighted.

## 2.2 Review of Current Technologies

This thesis focusses on the WaveCat WEC, a floating moored overtopping device. Other WECs have been designed and tested in physical model tests and in small scale prototype deployments. A summary of these devices performance is presented here to contextualise the results of this thesis within the wider community of devices. Devices were selected for comparison where data was available for their performance, as well as devices with similar operation to WaveCat.

### 2.2.1 WaveCat

Iglesias et al. (2011) and Fernández et al. (2012b) presented the concept of the WaveCat, the subject of this thesis. They also demonstrated the proof of concept of the WaveCat and presented a selection of fixed physical model tests performed on a 1:30 scale model showing the devices ability to capture overtopping water, and described the development of a numerical model of the WaveCat. Two sets of wave conditions were tested for four different wedge angles. During the tests it was shown that the device was collecting water in the reservoirs using level sensors, however no quantities were given.

Fernández et al. (2012a) expands on the previous results with a floating model and showed the power generation,  $k_r$  and  $k_t$  values for the device, at various wedge angles. These tests showed that the wedge angle had little effect on the reflection and transmission coefficients of the device for the two sets of waves tested. It also showed that the device had the potential to generate the most power for waves of longer period and higher amplitude, when considering a constant wedge angle.

This thesis expands on the concept model with a redesigned overtopping measurement system, a changed hull design allowing greater control of the positioning of the device, in depth analysis of the frequency dependent nature of transmission, reflection and absorption, a detailed analysis of the motion of the device, and a numerical Computational Fluid Dynamics (CFD) model of the device motion. The research



FIGURE 2.1: The Wave Dragon in Nissum Bredning (Tedd et al., 2006)

aims of this thesis are to expand the range of wave conditions tested previously, and to use monochromatic as well as random sea states whilst investigating the impact on the wave field.

The key difference between WaveCat, the Wave Dragon and the SSG, discussed below, is that the WaveCat uses oblique overtopping rather than frontal overtopping. This presents an additional factor to consider in that the waves interacting with the WaveCat will be approaching the device at an angle, however they will also be guided into an ever decreasing horizontal space which will increase wave height in the wedge, causing continuous overtopping along the inner edge of the device and spreading the wave forces (Allen et al., 2016; Iglesias et al., 2011).

The WaveCat is also able to be closed in storm situations, as described in the concept (Iglesias et al., 2011; Fernández et al., 2012b), allowing the device to behave more akin to a traditional ship, for which established methods of construction and performance will reduce costs towards commercialisation.

### 2.2.2 Wave Dragon

The Wave Dragon OWEC, Figure 2.1, is a floating slack-moored device with two large patented wave reflector arms to direct and enhance wave height towards a ramp

and into a reservoir above sea level (Martinelli and Frigaard, 1999). The collected water is then released through low-head Kaplan turbines (Frigaard et al., 2004) to generate power. The Wave Dragon has undergone extensive tank and prototype testing following a Technology Readiness Assessment approach in which each new phase of development is justified by good results in prior phases (Friis-Madsen et al., 2012). The development of the device has largely been carried out through physical testing, both wave tank testing and large scale prototype, the latter of which had over 20,000 hours of testing (Sorensen, 2006). It was shown that the wave transmission is sensitive to the wavelength, with longer wavelengths resulting in higher transmission of wave power (Nørgaard and Andersen, 2012).

Wave tank testing of the Wave Dragon occurred at 1:45 scale to gather data on the reflectors, ramp and the energy efficiency of the device (Nielsen and Kofoed, 1997). Further tests were also performed (Kofoed et al., 1998; Kofoed et al., 2000) to establish design parameters of important components, such as turbine flow, reflector arms and type of turbine. Physical model testing of the Wave Dragon at various stages of its development was carried out (Kofoed et al., 2006), primarily on the 1:4.5 prototype deployed at a sheltered inland sea area in Denmark (Nissum Bredning) (Tedd et al., 2006), but also on smaller scale physical models in wave tanks (Parmeggiani et al., 2010). Specific attention was paid to the PTO (Frigaard et al., 2004) and control strategies studied (Zhou et al., 2009; Igic et al., 2011).

A wave propagation model in MIKE21BW measured wave height reduction of the Wave Dragon during 1:51.8 physical model testing. The outputs are compared to a simplified approach using integration of wave energy flux and show a maximum deviation in transmitted wave power behind the device of 4.63% (Nørgaard and Andersen, 2012).

The power matrix of the Wave Dragon (Silva et al., 2013; Kofoed et al., 2006) is shown in Figure 2.2. It shows the power generated by the full scale Wave Dragon for  $H_s$  in the range of 1 m to 7 m at 1 m intervals, and the  $T_p$  in the range of 5 s to 17 s in 1 s intervals. Power generation is highest in the largest wave height conditions of 7 m and between periods of 10 s to 15 s. At lower wave heights the maximum power

$T_p$ (s) $H_s$ (m)	Power matrix (in kW)												
	5	6	7	8	9	10	11	12	13	14	15	16	17
1	160	250	360	360	360	360	360	360	320	280	250	220	180
2	640	700	840	900	1190	1190	1190	1190	1070	950	830	710	590
3	0	1450	1610	1750	2000	2620	2620	2620	2360	2100	1840	1570	1310
4	0	0	2840	3220	3710	4200	5320	5320	4430	3930	3440	2950	2460
5	0	0	0	4610	5320	6020	7000	7000	6790	6090	5250	3950	3300
6	0	0	0	0	6720	7000	7000	7000	7000	7000	6860	5110	4200
7	0	0	0	0	0	7000	7000	7000	7000	7000	7000	6650	5740

FIGURE 2.2: Power matrix (kW) of the Wave Dragon against  $H_s$  on the vertical axis and  $T_p$  on the horizontal axis (Silva et al., 2013; Kofoed et al., 2006)



FIGURE 2.3: The SSG design (Vicinanza and Frigaard, 2008)

for that height is achieved at wave periods of between 10 s and 12 s, representing the ideal operating conditions of the Wave Dragon.

### 2.2.3 Sea Slot-Cone Generator

The SSG, Figure 2.3 (Vicinanza and Frigaard, 2008), is a shore mounted OWEC. It consists of multiple chambers which collect water from wave run-up, the chambers are at varying heights allowing water to be captured at higher potential energy between reservoirs (Kofoed et al., 2002). The wave pressure acting on the SSG was experimentally assessed (Vicinanza and Frigaard, 2008), as well as the wave loading (Vicinanza et al., 2011). Different breaker types were experimentally analysed to determine the pressure exerted on an SSG device by the differing types of breaker (Buccino et al., 2013). It was shown that steep run-up ramps favour the occurrence

$T_e$ (s) $H_s$ (m)	Power matrix (in kW)													
	5	5.5	6	6.5	7	7.5	8	8.5	9	9.5	10	10.5	11	11.5
0.5	99	109	119	129	139	149	159	169	179	189	198	208	218	228
1	397	437	476	516	556	595	635	675	715	754	794	833	873	913
1.5	893	982	1072	1161	1250	1340	1429	1518	1608	1697	1786	1875	1965	2054
2	1588	1746	1905	2064	2223	2381	2540	2699	2858	3016	3175	3334	3493	3651
2.5	2481	2729	2977	3225	3473	3721	3969	4217	4465	4713	4961	5209	5457	5705
3	3572	3929	4287	4644	5001	5358	5715	6073	6430	6787	7144	7501	7859	8216
3.5	4862	5348	5834	6321	6807	7203	7779	8265	8751	9238	9724	10210	10695	11183
4	6350	6985	7620	8256	8891	9526	10161	10796	11431	12066	12701	13336	13971	14606
4.5	8037	8841	9645	10448	11252	12056	12860	13663	14467	15271	16074	16878	17682	18486
5	9923	10915	11907	12899	13892	14884	15876	16868	17860	18853	19845	20837	21829	22821
5.5	12,006	13,207	14,407	15,608	16,809	18,009	19,210	20,410	21,610	22,810	24,010	25,210	26,410	27,610
6	14,288	15,717	17,146	18,575	20,000	20,000	20,000	20,000	20,000	20,000	20,000	20,000	20,000	20,000
6.5	16,769	18,446	20,000	20,000	20,000	20,000	20,000	20,000	20,000	20,000	20,000	20,000	20,000	20,000
7	19,448	20,000	20,000	20,000	20,000	20,000	20,000	20,000	20,000	20,000	20,000	20,000	20,000	20,000
7.5	20,000	20,000	20,000	20,000	20,000	20,000	20,000	20,000	20,000	20,000	20,000	20,000	20,000	20,000
8	20,000	20,000	20,000	20,000	20,000	20,000	20,000	20,000	20,000	20,000	20,000	20,000	20,000	20,000

FIGURE 2.4: Power matrix (kW) of the SSG against  $H_s$  on the vertical axis and  $T_e$  on the horizontal axis (Silva et al., 2013; Vicinanza et al., 2012)

of surging breakers which dissipate less energy than spilling or plunging breakers (Vicinanza et al., 2012), however this also increases reflection. The structural response of the SSG under random waves was modelled using the Flow3D (Flow Science Inc, 2021) CFD package and compared to the experimental results (Vicinanza et al., 2011), with differences attributed to the presence of air in the physical model tests (Vicinanza et al., 2015).

The power matrix of the SSG (Silva et al., 2013; Vicinanza et al., 2012) is shown in Figure 2.4. It shows the power generated by the full scale SSG for  $H_s$  in the range of 0.5 m to 8 m at 0.5 m intervals, and the  $T_e$  in the range of 5 s to 11.5 s in 0.5 s intervals. The power matrix shows that SSG generates the most power at larger periods, and when wave height increases waves of shorter period are able to generate high power too.

## 2.2.4 Pelamis

The Pelamis, Figure 2.5 (Yemm et al., 2012), is an attenuator consisting of multiple tubular sections attached via hinge joints. Relative motion between the sections is restrained by hydraulic rams that pump fluid into high-pressure containers, from





FIGURE 2.5: The Pelamis attenuator in Portugal (Yemm et al., 2012)

$T_e(s)$ $H_s(m)$	Power matrix (in kW)																
	5	5.5	6	6.5	7	7.5	8	8.5	9	9.5	10	10.5	11	11.5	12	12.5	13
0.5	0	0	0	0	0	0	0	0	0	0	0	0	0	0	0	0	0
1	0	22	29	34	37	38	38	37	35	32	29	26	23	21	0	0	0
1.5	32	50	65	76	83	86	86	83	78	72	65	59	53	47	42	37	33
2	57	88	115	136	148	153	152	147	138	127	116	104	93	83	74	66	59
2.5	89	138	180	212	231	238	238	230	216	199	181	163	146	130	116	103	92
3	129	198	260	305	332	340	332	315	292	266	240	219	210	188	167	149	132
3.5	0	270	354	415	438	440	424	404	377	362	326	292	260	230	215	202	180
4	0	0	462	502	540	546	530	499	475	429	384	366	339	301	267	237	213
4.5	0	0	544	635	642	648	628	590	562	528	473	432	382	356	338	300	266
5	0	0	0	739	726	731	707	687	670	607	557	521	472	417	369	348	328
5.5	0	0	0	750	750	750	750	750	737	667	658	586	530	496	446	395	355
6	0	0	0	0	750	750	750	750	750	750	711	633	619	558	512	470	415
6.5	0	0	0	0	750	750	750	750	750	750	750	743	658	621	579	512	481
7	0	0	0	0	0	750	750	750	750	750	750	750	750	676	613	584	525
7.5	0	0	0	0	0	0	750	750	750	750	750	750	750	750	686	622	593
8	0	0	0	0	0	0	0	750	750	750	750	750	750	750	750	690	625

FIGURE 2.6: Power matrix (kW) of Pelamis against  $H_s$  on the vertical axis and  $T_e$  on the horizontal axis (Silva et al., 2013; Henderson, 2006)

which controlled flow is released to drive induction generators. Model tests were performed at scales between 1:80 and 1:7 to develop knowledge of device absorption and survivability (Yemm et al., 2012).

The power matrix of the Pelamis (Silva et al., 2013; Henderson, 2006) is shown in Figure 2.6. It shows the power generated by the full scale 180 m long Pelamis for  $H_s$  in the range of 0.5 m to 8.0 m at 0.5 m intervals, and the  $T_e$  in the range of 5 s to 13 s in 0.5 s intervals. The Pelamis power matrix shows greater power generation when the waves are higher and shorter.

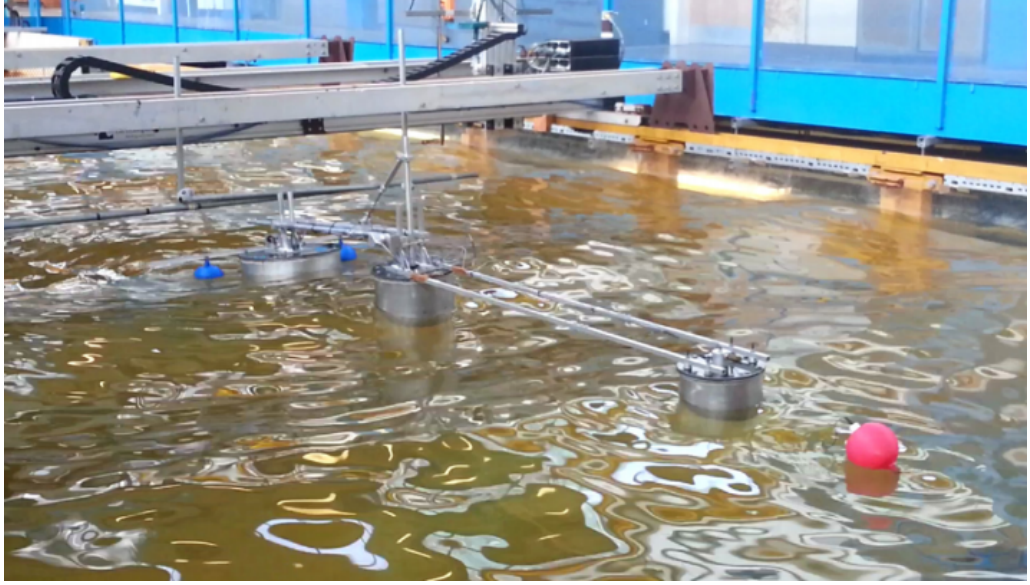


FIGURE 2.7: The M4 device in experimental tests (Stansby et al., 2017)

### 2.2.5 M4

The M4, Figure 2.7 (Stansby et al., 2017), is an attenuator with bow and stern floats that are individually attached to a central float via rigid bars, providing relative movement between the two pairs of floats (Stansby et al., 2014). The device geometry was optimised to allow high crest capture widths for a wide band of frequencies (Stansby et al., 2015b). Capture Width Ratios (CWRs) of the device were shown to be highest when the wavelength is approximately half that of the float spacing (Stansby et al., 2015c). It has been speculated that PTO optimisation may yield better results (Liao et al., 2020), with the PTO concept further developed (Gaspar et al., 2021). A version of the device with 6 floats in total has also been tested (Carpintero Moreno and Stansby, 2019), based on time-domain linear modelling (Stansby et al., 2017), which showed an increase in capacity for the device.

### 2.2.6 AquaBuOY

The AquaBuOY, Figure 2.8 (Munteanu, 2015), is a heaving point absorber that uses the motion of the buoy in waves relative to an underwater tube to pressurise water directed into a Pelton turbine to generate electricity (Weinstein et al., 2003). Each

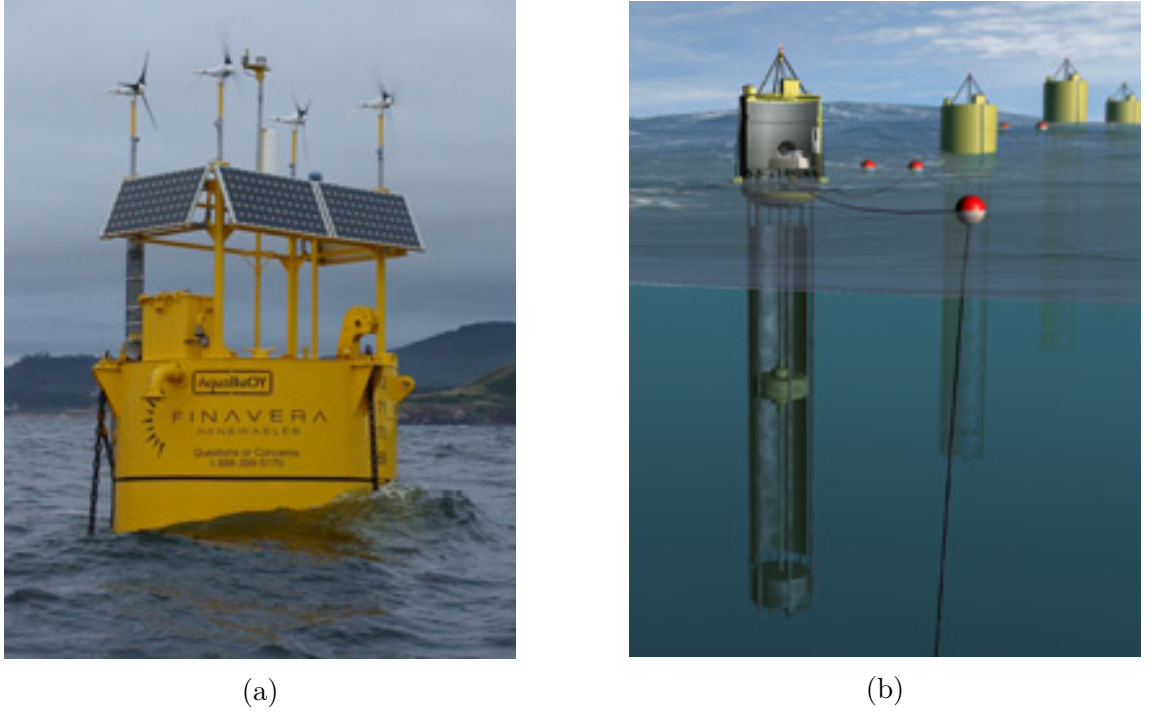


FIGURE 2.8: a) The AquaBuOY device, b) section view (Munteanu, 2015)

$T_p$ (s) $H_s$ (m)	Power matrix (in kW)												
	5	6	7	8	9	10	11	12	13	14	15	16	17
1	0	0	8	11	12	11	10	8	7	0	0	0	0
1.5	0	13	17	25	27	26	23	19	15	12	12	12	7
2	0	24	30	44	49	47	41	34	28	23	23	23	12
2.5	0	37	47	69	77	73	64	54	43	36	36	36	19
3	0	54	68	99	111	106	92	77	63	51	51	51	27
3.5	0	0	93	135	152	144	126	105	86	70	70	70	38
4	0	0	0	122	176	198	188	164	137	112	91	91	49
4.5	0	0	0	223	250	239	208	173	142	115	115	115	62
5	0	0	0	250	250	250	250	214	175	142	142	142	77
5.5	0	0	0	250	250	250	250	250	211	172	172	172	92

FIGURE 2.9: Power matrix (kW) of the AquaBuOY against  $H_s$  on the vertical axis and  $T_p$  on the horizontal axis (Silva et al., 2013; Weinstein et al., 2004)

device is approximately 4.5 m to 6 m in diameter and was installed in water depths of up to 45 m to 75 m during ocean trials.

The power matrix of the AquaBuOY (Silva et al., 2013; Weinstein et al., 2004) is shown in Figure 2.9. It shows the power generated by the full scale AquaBuOY for  $H_s$  in the range of 1 m to 5.5 m at 0.5 m intervals, and the  $T_p$  in the range of 5 s to 17 s in 1 s intervals.



FIGURE 2.10: The Oyster device (Whittaker and Folley, 2012)

### 2.2.7 Oyster

The Oyster, Figure 2.10 (Whittaker and Folley, 2012), is an OWSC type device that uses the surge of the waves to drive hydraulic pistons, pumping high-pressure water to an onshore generator. It is intended to be mounted to the seabed in shallow, near-shore areas (Folley et al., 2004). It was shown that the natural frequency of the device varied depending on water depth and width of the device (Folley et al., 2007b), and overall performance was also enhanced in shallower water (Folley et al., 2007a). After test deployment it was shown that OWSCs have a natural survival aspect, as they decouple from larger waves and the overall flap sweep is increased (Whittaker and Folley, 2012).

The power matrix of the Oyster (Silva et al., 2013; Whittaker et al., 2007) is shown in Figure 2.11. It shows the power generated by the full scale Oyster for  $H_s$  in the range of 0.5 m to 6.0 m at 0.5 m intervals, and the  $T_e$  in the range of 5 s to 13 s in 1 s intervals. The Oyster generates the most power in high wave heights, and

$T_e$ (s) $H_s$ (m)	Power matrix (in kW)								
	5	6	7	8	9	10	11	12	13
0.5	0	0	0	0	0	0	1	3	3
1	20	30	38	42	44	44	45	47	45
1.5	80	85	92	97	102	103	104	100	104
2	140	147	152	158	155	155	160	161	156
2.5	192	197	208	202	203	209	211	201	204
3	241	237	237	241	243	230	236	231	235
3.5	0	271	272	269	268	267	270	260	260
4	0	291	290	290	280	287	276	278	277
4.5	0	291	290	290	280	287	276	278	277
5	0	0	290	290	280	287	276	278	277
5.5	0	0	290	290	280	287	276	278	277
6	0	0	290	290	280	287	276	278	277

FIGURE 2.11: Power matrix (kW) of the Oyster against  $H_s$  on the vertical axis and  $T_e$  on the horizontal axis (Silva et al., 2013; Whittaker et al., 2007)

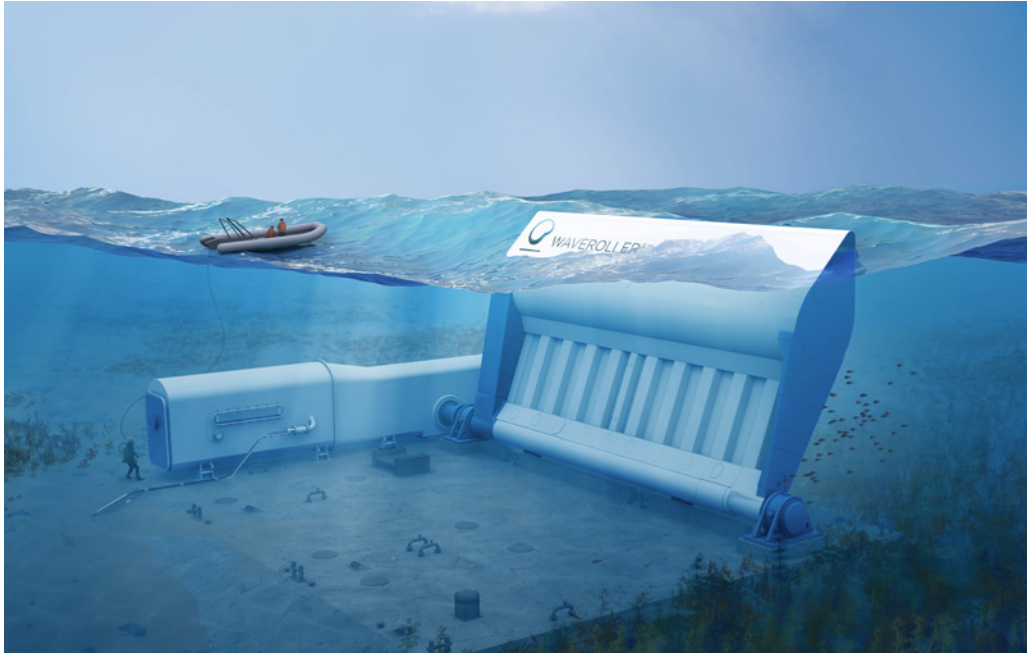


FIGURE 2.12: The WaveRoller device (AW-Energy, 2020)

when wave period is larger it generates comparatively less power for the same wave height.

## 2.2.8 WaveRoller

The WaveRoller, Figure 2.12 (AW-Energy, 2020), is an OWSC similar in working principle to Oyster and is deployed completely submerged (Mäki et al., 2014). Physical experiments at 1:24 scale were carried out (Lucas et al., 2012) and the results



$\frac{T_e(s)}{H_s(m)}$	5	6	7	8	9	10	11	12	13	14	15
1	0.043	0.051	0.060	0.062	0.065	0.065	0.064	0.061	0.061	0.057	0.057
2		0.198	0.226	0.238	0.232	0.240	0.233	0.225	0.212	0.197	0.191
3			0.465	0.485	0.491	0.454	0.463	0.454	0.440	0.408	0.399
4				0.744	0.697	0.782	0.745	0.698	0.722	0.659	0.631
5					0.973	1.000	0.998	0.982	0.953	0.889	0.844

FIGURE 2.13: The WaveRoller normalised power matrix (adapted from Mäki et al. (2014))

validated in a WaveDyn model for a number of parameters, including position of the flap and velocity of the flap movement. An OpenFOAM model was also validated (Tan Loh et al., 2016) for flap motion and the PTO replicated using a linear damper system.

Figure 2.13 (Mäki et al., 2014) shows the WaveRoller power matrix normalised with respect to the highest power state, which occurs at  $H_s$  of 5 m and  $T_p$  of 10 s. The power matrix shows  $H_s$  in the range of 1.0 m to 5.0 m at 1.0 m intervals, and the  $T_e$  in the range of 5 s to 15 s in 1 s intervals. It is unknown how much power is produced, but trends between conditions can be determined.

### 2.2.9 Limpet

The LIMPET, Figure 2.14 (Boake et al., 2002), is a shore-mounted OWC on the Isle of Islay, Scotland. It has an installed capacity of 500 kW through two counter-rotating Wells turbines (Heath, 2003). The primary structure consisted of three water columns made from concrete and inclined at a  $40^\circ$  angle to the horizontal (The Queen's University Belfast, 2002).

A series of 1:40 scale model tank tests were performed and the turbine efficiency compared between model and full-scale (Boake et al., 2002). It was shown that the model efficiency was higher than the real efficiency due to the LIMPET turbine stalling thanks to the oscillatory nature of the air flow (Folley et al., 2002). The power generated by the LIMPET was heavily dependent on the bathymetry at the



FIGURE 2.14: The LIMPET device (Boake et al., 2002)

site, with research suggesting that a water depth 2 m deeper and a sloping sea bed would have increased the power production (Whittaker et al., 2004).

The LIMPET was decommissioned in 2018, with the majority of the structure removed except for the concrete wave chamber (Scottish Government, 2019).

### 2.2.10 Pico Power Plant

The Pico power plant, Figure 2.15 (Falcão et al., 2020), is a shore-mounted OWC on the island of Pico, in the Azores. It was designed as a dual purpose facility, to provide power to the local island and to be used as a research and development facility. A 1:35 scale model (Sarmiento, 1993) was tested as well as a 1:25 model (Holmes et al., 1995) to provide information on the PTO. The performance of the plant was also simulated numerically (Brito-Melo et al., 2001), from which the decision to use Wells turbines was made. During operation the efficiency of the 12 m wide plant plant was examined and found to be 20% in wave resource of 38 kW/m (Pecher et al., 2011).

Figure 2.16 (Monk et al., 2013), shows the Pico power plant power matrix using data recorded from the installation site. The conditions that produced the highest



FIGURE 2.15: The Pico device (Falcão et al., 2020)

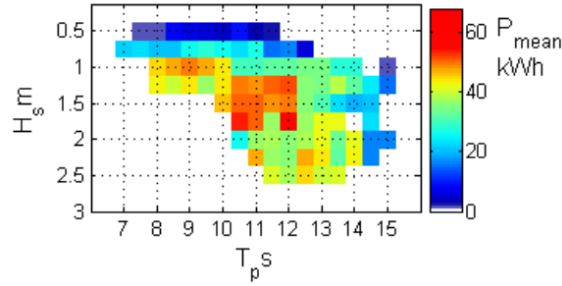


FIGURE 2.16: Power matrix of the Pico power plant (Monk et al., 2013)

power were at  $H_s$  between 1.25 m and 1.75 m and  $T_p$  between 10 s and 12 s. Higher wave heights were recorded but they produced less power.

### 2.2.11 OE Buoy

The OE Buoy, Figure 2.17 (OceanEnergy, 2020), is a floating OWC tested at 1:4 scale in Galway Bay, Ireland (Rourke et al., 2009). It behaves like a shore mounted OWC with added motion from the device contributing to the water surface elevation velocity (Greaves and Iglesias, 2018). Testing was shown to have unforeseen problems (Kelly et al., 2014), such as a seal in the water cooling system for the diesel





FIGURE 2.17: The OE Buoy device (OceanEnergy, 2020)

generator failing completely leaving the device unable to charge batteries. This can be mitigated in newer devices with forewarning and preparation. Valuable data was still collected, including motion data, wind speed and direction and rotational speed of the generator shaft. The report recommends several lessons to future deployments, such as installation of multiple redundant sensors to protect against single points of failure and the ability to remotely reset all control elements to minimise maintenance operations on the device.

Figure 2.18 (Lavelle and Kofoed, 2011), shows the OE Buoy power matrix based on the measured efficiency of the device when at the Galway Bay test site. Only conditions that occurred in the Galway Bay test site were measured, thus the power matrix is limited to those conditions. The conditions that produced the most power were those of the highest wave heights. When wave height was constant the conditions with the lower wave period produced more than those of higher wave periods.

## 2.3 Wave Energy Theory

As described in Chapter 1, the ocean is excited by winds blowing across the ocean surface and imparting energy into the water through friction and pressure variation.

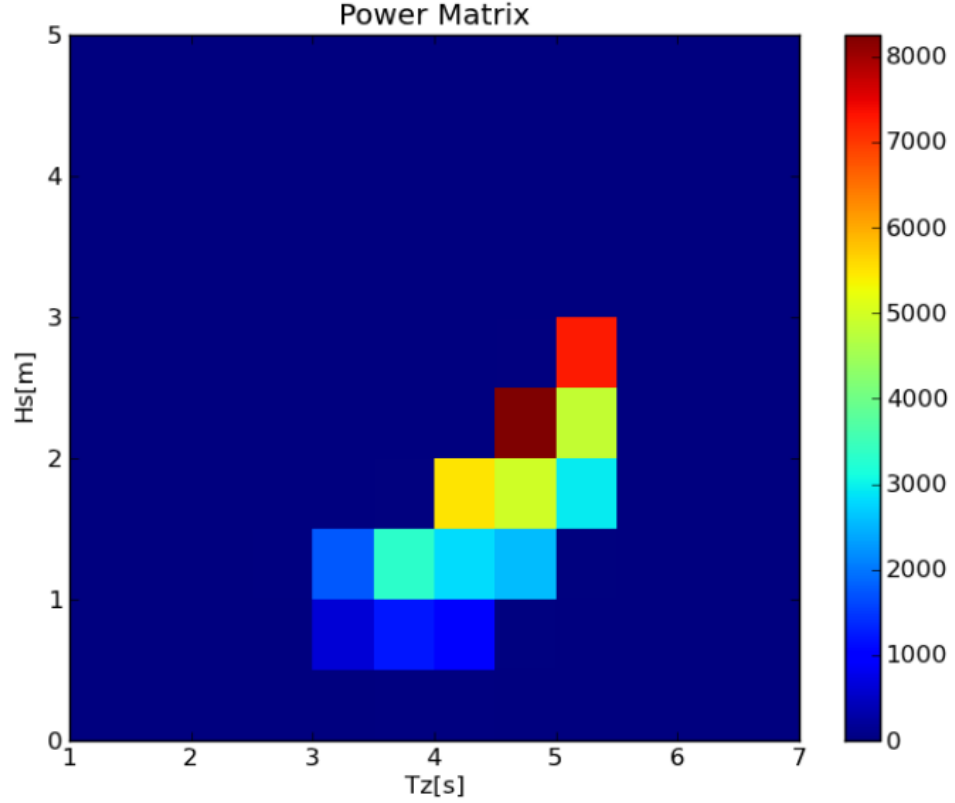


FIGURE 2.18: Power matrix of the OE Buoy with power in Watts (Lavelle and Kofoed, 2011)

The energy in ocean waves is transferred through the movement of the particles that make up the wave, as the energy passes through the water surface the particles are set into motion. When under a peak the particles travel with wave propagation direction and under a trough they travel in the opposite direction. The magnitude of motion is dependent on several factors, including the wave height, the water depth and the wave period.

Figure 2.19 shows the stages of water particle orbital motion under a progressive wave peak (Straume, 2014). The orbit is effectively circular when the water is deep and becomes more elliptical as the depth becomes shallower. The WaveCat is designed to capture water from the surface of the ocean as the region is most energetic.

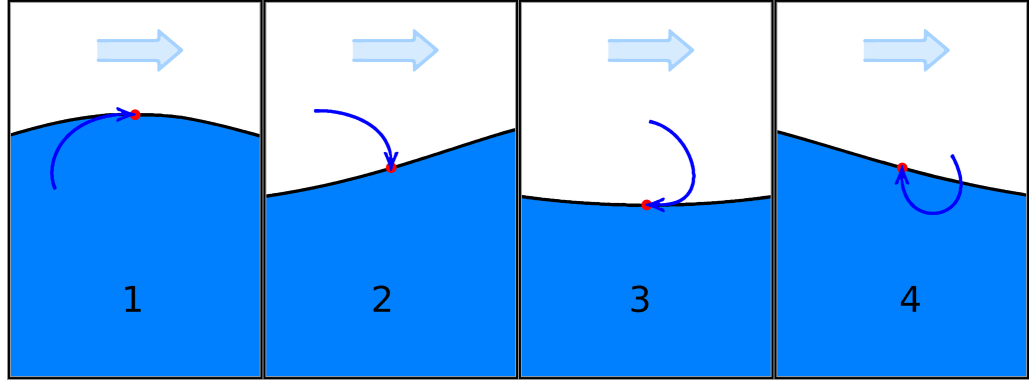


FIGURE 2.19: Orbital motion displacement direction under wave action, panel 1 showing the motion in the same direction as wave propagation when under a wave peak. Panel 2 shows displacement changing from horizontal to vertical between peak and trough. Panel 3 shows the displacement in the opposite direction to propagation under a trough. Panel 4 shows the motion returning from horizontal to vertical between trough and peak (Straume, 2014).

In linear wave theory, alternatively known as Airy wave theory, the displacement of the free surface is given by

$$\eta = \frac{H}{2} \cos \left( \frac{2\pi}{\lambda} x - \frac{2\pi}{T} t \right) \quad (2.1)$$

where  $\eta$  (m) is the free surface elevation,  $H$  is the wave height (m),  $\lambda$  the wavelength (m) and  $T$  the wave period (s). Wave amplitude (m), wavenumber ( $\text{m}^{-1}$ ) and angular frequency ( $\text{rads}^{-1}$ ),  $A$ ,  $k$  and  $\omega$  respectively, are related to the above equation by

$$A = \frac{H}{2} \quad (2.2)$$

$$k = \frac{2\pi}{\lambda} \quad (2.3)$$

and

$$\omega = \frac{2\pi}{T} \quad (2.4)$$

respectively. The wavenumber and angular frequency are related through the dispersion relationship

$$\omega^2 = gk \tanh(kd) \quad (2.5)$$

where  $d$  is the water depth (m) and  $g$  is gravitational acceleration ( $\text{ms}^{-2}$ ). Using equations 2.3 and 2.4, the dispersion relationship can be redefined in terms of wavelength, wave period and water depth.

$$\lambda = \left( \frac{gT^2}{2\pi} \right) \tanh \left( \frac{2\pi d}{\lambda} \right) \quad (2.6)$$

for which  $\lambda$  can be solved iteratively.

The power contained within an area of wave surface,  $E$  ( $\text{Jm}^{-2}$ ), can be expressed as

$$E = \frac{1}{8} \rho g H^2 \quad (2.7)$$

where  $\rho$  is the density of the medium ( $\text{kgm}^{-3}$ ). The wave power per metre of wave front,  $P$  ( $\text{Wm}^{-1}$ ), can be expressed as

$$P = E c_g \quad (2.8)$$

where  $c_g$  is the group velocity of the waves ( $\text{ms}^{-1}$ ).  $c_g$  is related to the phase velocity,  $c$  ( $\text{ms}^{-1}$ ) by

$$c_g = n c \quad (2.9)$$

with  $n$  (-) and  $c$  given by

$$n = \frac{1}{2} \left( 1 + \frac{2kd}{\sinh(2kd)} \right) \quad (2.10)$$

$$c = \frac{gT}{2\pi} \tanh \left( \frac{2\pi d}{\lambda} \right) \quad (2.11)$$

respectively. These relations are valid for intermediate depth waters, i.e. all values of  $\lambda$  and  $d$ .

When considering random sea states, which consist of a superposition state of many individual waves, wave power takes the form of

$$P = \frac{\rho g^2}{64\pi} H_s^2 T_e \quad (2.12)$$

where  $H_s$  (m) is the significant wave height and  $T_e$  (s) is the energy period (Greaves and Iglesias, 2018). Significant wave height can be defined in several ways as shown below

$$H_{1/3} = 4\sigma_\eta = 4.004\sqrt{m_0} \approx 4\sqrt{m_0} = H_s \quad (2.13)$$

in which  $H_{1/3}$  (m) the  $H_s$  derived from zero-upcrossings,  $\sigma_\eta$  is the standard deviation of the surface elevation and  $m_0$  ( $\text{m}^2$ ) is the zeroth-order moment of the variance spectrum, given as

$$m_0 = \int_0^\infty S(f)df = \sigma_\eta^2 \quad (2.14)$$

with  $S(f)$  ( $\text{m}^2\text{s}^{-1}$ ) the variance spectral density (Holthuijsen, 2007).

$T_e$  is related to the  $T_p$ , peak period, of a spectrum depending on its shape. A JONSWAP spectrum, for example, follows the relationship

$$T_e = \frac{T_p}{1.11} \quad (2.15)$$

whereas a Bretschneider spectrum follows (Cahill and Lewis, 2014)

$$T_e = \frac{T_p}{1.17} \quad (2.16)$$

JONSWAP spectra represent a fetch limited sea state typical of the North Sea in which the sea state is never fully developed (Isherwood, 1987). A Bretschneider spectrum represents a fully developed sea state (Tucker, 1991). The choice of spectrum type when generating waves during physical model tests therefore has an impact on the individual wave constituents of the spectra, as properties will be different depending on the spectral shape.

The concept of the Capture Width (CW) (m) (Budar and Falnes, 1975) allows power captured by a device to be compared to the wave power available.

$$CW = \frac{P_{out}}{P} \quad (2.17)$$

where  $P_{out}$  is the power generated by the device and  $P$  is the wave resource given by Equation 2.12. The CW, therefore, is a length in metres representing the width of wave crest absorbed by the device.

CWR (-) is obtained by dividing the CW by a characteristic length scale of the device, and is an indication of device efficiency (Babarit, 2015).

$$CWR = \frac{CW}{B} \quad (2.18)$$

The characteristic dimension,  $B$  (m), is selected based on the method of operation of the device. For example, a point absorber would use the width of the buoy as

the characteristic dimension. The CWR allows devices of different sizes and power rating to be compared to each other, using a compiled database (Babarit, 2015).

### 2.3.1 Wave Reflections

When the propagating waves enter the WaveCat wedge and begin interacting with the structure of the device reflections will occur, particularly as the inner side of the device is a vertical solid wall.

When the incident angle is shallow and the propagating waves meet the inner structure of the WaveCat an edge wave may form. Edge waves exhibit an increase in wave height as they travel along the obstacle (Greenspan, 1956; Wiegel, 1964). This may enhance the overtopping rate of the WaveCat as it has several tanks along its hull and can capture overtopping along the majority of its length.

If the angle is such that waves are normally incident to the structure, and the waves retain the same phase upon reflection, a standing wave can form (Silvester, 1974). This can also occur at an angle, known as a clapotis gaufre (Silvester, 1987). The standing wave results in areas in the wedge where the wave height is significantly amplified, and if it is located against the device can contribute to overtopping.

The exact behaviour of the water surface within the WaveCat wedge is difficult to measure experimentally, as the model is in motion during the tests.

### 2.3.2 Overtopping Flow Rate

A method to compare OWECs is to compare the overtopping flow by considering the WaveCat as a breakwater (Owen, 1982). The overtopping flow over a breakwater can be defined as

$$Q_N = \frac{\bar{Q}}{W\sqrt{gH_s^3}} = 0.2\exp\left(-2.6\frac{R_c}{H_s\gamma_f\gamma_b\gamma_\beta\gamma_\mu}\right) \quad (2.19)$$

where  $Q_N$  (-) is the non-dimensional overtopping discharge per metre of wave crest width,  $\bar{Q}$  is the average overtopping flow discharge (-),  $W$  is crest width (m),  $g$  is gravitational acceleration and  $H_s$  is the significant wave height.  $R_c$  (-) is the crest freeboard, the height of the freeboard above the still water level,  $\gamma_f$  (-),  $\gamma_b$  (-) and  $\gamma_\beta$  (-) are coefficients representing reduction factors for slope roughness, berm influence and oblique wave attack respectively, while  $\gamma_\mu$  (-) is the influence factor for a vertical wall on top of the slope (Van der Meer et al., 2018).

Kofoed (2002) incorporated factors specific to Wave Dragon into Equation 2.19 to give:

$$Q_N = \frac{1}{\Lambda_s \Lambda_\alpha \Lambda_m \Lambda_{dr}} \frac{\bar{Q}}{W \sqrt{g H_s^3}} = 0.2 \exp \left( -2.6 \frac{R_c}{H_s \gamma_f \gamma_b \gamma_\beta \gamma_\mu} \right) \quad (2.20)$$

where the  $\Lambda$  factors are coefficients to modify the overtopping discharge based on device properties.  $\Lambda_s$  (-) represents a correcting factor adapting the formula for the case of low crest freeboards, when  $R_c$  is  $< 0.75$ .  $\Lambda_\alpha$  (-) is a modifier based on the slope of the ramp and  $\Lambda_m$  (-) is a modifier based on the shape of the ramp and guiding walls.  $\Lambda_{dr}$  (-) expresses the effect of the limited device draft on the available energy in the water column. Kofoed (2002) showed that if the device has a fixed draft then it will only interact with a proportion of the wave energy available, which depends on the ratio of  $kd$  as shown in Figure 2.20 and summarised by Equation 2.21.

$$\Lambda_{dr} = 1 - \frac{\sinh(2kd(1 - \frac{d_r}{d})) + 2kd(1 - \frac{d_r}{d})}{\sinh(2kd) + 2kd} \quad (2.21)$$

in which  $k$  is the wavenumber associated with peak wave period,  $d$  is the water depth and  $d_r$  is the device draft (m). For a device with fixed draft and constant water depth, increasing  $k$  will increase the proportion of energy available to the device.

For the WaveCat, the reduction factors in Equation 2.19 reduce to one except for  $\gamma_\beta$ , as waves entering the wedge will impinge the inner sides of the device at an angle.



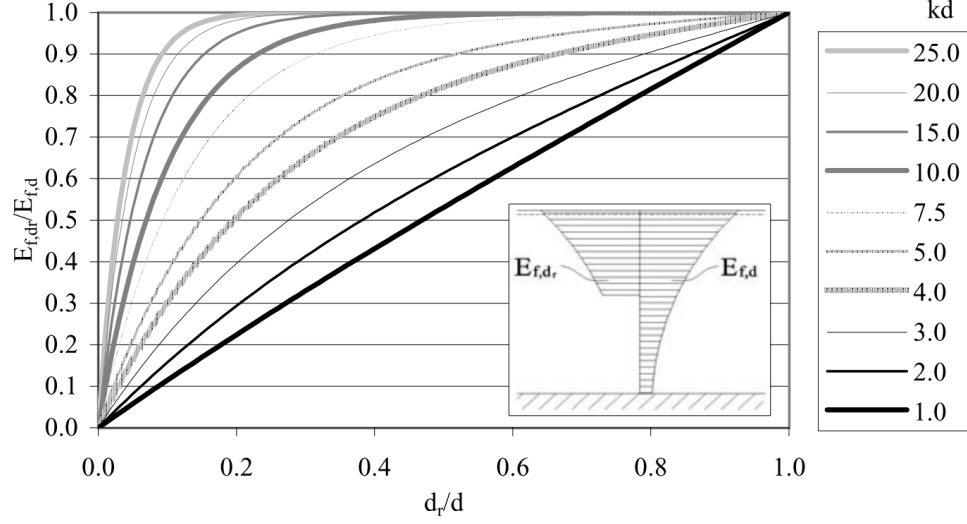


FIGURE 2.20: Ratio of energy available to a device of draught  $d_r$  in water depth  $d$  for a range of  $kd$  values

$\Lambda_{d_r}$  also needs to be considered from Equation 2.20 for the conditions. In addition, there is no slope in the WaveCat inner edge therefore  $\Lambda_m$  tends to one.

The tests for Wave Dragon showed that increasing the draft of the device increased the amount of overtopping discharge, as it can access a greater amount of energy in the waves due to less energy passing under the slope (Kofoed, 2002).

### 2.3.3 Hydraulic Pipe Friction

Within the new WaveCat model there are internal pipe channels that allow the model to drain water through the overtopping tanks and back into the basin in a facsimile of real scale operations. A system with a hydraulic head, such as the one installed in the WaveCat, will experience a head difference between the reservoir and the outlet due to frictional losses in the pipe. These losses depend on the pipe roughness, length and flow velocity in the pipe. In long pipes, where the pipe length is large compared to the pipe diameter, the friction loss can be described as

$$h_f = \frac{\lambda_F L_p V_p^2}{2gD} \quad (2.22)$$

where  $h_f$  is the head loss due to friction (m),  $\lambda_F$  (-) is a friction coefficient,  $L_p$  (m) is the pipe length,  $V_p$  ( $\text{ms}^{-1}$ ) is the flow velocity,  $g$  is acceleration due to gravity and  $D$  (m) is pipe diameter (Hamill, 2011). In long pipes the friction loss due to the pipe is large compared to the head loss at the pipe entrance and exit, so head loss can be assumed to be comprised solely of frictional losses. The friction coefficient,  $\lambda_F$ , can be determined by the roughness of the pipe and the Reynolds number of the flow with the Moody diagram (Moody, 1944) or the Colebrook-White equation (Hamill, 2011).

### 2.3.4 Turbine Selection

Turbine selection is critical to generation of power in WECs. Turbines can be categorised as impulse or reaction turbines. Impulse turbines direct jets of water at buckets on the drive shaft which redirect the flow of water, thereby imparting momentum to the turbine (Barbarelli et al., 2018), the most common type of impulse turbine is the Pelton turbine. Reaction turbines are immersed in the flow of water and their blades generate tangential force with the flow primarily from the pressure energy of the fluid (Knapp et al., 2000). The most common types of reaction turbine are the Kaplan and Francis turbines.

The choice of turbine for a given application will depend on head and flow characteristics for the device. Figure 2.21 shows head and flow with regions marked for turbine suitability (Greaves and Iglesias, 2018). Pelton turbines work most efficiently in high head and low flow conditions, whereas Kaplan turbines operate best at low head and high flow conditions. Francis turbines lie between the other two types but are generally less efficient than Pelton and Kaplan turbines. Kaplan turbines are most suited to OWECS as they typically have low head reservoirs. Wave Dragon (Frigaard et al., 2004) and the SSG (Vicinanza et al., 2012) both use Kaplan turbines.

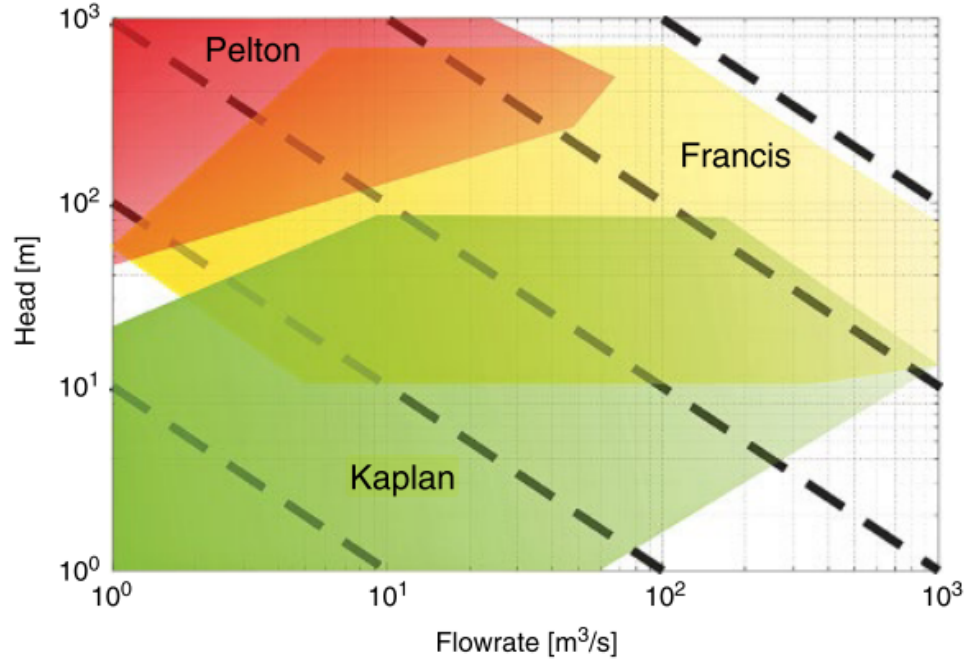


FIGURE 2.21: Comparison of operating regions for different turbines relative to head and flow, from Greaves and Iglesias (2018)

The efficiency of the turbine,  $\eta_T$  (-), is given by (Ingram, 2009)

$$\eta_T = \frac{P_{out}}{P_{in}} \quad (2.23)$$

where  $P_{out}$  (W) is the power output of the turbine and  $P_{in}$  (W) is the power input to the turbine given as

$$P_{in} = \rho g Q_T h \quad (2.24)$$

where  $\rho$  is the fluid density,  $g$  is the acceleration due to gravity,  $Q_T$  ( $\text{m}^3\text{s}^{-1}$ ) is the flow rate and  $h$  is the head. A typical Kaplan turbine power conversion efficiency is 90% to 94% (Dixon and Hall, 2010). In addition to conversion efficiency there will be additional minor losses in the pipes through bends, constrictions and fittings (Hamill, 2011).

Kaplan turbines are suitable for applications with low head. A Kaplan turbine guides water through vanes directed onto rotor blades placed lower than the water, extracting power from both the kinetic energy of the water and the hydrostatic head. The vanes are adjusted to regulate the flow rate and the rotor pitch adjusted to improve efficiency. Wave Dragon (Knapp et al., 2000) and SSG (Margheritini et al., 2009) both use Kaplan turbines for power conversion.

## 2.4 Physical Model Testing

Physical model testing is a common way of determining device behaviour in controlled situations (Hughes, 1993). Due to the cost associated with testing and deploying devices at sea (Beels et al., 2011), it is beneficial to device developers to minimise costs until they are at a development stage suitable to operating in potentially extreme conditions (Rij et al., 2018; Göteman et al., 2015b). One method of keeping costs down is to perform laboratory based testing using scaled models and conditions, afterwards moving on to small scale deployments in sheltered conditions or at a nursery site (Tedd and Kofoed, 2009; Sjolte and Hjetland, 2016).

To successfully scale an experiment all the relevant parameters that affect the model's responses must be in proportion between the experimental model and full-scale device. Additionally, any factors that are not in proportion must have a negligible effect on the experiment. There are several scaling methods used to scale experimental models, Froude scaling is typically used for WECs over Reynolds scaling as it ignores any viscous effects acting on the device and gravity is the dominant force (Greaves and Iglesias, 2018). This is an assumption which is generally accepted in most hydraulic and coastal engineering applications (Hughes, 1993).

Laboratory testing has several advantages. First, the waves tested can be tailored to specific conditions associated with potential deployment sites or weather conditions (Hann et al., 2018). Some facilities also offer the addition of currents with waves to better simulate tidal regions and real sea conditions (Collins et al., 2014; Toffoli

et al., 2015). This allows for targeted testing to take place and for conditions to be replicated from test to test (Collins et al., 2013). Second, it is straightforward to modify a model between tests, particularly to observe the similarities, or differences between certain model configurations. Third, laboratory testing is safer as conditions can be controlled and tests halted if it becomes dangerous (The European Marine Energy Centre, 2009). It is also a contained area where there is no risk of collisions with other marine objects should it become detached from its moorings (ITTC, 2014a). Fourth, there is no need for expensive environmental surveys to conduct laboratory testing, saving both time and money prior to physical testing. Last, the test conditions can be systematically cycled through combinations of wave height, wave period and other parameters that may be likely or unlikely to occur at a particular test site, in order to test conditions that may be of particular interest.

While physical modelling has advantages it is also not without disadvantages. Data can be difficult to measure at the required resolutions, and in some cases the influence of the measuring device may disturb the experimental area or be prohibitively expensive. In complex experiments scalability issues can make the assessment of full scale conditions difficult, and have attached to them large costs in terms of finances required and time needed to design and perform the experiments (Cruz, 2007). As modern computers become more powerful numerical models can contribute more towards the development of devices, once validated, with finer resolution sweeps of the test conditions without the requisite time and costs associated with physical testing (Ransley, 2015).

Increasingly, the concept of Technology Readiness Level (TRL) is used to show progress towards commercial viability (Nielsen, 2010), in which wave energy technology passes through nine levels of readiness in five stages before entering the commercial stage. TRLs 1-3 concern concept validation of the basic premise in small scale tests, moving on to TRL 4 consisting of subsystem testing, numerical modelling and feasibility studies. TRLs 5 and 6 concern testing at scale at sea, TRLs 7 and 8 are limited full scale testing at sea and TRL 9 is economic validation.

## 2.5 Numerical Modelling

Alongside physical model experiments numerical models are a powerful tool in the development of WECs. Computational capability increases as technology is developed further, bringing cost-to-performance ratios down such that modern computers are able to provide enough computational power to run numerical simulations in reasonable time frames (Cruz, 2007). Numerical models still require validation from physical testing, however once validated for a device can be used to refine the resolution of conditions tested without further physical model testing, which can be time-consuming and dependent on the facility availability. A numerical model can offer estimations of quantities that would otherwise be difficult to measure, impossible to measure or the act of measuring would disturb the system being measured (Cruz, 2007).

Commonly used types of numerical model include potential flow solvers, such as WAMIT (Lee and Newman, 2013) and NEMOH (Babarit and Delhommeau, 2015), which solve linear frequency domain potential flow theory and are lightweight and quick to run, with solutions offered quicker than real time experiments. These solvers, however, are unable to capture nonlinear time-domain responses from extreme waves (Rij et al., 2019), nor account for overtopping effects (Rij et al., 2017b).

Full CFD packages, such as OpenFOAM (OpenFOAM, 2020), ANSYS (ANSYS, n.d.) and STAR-CCM+ (CD-Adapco, 2017), are based on Navier-Stokes equations. These models have the capability to capture boundary layer viscous flow separation, wave breaking and overtopping in the model. Because of this additional capability, CFD solver simulation times can be orders of magnitude longer than real time, in some cases  $\sim 10^4 - 10^8$  times longer. The simulations are still attractive to use however, as they require minimal supervision once started and do not require expensive and time intensive laboratory set-up for different model configurations.

Other types of numerical solver include SNL-SWAN, which models the effects of the WEC on the wave field based on its energy absorption characteristics independent

of the actual device geometry, by modelling the WEC as an energy sink (McNatt et al., 2020).

A range of devices with varying modes of operation have been simulated in STAR-CCM+; point absorbers (Rij et al., 2018; Bharath et al., 2016), oscillating wave surge converters (Yuan et al., 2019) and attenuators (Stansby et al., 2015a) showing its applicability to novel cases.

Rij et al. (2018) modelled the RM3 WEC, which is one of the U.S. Department of Energy’s WEC reference models. The heave, surge and pitch RAOs were simulated and compared with experimental data, showing absolute errors of 0.166, 0.162 and 0.522 respectively. The paper describes a resolution of 60 cells per wavelength in the horizontal direction and 8 cells per wave height in the vertical direction, however it was recommended to use a finer resolution, particularly in cases where the waves were steep.

Bharath et al. (2016) modelled a submerged heaving sphere and measured the heave and surge force amplitudes, with good agreement between the simulation and linear models. This model used 40 cells per wavelength and 20 cells per wave height. Some non-linearities were observed in the force amplitudes were observed where the submerged sphere was in close proximity to the free surface.

Yuan et al. (2019) modelled the Oyster oscillating wave surge converter in 2D under non-linear wave conditions. The angular velocity and angular displacement were simulated and showed good agreement with past experimental results, as well as other simulations of the device. From this the device performance at different incident wave frequencies was simulated and showed that the device had the best performance when its natural frequency was close to that of the incident waves.

Stansby et al. (2015a) performed a free decay test of the M4 attenuator using on overset mesh and compared this with experimental data. Forced oscillations of the device in the simulation to determine the drag coefficient term of the Morrison equation (Morison et al., 1950). Some discrepancy is seen between the simulated and experimental results however this is not quantified.

STAR-CCM+ has also been used to simulate vessel motions (Tezdogan et al., 2016; Ozdemir and Barlas, 2017) and the wake behind vessels (Park et al., 2015), further showing its suitability for ocean bound cases with floating bodies.

STAR-CCM+ has been shown to more accurately predict experimental surge, heave and pitch RAOs compared to WAMIT and WEC-Sim of a heaving buoy type WEC, as well as providing more accurate axial loading forces compared to WAMIT and WEC-Sim (Rij et al., 2019). It also benefits from overset meshes, where two internally static meshes can move relative to each other. This allows large displacements in the experimental body without changing the mesh topology (Benek et al., 1983). For these reasons, as well as the added support that is provided with a commercial code, STAR-CCM+ was chosen to model WaveCat.

## 2.6 Wave Field Coefficients

Venugopal and Smith (2007) evaluated the change in wave climate behind an array of hypothetical WECs with associated hypothetical reflection and transmission characteristics, using the depth integrated MIKE21BW Boussinesq model. The WECs were implemented as porous structures with variable reflection and transmission properties depending on wave conditions. It was found that placing structures resulted in areas in the lee of the devices, about 3,000 m downstream, where the wave height reduction was independent of structure porosity. In regions either side of this the wave height was reduced most by structures with the lowest porosity.

Beels et al. (2010b) used MILDwave, a depth integrated, mild-slope wave propagation model which was calibrated against analytical integration of energy from the draft of the model to the seabed (Beels et al., 2010a). The wave height reduction of a single Wave Dragon and multiple Wave Dragons was studied for short and long crested waves.

Palha et al. (2010) used an adapted REFDIF model to study the effect of wave energy absorption by a farm of Pelamis WECs, using wave transmission values specified by



the developer. Sinusoidal incident waves and five wave farm configurations were considered.

When an object is placed in waves it reflects a portion of wave energy. This results in reflected waves travelling away from the object superposing with subsequent incident waves and influencing any surface elevation measurements in the area. The wave spectra of the incident and reflected waves can be separated if information about the Wave Gauges (WGs) location are known and their positioning relative to the object. Thornton and Calhoun (1972), Goda and Suzuki (1976) and Morden et al. (1977) developed laboratory techniques using two known positions in the direction of wave propagation and deriving the incident and reflected wave spectra. Using only two points of measurement has limitations, most notable is that the methods cannot resolve spectra if the WG separation is the same length as the wavelength.

Mansard and Funke (1980) further improved the technique by introducing a third point of measurement and using a least-square analysis to decompose the measured combined spectra into incident and reflected spectra over a greater range. Baquerizo (1995) further refined Mansard and Funke's technique to account for small changes in the water depth as waves approach a beach.

Fernández et al. (2012a) used the Baquerizo method with a group of three WGs placed in front of the WaveCat model during initial laboratory tests on a 1:30 scale model to obtain reflection spectra of the model, from which reflection and transmission coefficients were calculated. Nørgaard and Andersen (2012) investigated the transmission coefficient of the Wave Dragon and concluded that increasing the wavelength of the incident waves also increased the wave transmission coefficient, during fixed depth and freeboard model tests at 1:51.8 scale.

The energy absorbed can be determined from the reflection and transmission coefficients. From this absorbed energy, the device will convert a proportion to available power (Greaves and Iglesias, 2018).

A research gap has been identified in this area as the numerical studies described above used depth integrated models to evaluate the wave climate behind the device

the movements of the device are neglected. The studies were also not validated against actual measured wave height reduction behind a device. This requires scaled physical model tests in a laboratory basin, where tailored wave conditions close to the device can be measured.

## 2.7 Motion and Response Amplitude Operators

Whilst the WaveCat is situated in an ocean environment it will be subjected to incoming waves which will cause the device to move on the ocean surface. There are six primary forms of motion, the 6 Degrees of Freedom (6DOF). These are further split into two types, translational and rotational about the three cartesian axes, shown in Figure 2.22.

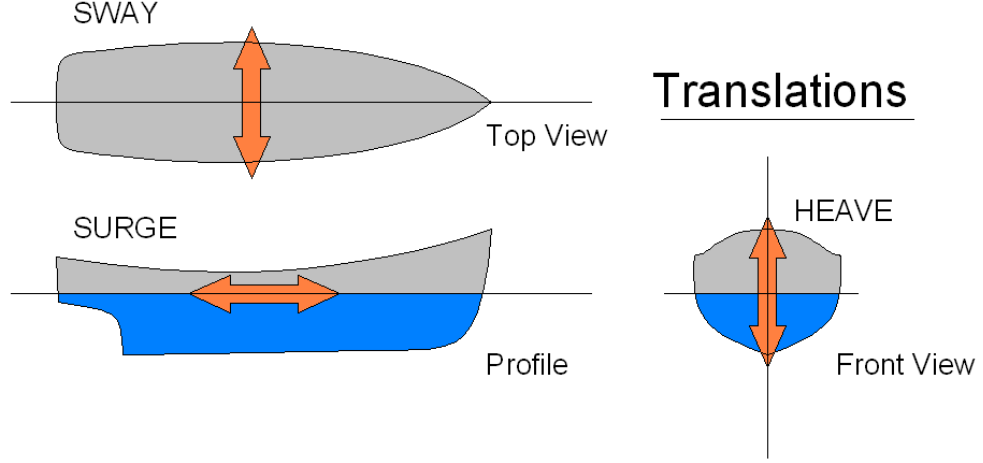
In a perfect system when testing WaveCat with waves that propagate perpendicular to the model, the symmetry of the device and the angle of the waves would mean that sway, yaw and roll motions would tend to zero. In real world situations there are small movements in the sway, yaw and roll motions as the device will be subjected to random reflections and external factors present in the system.

The motion of the device can be quantified in terms of the RAO, a transfer function that describes the effect a sea state will have on a vessel or floating structure. RAOs are dimensionless factors used to describe the specific 6DOF motions of the structure with respect to a wave excitement, for example a surge RAO of 2 means the structure surge amplitude will be twice the wave amplitude (Lopes, 2011).

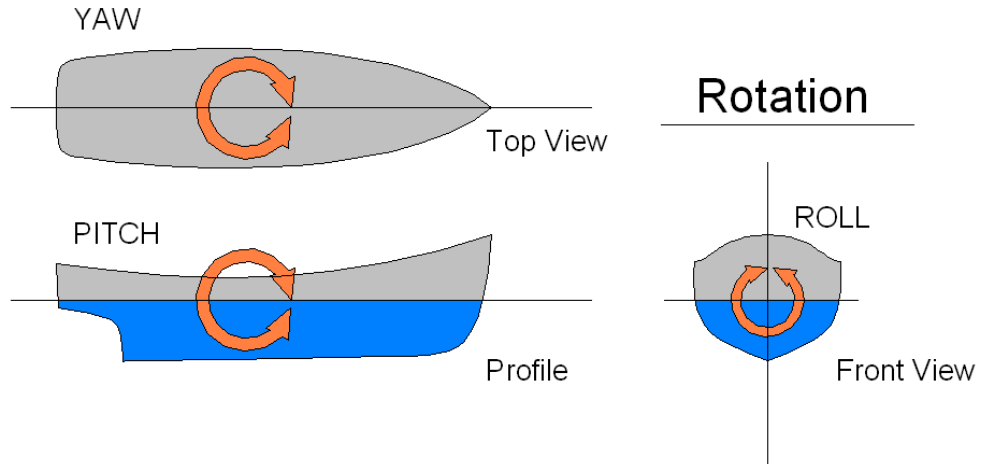
The RAOs of surge (-), heave (-) and pitch (-) are given by

$$RAO_{\text{surge}} = \frac{\text{surge amplitude}}{\text{wave amplitude}} \quad (2.25)$$

$$RAO_{\text{heave}} = \frac{\text{heave amplitude}}{\text{wave amplitude}} \quad (2.26)$$



(a) Translational degrees of freedom (Jmvolc, 2006b)



(b) Rotational degrees of freedom (Jmvolc, 2006a)

FIGURE 2.22: Translational and rotational degrees of freedom

$$RAO_{\text{pitch}} = \frac{\text{pitch amplitude}}{\text{wave amplitude}} \quad (2.27)$$

The RAOs for translational motions are dimensionless, however the RAOs for rotational motions are not dimensionless. One convention is to define the pitch RAO as

rotation per unit of wave steepness (Orcaflex, 2020), which is a dimensionless value thus

$$RAO_{\text{pitch}} = \frac{\text{pitch amplitude}}{\text{maximum wave slope}} \quad (2.28)$$

Floating bodies behave differently depending on the the wavelength to body length ratio. Waves with wavelengths that are short compared to the ship will generally not effect the ship, while waves of long wavelengths will (Thoresen, 2018). There is also a risk of resonance with the natural period of the vessel if moored which can increase the loads on the moorings and vessel structure (Davidson and Ringwood, 2017).

## 2.8 Summary

The WaveCat is a device with great versatility in its design and at an early stage of development. Following on from the concept design of Iglesias et al. (2011) and Fernández et al. (2012b) further experimental work on the WaveCat would benefit the understanding of the device, as limited conditions and aspects of the device has been tested thus far. This would bring the knowledge of the device and close the gap to that of more established technologies such as Wave Dragon.

The effect of the WaveCat on the reflection and transmission of the wave field over a wide range of random wave conditions is a key avenue of progression. The approaches of Mansard and Funke (1980) and Baquerizo (1995) will be used to determine device reflection and transmission. From this the absorption of the device can be inferred and the power generation measured using onboard instrumentation. The efficiency of the WaveCat at this stage of development will also be explored. These results will then be available for other numerical studies, filling a gap where typically analytical or fixed coefficients have been used.

Following this the motions of the WaveCat under wave action will be measured to identify behaviour that influences power generation. From this guidelines for the WaveCat design can be suggested which contribute to desired device motions and suppress those that are undesired, further progressing the device to higher TRLs.

The gathering of the above results will allow the WaveCat to be compared to other technologies in the field, including those that share modes of operation and those that are different.

The applicability of a numerical model will also be investigated, with STAR-CCM+ being identified as a suitable candidate capable of incorporating the overtopping aspect of the device as well as the overset mesh feature to handle large body displacements without changing the background mesh topology. Preliminary studies into the replicability of the device motion will be investigated in this thesis, with specific model tests conducted on a simple WaveCat model to provide validation data.

The above opportunities all assist in quantifying the WaveCat performance and contribute to further development of the device.

# Chapter 3

## Modelling Methodology

### 3.1 The COAST Laboratory Ocean Basin

Amongst the facilities in the Coastal, Ocean and Sediment Transport (COAST) Laboratory is the Ocean Basin, a 35 m long, 15.5 m wide basin equipped with 24 individually controlled paddle wavemakers and an adjustable floor of up to 3 m depth. The wavemakers are capable of producing waves up to 0.9 m in height with a frequency range of 0.166 Hz to 2 Hz (COAST Laboratory, 2020). The paddles are equipped with active wave absorption, which, along with a convex beach at the opposite end of the basin, minimises reflections back into the experimental area. Based on the capabilities of the wave tank, the size of the prototype model and the planned conditions to test in, a scale of 1:30 was chosen for the physical model and experimental conditions as a balance between model size and wave size.

To scale the model and wave conditions Froude scaling was used as gravity is the dominant force compared to viscosity, as the model is made from rigid materials and has no operations based on air compressibility or friction (Thiébaud et al., 2015).

TABLE 3.1: Froude scaling factors to convert from model scale to full scale, where  $S$  is the scaling factor

Property	Scaling Factor ( $S$ )	Units
Length	$S$	m
Volume	$S^3$	$m^3$
Time	$S^{0.5}$	s
Mass	$S^3$	kg
Density	1	$kgm^{-3}$
Power	$S^{3.5}$	W
Angle	1	$^\circ$

## 3.2 The WaveCat Model

A 1:30 scale model was constructed as part of this project, based on the concept designs shown in Chapter 1.2 and previous versions of the model (Fernández et al., 2012b; Fernández et al., 2012a; Iglesias et al., 2011). The model consisted of two symmetrical hulls joined at the stern by a hinge with the angle between fixed by a pair of steel trusses. Each hull was 3 m in length, 0.4 m wide and 0.6 m in height at the tallest point. The displacement of the model was 520 kg with fixed ballast positioned to give the model a freeboard of 200 mm along the inner edge of the device when empty. The dimensions of the model are shown in Figure 3.1, in mm. The overall structure of the model was constructed from a rectangular section housing the overtopping tanks, ballast and pipework forming the main body of the device. The bow was formed from a triangular section, when viewed from above, to better cut through the incoming wave field. This section also housed additional ballast. These shapes were chosen for their manufacturing simplicity and closeness to the prototype design.

The primary change compared to the original iteration of the design was the increase of the freeboard, and thus overall height of the model, to accommodate the tanks and associated pipework underneath. This enabled an area in which ballast was flexibly positioned to fine-tune the orientation of the model when stationary. The area of the model covered by the overtopping tanks was also increased and a guide for overtopping water designed to attempt to funnel the water into the tanks. The

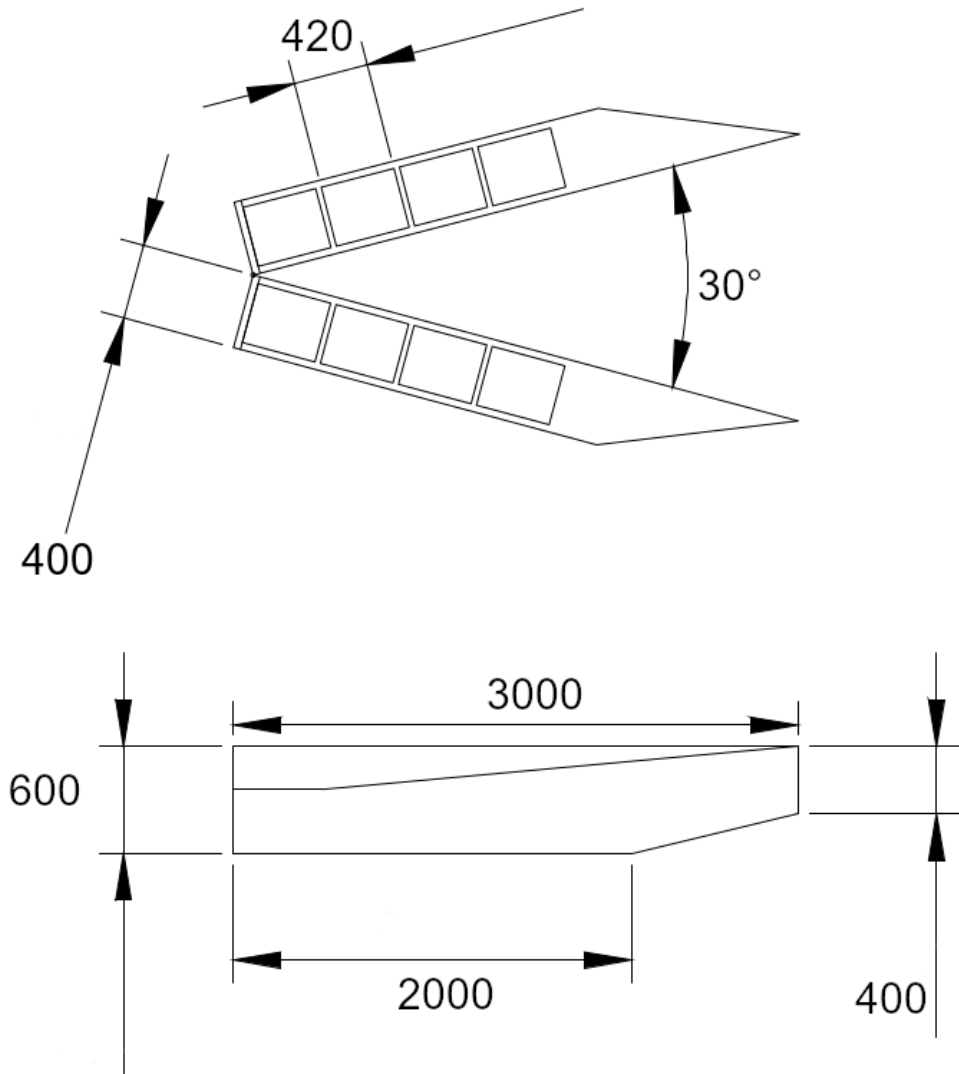


FIGURE 3.1: WaveCat 1:30 model with 30° wedge angle diagram. Dimensions are in mm

measurement of water in the tanks was also measured directly through the flowmeters, rather than pumping water out and inferring the volume based on the activation time of the pump.

The WaveCat model was constructed from four main components, described in detail below: (i), the aluminium main structure; (ii), the overtopping chambers; (iii) the wave deflector; and (iv), the electrical and mechanical control systems. Prior to building the physical model a Computer Aided Design (CAD) model was made in SolidWorks. Figure 3.2 shows the CAD model built. The model was designed in



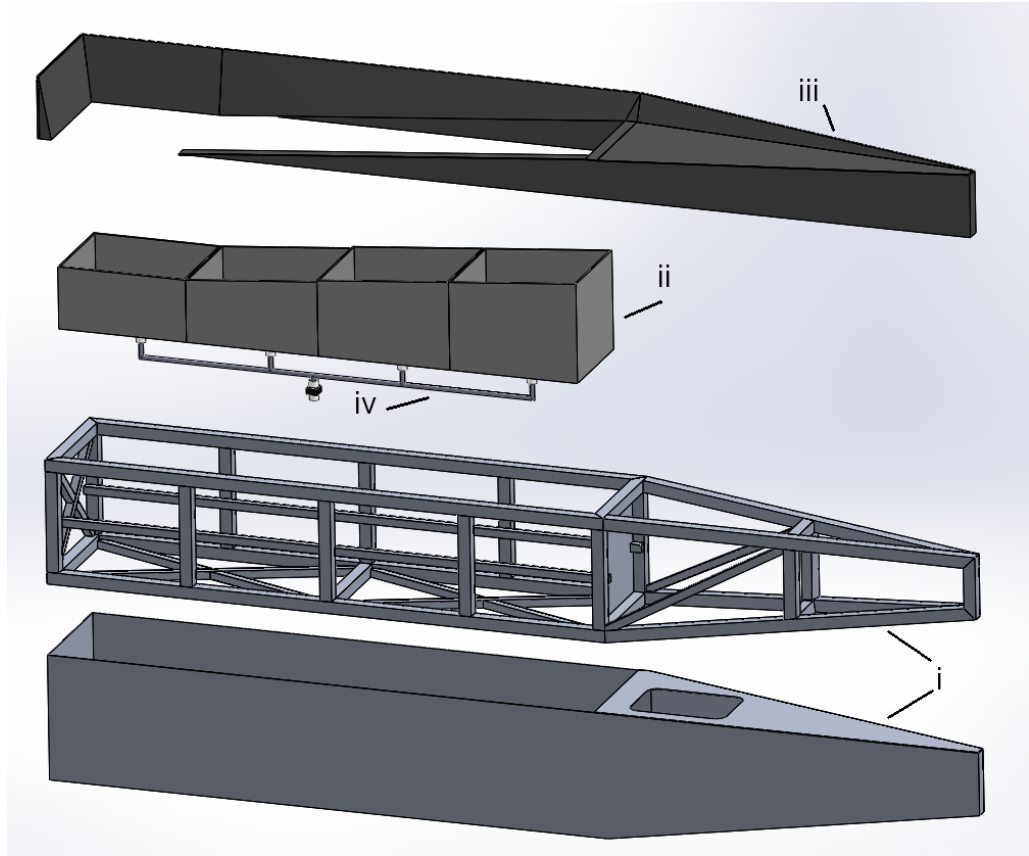


FIGURE 3.2: Exploded view of the WaveCat CAD design in SolidWorks. Shown is (i) the aluminium sub frame, above, and the skin, below, comprising the main structure, (ii) the overtopping chambers, (iii) the wave deflector, and (iv) the pipework allowing water to be removed from the chambers

CAD first so that information about the eventual model mass and mass distribution could be investigated.

The aluminium main structure consisted of aluminium square profiles, forming the frame of the device, and aluminium sheet forming the skin of the model. The skin was riveted to the frame and sealed with Sikaflex sealant then leak tested prior to deployment. Figure 3.3 shows the frame on the left, and part way through attaching the aluminium skin on the right. The nose of the device was sectioned from the main body to provide a sealed compartment to locate on board electronics and ballast, as well as to act as additional buoyancy.

The overtopping chambers were constructed from heat-welded polypropylene. Each chamber measured 310 mm wide and 420 mm long with variable depths depending on

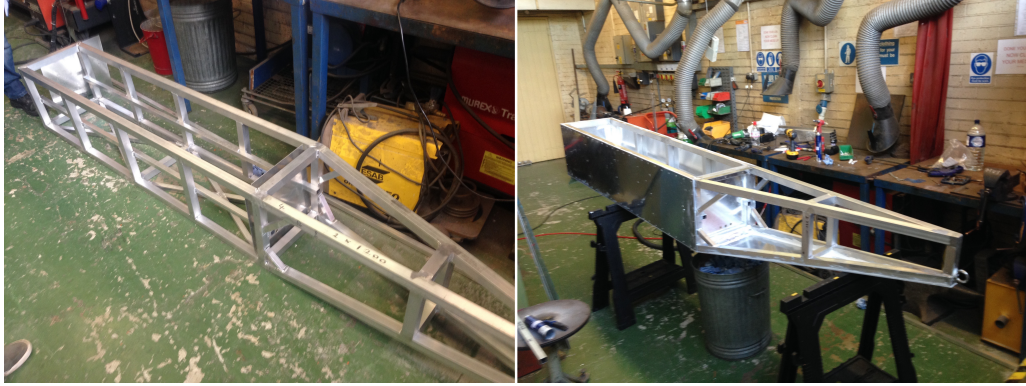


FIGURE 3.3: The WaveCat model construction. Left: The aluminium framework; right: the aluminium skin part way through construction

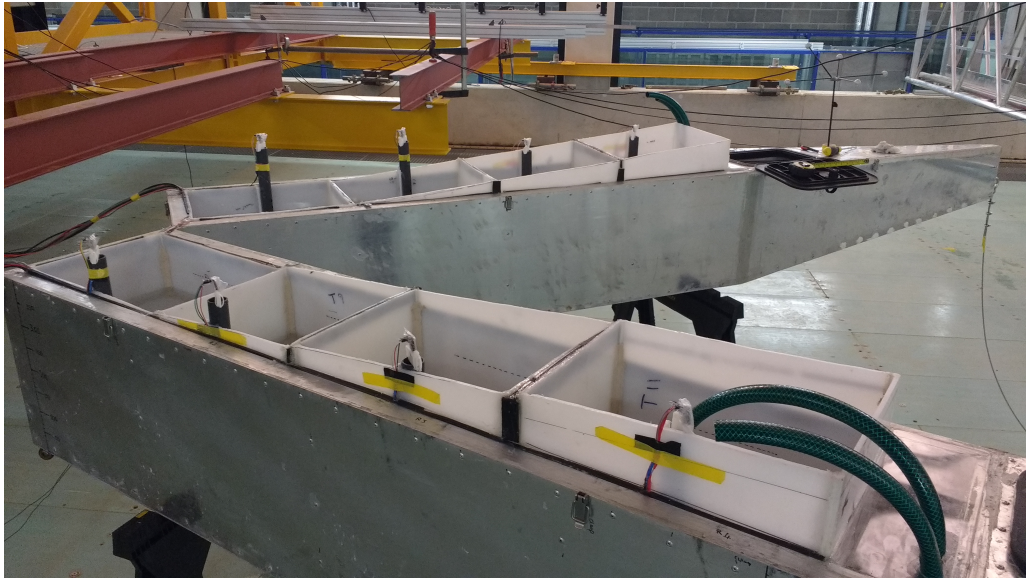


FIGURE 3.4: The WaveCat overtopping chambers onboard the model

its position in the hull. Chambers more toward the aft of the device were shallower to take into account the reducing freeboard. Each chamber was connected to the pipework located in the main body of the device to allow collected water to be exhausted through the keel of the device.

Within each chamber was a remotely controlled solenoid valve and a level sensor. The level sensor monitored the water level in each tank. Once a predetermined level was reached the solenoid valve opened and allowed the collected water to drain out of the tank. Once enough water was drained to reach a second, lower water level the valve was closed again and overtopping water allowed to collect. The levels were set

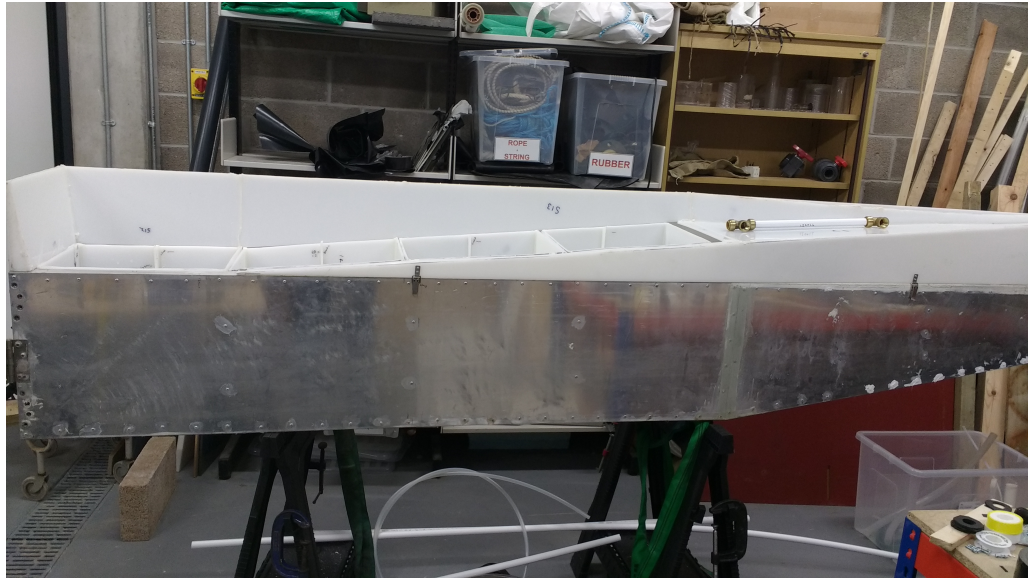


FIGURE 3.5: The WaveCat wave deflector mounted on the model

per tank in software, so a minimum level was maintained to prevent water flowing back in to the tanks should they be below the free surface.

The wave deflector was constructed in the same manner as the chambers, from heat-welded polypropylene and mounted on top of the aluminium body. It was designed to guide overtopping water into the overtopping chambers. Figure 3.5 shows the deflector in place on top of the model. The deflector also provided the inner freeboard level and bridged the gap between the chambers and the aluminium frame.

The electrical and mechanical control systems of the device were part mounted in the model and part mounted externally within the laboratory. Located on the model within each overtopping chamber were the level sensors. Below each chamber was pipework taking the collected water out of the keel of the device. In this pipework was a solenoid valve per chamber and one flowmeter per hull. By monitoring the activation of each valve it can be determined from which chamber water was exhausted from. The combined flow rate of up to four chambers per hull was measured via the flowmeters. In addition, there were two bilge pumps in each hull to combat any leaks that might have occurred and maintain a constant draft.



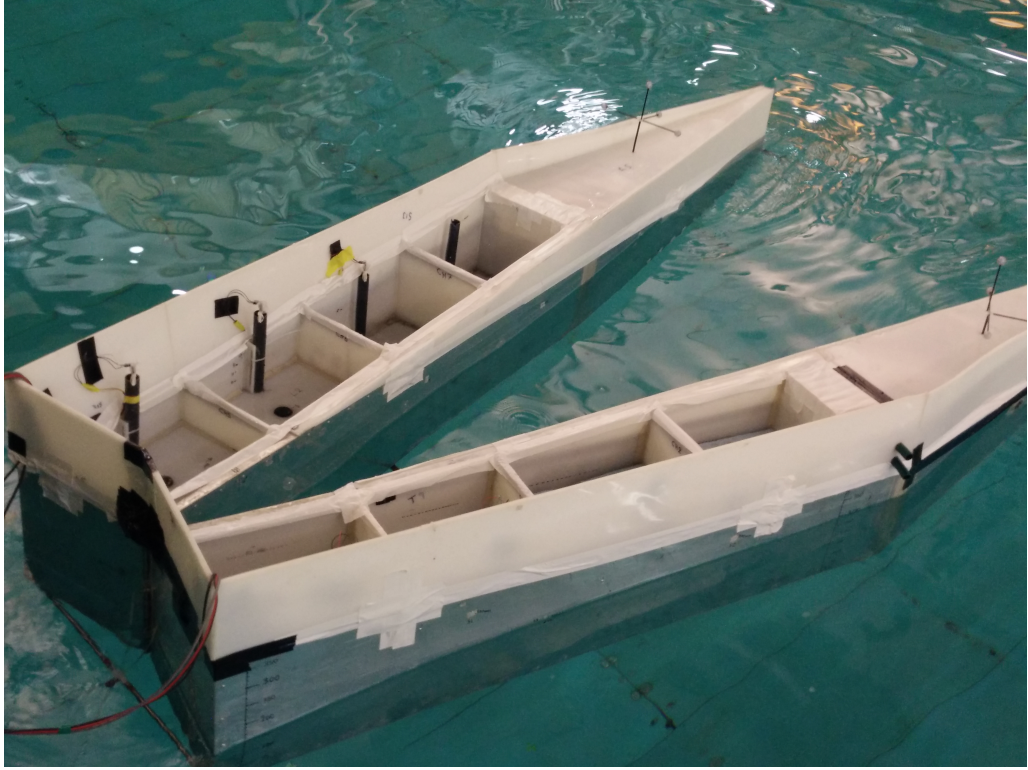


FIGURE 3.6: WaveCat 1:30 model with  $30^\circ$  wedge angle in the Ocean Basin

An externally mounted control system for the level sensors and solenoid valves consisted of latching relays with values for automatic opening and closing controlled from National Instruments Data Acquisition software. The software also allowed for manual control of the valves.

Figure 3.6 shows the completed model in situ during an experimental campaign at a  $30^\circ$  wedge angle in the Ocean Basin.

The mooring system used in the lab was a CALM system (Harris et al., 2004) similar to the final intended prototype. A single point fixed to the Ocean Basin movable floor was moored to a float point, from which each bow of the WaveCat hulls were tethered.

Figure 3.7 shows the plan view of the moorings, above, and the lateral view of the moorings, below. The line from floor to float was 3.8 m long and allowed to rest at equilibrium. The two lines from float to model were 3 m long each. It was designed such that the WaveCat can orient itself with the prevailing wave direction similar to

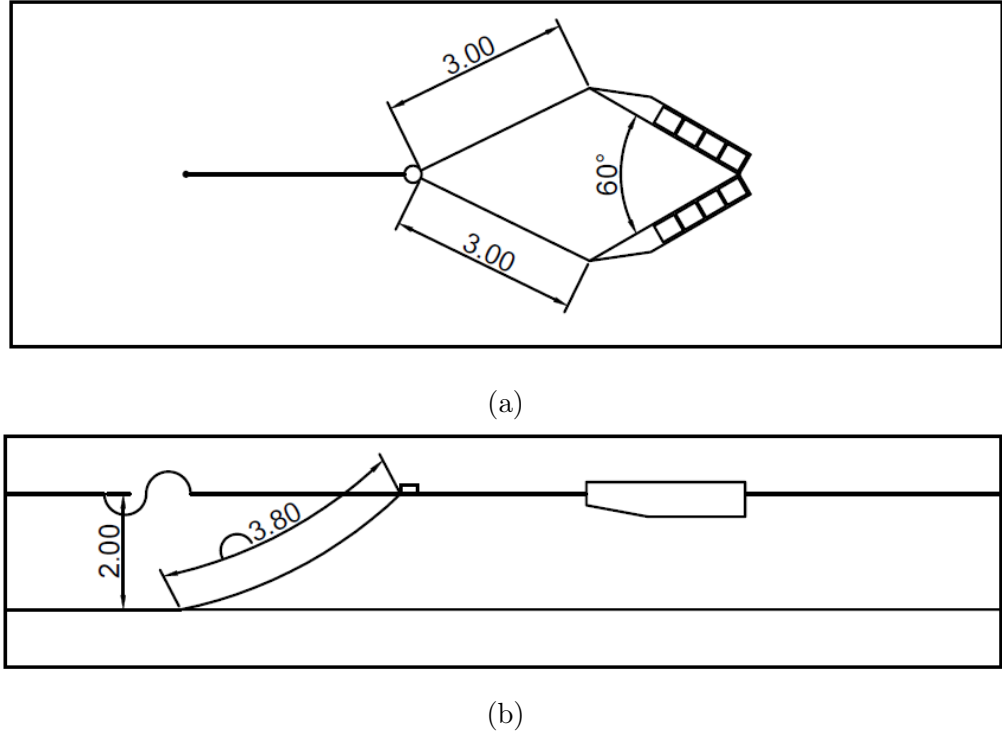


FIGURE 3.7: Mooring plan showing (a) above view and (b) lateral view for 60° setup

that of a vessel around a turret mooring (Kaasen et al., 2017). For additional safety a manual slackline was attached to the rear of the device to prevent drift outside of the experimental area. It was primarily used in positioning the model and never during a test, however left attached for the safety aspect.

### 3.3 Testing Objectives

The objective of the physical modelling was to examine effects of the WaveCat on the wave field, through the estimation of energy absorption and reduction in the lee of the device. As well as this, potential power generation and device motions were also analysed. Additionally, a subset of tests were performed for the validation of a numerical model, investigating the device motions in the absence of overtopping.

## 3.4 Instrumentation

The following section describes the instrumentation that was used during the experimental tests of the WaveCat.

### 3.4.1 Wave Gauges

Resistance WGs were used during all experimental tests to determine elevation of the water surface at discrete points in the experimental area with an accuracy of 0.1% EDesign (2016a). Three WGs were typically located between the models and the wavemakers, with a fourth at the same distance as the model to the wavemakers and off to the side, and the remainder located after the model, as shown in Figure 3.14.

The data from the WGs was used in the analysis, described in Section 4.2, to determine the reflection, transmission and absorption coefficients of the device through the change in wave field surface elevation.

### 3.4.2 Qualisys Motion Capture System

The Qualisys system was used to measure the motions of the devices (Qualisys, 2018), and used a series of reflective markers fixed to the model. 6DOF motion can be accurately measured to within 1.5 mm using this system and, given a position and angle of the device origin, any point on the structure can be located and its position determined. Qualisys used multiple infra-red cameras positioned around the basin which measured the distance to the reflective markers mounted on the device. Based on initial calibrations the apparent distance between each marker was measured and the actual device position calculated.

Figure 3.8 shows one of the reflective marker clusters mounted on the WaveCat prow. Each hull had an independent marker cluster mounted on the prow as a redundancy measure, as the hulls were rigidly fixed together. Qualisys was used primarily to determine the position of the device in the experimental area.



FIGURE 3.8: Reflective Qualisys markers mounted on the WaveCat, with infra-red cameras visible in the background

The Qualisys coordinate system consisted of a global coordinate system and local device body coordinate systems. The global coordinate system origin was set to the centre of the experimental area at the still water surface level, 17.5 m from the wavemaker paddles. The body co-ordinate system was individually set for each hull, with the origin located at the top of the hinge joint between the hulls. Each body co-ordinate system, however, was orientated to point along its respective hull, as shown in Figure 3.9 following the red arrows. The cameras were located to the right of the model, hence the markers being on different sides of the hulls.

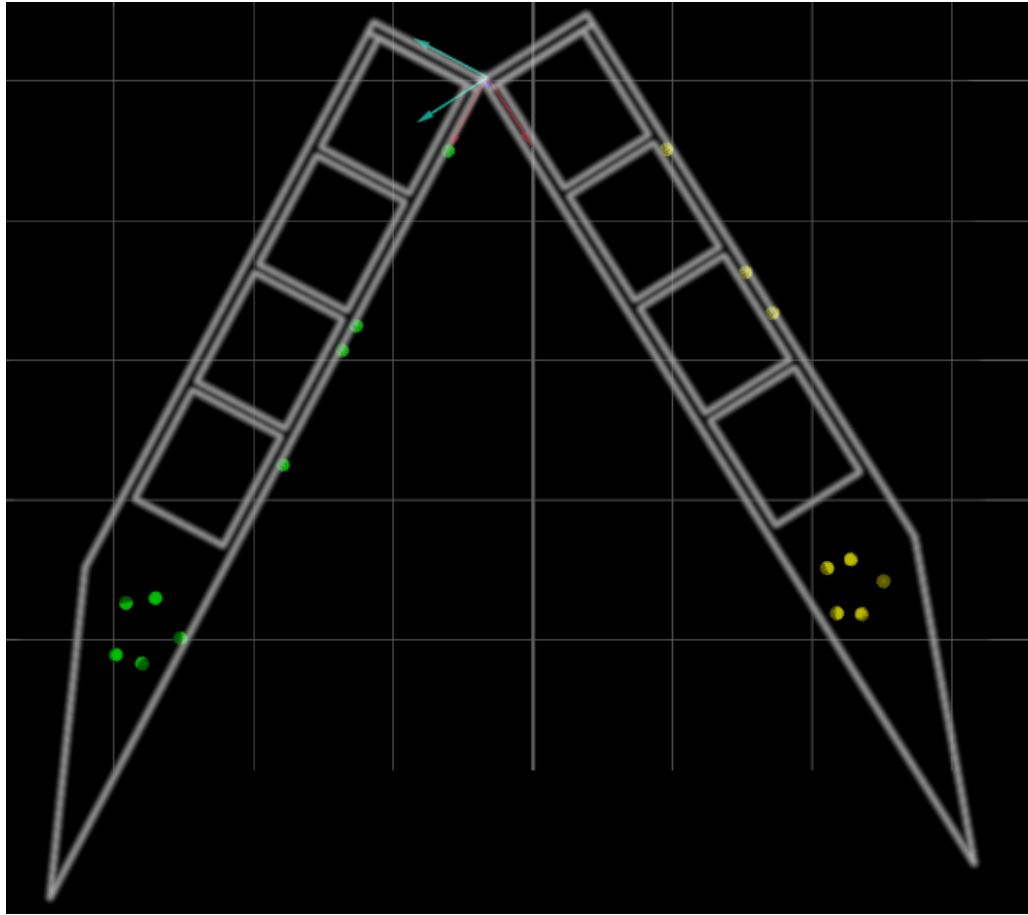


FIGURE 3.9: The body co-ordinate systems and locations of Qualisys markers

### 3.4.3 Mounted Video Cameras

A Closed-Circuit Television (CCTV) system was used during experimental tests to record the device from several angles, including underwater. This was performed to allow reference observations of the tests after the conclusion of the experimental period.

### 3.4.4 Onboard Controls

As well as instrumentation situated in the experimental area and external to the model there was also instrumentation and control systems mounted locally. Level sensors were placed in each tank to monitor the water level and a flowmeter in each hull to measure discharge from the tanks.



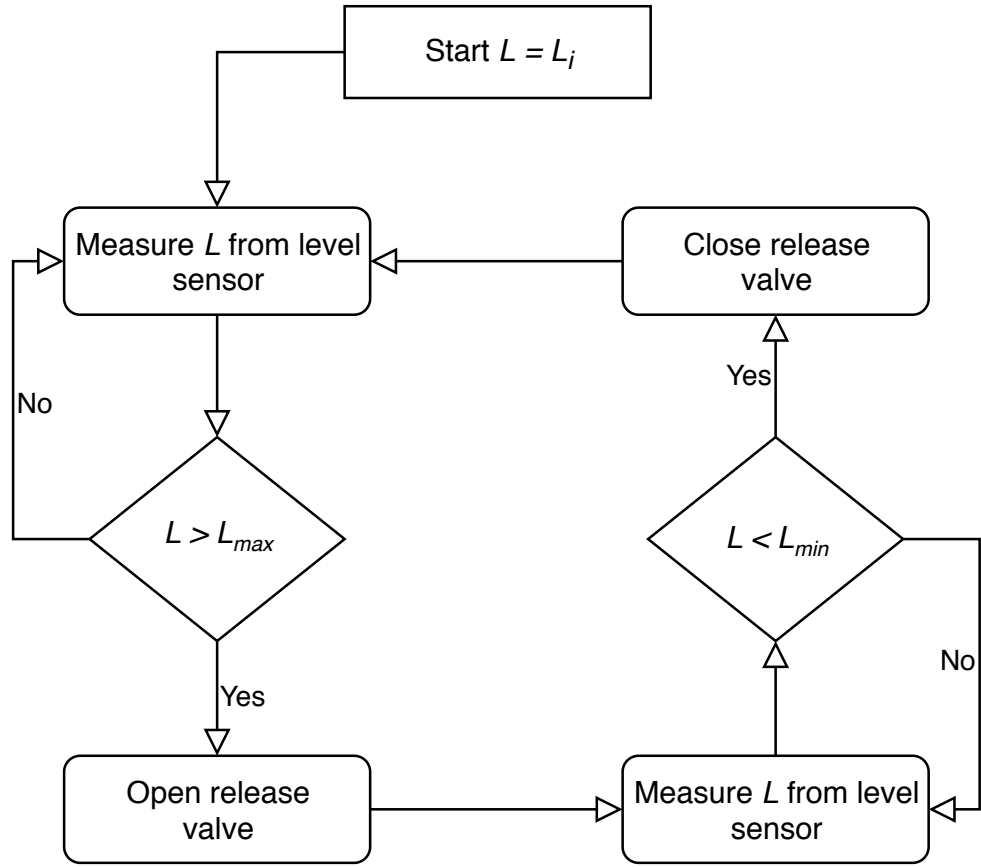


FIGURE 3.10: Flowchart showing the decision process controlling the overtopping chambers

Figure 3.10 shows the decision making tree for the control system, which governed when to open the valves in the overtopping chambers and release collected water. Each tank in the system started at an initial state,  $L_i$ , which was determined as the amount of water required in each tank so that the WaveCat would sit with the required freeboard in still water. Once the test began the software governing the valve release began measuring the level in each tank, using level sensors described in Section 3.4.5. It took multiple readings per second and a rolling average over three seconds to mitigate any rippling. When the average reached a predetermined level,  $L_{max}$ , the valve was opened in the respective tank and the collected water began to drain through the exhaust in the bottom of the tank. This exhausting water was measured by a flowmeter, described in Section 3.4.6, from which power and collected water volume was inferred. Once the level in the tank had receded to a set lower

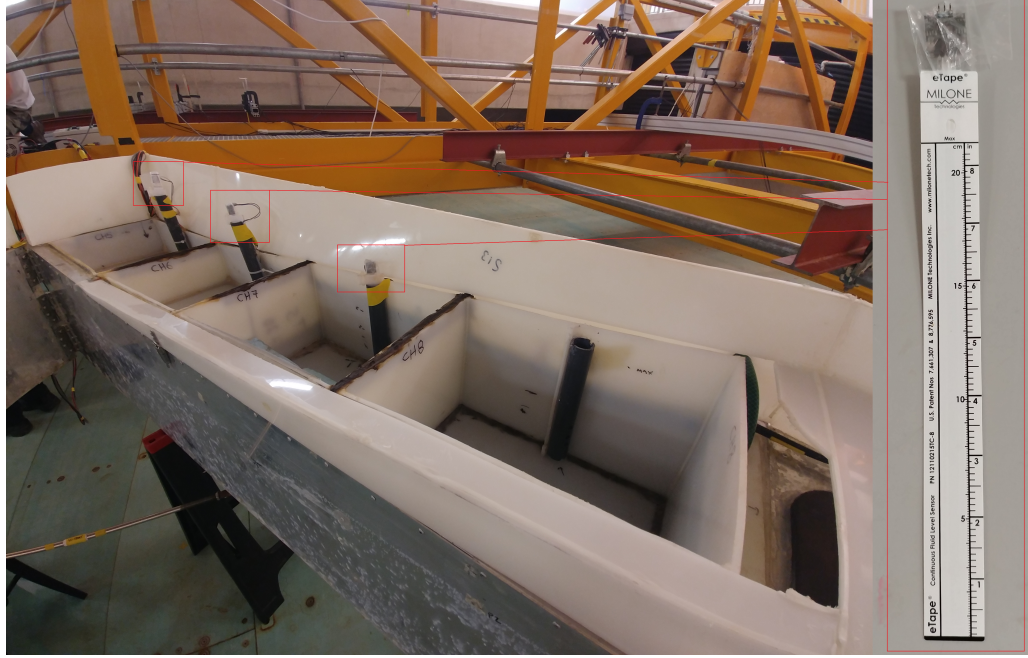


FIGURE 3.11: Level sensor mounted in WaveCat overtopping tank within an open pipe

level,  $L_{min}$ , the valves were closed to allow the tank to fill up again. The cycle then repeated until the end of the experimental run.

The valves also had the option of manual control in case of emergency and to restore the device to its original water levels once a test had completed, ready for subsequent tests.

### 3.4.5 Level Sensors

Liquid level sensors (Milone Tech, 2018) were used in the WaveCat device to measure the level of water in each overtopping tank to feedback into the control systems. Each sensor was mounted in an open pipe secured to the opposite side of the tank to overtopping water, as shown in Figure 3.11. The open pipe is used for two reasons: (i), the sensor is made of a flexible material so the pipe provides support to keep the sensor vertical relative to the tank; and (ii), it reduces the sloshing experienced by the sensor from water cascading over the side of the device or between overtopping tanks.

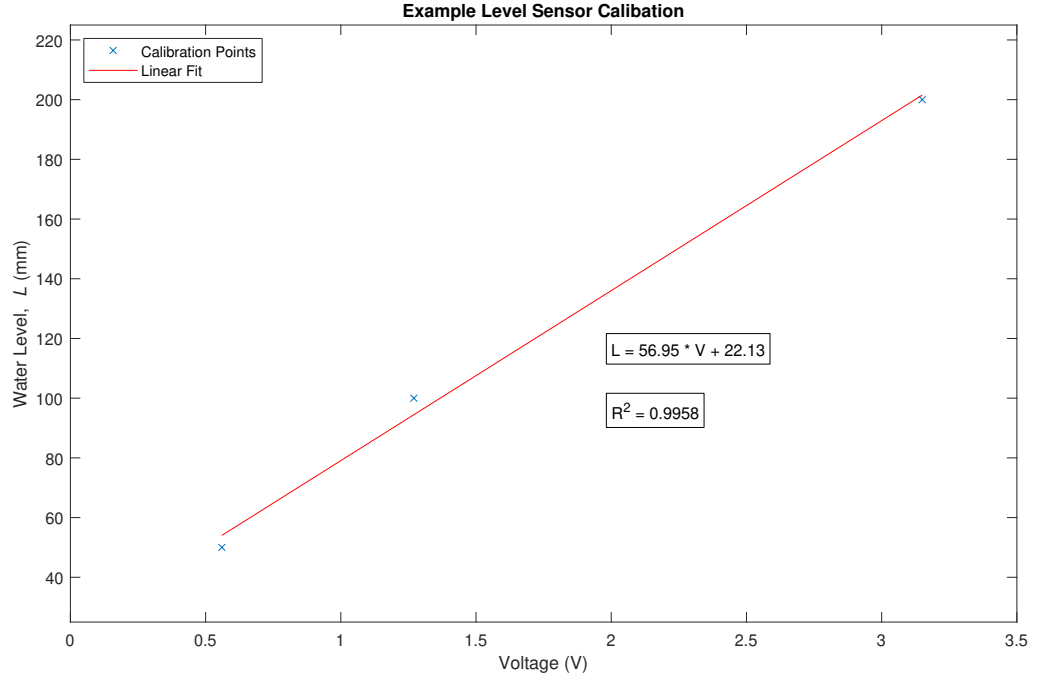


FIGURE 3.12: Example calibration of level sensor

The level sensors were calibrated in the same way as the WGs used to measure surface elevation. Three points in the range of levels expected were chosen based on the range of levels expected during testing and the respective voltage reading for each point measured. This gave a linear relationship between voltage and level from which any level in the tank could be determined. Figure 3.12 shows a typical calibration graph, with measurement points at 50 mm, 100 mm and 200 mm water depth in the tank. From this a linear fit was calculated, giving an equation for surface level,  $L$ , in the tank based on a voltage reading,  $V$ . In the example shown this was  $L = 56.95V + 22.13$  with an  $R^2$  value of 0.9958. This was performed for each tank prior to each experimental campaign, with similar levels of accuracy.

### 3.4.6 Flowmeters

Flowmeters were used in the WaveCat device to measure the volume of water released through the device. One was mounted in each hull, with a communal exhaust from the four overtopping tanks passing through it and out of the keel of the device, as shown in section (iv) of Figure 3.2.



FIGURE 3.13: Flowmeter mounted in WaveCat in the centre, solenoid valves are visible to the left and right which connect the overtopping tanks to the pipework

Omega FTB604-T (OMEGA Engineering, 2018) flowmeters were used for their accuracy at low flow readings and flexibility in mounting positions. Figure 3.13 shows the location of the flowmeter in the WaveCat, under the centre brass ‘T’ junction, with solenoid valves to the left and right.

### 3.5 Physical Modelling Experimental Configurations

Three configurations of tests were performed over the course of this project; (i) the WaveCat with the wedge angle set at  $60^\circ$ ; (ii) the WaveCat alone with the wedge angle set at  $30^\circ$ ; and (iii) the WaveCat with the wedge angle set at  $60^\circ$ .

During these tests the freeboard of the WaveCat was set to be parallel with the free surface, through ballasting the model with lead shot. An initial freeboard of 200 mm at the stern of the device was used, and the device returned to initial conditions prior to each test.

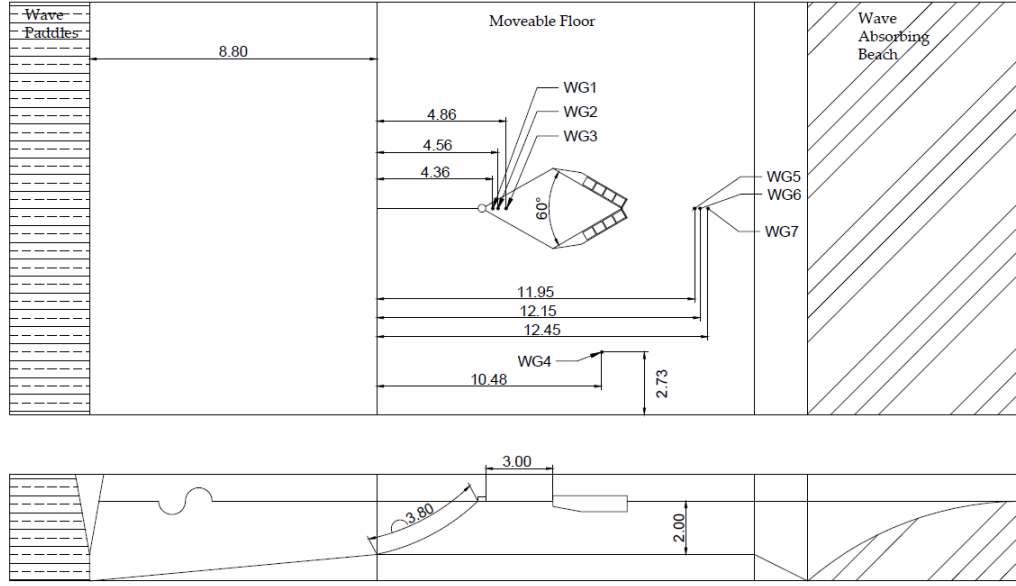


FIGURE 3.14: Ocean Basin layout for  $60^\circ$  single device tests. Distance in m

### 3.5.1 $60^\circ$ Tests - Scoping

The WaveCat was set to an angle of  $60^\circ$  for the first series of individual model tests. Regular waves and random wave series were performed during this series of tests. The primary objective for this set of tests was to test the model in a range of conditions for general survivability and robustness of onboard systems prior to performing a more rigorous testing campaign. This was done in order to identify, fix and improve the model given that it was a built specifically for this project from a new design.

Figure 3.14 shows the Ocean Basin layout for the  $60^\circ$  device tests. Seven wave gauges were used, three between the model and wavemakers, three after the model and one in line with the model. Table A.7 gives the location of each wave gauge.

### 3.5.2 $30^\circ$ Tests

For the second series of tests the WaveCat was set to a wedge angle of  $30^\circ$ . 7 WGs were used, three between the model and wavemakers, one in line with the model but

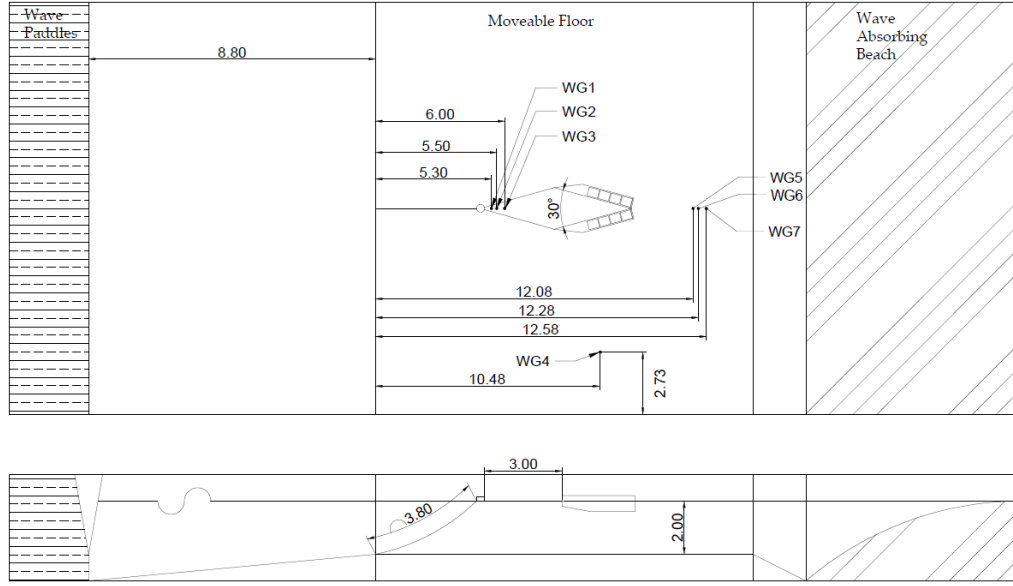


FIGURE 3.15: Ocean Basin layout for 30° single device tests. Distance in m

off from the centre line and the remaining three located behind device. Figure 3.15 shows the layout of the Ocean Basin and Table A.8 gives the location of the WGs.

### 3.5.3 Numerical Modelling Verification Tests Model Configuration

In addition to tests performed at  $\theta_w = 30^\circ$  to measure overtopping and device motions, further tests were performed with the overtopping chambers covered. These additional tests were performed to provide validation data for the WaveCat motions under the influence of regular waves in a simple system due to the lack of overtopping water. The experimental setup was the same as that of the tests with overtopping, shown in Figure 3.15 with WGs in the same locations described in Table A.8.

### 3.5.4 60° Tests

For the final series of tests the WaveCat was set to a wedge angle of 60°. 16 WGs were used, three between the model and wavemakers, one in line with the model and

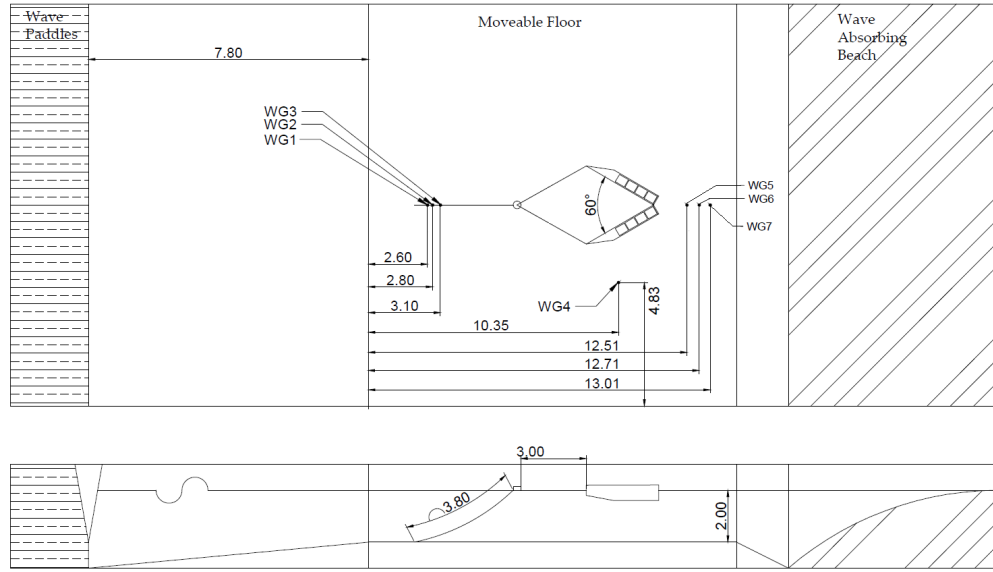


FIGURE 3.16: Ocean Basin layout for second set of tests with the WaveCat at  $60^\circ$ . Distance in m

off from the centre line and the remaining twelve located behind devices covering the width of the experimental area.

Figure 3.16 shows the layout of the Ocean Basin and Table A.9 shows the location of wave gauges with respect to the wave paddles. WG 1 to WG 3 form the front bank of gauges used for measuring and separating incident and reflected waves. WG 4 is placed to match the distance of the WaveCat to the paddles but away from the test area to provide a reference point for surface elevation used in power calculations. WG 5 to WG 7 are arranged behind the array to measure the wave field transmitted along the centre line of the experiment.

### 3.6 Physical Modelling Test Conditions

During the three test series regular waves and random waves were used, scaled using Froude scaling methods. Regular waves consisted of 55 sinusoidal wave cycles and random waves consisted of at least 30 minutes full-scale in accordance with International Towing Tank Conference (ITTC) recommended guidelines (ITTC, 2014b; ITTC, 2014a). These guidelines were used as they are designed specifically for scale

model testing of WECs by experts in the field and have been used by other studies (Kurniawan et al., 2019; Greaves and Iglesias, 2018; Tezdogan et al., 2016; Thiébaud et al., 2015). All tests were performed at a scale of 1:30, and as such wave properties were scaled following the scaling factors shown in Table 3.1.

The control system governing the Ocean Basin wave paddles, Njörðr Wave Synthesis, provides tools for generating the tested waves (EDesign, 2016b), in which several characteristics were adjusted as the tests required. The program interface is described in Figure A.3.

### 3.6.1 Preliminary Test Results - 60° Scoping Tests

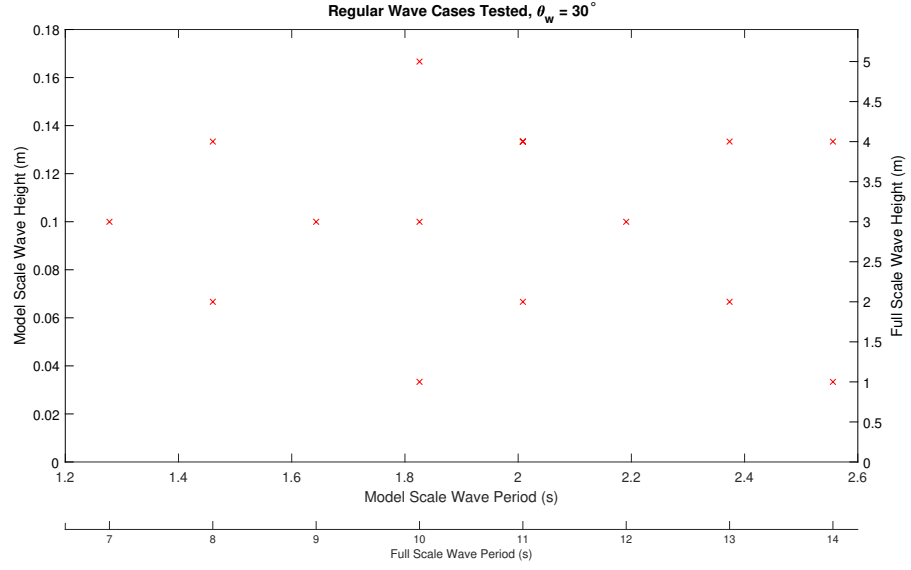
The first set of tests performed on the WaveCat with  $\theta_w$  of 60° were used to determine if the onboard control system was working correctly under a range of conditions and was used to inform the extent of conditions to test in the further 30° and 60° tests.

### 3.6.2 30° Tests

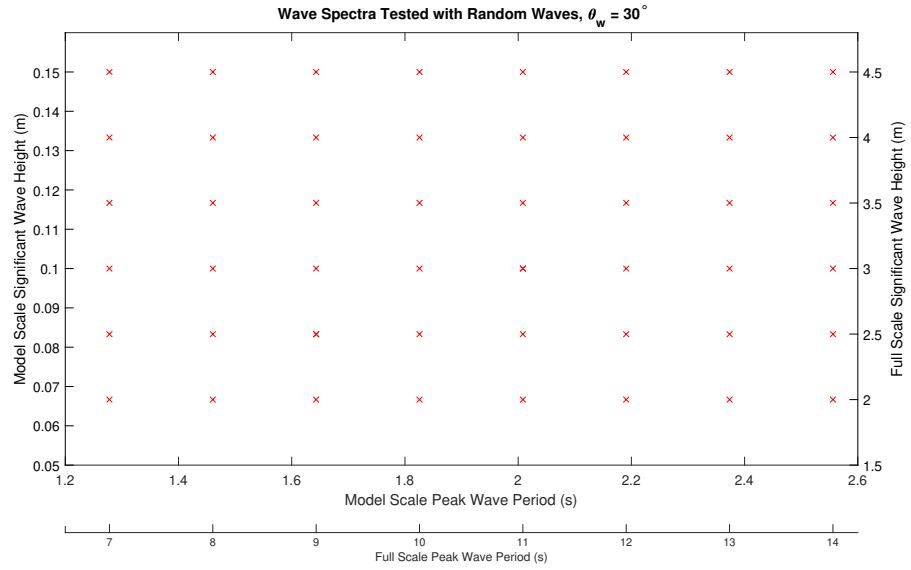
From the scoping tests performed a range of tests were generated for the  $\theta_w = 30^\circ$  model configuration tests. Due to time limits when performing the tests it was decided to focus on random waves over regular waves, thus limited regular wave experiments were run.

Figure 3.17 shows the regular and random waves tested, with regular waves shown in Figure 3.17a and random spectra shown in Figure 3.17b. Each red cross marks a completed test run. Regular wave tests were variable in length, depending on the wave period, and lasted for 55 wave periods plus an additional amount to account for the time taken for the waves to travel to the experimental area. Random waves were recorded for 392 s, containing 328 s of repeating wave sequence which represents 30 minutes at full scale. Random wave spectra were tested with  $H_s$  ranging between 0.07 m and 0.15 m, representing 2.0 m to 4.5 m at full scale. The  $H_s$  range had





(a) Regular waves tested with WaveCat at  $\theta_w = 30^\circ$



(b) Random wave spectra tested with WaveCat at  $\theta_w = 30^\circ$

FIGURE 3.17: Targeted conditions for regular waves and random spectra tested for  $\theta_w = 30^\circ$

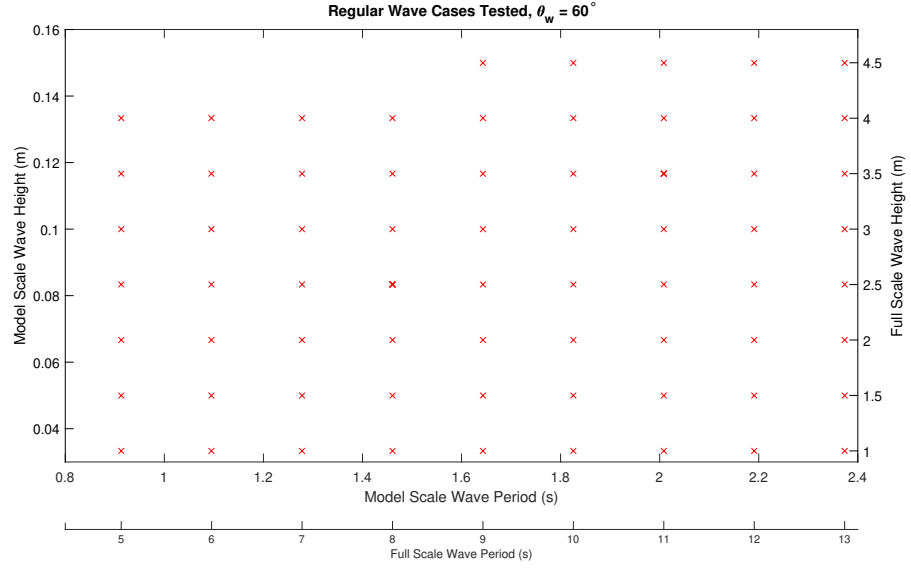
TABLE 3.2: Test conditions of regular waves for numerical modelling verification experiments

Test Case	$H_m$ (m)	$H_{pr}$ (m)	$T_m$ (s)	$T_{pr}$ (s)
1	0.05	1.5	1.83	10
2	0.05	1.5	2.56	14
3	0.08	2.5	1.46	8
4	0.08	2.5	2.01	11
5	0.12	3.5	1.64	9
6	0.12	3.5	1.83	10
7	0.12	3.5	2.19	12
8	0.15	4.5	1.46	8
9	0.15	4.5	2.01	11

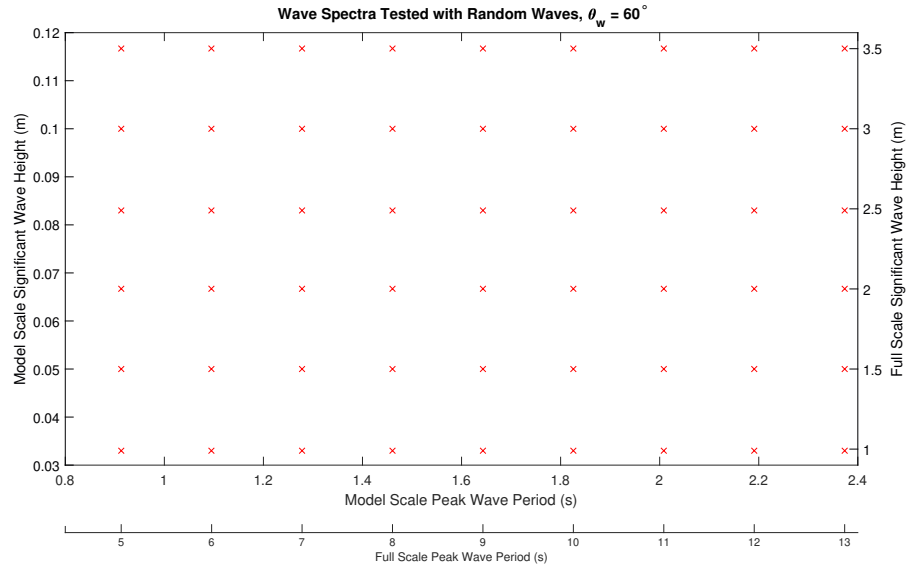
an interval of approximately 0.02 m, equivalent to 0.5 m at full scale. The  $T_p$  of the tests ranged between 1.27 s up to 2.55 s at intervals of approximately 0.18 s, representing 7 s up to 14 s at full scale in intervals of 1 s. There were a total of 48 unique test conditions across the ranges of characteristics tested. For regular wave tests at least one case was tested at each period interval at various heights due to the aforementioned time constraints.

### 3.6.3 30° Numerical Model Verification Tests

In addition to tests performed with a full physical model further tests were performed with the onboard tanks covered. Regular waves were used to measure device motions in the absence of any water overtopping. Table 3.2 shows the test conditions of the tests performed on the WaveCat model when it was modified with the onboard tanks covered. The motion data was captured with Qualisys for comparison with the numerical model, of which further detail can be found in Chapter 3.8, and the results of the verification in Chapter 7.



(a) Regular waves tested with WaveCat at  $\theta_w = 60^\circ$



(b) Random wave spectra tested with WaveCat at  $\theta_w = 60^\circ$

FIGURE 3.18: Targeted conditions for regular waves and random spectra tested for  $\theta_w = 60^\circ$

### 3.6.4 60° Tests

Regular and random spectra were tested with the setup described in Section 3.5.4. Figure 3.18 shows the regular and random waves tested, with regular waves shown in Figure 3.18a and random spectra shown in Figure 3.18b. Each red cross marks a completed test run. A more comprehensive sweep of regular wave tests were performed during this experimental campaign compared to the  $\theta_w = 30^\circ$  tests to better understand the motions of the device under wave action. The wave height for these tests range between 0.03 m up to 0.13 m, representing 1 m to 4 m at full scale. The wave height range had an interval of approximately 0.02 m, equivalent to 0.5 m at full scale. The wave period was between 0.91 s and 2.37 s with intervals of approximately 0.18 s, representing 5 s up to 13 s at full scale in intervals of 1 s. An additional five tests at wave height of 0.15 m, representing 4.5 m at full scale and wave periods of 1.64 s up to 2.37 s with the same intervals, representing 9 s to 13 s inclusive were also performed. A total of 68 tests were performed. Additional tests were performed at shorter periods than the  $30^\circ$  tests as it was observed analysis the  $30^\circ$  tests that there were potentially interesting interactions occurring at shorter periods.

Random wave spectra were tested with  $H_s$  ranging between 0.03 m and 0.12 m, representing 1 m to 3.5 m at full scale. The  $H_s$  range had an interval of approximately 0.02 m, equivalent to 0.5 m at full scale. The  $T_p$  of the tests ranged between 0.91 s up to 2.37 s at intervals of approximately 0.18 s, representing 5 s up to 13 s at full scale in intervals of 1 s. There were a total of 54 unique test conditions across the ranges of characteristics tested.

## 3.7 Ocean Basin Characteristics

The Ocean Basin is a state-of-the-art facility designed to generate repeatable and accurate sea states (COAST Laboratory, 2020). Tests were performed, without the model present, with regular and random sea states to ensure repeatability during

TABLE 3.3: Reflection coefficient of the Ocean Basin beach for regular waves in an empty tank

Test Run	Model Scale (1:30)		Full Scale (1:1)		$k_r$
	$H$ (m)	$T$ (s)	$H$ (m)	$T$ (s)	
1					0.0539
2					0.0537
3					0.0538
4					0.0540
5	0.05	1.59	1.5	8.71	0.0534
6					0.0537
7					0.0545
8					0.0542
9					0.0533

experimental phases. One WG was placed at the model position, the centre of the movable floor, and surface elevation readings taken during the wave runs. The absorption beach at the rear of the basin is designed to minimise reflections propagating back into the experimental area, however this is not a perfect process and some reflections inevitably return to the experimental area. During experimental campaigns tests were also repeated with the model in place to examine the repeatability of the system, both in terms in wave generation and model response.

### 3.7.1 Beach Reflection

To test the reflection of the beach the Ocean Basin was set up the same as the array experiments, minus the models, and an extra WG in place of the WaveCat model. Tests of regular waves with wave height of 0.05 m and wave period of 1.59 s were used. An initial reflection analysis was then performed on the surface elevation to determine the reflection from the beach, the process of which is further detailed in Section 4.2. Table 3.3 shows the reflection coefficients,  $k_r$ , for the beach for each test. Whilst  $k_r$  is low, on the order of 5% of incident waves, it is consistent across the tests and thus was taken into account during reflection analysis with the model in place. This agrees with other repeatability tests performed in the Ocean Basin at these periods (Collins et al., 2014).

### 3.7.2 Wave Repeatability

The surface elevation of the WG at the model position was also monitored to examine repeatability between tests, the characteristics of which are shown in Table 3.4.

TABLE 3.4: Summary of repeated wave conditions tested

Wave Type	Model Scale (1:30)		Full Scale (1:1)		Number of Repeats
Regular Waves	$H$ (m)	$T$ (s)	$H$ (m)	$T$ (s)	
	0.05	1.59	1.5	8.71	10
Random Waves	$H_s$ (m)	$T_p$ (s)	$H_s$ (m)	$T_p$ (s)	
	0.07	2.01	2.0	11	4
	0.10	2.37	3.0	13	4
	0.15	2.37	4.5	13	2

The repeatability of the regular waves was good, with the  $R^2$  value typically above 99%. The random waves also showed good repeatability, with smaller amplitudes showing  $R^2$  of above 99% and the higher amplitudes 97%.

## 3.8 Numerical Modelling

The suitability of numerical modelling was also investigated in relation to the WaveCat using STAR-CCM+. Numerical models assist in the development process of WECs by allowing investigations into device parameters without necessitating additional laboratory time. Numerical models must first be validated against real results to ensure trust in the predictions. STAR-CCM+ is an unsteady Reynolds-Averaged Navier Stokes (RANS) based CFD package. For this application the unsteady incompressible flow was expressed as the continuity equations

$$\begin{aligned} \nabla \cdot [\rho(\bar{\mathbf{v}} - \mathbf{v}_g)] &= 0 \\ \frac{\delta}{\delta t}(\rho\bar{\mathbf{v}}) + \nabla \cdot [\rho\bar{\mathbf{v}}(\bar{\mathbf{v}} - \mathbf{v}_g)] &= -\nabla \bar{p} + \mathbf{F}_b + \nabla \cdot \mathbf{T} \end{aligned} \quad (3.1)$$

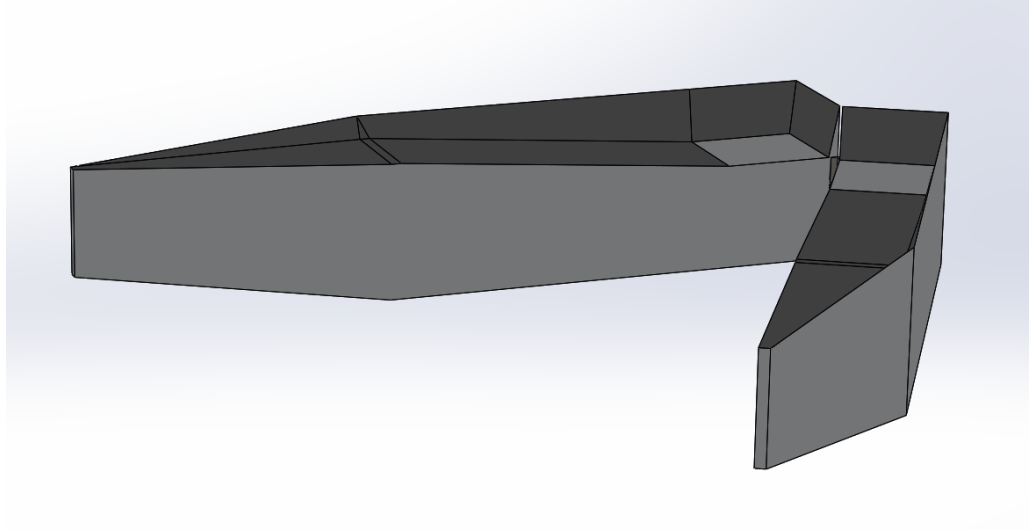


FIGURE 3.19: The SolidWorks mesh of the WaveCat with tanks covered

where  $\rho$  is the density of the medium,  $\bar{v}$  ( $\text{ms}^{-1}$ ) and  $\bar{p}$  (Pa) are the mean velocity and pressure respectively,  $v_g$  ( $\text{ms}^{-1}$ ) is the reference frame velocity relative to the laboratory frame,  $\mathbf{T}$  ( $\text{Nm}^{-2}$ ) is the stress tensor and  $F_b$  ( $\text{Nm}^{-3}$ ) is the resultant of body forces e.g. gravity. A  $k - \epsilon$  turbulence model and second order time step scheme were applied. The all  $y^+$  wall treatment was also applied to the domain, which is a hybrid treatment suitable for both high and low  $y^+$  numbers and delivers the appropriate Reynolds number for each situation (CD-Adapco, 2017).

The computational domain was made 15 m long, 8 m wide and 4 m in height with the water depth set to 2 m to match experiments, using cubic cells with edge length of 0.25 m. The region close to the free surface was further refined to a cell size of 0.1 m and a finer refinement made to reduce the cell size further to 0.03 m in the direction of wave propagation and 0.002 m in the vertical direction.

A mesh representation of the WaveCat was designed in SolidWorks and simulated in STAR-CCM+ under the influence of regular waves as described in Section 3.5.3. To match the experiments the mesh representation also had the onboard tanks covered.

Figure 3.19 shows the constructed mesh prior to importing into STAR-CCM+. The area around the WaveCat model was further refined using an overset mesh. An

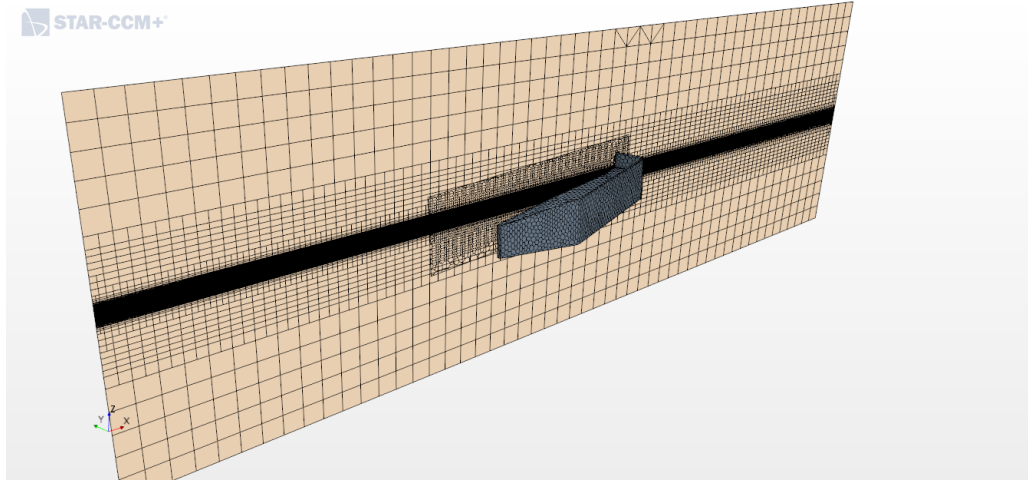


FIGURE 3.20: A plane section of the computational domain with the WaveCat model. Refined sections are seen around the model and free surface

overset mesh captures data from a background region, in this case the larger computational domain, and transfers it to the active domain, the area around, and including, the WaveCat. This allows areas of finely detailed mesh without the necessity to make the large full domain equally detailed, thus saving computational resources. The active region was modelled with polyhedral cells of the same base size at the boundary to facilitate the data transfer between the overset and background regions (Schreck et al., 2012). The WaveCat model was meshed with a polyhedral mesh with a prism layer around the exterior surface and volume refinement around the model, as shown in Figure 3.20.

The first stage of a numerical study is to perform mesh convergence on the proposed model to ensure the simulation is generating comparable conditions to the experimental tests. The purpose of the grid convergence study is to refine the mesh within the numerical model until further refinement produces results of the same accuracy, at which point the simulation can be considered mesh independent. As the mesh size becomes more refined the simulation requires greater computational resources to run, thus a balance between accuracy and efficiency must be reached.

Four different mesh resolutions were tested and compared to the theoretical waves and waves produced during the experiments of the same characteristics. The mesh around the free surface was refined to varying degrees, shown in Table 3.5. Fig 3.21



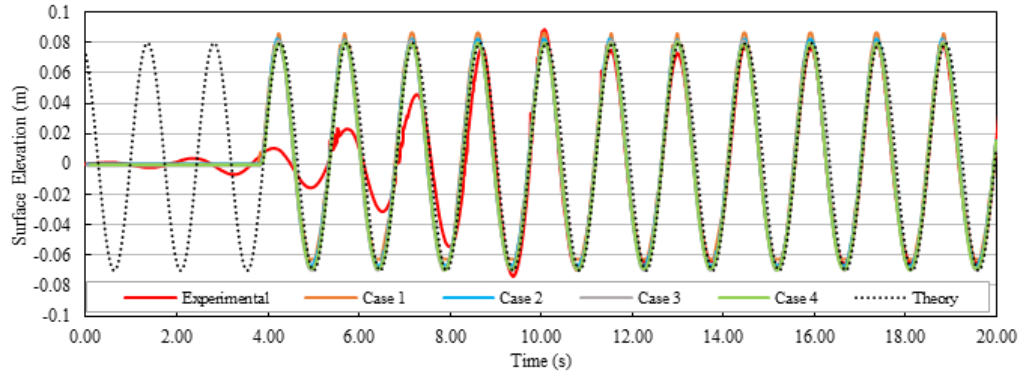


FIGURE 3.21: Mesh convergence results compared to the experimental and theoretical waves. Case 3 was chosen as a balance between reproduction of the regular wave and computational time

TABLE 3.5: The cell dimensions and runtime for each convergence case

Case	Cell height (m)	Cell length (m)	Cells per $H$	Cells per $\lambda$	Run time (s)
1	0.008	0.125	18	26	5,500
2	0.004	0.062	36	52	25,000
3	0.002	0.031	72	104	69,000
4	0.001	0.015	144	208	530,000

shows the results of the mesh convergence tests in relation to surface elevation. From these results mesh Case 3 was chosen as a balance between accurately modelling the waves and keeping the run time realistic, as Cases 1 and 2 produced heights greater than measured and Case 4 resulted in run times approximately 7.5 times as long as Case 3 with comparable heights generated. The time step was set to allow 240 steps per wavelength as suggested in the STAR-CCM+ user manual (CD-Adapco, 2017).

The numerical model was setup to use Volume Of Fluid (VOF) waves (Hirt and Nichols, 1981), generating the waves described in Table 3.2, and to control the free surface, shown in Figure 3.22. The blue cells represent the cells that form the air-water interface, i.e. the free surface.

The model was designated a 6DOF rigid body and allowed to rotate freely about the y-axis, pitch, and move along the z-axis, heave, in a simple approximation of a mooring system. The model mass was set to 520 kg and the centre of mass at (1.2, 0, 0.125) m, m, m, from an origin at the base of the hinge joint on the model, with the x-axis aligned along the axis of symmetry from stern to bow. This allows the

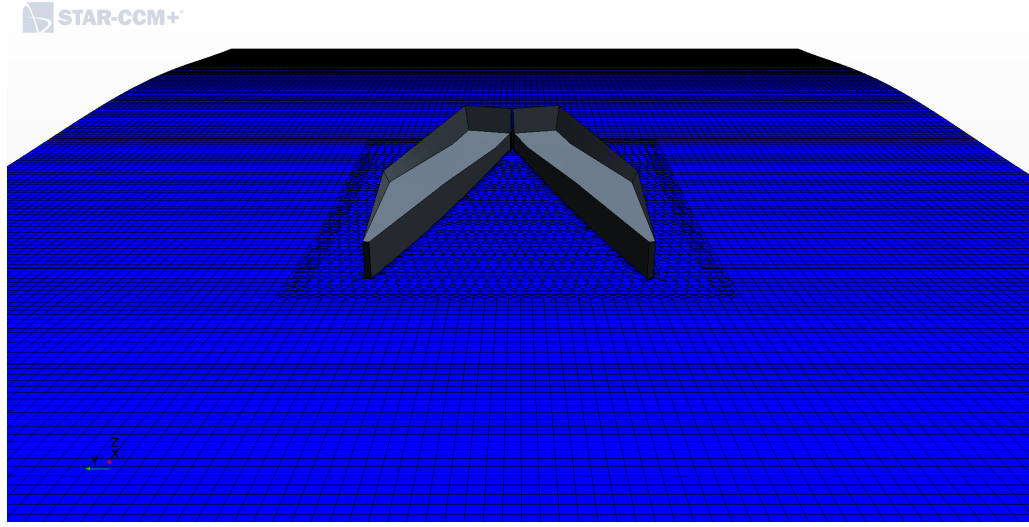


FIGURE 3.22: The free surface of the VOF wave during simulation. The overset mesh can be observed around the WaveCat device, where the cells change from cubic to polyhedral

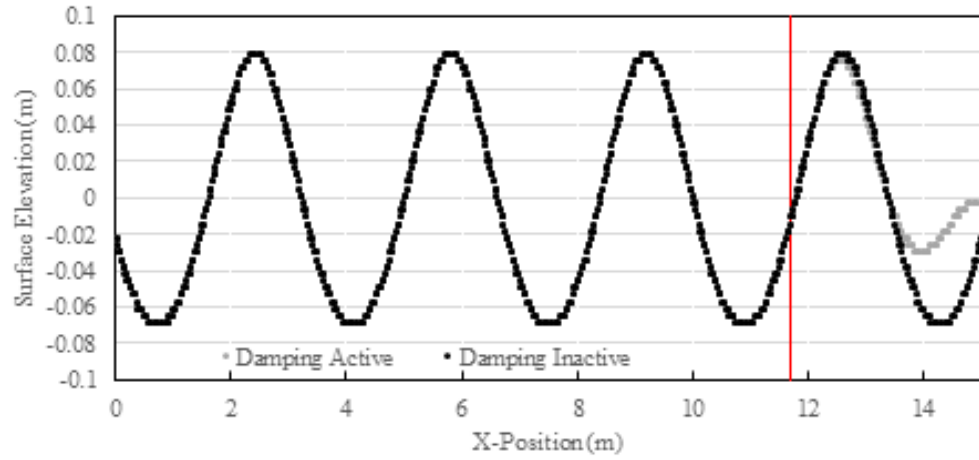


FIGURE 3.23: A comparison between a regular wave after the same time period with and without a damping zone active

numerical model to resolve force components on the WaveCat from the incoming VOF waves and determine the device movements.

A damping zone one wavelength in length at the outlet of the domain was used to limit reflection returning to the experimental zone (Choi and Yoon, 2009), similar to the absorbing beach present in the physical test basin. Figure 3.23 shows the effect the damping zone has on the wave field, the red line shows where the damping zone begins in the computational domain, at which point the grey line diverges from the

black line and tends to zero surface elevation the further it progresses through the damping zone. Longer length beaches may be used however it was shown that one wavelength was sufficient in Figure 3.23. A damping zone was used instead of a wall to stop reflections, and instead of an open end of the domain to preserve properties such as pressure in the air domain.

The responses of the numerical model were measured at the hinge point of the model, in the same location as that of the experimental model. As such the numerical result was subjected to the pitch modification as shown in Figure 4.14. The numerical model outputs the pitch and heave motion of the model which can be compared to the same motions from experimental tests. If the model recreates the motion from the experiment accurately then the model is validated.

### **3.9 Conclusion**

The testing objectives have been outlined with the methods of gathering data for analysis detailed. The experimental and numerical setups have been described with initial calibration and repeatability checks completed.

# Chapter 4

## Data Analysis Methodology

Once tests were completed data was analysed to determine the effect of the device on the wave field and the effect of the wave field on the device. As the wave field passed around and was influenced by the WaveCat it underwent transformation. A portion of the incident waves was reflected back in the original direction. Another portion was absorbed by the device either to generate electricity through overtopping, or transfer energy to the motions of the device. The remaining was transmitted through the device and continued on to the beach end of the basin. Overtopping water was released through the flowmeters in an emulation of generated power, which can be quantified.

The general process for data analysis is examined in this Chapter. The analysis followed the same process for all tests and is described in detail in the following Chapter.

The 3 point least-squares method (Baquerizo, 1995), based on Mansard and Funke (Mansard and Funke, 1980), was used to split incident and reflected waves at the model, as well as the reflected waves from the absorbing beach in the Ocean Basin. From the incident, reflected and transmission data, spectra were constructed and an absorption spectra calculated. Coefficients of reflection, transmission and absorption were then calculated to observe how the device was impacting the incident wave field.

The RAOs were also calculated to better understand how device motions impact power generation and the effect on the wave field. The WaveCat power generation was also examined to determine the wave conditions that would encourage energy generation, and conversely, the conditions in which the WaveCat would allow the incoming wave field to pass through with minimal interaction.

## 4.1 Analysis Setup and Core Concepts

To begin, the analysis characteristics of the physical modelling were taken into account. The initial data were also examined to ensure good quality readings were used for the analysis, experiments where there were data gaps or inconsistencies were re-run. Typically, for a test involving regular sinusoidal waves, such as the ones used for RAO tests, 50 waves are analysed. When using random sea states, such as the ones used to measure power generation and impact on the wave field, a minimum of 30 minutes of data is recommended (ITTC, 2014b). 30 minutes were taken at full scale and thus for the WaveCat tests, which take place at 1:30 scale, 328 seconds are equivalent to 30 minutes.

An additional 30 s plus 10% test time was added to the total recording time for each run to account for the time it took for the waves to travel from the wavemaker to the experimental area and to record the ramp down in waves after the test had finished. In addition to this, the wave train for the random waves was repeated once the first 328 s were complete. This ensured that as long as a continuous selection of 328 s of data was taken it would result in the same overall spectra.

The effective model length  $L_m$  (m) is the length of the inner opening in the direction of wave propagation. It is calculated from  $\theta_w$  and  $L_e$  as

$$L_m = L_e \cos\left(\frac{\theta_w}{2}\right) \quad (4.1)$$

where  $L_e$  (m) is the length of the inner edge of the model. The frequency which corresponds to waves of wavelength  $L$  is given by

$$f_L = \frac{2\pi}{\sqrt{\frac{2\pi g}{L_m} \tanh \frac{2\pi d}{L_m}}} \quad (4.2)$$

where  $f_L$  is the wave frequency that corresponds to a wavelength of length  $L_m$  and  $d$  is the water depth.

The width of the wedge of the device,  $B$  (m), can also be calculated

$$B = 2L_e \sin\left(\frac{\theta_w}{2}\right) \quad (4.3)$$

TABLE 4.1: Constants used during experimental campaigns

Property	Symbol	Value	Units
Water Depth at Model	$d$	2.0	m
Water Density	$\rho$	997.5	kgm <sup>-3</sup>
Gravity	$g$	9.81	ms <sup>-2</sup>
Sampling Frequency	$f_s$	128	Hz
Sampling Frequency (Flow)	$f_{sf}$	1613	Hz

Table 4.1 shows a summary of the constants used during the analysis of the test data. The water depth in the experimental area was the depth at which the moveable floor was set and was primarily used in the reflection analysis. The water density was that of fresh water at 21° C, as the Ocean Basin used fresh water rather than salt water and forms part of the energy equation. Acceleration due to gravity is the standard constant and was used as part of the dispersion relation to calculate wavelengths. The sampling frequency is the number of measurements per second that the WGs and the Qualisys system take and forms the basis for other constants such as the Nyquist Frequency during analysis. The flowmeters sampled at a different frequency than the WGs and Qualisys systems.

A water depth of 2 m was used at the model, representing 60 m at full scale. This is the typical water depth at the WaveHub test site (Smith, 2011). Wavelength is related to water depth through the dispersion relation:

$$\lambda = \left( \frac{gT^2}{2\pi} \right) \tanh \left( 2\pi \frac{h}{\lambda} \right) \quad (4.4)$$

TABLE 4.2: Wave period to wavelength conversion in 2 m water depth

Scaled Period (s)	Scaled Wavelength (m)	Depth Regime
0.91	1.29	Deep
1.09	1.85	
1.28	2.52	
1.46	3.32	
1.64	4.17	Intermediate
1.83	5.14	
2.01	6.10	
2.19	7.07	
2.37	8.03	
2.55	8.98	

Using the dispersion relation the periods chosen to test at, detailed in Figures 3.17 and 3.18, have their corresponding wavelength calculated iteratively and shown in Table 4.2. For periods of 1.46 s and less the waves were classed as deep water waves, and for periods of 1.64 s and above they were classed as intermediate water waves.

The Fast Fourier Transform (FFT) is a useful tool to convert a signal from its original domain to the frequency domain, a time series of surface elevation data can thus be transformed into the frequency domain using a Fourier transform. Within Matlab a computationally efficient method of performing a Fourier transform can be used, a FFT. The FFT algorithm utilised by Matlab is a fast Radix-2 FFT, a common form of the Cooley-Tukey algorithm (Cooley and Tukey, 1965). Further information on FFTs can be found in Frigo and Johnson (1998) and Bendat and Piersol (1986).

The FFT of a data series with N points is evaluated as an N-1 series of complex numbers anti-symmetrical around zero frequency. The first half of the FFT can be discarded with the remaining N/2 data points comprising the magnitude and phase

of the sine waves in the original data signal. When considering an  $N$  point time series, designated  $x(t)$ , an FFT is carried out and the general equation is achieved

$$x(t) \xrightarrow{\text{FFT}} X(f) = \sum_{n=1}^{N/2} (a + ib) \quad (4.5)$$

where the magnitude and phase are

$$|X| = \sqrt{a^2 + b^2} \quad (4.6)$$

and

$$\theta = \tan^{-1} \left( \frac{b}{a} \right) \quad (4.7)$$

respectively. To calculate and separate the incident and reflected wave trains the combined wave train must first be analysed in the frequency spectrum. The Nyquist frequency is the maximum frequency covered by the FFT and is defined by

$$f_N = \frac{f_s}{2} \quad (4.8)$$

where  $f_s$  (Hz) is the sampling frequency of the data signal. For the surface elevation data recorded by the WGs the  $f_s$  is 128 Hz, therefore  $f_N$  is 64 Hz.

The combined wave train measured by the WG at discrete points can be split into magnitudes of power at specific frequencies for incident and reflected waves,  $Z_i$  and  $Z_r$  respectively, up to the Nyquist frequency using a Fourier transform.  $Z_i$  and  $Z_r$  are defined as

$$Z_i = 3B_r - B_i S_{max} / (9 - S_{max} S_{min}) \quad (4.9)$$



$$Z_r = 3B_i - B_r S_{min} / (9 - S_{max} S_{min}) \quad (4.10)$$

subject to the following definitions

$$B_i = \sum_{k=1}^N C e^{-ikx_{WG}} \quad (4.11)$$

$$B_r = \sum_{k=1}^N C e^{ikx_{WG}} \quad (4.12)$$

and

$$S_{max} = \sum_{k=1}^N e^{2ikx_{WG}} \quad (4.13)$$

$$S_{min} = \sum_{k=1}^N e^{-2ikx_{WG}} \quad (4.14)$$

$B_i$  and  $B_r$  are the vectors containing the sum of all three WGs after having a FFT applied to the incident surface elevation data at each frequency bin,  $C$ , multiplied by  $e^{-ikx}$  and  $e^{ikx}$  respectively.  $i$  is the imaginary unit,  $k$  is the wavenumber associated with the frequency of the FFT at each bin and  $x$  is the position of the WG as shown in Table A.10.  $S_{max}$  and  $S_{min}$  are the vectors of the maximum and minimum values of the three WGs for each frequency bin, where  $i$ ,  $k$  and  $x$  are defined in the same way as Equation 4.11 and 4.12.

Using  $Z_i$  and  $Z_r$  the incident and reflected wave trains can be reconstituted separately from the spectral analysis by performing an inverse-FFT on

$$N Z_i e^{ikx} \xrightarrow{\text{IFFT}} \eta_i \quad (4.15)$$

$$NZ_re^{-ikx} \xrightarrow{\text{IFFT}} \eta_r \quad (4.16)$$

where  $N$  is the number of data points in the data set,  $Z_i$  and  $Z_r$  are the incident and reflected power amplitude spectra respectively for the three input wave gauges,  $k$  is the wavenumber and  $x$  is the position array for the three wave gauges.

The wave train was then reconstructed from the original WG data, with the incident and reflected trains as two separate entities also available for analysis. The incident wave train for this initial beach reflection was then used as the transmission wave train for the model reflection analysis. The Baquerizo method (Baquerizo, 1995), a reflection analysis based on Mansard and Funke (Mansard and Funke, 1980), was then performed on the data from the WG array around the model, incorporating the data described above with beach reflections mitigated. This is a 2D technique and was performed on the centreline of the experiment. Diffraction around the device may introduce errors but other studies found them small (Fernández et al., 2012a; Carballo and Iglesias, 2013).  $\eta_i$  and  $\eta_r$  were calculated in the same manner, with the appropriate input data now including the regenerated surface elevation data from the transmission gauges.

In addition to  $\eta_i$  and  $\eta_r$  the analysis also reconstructed  $\eta_t$ , the transmitted surface elevation time series using the following method

$$Z_t = 3B_t S_{max} / (9 - S_{max} S_{min}) \quad (4.17)$$

where  $S_{max}$  and  $S_{min}$  are described in Equations 4.13 and 4.14 respectively using the appropriate incident and reflected wave trains and subject to the following definition

$$B_t = \sum_{k=1}^N D e^{-ikx_{WG}} \quad (4.18)$$

where  $D$  is the FFT of the transmitted surface elevation data. The incident, reflected and transmitted data is then regenerated as shown above, with  $\eta_t$  windowed according to test length. From the separated wave trains of  $\eta_i$ ,  $\eta_r$  and  $\eta_t$  spectral analysis was conducted on each.

## 4.2 Reflection and Transmission Analysis

WGs measure the surface elevation at a point in the experimental area with no knowledge of wave direction, thus waves travelling in different directions are able to superpose at the point of measurement and result in a larger surface elevation than each wave individually. Incident waves propagate from the wavemaker, impact the model and are reflected, transmitted or absorbed to varying degrees depending on the model characteristics. As such it was necessary to split the measured data into the incident and reflected components. The first step for analysing the impact of the WaveCat on the wave field was to remove any reflections that were generated at the absorbing beach in the Ocean Basin from the data received at the transmission WGs located beachward of the model. This was done using a reflection analysis to split the data from 3 transmission WGs into the incident data, or wave train heading towards the beach, and the reflection wave train coming back from the beach.

To begin with the data was corrected to match still water conditions to a zero reading on the WG surface elevation measurements to mitigate any creep caused by temperature variations in the laboratory over the course of a days testing. The data was then windowed to only contain the relevant test data and not the extra recorded time at the beginning and end of the test.

After data correction and windowing the complex amplitudes of the incident, reflected and transmitted wave trains were calculated from the three WG time series of the incident wave data. The surface elevation at a specific point along the 2D

experimental plane,  $\eta(x, t)$  (m), can be expressed as the following superposition of waves

$$\eta(x_a, t_b) = \eta_i(x_a, t_b) + \eta_r(x_a, t_b) + \eta_t(x_a, t_b) \quad (4.19)$$

where  $\eta_i$ ,  $\eta_r$  and  $\eta_t$  are the incident, reflected and transmitted surface elevations from the WaveCat respectively,  $x_a$  is the surface elevation at the non-zero position  $a$  in the  $x$  direction and  $t_b$  is the surface elevation at a non-zero time,  $b$ . The surface elevation at the position  $a$  and time  $b$  is thus the addition of the incident surface elevation and the reflected surface elevation at the same position,  $a$  and time  $b$ .

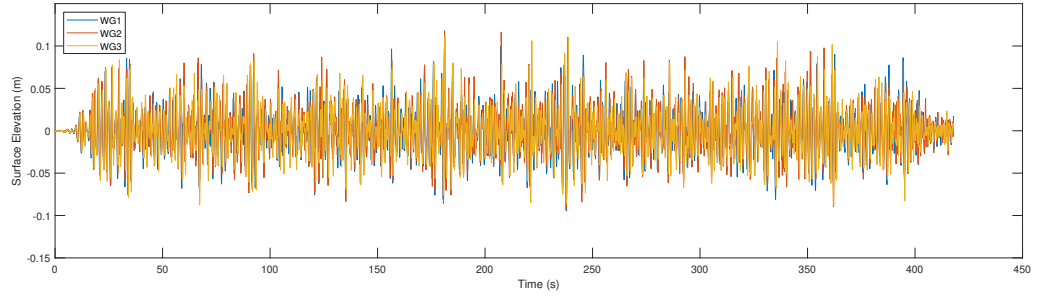
### 4.3 Interpolated Test

During the analysis it was discovered that a wave gauge surface elevation data file was corrupted, thus no useful data for that particular test could be extracted. This was for the test with  $H_s = 0.12$  m and  $T_p = 1.83$  s. When plotting the tests by period it was observed that the tests of higher and lower wave heights were of a linear relationship around a wave period of 1.83 s, therefore the data point was linearly interpolated using the tests of the periods either side of the missing result at the same wave height. The interpolated result has been marked on relevant following results.

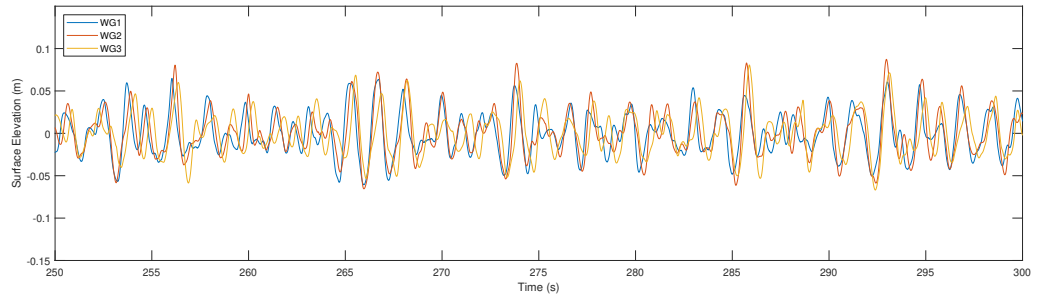
Using a random wave test with  $H_s$  of 0.12 m and  $T_p$  of 1.46 s as a worked example, the initial raw data from the WGs 1, 2 and 3 are shown in Figure 4.1.

The raw WG data is translated to the origin and windowed to the length of time containing the required amount of data at 1:30 scale, shown in Figure 4.2.

The example data shown was subjected to the reflection analysis along with the raw data windowed in the same manner from the transmission WG in the lee of the device. This resulted in the incident, reflected and transmitted wave trains, shown in Figure 4.3, which were used in the spectral analysis.



(a)



(b)

FIGURE 4.1: Example time series of raw WG data showing (a), a complete test and (b), a segment of a complete test of the front three WG

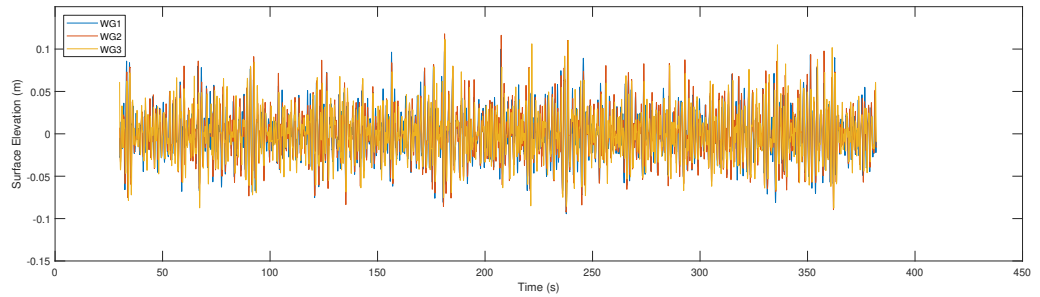
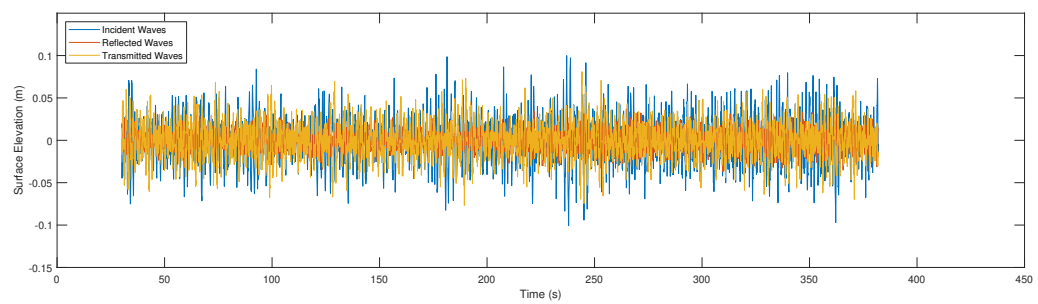
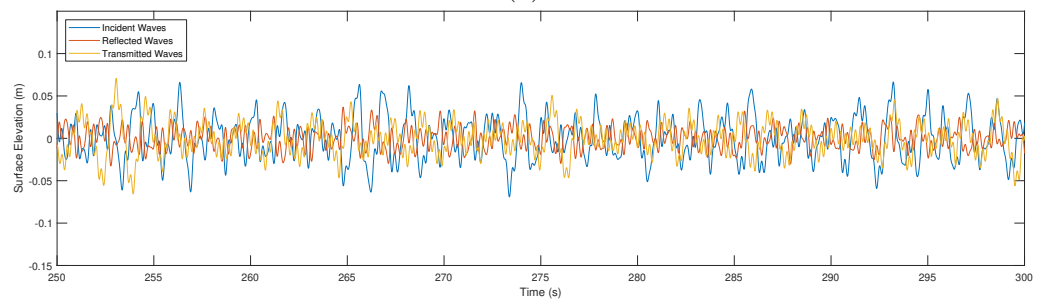


FIGURE 4.2: Windowed and mean-adjusted raw WG data of the front three WG



(a)



(b)

FIGURE 4.3: Example complete, (a), and segment of time series of incident, reflected and transmitted wave trains reconstructed from the reflection analysis on the WaveCat, (b)

## 4.4 Spectral Analysis

Once the combined surface elevation readings were split into the incident, reflected and transmitted wave trains, analysis was performed to examine the effect of the model on the wave field across the frequency spectrum of the random waves tested. The incident, reflected and transmitted wave trains were each individually analysed using Matlab's spectral analysis routine to provide a power spectrum estimate of the incident, reflected and transmitted waves respectively, taken from the appropriate WGs closest to the model.

The first stage to the spectral analysis was to remove the mean of each signal. Any large scale trends were also removed at this point using a moving average over two wave periods. The data interval to be analysed was then separated from the full time series. This was done to remove the initial time in the test when the waves were travelling from the wavemakers to the model area and the end of the test when the waves have ceased and the model returns to its start position. The resultant data was then divided into sections of  $m$  points, with each section subsequently windowed to ensure the start and end of each data section is zero.

To reduce leakage between frequencies in the Welch method (Welch, 1975) a Hanning window was used (Smith, 2011), however the action of windowing data resulted in data at the edge of the window being lost. This is mitigated by taking further windows of data at an offset to the original windows, typically half a windows width apart, and also analysing this selection. Figure 4.4 shows an example of window

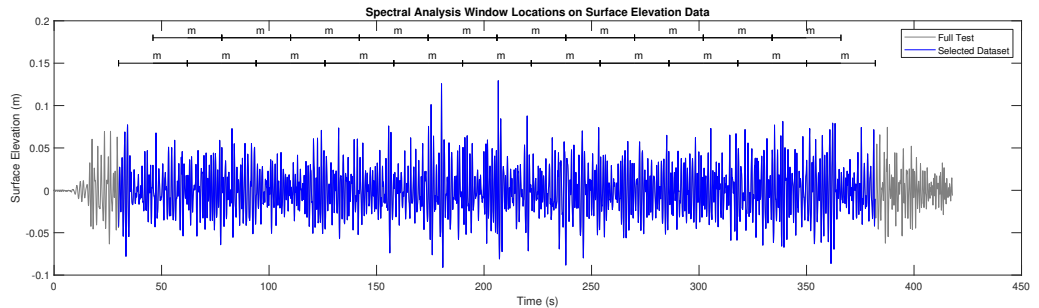


FIGURE 4.4: An example of the location of windowed data compared to a complete test series and how the windows of  $m$  length overlap to reduce information loss

location. The first set of windowed data comprises of eleven sections of length  $m$ , the overlapped series consists of ten more sections of length  $m$  offset by  $m/2$  data points.

Each of the windowed segments was then Fourier transformed, from which power spectra were calculated. The power spectrum, or Spectral Density Function (SDF) denoted as  $S_{xx}$ , is the square of the amplitude of the signal, and as such is related to the variance of the surface elevation, as shown in Equation 2.13. Missing data was interpolated then the data was de-spiked by removing peaks that were more than three times the standard deviation of the signal. For each frequency bin the power is calculated from the raw Fourier estimate

$$\begin{aligned} P_{xx} &= (a + ib) \times (a - ib) \\ P_{xx} &= a^2 + b^2 \end{aligned} \tag{4.20}$$

The  $P_{xx}$  for each segment is then transformed into a periodogram which are then averaged according to the frequency, from which the power spectrum,  $S_{xx}$ , is calculated by dividing through by the bandwidth

$$S_{xx} = \frac{P_{xx}}{\Delta f} \tag{4.21}$$

The likelihood of each peak in the resultant spectra being statistically significant at the given confidence level can be quantified. This depends on the number of degrees of freedom in the windowing criteria and is directly related to the number of windows chosen and the amount of data that is overlapping within the offset windows, given by Nuttall (1971) as

$$\text{NDF} = 3.82 \text{ Nd} - 3.24 \tag{4.22}$$

where the window is overlapping 50%.



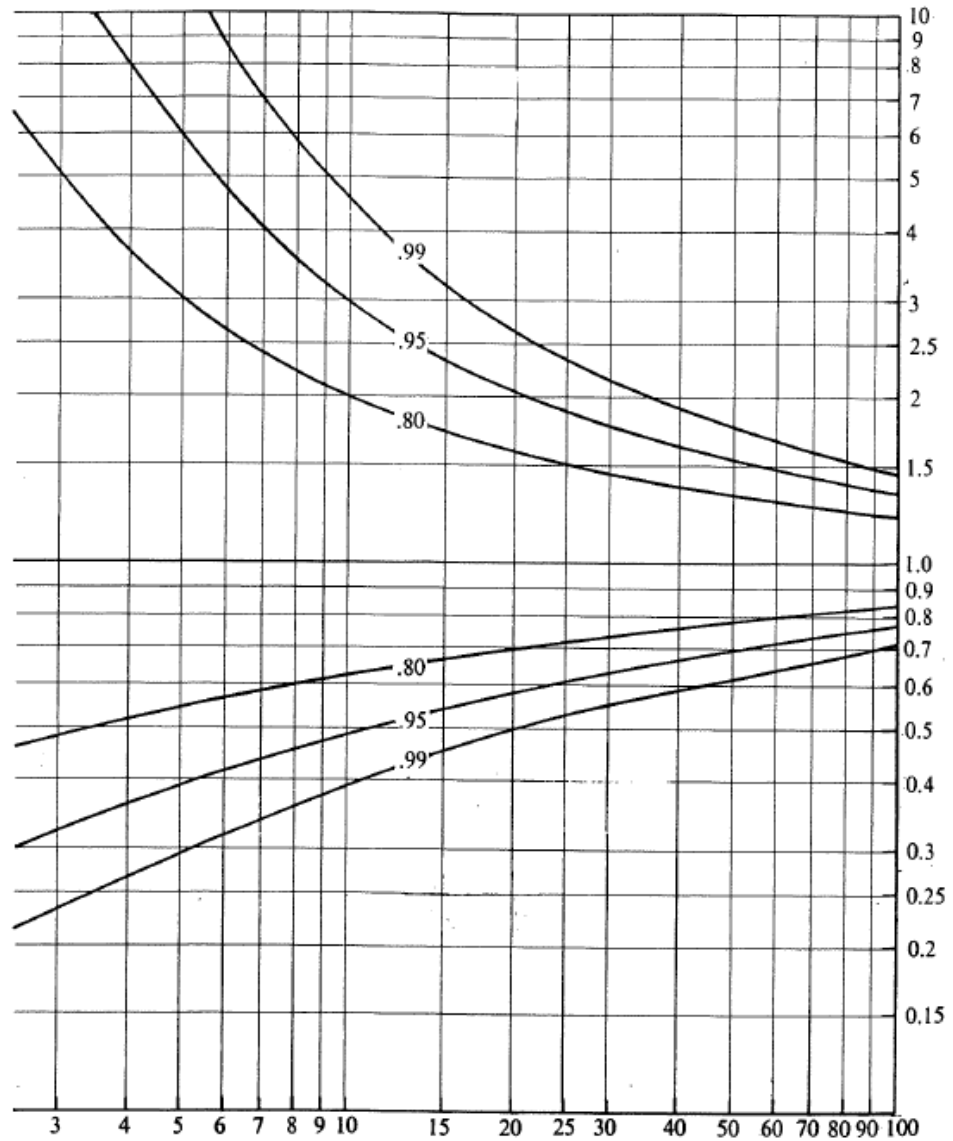


FIGURE 4.5: Spectral peak multiplication factor, y-axis, against NDF, x-axis, for 99%, 95% and 80% confidence intervals (Jenkins and Watts, 1968)

Number of Degrees of Freedom (NDF) and  $N_d$  is the number of non-overlapping sections. In the example shown in Figure 4.4 there are eleven non-overlapping sections, resulting in  $NDF = 38.78$ . With NDF known, the upper and lower confidence bounds can be calculated using Figure 4.5. Increasing the number of overlapping sections will therefore increase the NDF and narrow the confidence limits at the cost of decreasing spectral resolution.

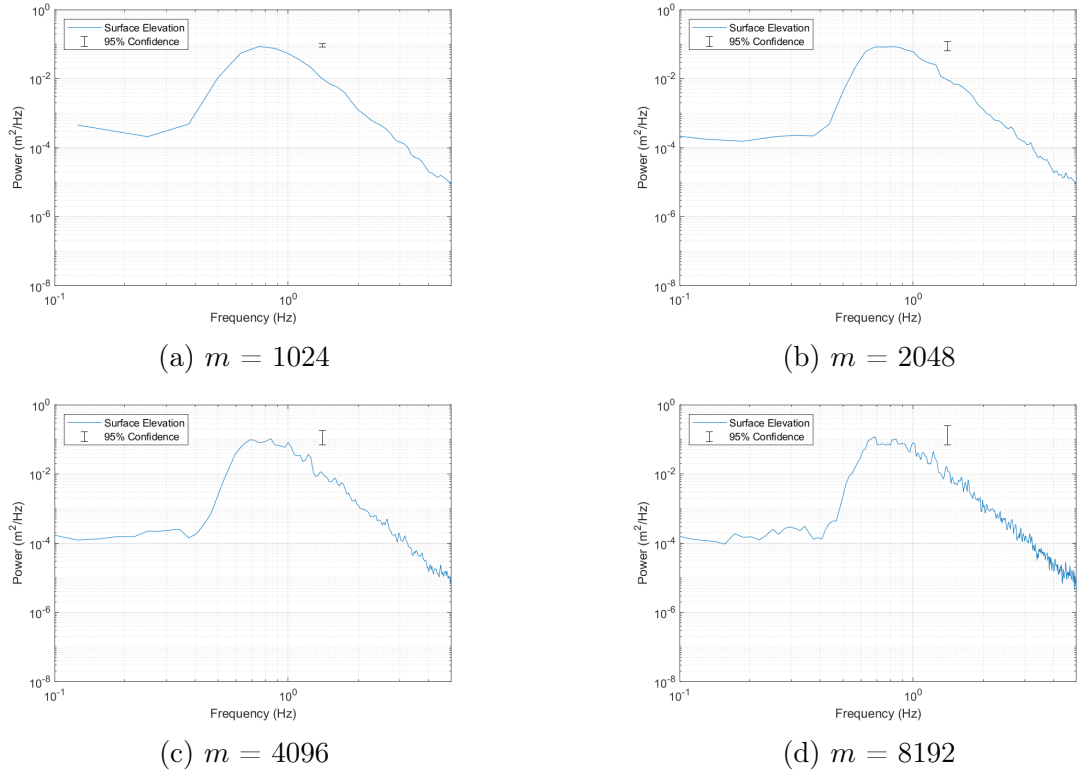


FIGURE 4.6: Example of differing overlapping window length,  $m$ , on the spectra resolution and confidence intervals

Following the random wave test with  $H_s$  of 0.12 m and  $T_p$  of 1.46 s, after the raw surface elevation data has been windowed and the reflection analysis completed, the surface elevation data was spectrally analysed to better understand the frequency distribution of the surface elevation.

The incident, reflected and transmitted reconstructed wave trains were windowed and detrended. The data was then further sub-windowed into sections 4096 data points in length, resulting in eleven non-overlapping windows. The eleven windows contain a total of 45056 data points, or 352 s, as data was sampled at 128 Hz. At 1:30 scale the required time to measure for the test to be equivalent to 30 minutes at full scale is 328 s, therefore there is sufficient data in the analysis window.

With a window length of 4096 data points there were 2048 frequency bins up to the Nyquist frequency of 64 Hz resulting in a bandwidth per bin of 0.03125 Hz. As described above, eleven non-overlapping sections resulted in  $NDF = 38.78$ , and

therefore 95% error bars can be applied to the data by multiplying the peak values by 0.65 and 1.8 for the lower and upper bounds respectively.

## 4.5 Calculation of Wave Field Coefficients

By definition, the sum of values in a periodogram is equal to the variance of the time series, as shown in equation 4.23

$$\sigma^2 = \sum_1^N S_{xx} \Delta f \quad (4.23)$$

where  $N$  is the number of frequency bins between zero and the Nyquist frequency and  $\Delta f$  is the bandwidth. The output  $S_{xx}$  from the Matlab routine ( $S_{xx\text{MATLAB}}$ ) is related to the true  $S_{xx}$  through the following relation

$$S_{xx} = \frac{S_{xx\text{MATLAB}}}{f_N} \quad (4.24)$$

With the variance of the periodogram known through equations 4.23 and 4.24 the wave height can be calculated through the following

$$\text{RMS} = \sqrt{\sigma^2} = \sqrt{\sum_1^N S_{xx} \times \Delta f} \quad (4.25)$$

The Root Mean Squared (RMS) of a signal is equivalent to the square root of the variance of the signal, from which statistical characteristics, primarily  $H_s$ , of the analysed wave trains can be calculated using the following equations

$$\begin{aligned}
 \text{RMS} &= \frac{A}{\sqrt{2}} \\
 H &= 2 \times A = 2\sqrt{2} \text{ RMS} \\
 H_s &= \sqrt{2} H \\
 H_s &= 4 \times \sqrt{\sum_1^N S_{\eta\eta} \times \Delta f}
 \end{aligned} \tag{4.26}$$

where  $A$  is the wave amplitude,  $H$  is the wave height,  $H_s$  is the significant wave height,  $\Delta f$  is the bandwidth and  $S_{\eta\eta}$  is the SDF in terms of surface elevation rather than the generic expression used in earlier equations. The resultant  $H_s$  is therefore dependant on the original wave train analysed, e.g. analysing the incident wave train will result in the  $H_s$  of the incident wave train,  $H_{si}$ .

The incident energy contained in a wave is transformed as it passed and influenced the model, a proportion was reflected, a proportion transmitted and a proportion absorbed by the model through movement and overtopping. The proportions were defined as dimensionless coefficients of reflection, transmission and absorption and are the dimensionless ratios of relevant significant wave height to the incident significant wave height thus

$$k_r = \frac{H_{sr}}{H_{si}} \tag{4.27}$$

$$k_t = \frac{H_{st}}{H_{si}} \tag{4.28}$$

$$k_a = \frac{H_{sa}}{H_{si}} \tag{4.29}$$

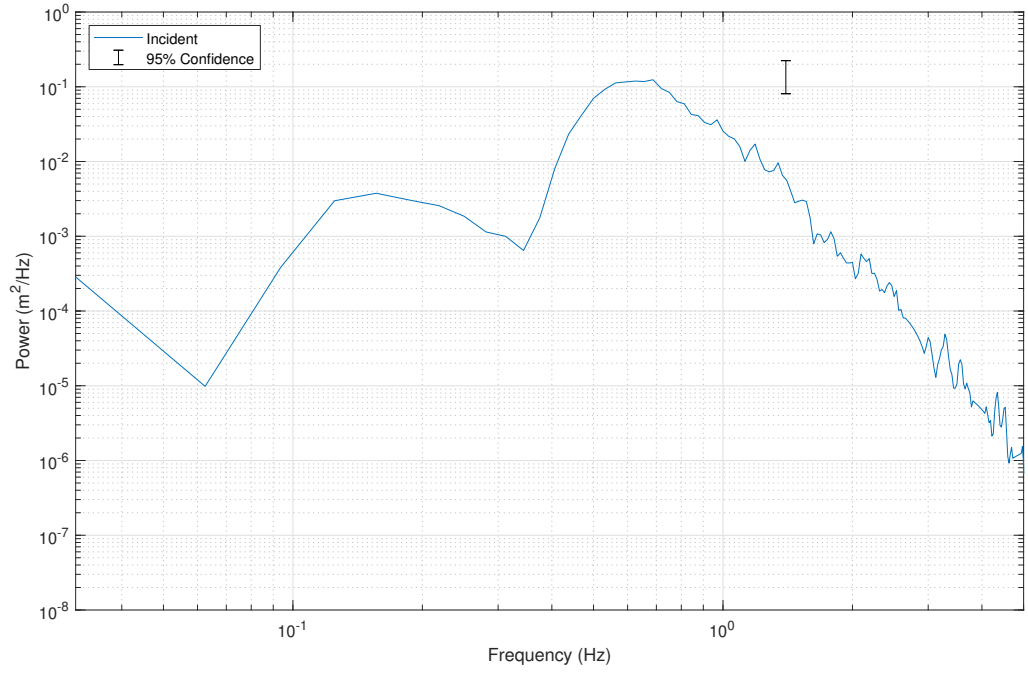


FIGURE 4.7: Example incident spectrum

$H_{sa}$  cannot be measured from the WG measurements but as energy is conserved  $k_a$ , and thus  $H_{sa}$ , can be calculated from the other coefficients (Thornton and Calhoun, 1972)

$$k_r^2 + k_t^2 + k_a^2 = 1 \quad (4.30)$$

In this application  $k_a$  refers to all energy that is not reflected or transmitted, as it is traditionally used in reference to breakwaters. In the area of wave energy conversion this term therefore encompasses energy that is lost in the system through friction, radiation and influencing the motion of the device.

From the incident, reflected and transmitted spectra obtained through spectral analysis, Figures 4.7, 4.8 and 4.9 respectively, the variance in the surface elevation can be calculated using Equations 4.23 and 4.24.

For the example shown, the variance of each spectra was calculated and the coefficients obtained,  $k_r = 0.32$  and  $k_t = 0.69$ . Using Equation 4.30,  $k_a$  was calculated as 0.64.

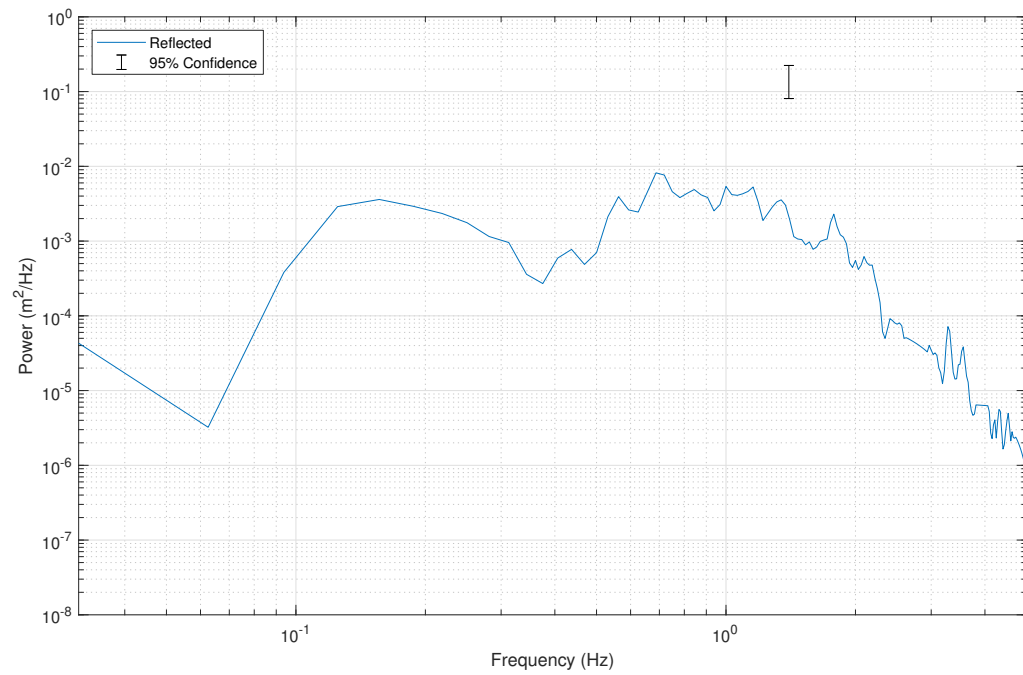


FIGURE 4.8: Example reflected spectrum

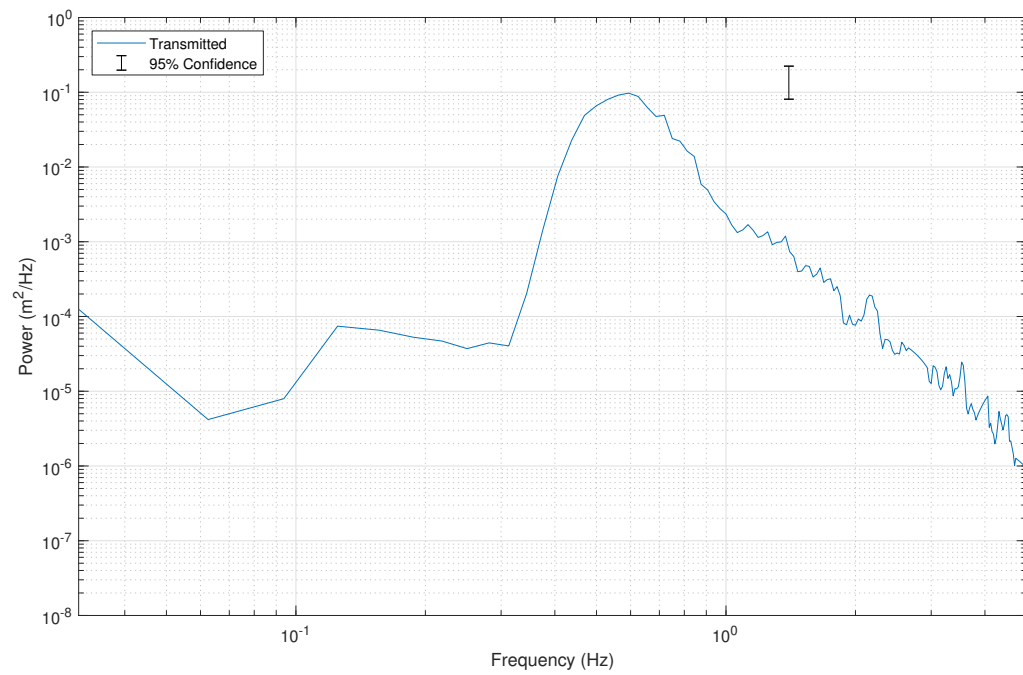


FIGURE 4.9: Example transmitted spectrum

## 4.6 Calculation of Power Captured by the Device

An estimation of the power captured during a test can be made from flowmeter and model position data. The flowmeter records the output of a light sensor within the instrument housing, which registers either high or low depending on if the paddles of the paddlemeter blocked the light. The number of pulses from high to low therefore represent the paddlemeter turning an amount of times which represents a volume of fluid based on a “K-Factor” calibrated in manufacture. For this flowmeter model 1,200 pulses is the equivalent of one litre of fluid.

With the volume of fluid known the energy captured by the device could be calculated using principles of Gravitational Potential Energy (GPE) (J) of water released with a head,  $h$

$$\text{GPE} = mgh \quad (4.31)$$

The GPE requires the mass of water,  $m$ , calculated from the following equation

$$m = \frac{N_p \rho}{1000K} \quad (4.32)$$

where  $N_p$  is the number of pulses recorded by the flowmeter,  $K$  is the dimensionless “K-Factor” of 1,200 specific to this meter model,  $\rho$  is the density of water and a factor of 1000 included to convert from  $\text{m}^3$  to litres. Combining this with Equation 4.31, where  $g$  is the acceleration due to gravity and  $h$  is the head of the water, GPE was calculated for each tank. The head of the water is measured by the level sensors in each tank, and the logging software in the control system monitors which valves, and therefore which tanks, the water is allowed to flow from through the flowmeters. If a valve is closed then the tank is not allowing water to flow through the flowmeter and therefore not contributing to the GPE.

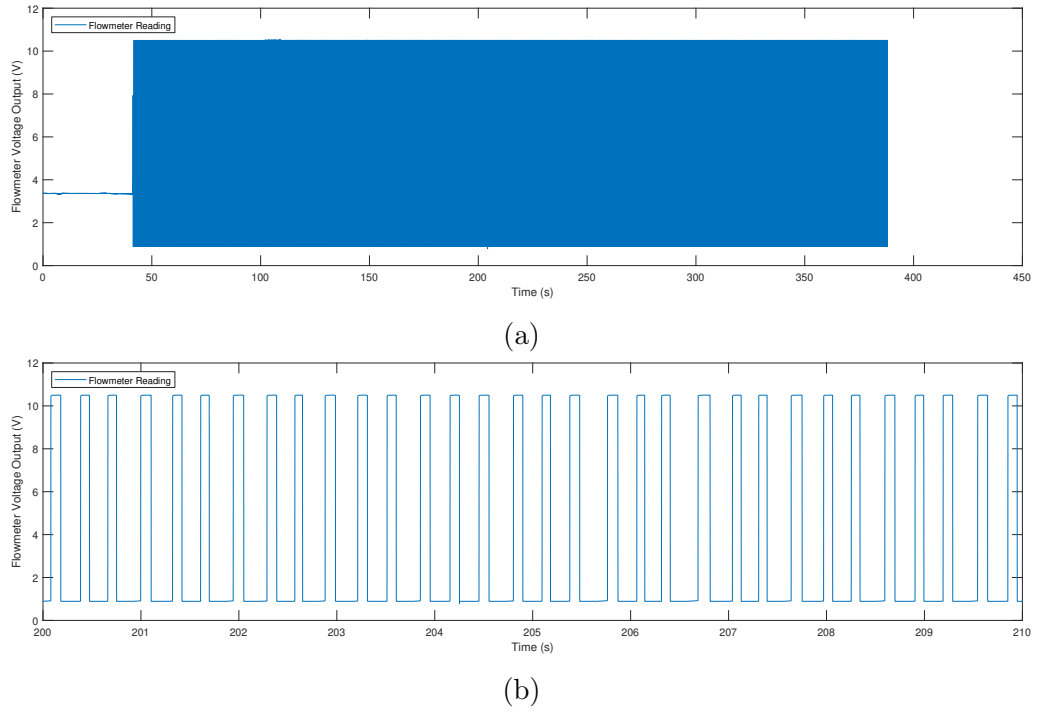


FIGURE 4.10: Example pulse output from a flowmeter for (a), a complete test and (b), a subsection of the test

The potential energy contained in the captured water was then compared to the energy contained within the incident waves to obtain a measure of the ratio of energy captured to the energy incident and absorbed by the device.

Figure 4.10 shows a sample of a time trace from one of the flowmeters in the WaveCat hulls during the example test. As can be seen in Figure 4.10a there was no flow until the tanks reach the predetermined level, at approximately 70 s into the test, at which point the valves open and the collected water starts flowing through the flowmeters. This then continues for the rest of the test as the level in the tank is replenished by further overtopping. Figure 4.10b shows a zoomed in section of the full test with individual pulses visible. From this the total mass of water, in kg, that flows through the flowmeter during the test can be calculated using Equation 4.32, where  $N_p$  is the total number of pulses in the test,  $K$  is 1,200 and  $\rho$  is the density of water in the tank,  $997.5 \text{ kgm}^{-3}$ .

Figure 4.11 shows the collected water level during the tests in the starboard tanks. The tanks start with an initial amount of water contained within that assists in



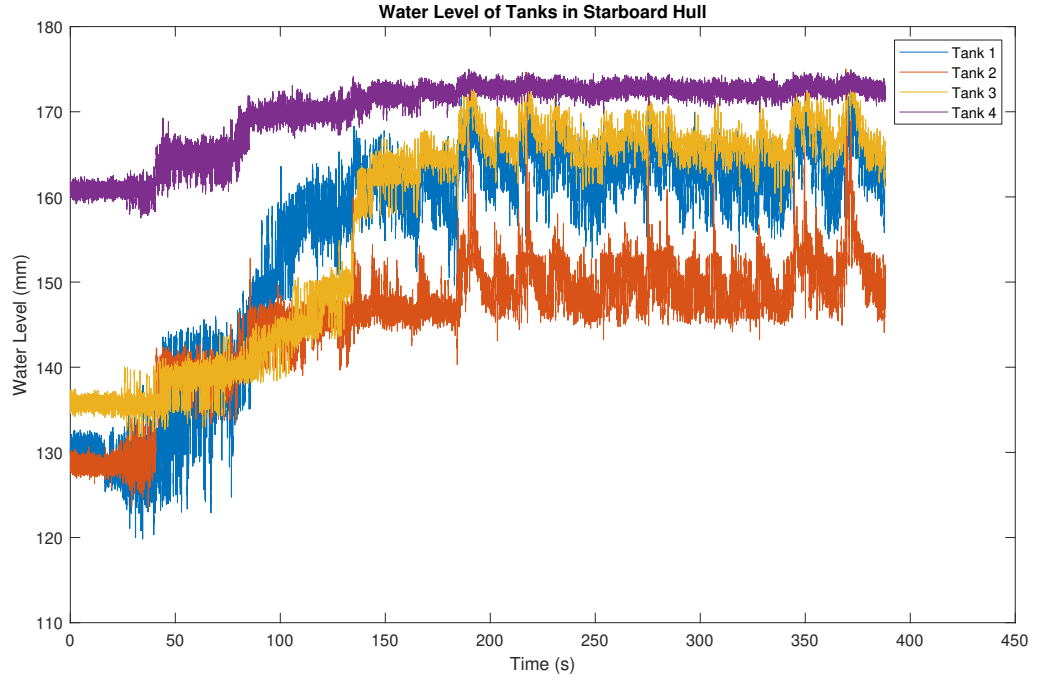


FIGURE 4.11: Levels in starboard tanks during example test

orientating the model at the beginning of each test. For example, Tank 4, the furthest tank towards the bow, has more water than the other tanks to allow the model to start the test with the inner freeboard parallel to the free surface. Through monitoring the water level in the tank the head height,  $L$ , was known. Combined with the known mass of water passed through the flowmeters in each hull, as well as  $g$ , an estimate of the GPE captured was made for the whole model throughout a test and compared to the energy contained in the incident, reflected, transmitted and absorbed waves.

## 4.7 Response Analysis to Regular Waves

The Qualisys motion capture system was used to capture information about device responses during tests performed with regular waves. The first step in response analysis was to apply the reflection analysis steps shown in Section 4.2 to the incident waves used in the tests. As the waves were impacting the model reflections were

produced, therefore the reflection analysis allows the incident waves to be considered without the superposition of the reflected waves from the model.

Once the incident waves were separated from the combined surface elevation recordings, the wave height of the test was calculated. As the waves were defined as regular waves they should have a consistent height and period throughout the test, however characteristics of the tank and model resulted in slight differences between each wave. For example, the reflections returning from the beach can superimpose on the incident wave field and changes in orientation of the device on the moorings can cause further reflections.

For this reason each wave in the wave train was analysed individually to determine its height, the waves were then ordered from highest to lowest in order to calculate the  $H_{1/3}$ . This was then taken as the representative wave height for the test.

Figure 4.12 shows the expected wave conditions against the actual generated wave conditions during regular tests for  $\theta_w = 60^\circ$ . Figure 4.12a shows the expected wave height against the actual generated wave height. In most cases the measured wave height was lower than the expected wave height but is generally consistent across the range of wave periods tested as wave height is increased. At  $T_p = 1.46$  s the wave heights generated were close to the expected wave height for the test. Figure 4.12b shows the expected wave period against the generated wave period. The waves generated are very close to the expected wave period for all the tests, with wave height making a negligible difference.

Figure 4.13 shows the expected wave conditions against the actual generated wave conditions during regular tests for  $\theta_w = 30^\circ$ . Figure 4.13a shows the expected wave height against the actual generated wave height. In all cases the measured wave height was consistently higher than the expected wave height but there is little variation beyond that across the range of wave periods tested as wave height is increased. Figure 4.13b shows the expected wave period against the generated wave period. The waves generated are very close to the expected wave period for all the tests, with wave height making a negligible difference.

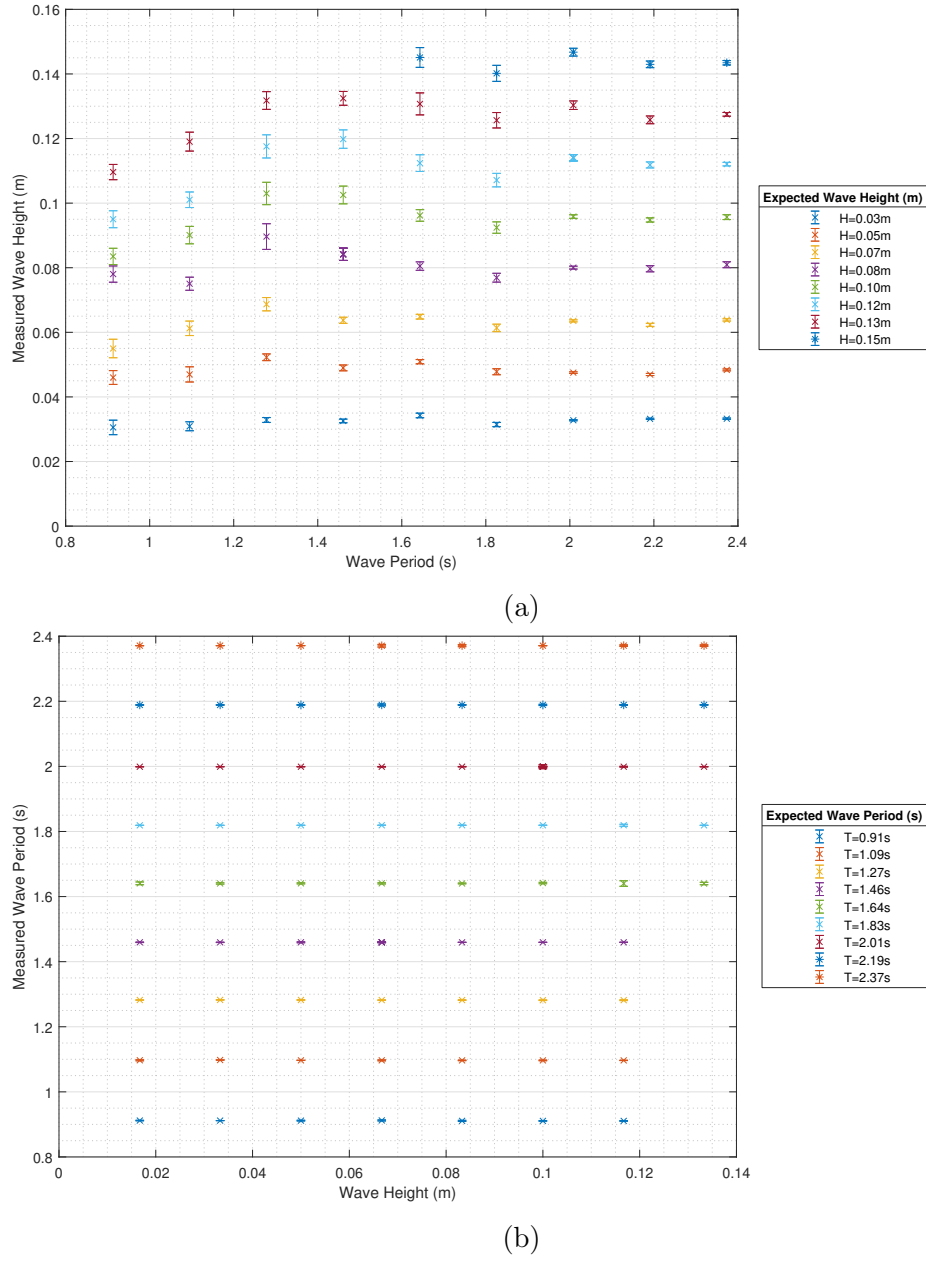
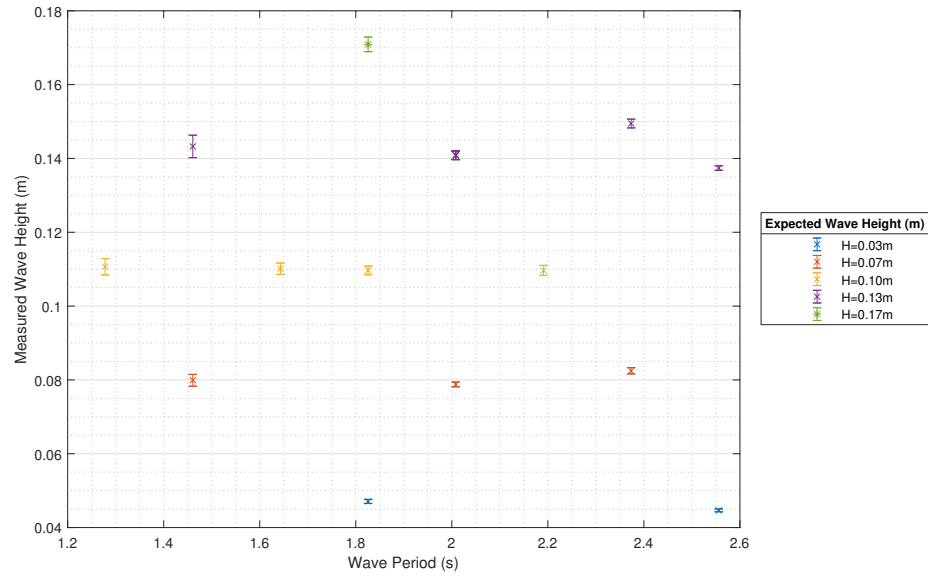
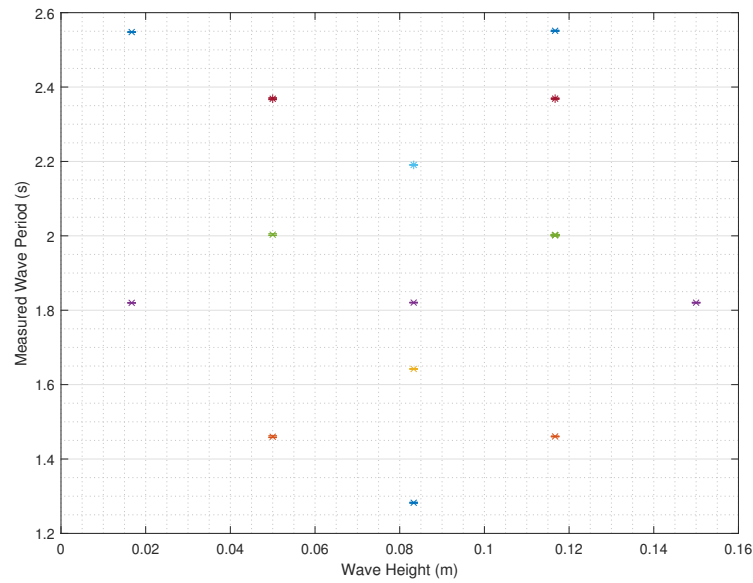


FIGURE 4.12: Test parameters against predicted values for a) wave period and b) wave height, for  $\theta_w = 60^\circ$



(a)



(b)

FIGURE 4.13: Test parameters against predicted values for a) wave period and b) wave height, for  $\theta_w = 30^\circ$

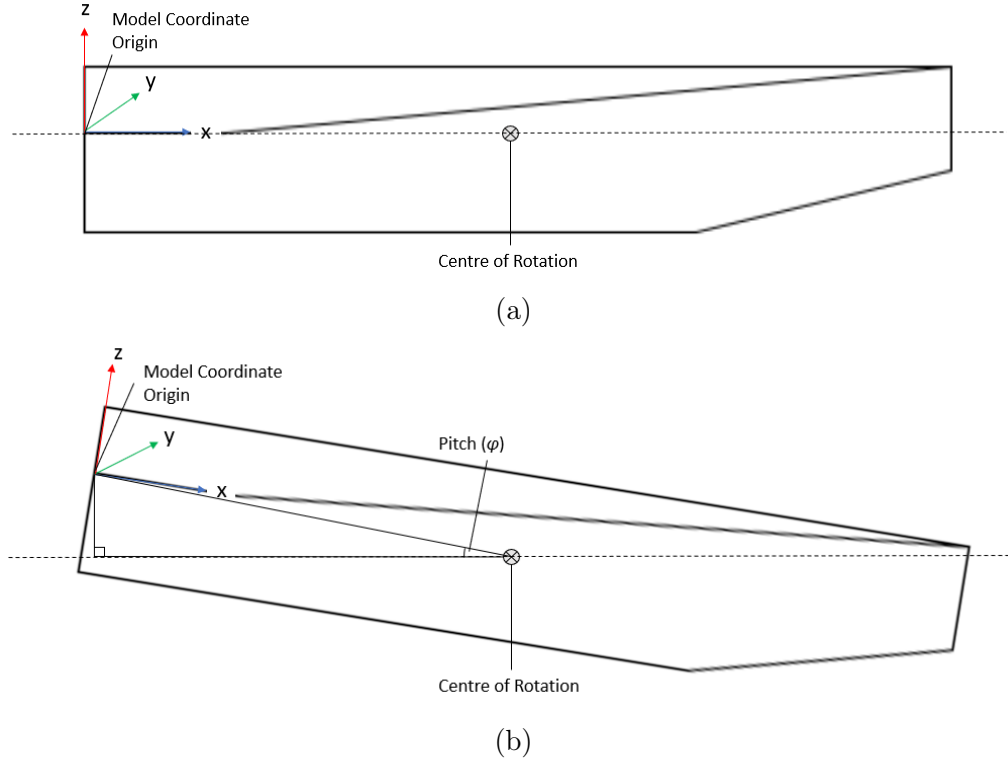


FIGURE 4.14: The WaveCat model coordinate origin comparison when level (a) and when ballasted (b), showing a pitch rotation affecting the heave location without model centre of rotation moving

The error ranges presented in the height graphs, Figures 4.12a and 4.13a, were defined as the variation in each individual waves height across the test. The error ranges presented in the period graphs, Figures 4.12b and 4.13b, were defined as the variation in each individual waves period across the test.

Motion was then analysed to determine the response of the device to the regular waves. The first step was to correct the initial offset of the measurements, as Qualisys measures relative to a globally defined origin point in the centre of the experimental area.

The second stage of analysis was to apply a pitch correction to the heave measurements. Qualisys measured each hull independently and each had its own local origin set in calibration. The origin was then recorded relative to the global experimental coordinates, from which the motions were registered. As motions were typically measured from the devices centre of rotation and the WaveCat origin was set apart

from the centre of rotation, as shown in Figure 4.14, a pitch motion around the centre of rotation would show a heave motion despite the centre of rotation remaining stationary. A heave modifier was therefore applied to the local device measurement based on the angle of the device. This allowed the translation of the measured heave to that of the centre of rotation.

The third step was to remove any large scale trends, most prominent in surge, to ensure that only the contribution from each wave was analysed. Thirdly, the data was windowed to only include an appropriate number of waves that were fully developed, excluding the ramp up at the beginning of the test and the extra time at the end of the test which contained the Ocean Basin returning to still water level.

The last step before analysis was to window the data to the same window as the surface elevation to avoid ramp up and settling waves at the beginning and end of the tests. Peaks were then identified in the same manner as the incident surface elevation data to determine a response for each degree of freedom during the test.

Using a regular wave test with  $H = 0.1$  m and  $T = 1.83$  s as a worked example, the initial raw surface elevation is shown in Figure 4.15. The two gauges closest to the model, WG 3 and WG 8, are shown. The gauges show slight differences, particularly with the minimum surface elevations.

The raw surface elevation data was then subjected to the reflection analysis, as described in Section 4.2. The incident, reflected and transmitted wave trains at the WG 3 location were reconstructed and this reconstructed incident wave was then analysed to determine the wave height of the test.

Figure 4.16 shows the identified peaks and troughs on the reconstructed incident waves. From this the individual wave heights were calculated and ordered from high to low before the mean of the top third,  $H_{1/3}$ , were taken as the height of waves during the test. For this test the calculated wave height was 0.103 m.

Figure 4.17 shows the measured Qualisys output from the example test of  $T = 1.83$  s and  $H = 0.1$  m. Surge, sway and yaw have large non-sinusoidal movements which

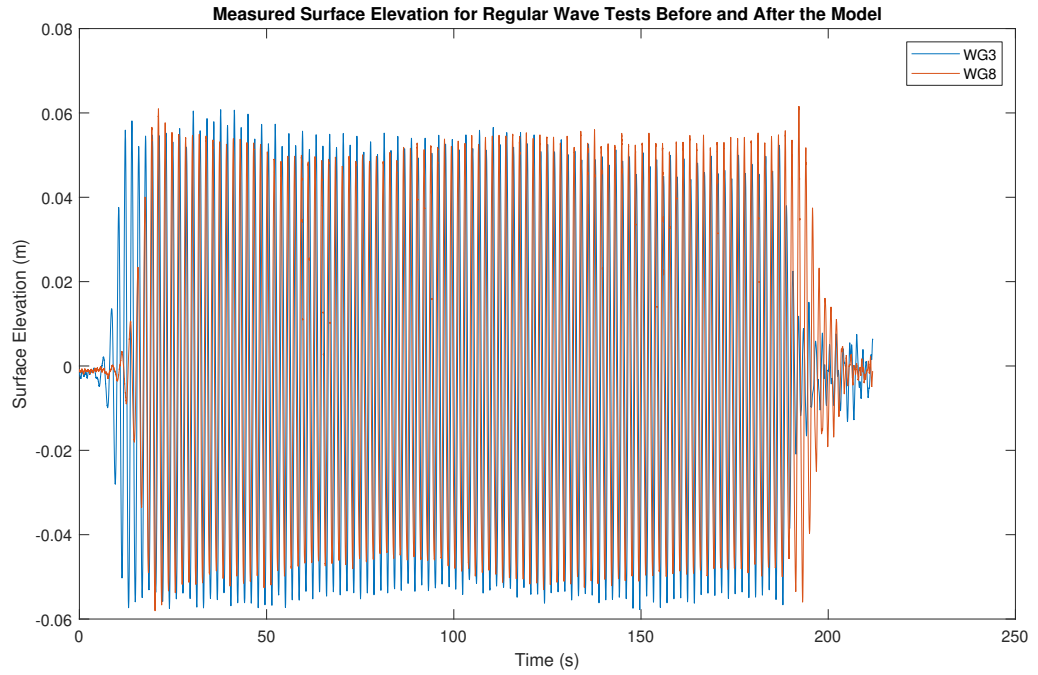


FIGURE 4.15: An example of the raw WG surface elevation data for WG 3 and WG 8 during a test with  $T = 1.83$  s and  $H = 0.1$  m

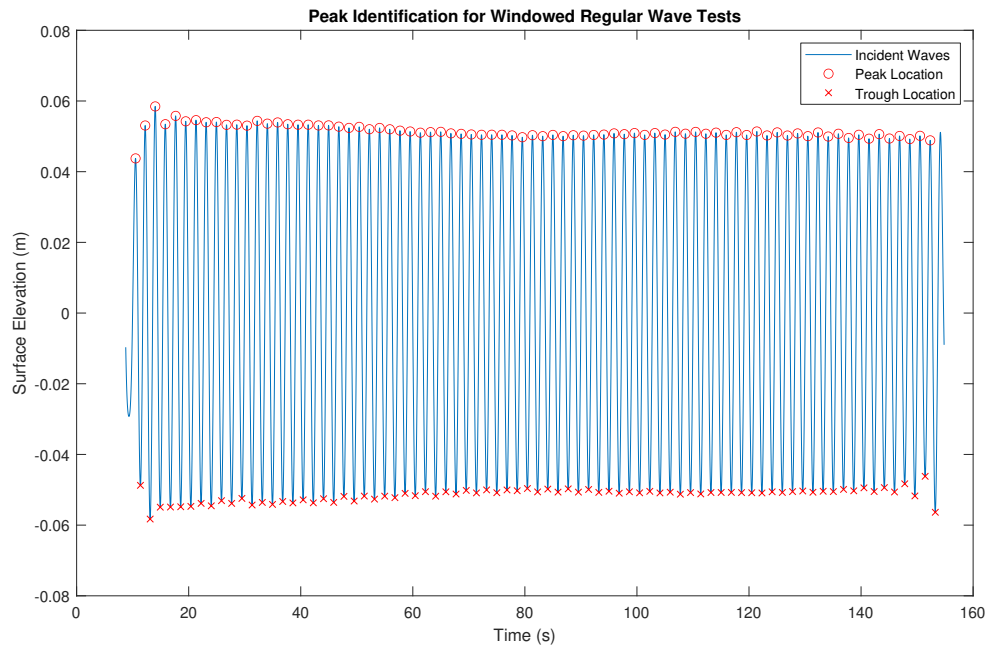


FIGURE 4.16: An example of peak identification within a test window of regular wave data during a test with  $T = 1.83$  s and  $H = 0.1$  m

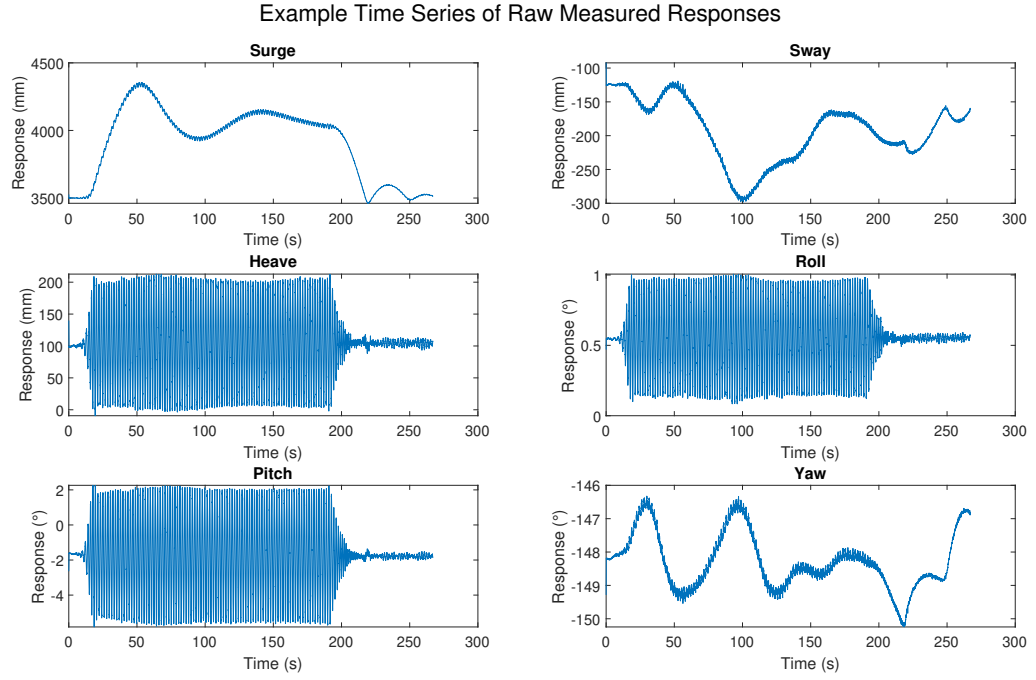


FIGURE 4.17: An example of the raw Qualisys data showing large trends in surge, sway and yaw during a test with  $T = 1.83$  s and  $H = 0.1$  m

arise as a result of the model moving in the experimental area due to a flexible mooring and non-symmetries in the system. Heave, pitch and roll do not show this behaviour. The large scale trends in the motions were removed through time-averaging the signal over two wave periods and removing this mean from the signal, leaving oscillations from the waves. In addition, the signals were adjusted to remove any initial offset and the pitch correction applied to the heave signal.

Figure 4.18 shows the motion data after large scale trends and offsets were removed, and the pitch modifier applied. The motions have been reduced to regular motion about zero displacement and can be compared to the incident waves. The surge, heave and pitch are the three key motions with head-on waves, as in a perfectly symmetrical system the motions of the other degrees of freedom, sway, roll and yaw, should tend to zero. As the experiment is not perfectly symmetrical there are small amounts of these motions, for example for this test case the sway was approximately 0.005 m in amplitude, compared to a 0.05 m wave amplitude. This was due to the model being free to move laterally, as it was only moored at the bows of the model.



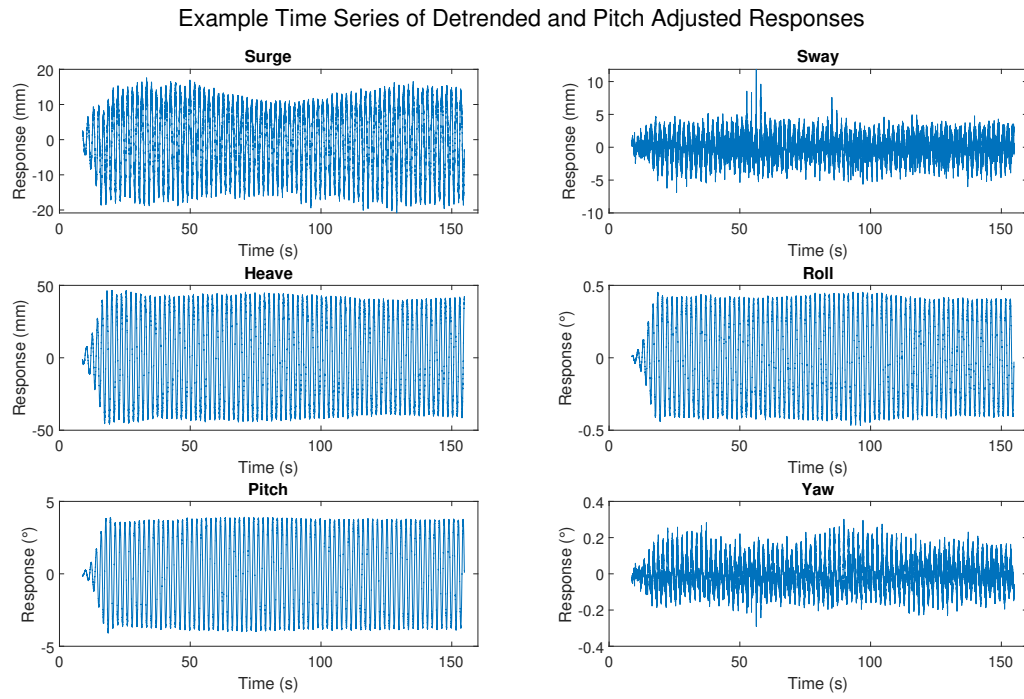


FIGURE 4.18: Qualisys data once large scale trends are removed and pitch correction applied during a test with  $T = 1.83$  s and  $H = 0.1$  m

The roll amplitude was approximately  $0.4^\circ$  and the yaw amplitude approximately  $0.2^\circ$ .

## 4.8 Response Analysis to Random Waves

The devices motion response to random waves was also measured. The incident, reflected and transmitted wave trains were separated from the combined surface elevation signal using the reflection analysis method outlined in Section 4.2. The motions were then modified to account for initial offsets as well as the heave adjusted for pitch effects before the surge, pitch and heave were subjected to the spectral analysis method described in Section 4.4.

# Chapter 5

## Wave Field Coefficient Results

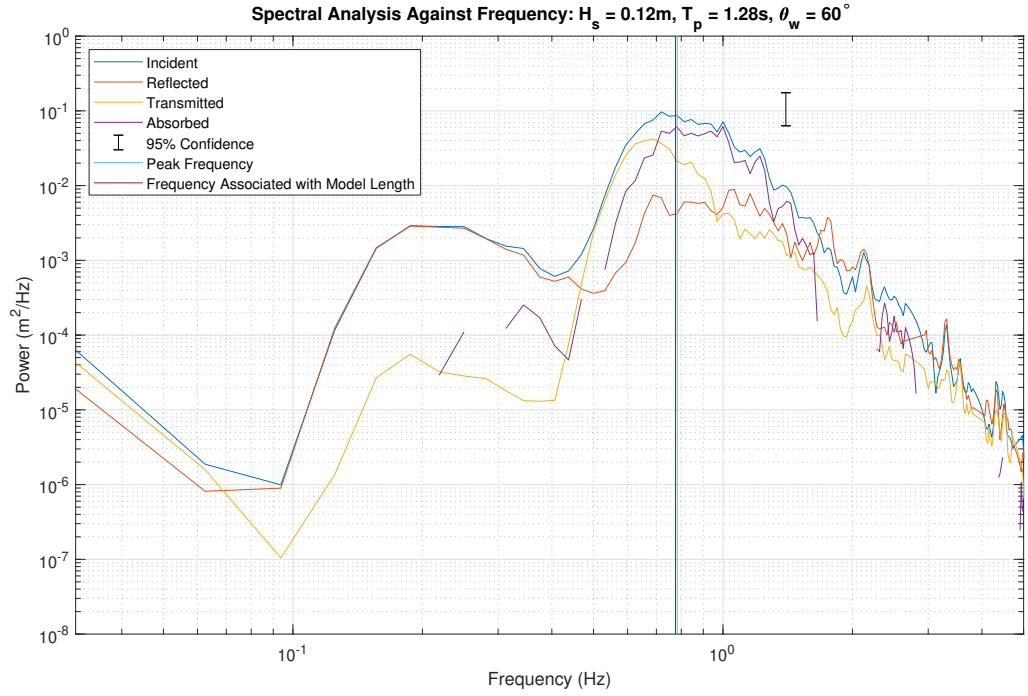
In this Chapter the device impact on the wave field is shown. First, the spectral analysis of the wave field of individual tests across the parameter space are shown. Second, the coefficients of energy are shown as functions  $T_p$ . Finally, power extraction results are combined with the wave field results to produce contour plots across the parameter space. Results for both wedge angles tested,  $\theta_w = 60^\circ$  and  $\theta_w = 30^\circ$ , are shown.

### 5.1 Results for $\theta_w = 60^\circ$

The model tests performed with  $\theta_w = 60^\circ$  are shown first.

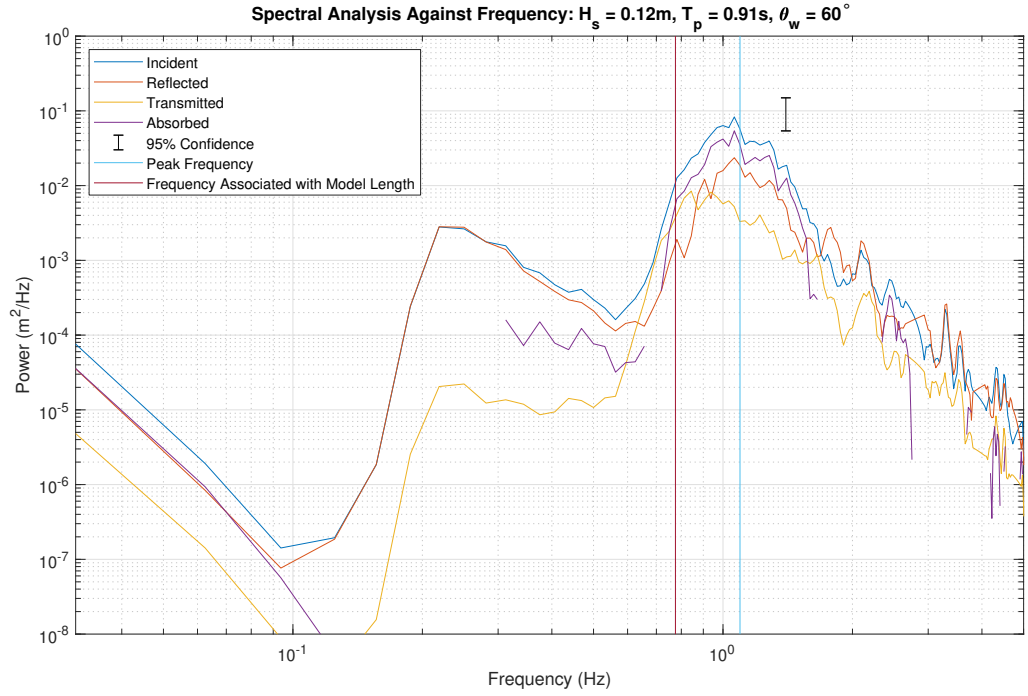
#### 5.1.1 Wave Field Spectral Analysis

Spectral analysis of the results was carried out for each individual test from which coefficient values were determined as described in Chapter 4. The spectra give detailed information on the frequency components that are affected by the WaveCat. The coefficient values are representative of the test as a whole and as such are based on the dominant wave frequencies determined by the  $T_p$  of a given test. However, the

FIGURE 5.1: Spectral analysis of  $H_s = 0.12\text{ m}$ ,  $T_p = 1.28\text{ s}$ ,  $\theta_w = 60^\circ$ 

spectral analysis shows how the coefficient was built from the spread of waves present in the test. Experiments where the  $T_p$  was large had different outcomes compared to those where the  $T_p$  was small or where the  $T_p$  value resulted in wavelengths close to that of the model length.

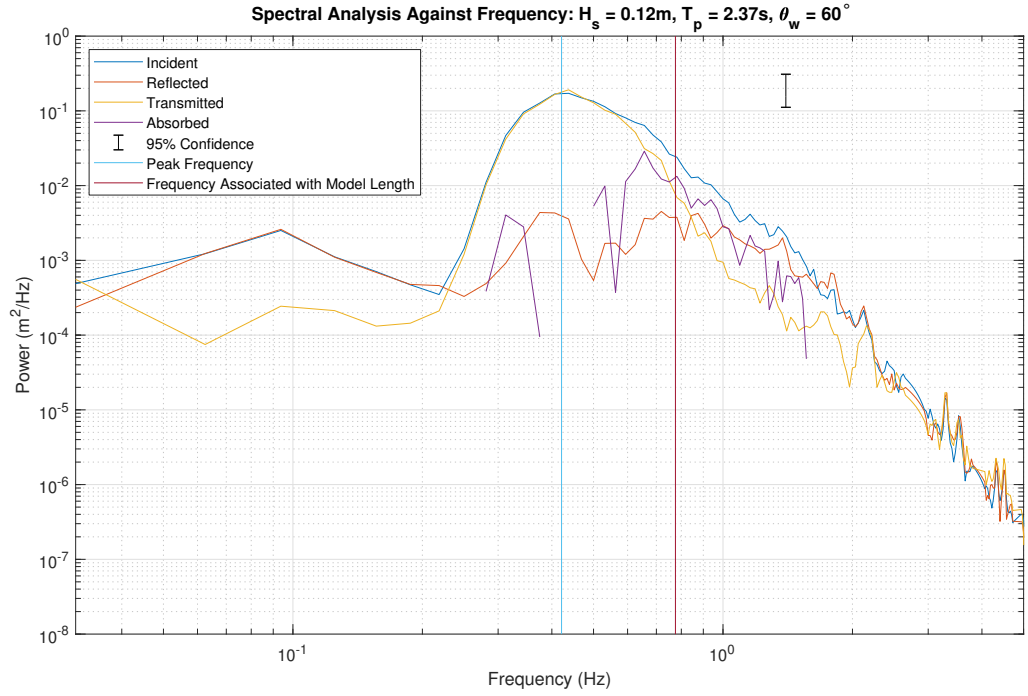
Figure 5.1 shows the spectral analysis of a test with characteristics  $H_s = 0.12\text{ m}$ ,  $T_p = 1.28\text{ s}$  and  $\theta_w = 60^\circ$ . The  $T_p$  parameter of this test closely aligned with the  $T_p$  of the wavelength of the model when  $\theta_w = 60^\circ$ , 1.29 s compared to 1.28 s, shown by the vertical lines. As expected the peak in incident energy was around the characteristic  $T_p$  of the test. Below the peak frequency, at lower frequencies and therefore longer period waves, the majority of energy was transmitted rather than reflected with little energy absorbed by the device. As the wave frequency approached the peak frequency of the test the amount of energy transmitted dropped but the amount of reflected energy remained constant, allowing a greater portion of energy to be absorbed. As the wave frequency increased, and therefore the wave period became shorter, the transmitted energy dropped further along with the reflected energy,

FIGURE 5.2: Spectral analysis of  $H_s = 0.12$  m,  $T_p = 0.91$  s,  $\theta_w = 60^\circ$ 

however the reflected energy was less affected resulting in more energy in reflected waves than transmitted.

Figure 5.2 shows the spectral analysis of a test with characteristics  $H_s = 0.12$  m,  $T_p = 0.91$  s and  $\theta_w = 60^\circ$ . The  $T_p$  parameter of this test represented waves of the highest frequency tested. Again, the most incident energy was around the test peak frequency, as expected. The reflected energy followed the shape of the incident energy throughout the test but at a lower level, peaking at the test frequency. On the other hand, the transmitted energy peaked around the frequency associated with the model frequency and was lower at the peak frequency. The absorbed energy was at a maximum around the peak frequency, following the trend of the incident energy closely.

Figure 5.3 shows the spectral analysis of a test with characteristics  $H_s = 0.12$  m,  $T_p = 2.37$  s and  $\theta_w = 60^\circ$ . The  $T_p$  parameter of this test represented waves of the lowest frequency tested. The peak incident energy was around the peak frequency of the test, along with the peak transmitted energy. For frequencies below 0.6 Hz, where the waves were longest, the transmitted energy was almost equal to the incident

FIGURE 5.3: Spectral analysis of  $H_s = 0.12\text{ m}$ ,  $T_p = 2.37\text{ s}$ ,  $\theta_w = 60^\circ$ 

energy, meaning very little was being reflected or was absorbed. As the waves shortened and approached model frequency the transmitted energy reduced at a faster rate than the incident energy. This resulted in energy being absorbed by the device. As the frequency continued to increase past the model frequency of 0.77 Hz the reflected energy approached the incident energy again resulting in little energy being absorbed.

Figure 5.4 shows the spectral analysis of a test with characteristics  $H_s = 0.08\text{ m}$ ,  $T_p = 0.91\text{ s}$  and  $\theta_w = 60^\circ$ . This is similar to the test shown in Figure 5.2, however at a lower  $H_s$ , showing the difference between the two  $H_s$  values. The test with the lower  $H_s$  followed the same trend as the larger  $H_s$  test in that the incident, reflected and absorbed energy all peaked around the test frequency. The transmitted energy was relatively constant for the frequency region where the incident energy was at its peak, slightly different to the trend for the larger  $H_s$  value, which dropped slightly when above model frequency.

Figure 5.5 shows the spectral analysis of a test with characteristics  $H_s = 0.08\text{ m}$ ,  $T_p = 2.37\text{ s}$  and  $\theta_w = 60^\circ$ . This is similar to the test shown in Figure 5.3, however at a lower

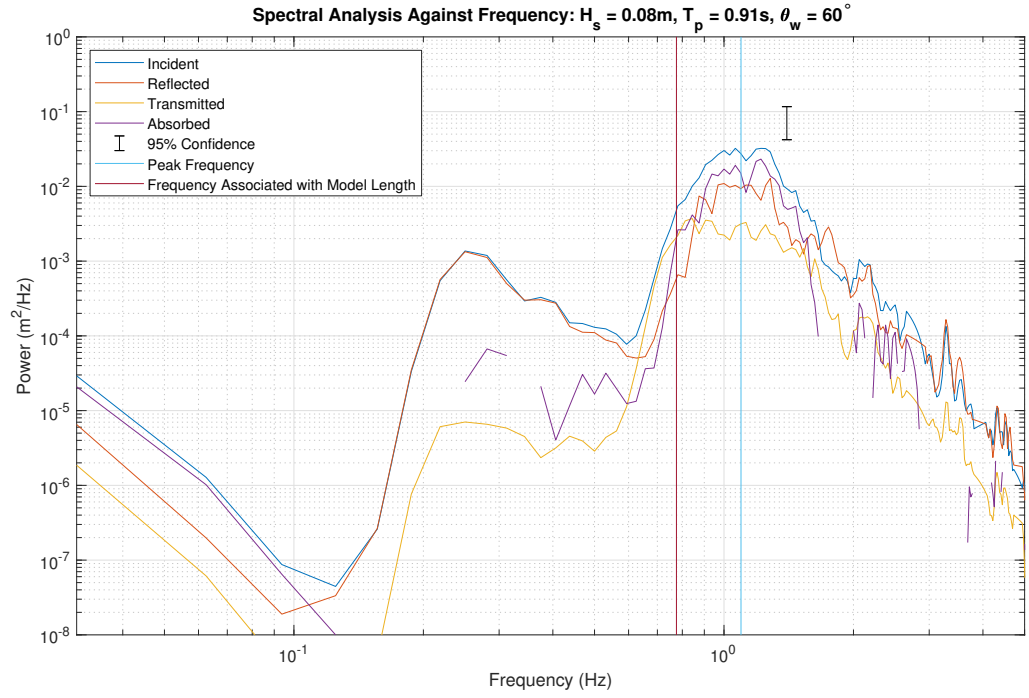


FIGURE 5.4: Spectral analysis of  $H_s = 0.08\text{ m}$ ,  $T_p = 0.91\text{ s}$ ,  $\theta_w = 60^\circ$

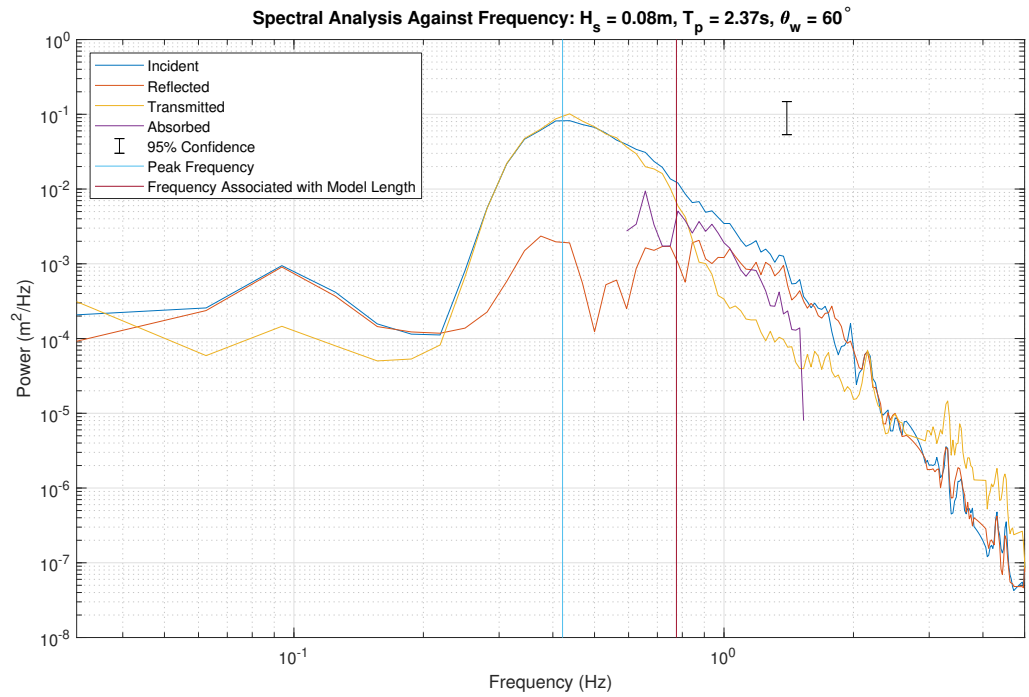


FIGURE 5.5: Spectral analysis of  $H_s = 0.08\text{ m}$ ,  $T_p = 2.37\text{ s}$ ,  $\theta_w = 60^\circ$

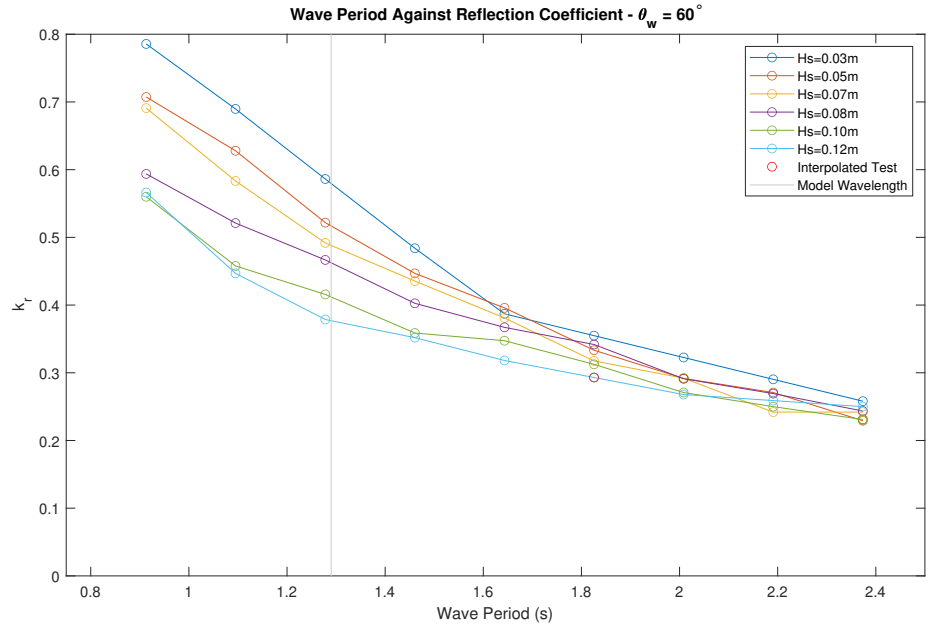
$H_s$ , showing the difference between the two  $H_s$  values. For lower frequencies, where the waves were longest, the transmitted energy was almost equal to the incident energy, meaning very little was being reflected or was available for overtopping. As the waves shortened and approached model frequency the transmitted energy reduced at a faster rate than the incident energy, resulting in energy being absorbed by the device. As the frequency continued to increase past the model frequency the reflected energy approached the incident energy resulting in little energy being absorbed.

### 5.1.2 Energy Coefficients

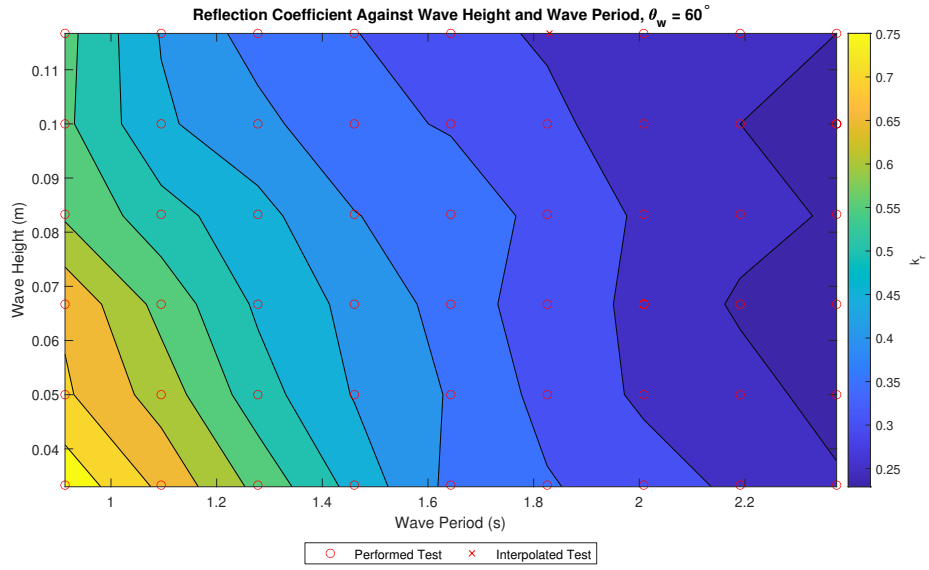
Using the spectral data from each test a total for reflected, transmitted and absorbed energy was calculated over the course of a complete test. This was accomplished through the method outlined in Section 4.5. This was then converted to a coefficient representing each as a fraction of the incident energy available to the test and plotted grouped by tests with the same  $T_p$  value. The coefficients  $k_r$ ,  $k_t$  and  $k_a$  are defined in Section 4.5.

Figure 5.6 shows the reflection coefficient,  $k_r$ , as a function of  $T_p$ , (a), and  $k_r$  as a contour plot against  $H_s$  and  $T_p$ , (b) with more yellow colours being higher values and more blue colours being lower values. For small  $T_p$  values the  $k_r$  values started initially high. This represented a large portion of the incident energy being reflected as the waves were not big enough to overtop the inner edge of the WaveCat. Once the  $H_s$  parameter had increased enough to allow steady overtopping, however,  $k_r$  began to reduce and became constant as  $H_s$  increased. In addition, tests with larger  $T_p$  showed near constant  $k_r$  values throughout the whole series of tests. When the tests were grouped by  $T_p$  higher  $T_p$  values caused the data points to be closely grouped. This confirmed that the  $k_r$  value was near constant at higher  $T_p$ . The wave period associated with the wavelength of the model also marked the region in which the  $k_r$  trend began to change to a more constant regime. This can also be observed on





(a)



(b)

FIGURE 5.6: a)  $k_r$  as a function of  $T_p$ , and b)  $k_r$  as a contour plot against  $H_s$  and  $T_p$ , for  $\theta_w = 60^\circ$

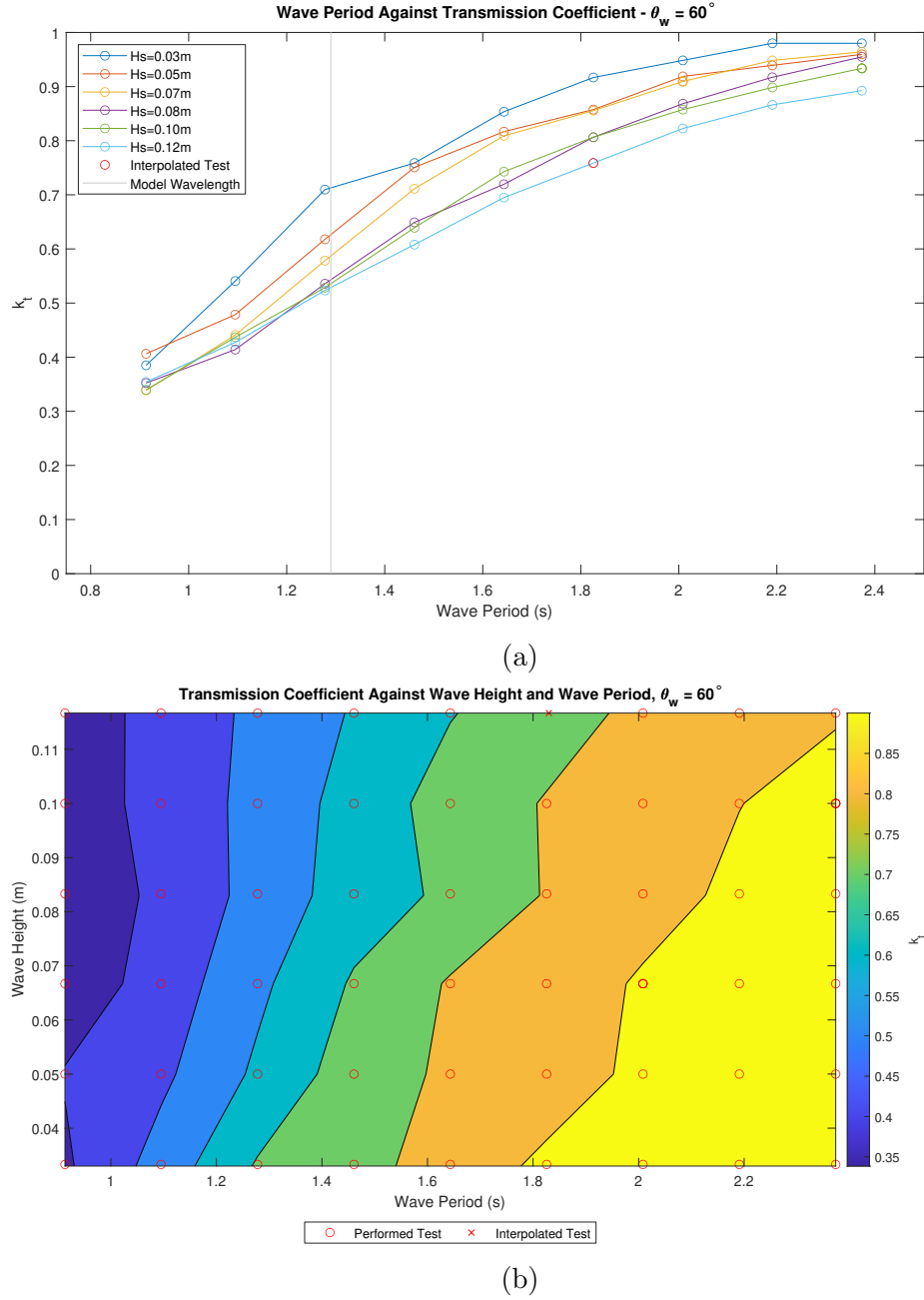


FIGURE 5.7: a)  $k_t$  as a function of  $T_p$ , and b)  $k_t$  as a contour plot against  $H_s$  and  $T_p$ , for  $\theta_w = 60^\circ$

the contour plot, where the highest  $k_r$  region is at the small height and short period tests.

Figure 5.7 shows the transmission coefficient,  $k_t$ , as a function of  $T_p$ , (a), and  $k_t$  as a contour plot against  $H_s$  and  $T_p$ , (b). When grouped by  $T_p$  the  $k_t$  value decreased slightly over increasing  $H_s$ , despite the total energy transmitted increasing with  $H_s$ .

When the data was grouped by  $H_s$  the  $k_t$  value started low with low  $T_p$  and increased as the  $T_p$  also increased. While all tests followed the same trend, the tests where the  $H_s$  was lower gave higher  $k_t$  values compared to a test of the same  $T_p$  but with larger  $H_s$ . Once again the wave period associated with model wavelength did not affect the trend of the coefficient. The highest  $k_t$  values were seen at tests of low  $H_s$  and high  $T_p$  conditions.

Figure 5.8 shows the absorption coefficient,  $k_a$ , as a function of  $T_p$ , (a), and  $k_a$  as a contour plot against  $H_s$  and  $T_p$ , (b). When grouped by  $T_p$  increasing the  $H_s$  generally also increased the  $k_a$ . At low  $H_s$  for high  $T_p$  the absorbed energy was essentially zero, as the device reflected or transmitted all energy. When grouped by  $H_s$  the peak  $k_a$  of most groups was at 1.09 s rather than 1.28 s, as observed when considering absolute energy values. In the higher  $H_s$  groups the  $k_a$  value for 1.28 s was close to the peak value at 1.09 s. The regions of highest absorption occurred at conditions where wave steepness was highest.

Figure 5.9 shows the energy captured and recorded as it passed through the flowmeters in the WaveCat hull. In general, more energy was captured as the  $H_s$  was increased as the random wave spectra contained more individual waves that were capable of overtopping. It followed the trend shown in Figure 5.8 with the highest amount of energy captured around the  $T_p$  associated with the model wavelength. At high  $T_p$  tests higher  $H_s$  was needed to produce energy equivalent to that of a lower  $T_p$  test. The captured energy dropped at high wave height and the lowest wave period, however reflection in these cases was highest as shown in Figure 5.6.

Figure 5.10 shows the CWR as a contour plot against  $T_p$  and  $H_s$ . Higher CWR obtained from the available energy represented cases where energy was not used in dissipation around the device, implying that the device was not moving as much as other cases where the captured percentage was smaller. The device motions are examined in further detail in Chapter 6. While the higher  $T_p$  tests gave good capture percentages when they did capture energy, these tests were not the most energetic in terms of energy captured, rather they were the most efficient in transforming the energy in overtopping water without the device using the energy as motion. The

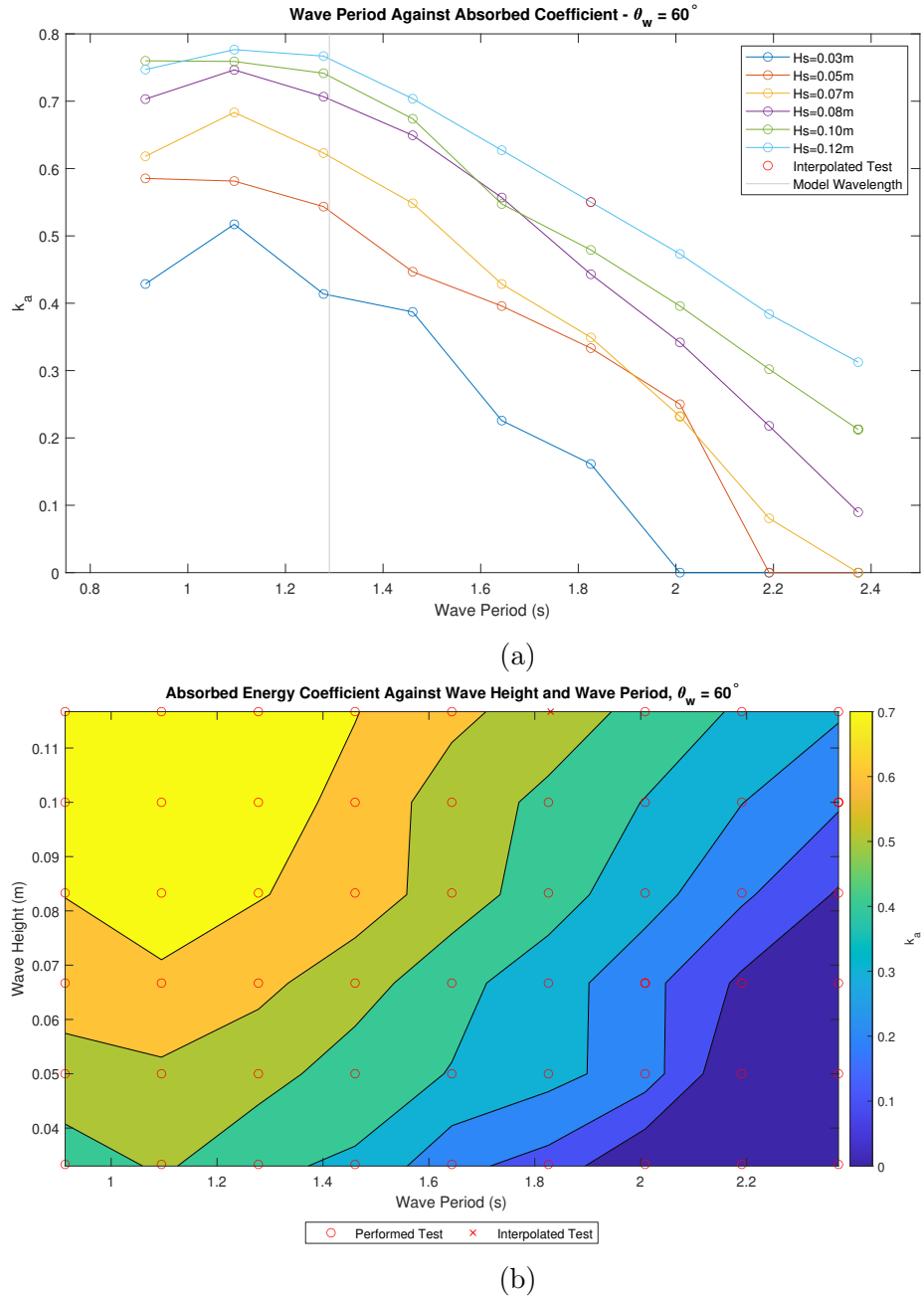


FIGURE 5.8: a)  $k_a$  as a function of  $T_p$ , and b)  $k_a$  as a contour plot against  $H_s$  and  $T_p$ , for  $\theta_w = 60^\circ$

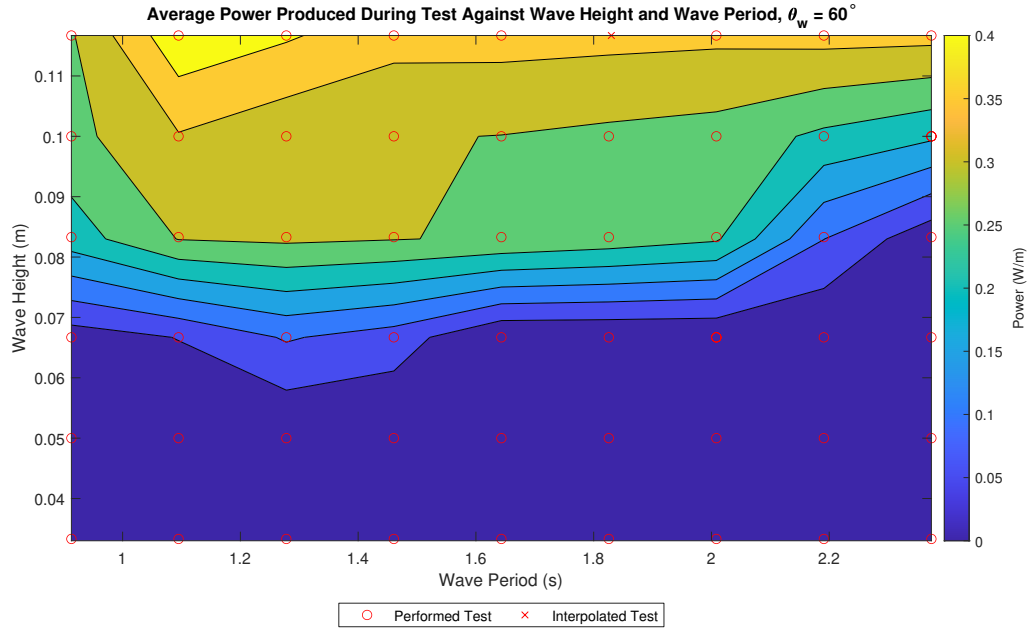


FIGURE 5.9: Measured energy captured from flowmeters against  $H_s$  and  $T_p$  for  $\theta_w = 60^\circ$

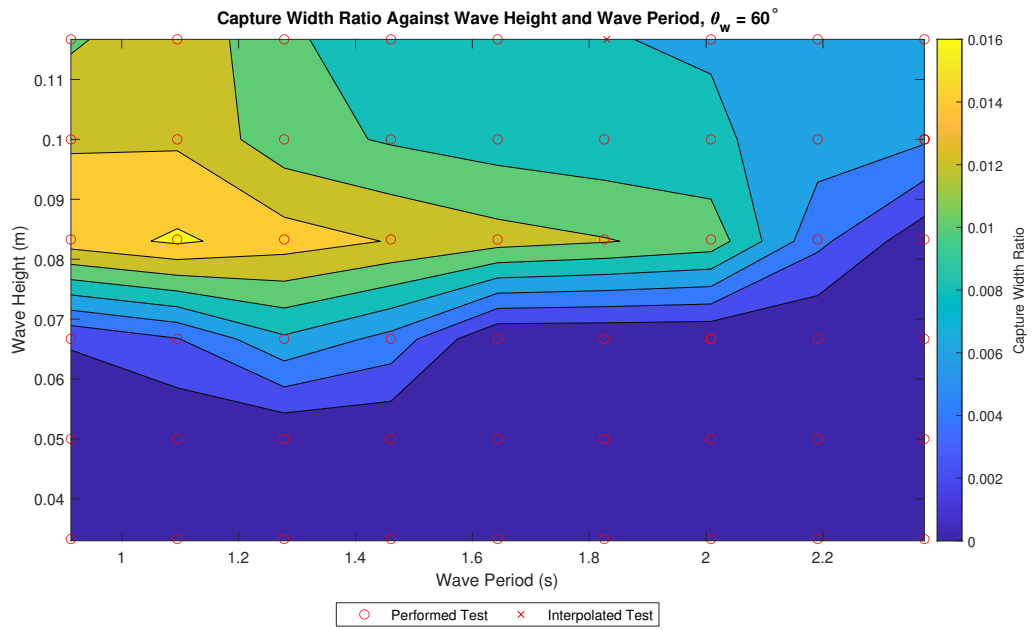


FIGURE 5.10: CWR against  $H_s$  and  $T_p$  for  $\theta_w = 60^\circ$

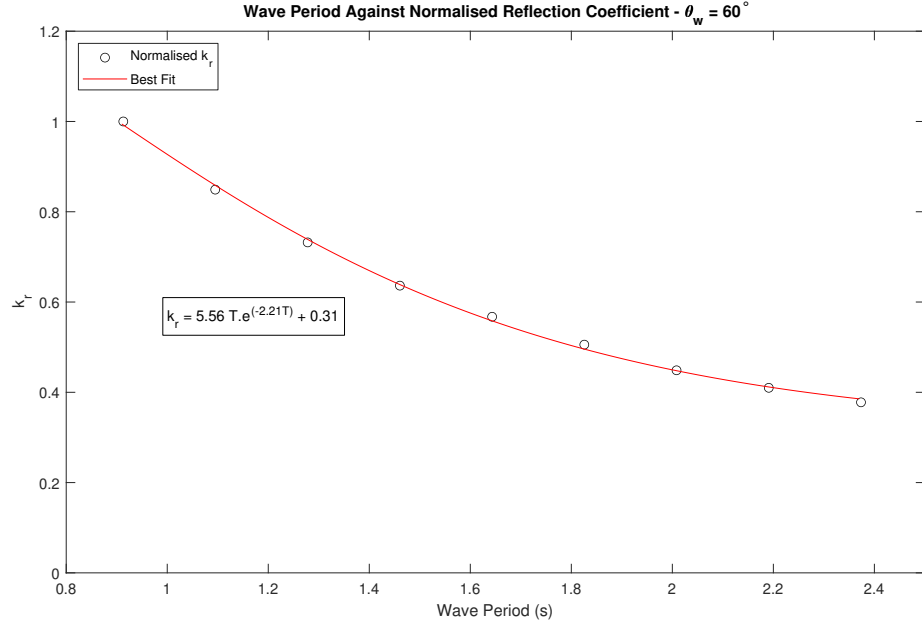
CWR decreases as wave height increases as the device was capturing more water than could be exhausted through the flowmeters, resulting in it returning to the basin without being measured. It was effectively reaching a maximum amount of power generated. Figure 5.9 shows increasing power as wave height increases because it reached the threshold to start producing power sooner, and was therefore capturing and measuring flow for a larger proportion of the test.

### 5.1.3 Generalised Coefficients

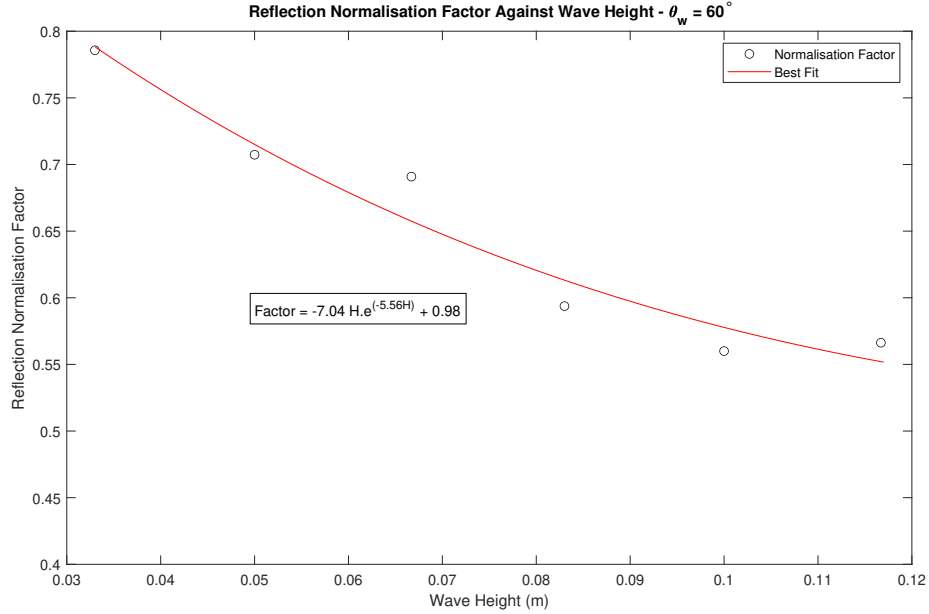
The coefficients  $k_r$ ,  $k_t$  and  $k_a$  shown in Section 5.1.2 were dependent on both  $H_s$  and  $T_p$ . Generalised equations for the respective coefficients were calculated into which the  $H_s$  and  $T_p$  test parameters could be input to receive a coefficient output. The generalised equation took the form of

$$\begin{aligned} \text{Coefficient} &= ABT_p \exp^{-CT_p} + D \\ A &= EH_s \exp^{-FH_s} + G \end{aligned} \tag{5.1}$$

where  $B$ ,  $C$  and  $D$  are constants based on the fit from the generalised equation relative to  $T_p$ .  $E$ ,  $F$  and  $G$  are constants based on the equation relative to  $H_s$ . The sets of tests with constant  $H_s$  were normalised between 0 and 1 and an average at each period bin taken. This average then formed the points in which the generalised curve was fit, with the parameters of the fit line forming part of the equation. The sets of tests with constant  $T_p$  were then normalised between 0 and 1 as well and an average at each height bin taken. A second curve was fitted to the resulting fit line and the second set of coefficients taken. The general method to reconstruct a specific coefficient for a set of wave conditions is to refer to the generalised fits for the normalised coefficient, based on  $T_p$ , and the normalisation factor based on  $H_s$ . The constants were obtained and the output to Equation 5.1 calculated.

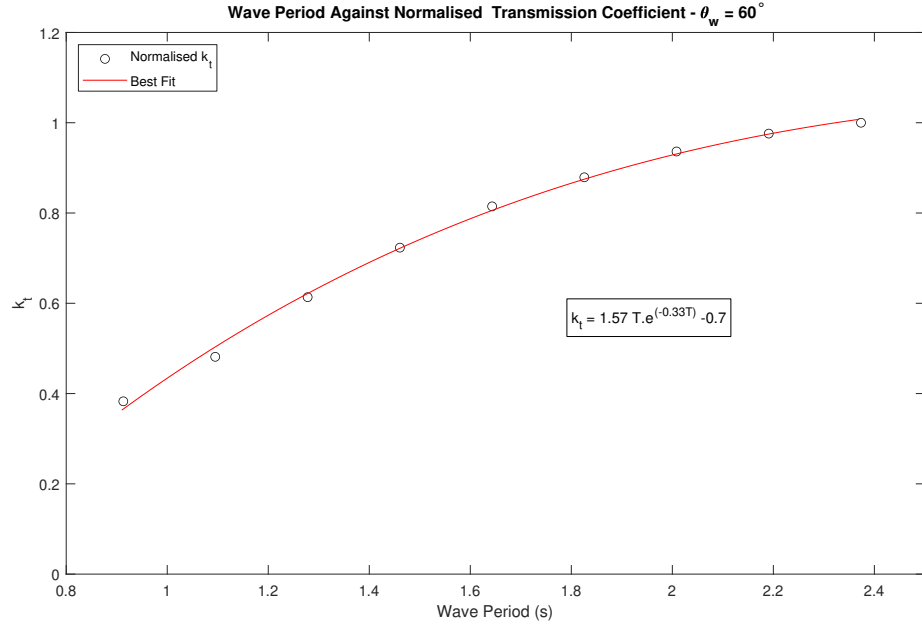


(a) Generalised normalised  $k_r$  coefficient graph against wave period for  $\theta_w = 60^\circ$ .  $R^2 = 99.8\%$

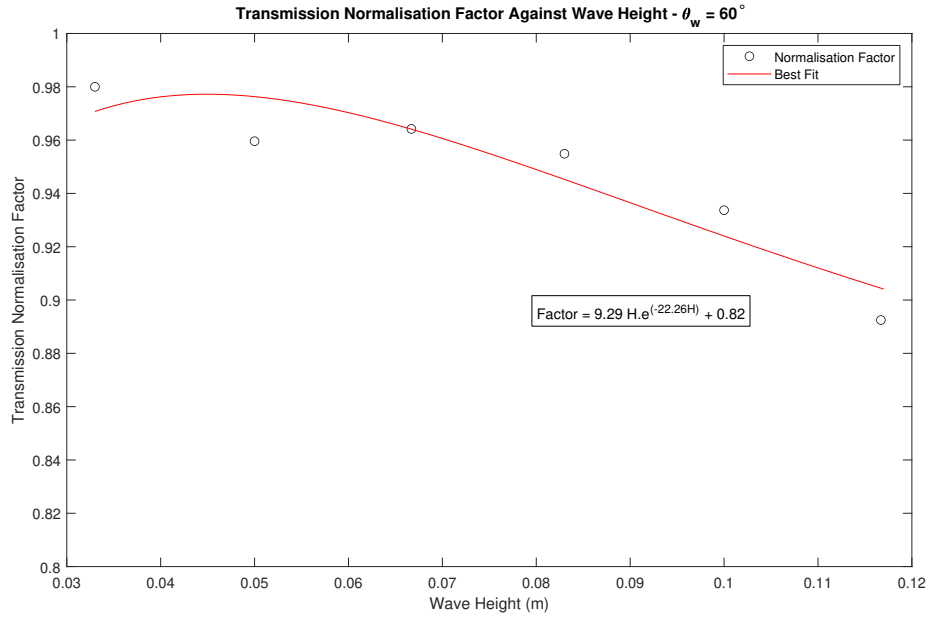


(b) Normalisation factor to obtain  $k_r$  against  $H_s$  for  $\theta_w = 60^\circ$ .  $R^2 = 91.7\%$

FIGURE 5.11: Equations to reconstruct  $k_r$  for  $\theta_w = 60^\circ$ , showing (a) generalised coefficient against  $T_p$ , and (b) normalisation coefficient against  $H_s$



(a) Generalised normalised  $k_t$  coefficient graph against wave period for  $\theta_w = 60^\circ$ .  $R^2 = 99.7\%$

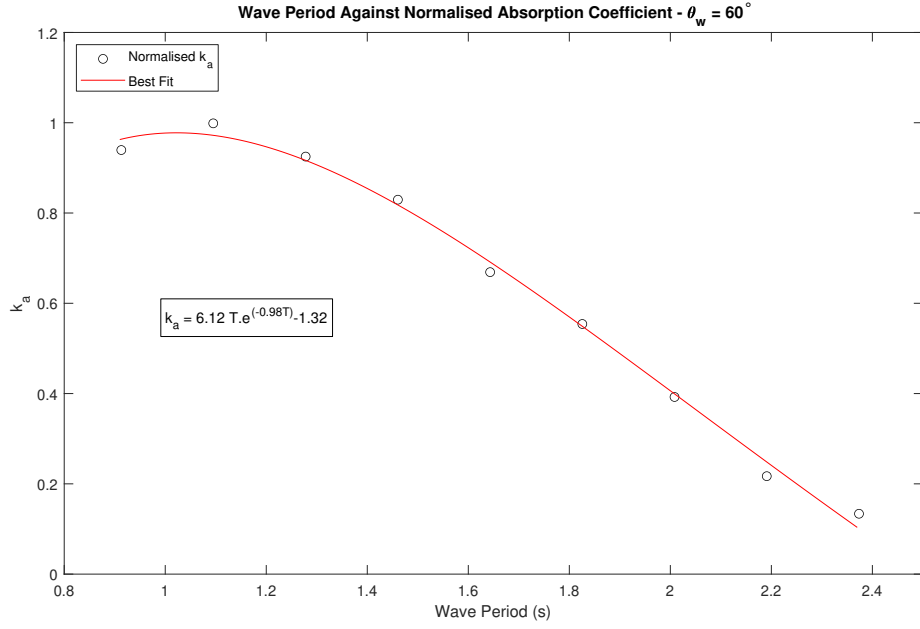


(b) Normalisation factor to obtain  $k_t$  against  $H_s$  for  $\theta_w = 60^\circ$ .  $R^2 = 75.6\%$

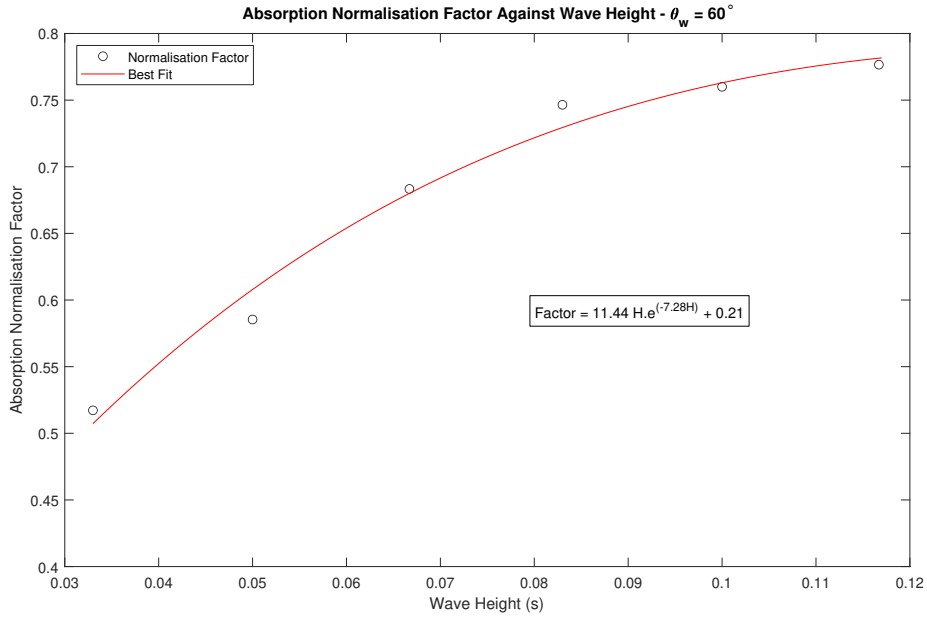
FIGURE 5.12: Equations to reconstruct  $k_t$  for  $\theta_w = 60^\circ$ , showing (a) generalised coefficient against  $T_p$ , and (b) normalisation coefficient against  $H_s$

Figure 5.11 shows the two equations to reconstruct  $k_r$  from  $T_p$ , Figure 5.11a, and  $H_s$ , Figure 5.11b. The results show that increasing  $T_p$  reduced normalised  $k_r$ , and increasing  $H_s$  also reduced the normalisation factor.





(a) Generalised normalised  $k_a$  coefficient graph against wave period for  $\theta_w = 60^\circ$ .  $R^2 = 99.3\%$



(b) Normalisation factor to obtain  $k_a$  against  $H_s$  for  $\theta_w = 60^\circ$ .  $R^2 = 97.2\%$

FIGURE 5.13: Equations to reconstruct  $k_a$  for  $\theta_w = 60^\circ$ , showing (a) generalised coefficient against  $T_p$ , and (b) normalisation coefficient against  $H_s$

Figure 5.12 shows the two equations to reconstruct  $k_t$  from  $T_p$ , Figure 5.12a, and  $H_s$ , Figure 5.12b. The results show that increasing  $T_p$  increased normalised  $k_t$ , and increasing  $H_s$  reduced the normalisation factor by a small amount.

Figure 5.13 shows the two equations to reconstruct  $k_a$  from  $T_p$ , Figure 5.13a, and  $H_s$ , Figure 5.13b. The results show that increasing  $T_p$  reduced  $k_a$ , however there was an initial rise at the lowest periods tested. The best fit line peaked at a slightly lower value of  $T_p$  compared to the test data. The data for the lowest period tests was checked to make sure the data quality was high, and the reduction in absorption appeared to be real. Increasing  $H_s$  increased the normalisation factor.

## 5.2 Results for $\theta_w = 30^\circ$

As well as the device operating at  $\theta_w = 60^\circ$ , tests were also run at  $\theta_w = 30^\circ$  to examine how a different wedge angle would alter the WaveCats effect on the wave field and its own power output. The overall performance was compared to the  $60^\circ$  configuration.

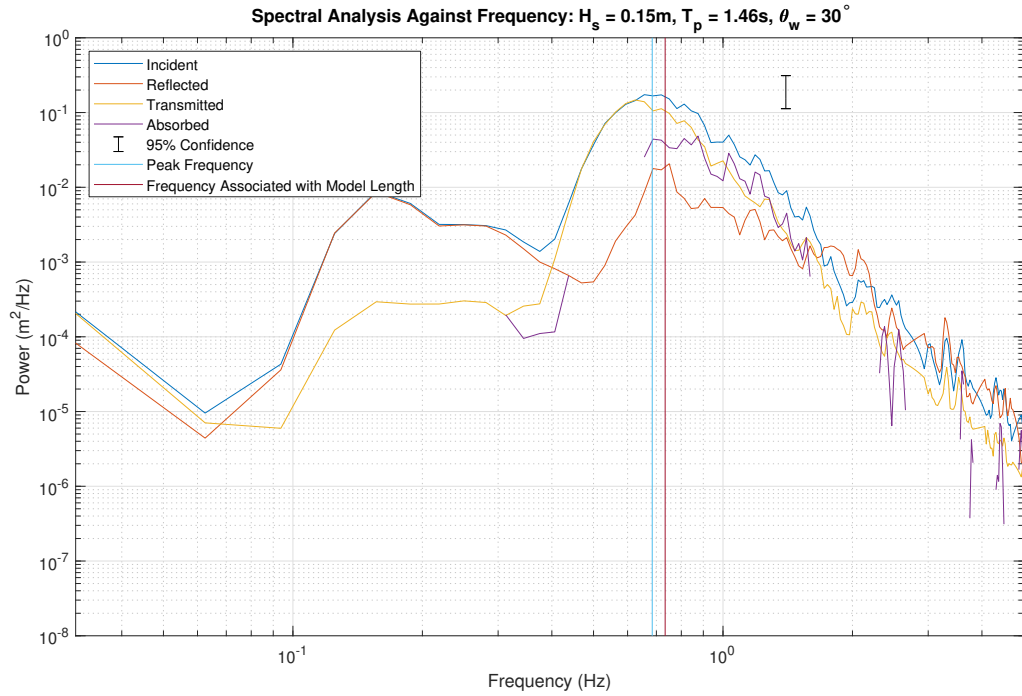
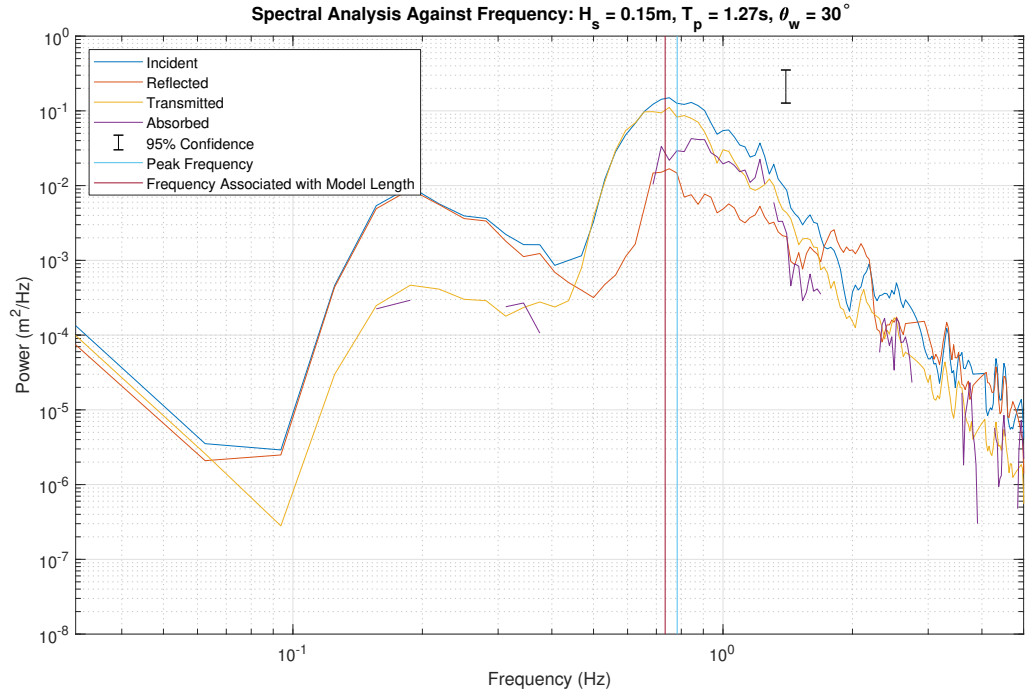


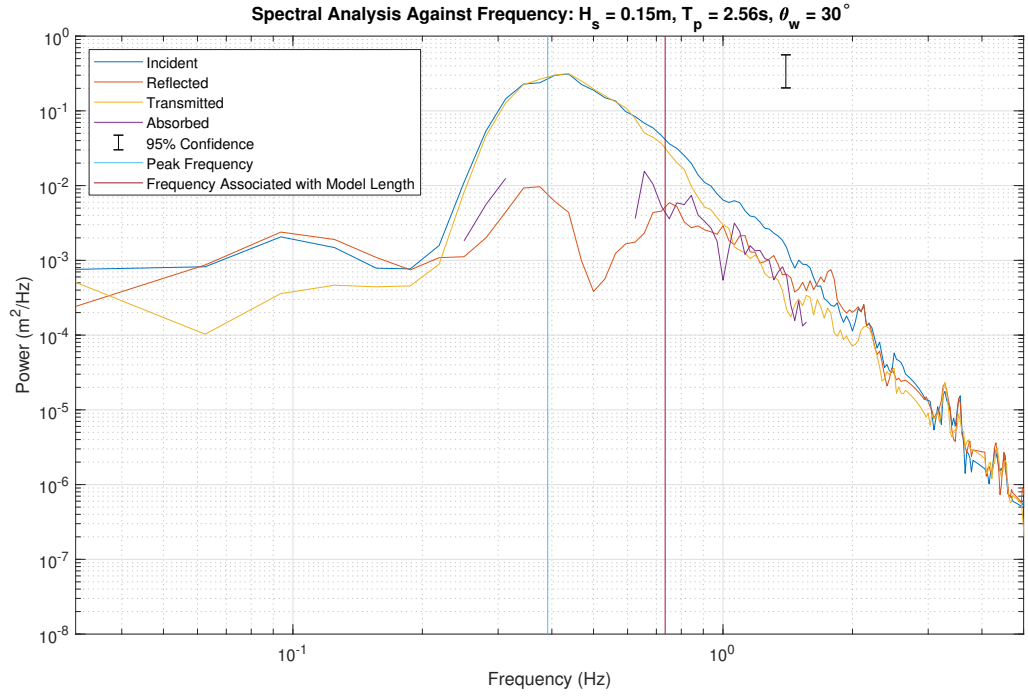
FIGURE 5.14: Spectral analysis of  $H_s = 0.15$  m,  $T_p = 1.46$  s,  $\theta_w = 30^\circ$

FIGURE 5.15: Spectral analysis of  $H_s = 0.15$  m,  $T_p = 1.28$  s,  $\theta_w = 30^\circ$ 

### 5.2.1 Wave Field Spectral Analysis

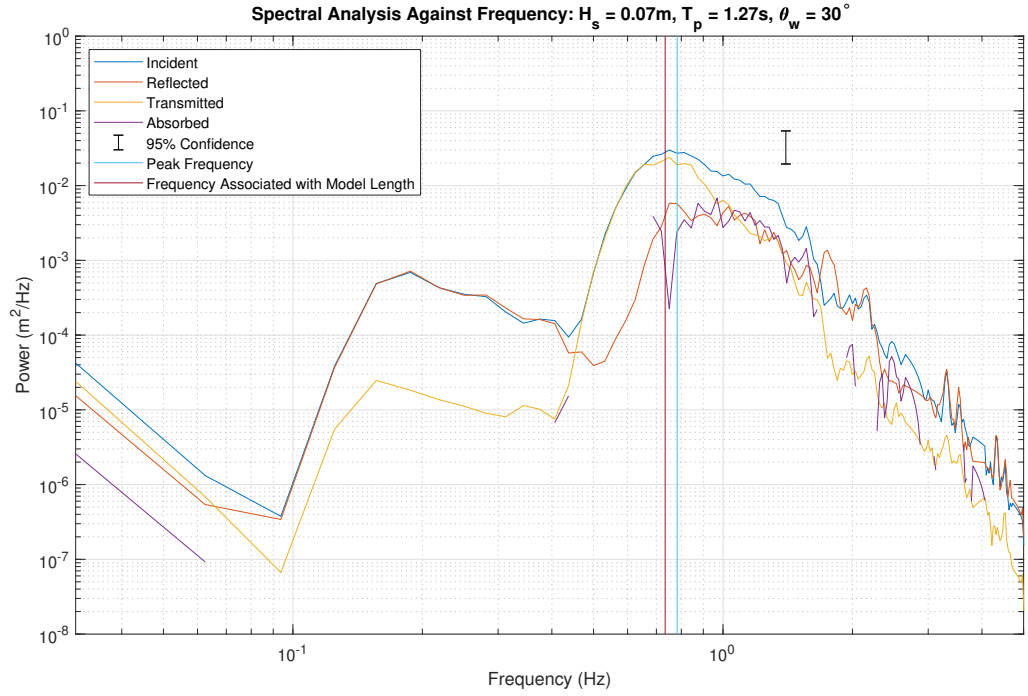
Figure 5.14 shows the spectral analysis of a test with characteristics  $H_s = 0.15$  m,  $T_p = 1.46$  s and  $\theta_w = 30^\circ$ . The  $T_p$  parameter of this test was close to  $T_p$  of the wavelength of the model when  $\theta_w = 30^\circ$ , 1.36 s compared to 1.46 s, shown by the vertical line. As expected, the peak in incident energy was around the characteristic  $T_p$  of the test. At frequencies below that of the peak frequency, the majority of energy was transmitted rather than reflected with little energy absorbed by the device. At wave frequencies higher than the peak frequency of the test the amount of energy transmitted dropped and the amount of reflected energy also dropped, but at a lower rate. This allowed a greater portion of energy to be absorbed. As the wave frequency continued to increase, and therefore the wave period became shorter, the transmitted energy dropped further along with the reflected energy, however the reflected energy was less affected, resulting in more energy in reflected waves than transmitted.

Figure 5.15 shows the spectral analysis of a test with characteristics  $H_s = 0.15$  m,  $T_p = 1.28$  s and  $\theta_w = 30^\circ$ . The  $T_p$  parameter of this test closely aligned with the

FIGURE 5.16: Spectral analysis of  $H_s = 0.15$  m,  $T_p = 2.56$  s,  $\theta_w = 30^\circ$ 

$T_p$  of the wavelength of the model when  $\theta_w = 30^\circ$ , 1.36 s compared to 1.28 s, shown by the vertical lines. Similar to the previous case shown in Figure 5.14, the peak in incident energy was around the characteristic  $T_p$  of the test. Prior to the peak frequency, at lower frequencies and therefore longer period waves, the majority of energy was transmitted rather than reflected with little energy absorbed by the device. Once the wave frequency was higher than the peak frequency of the test the amount of energy transmitted dropped and the amount of reflected energy also dropped at a lower rate, allowing a greater portion of energy to be absorbed. As the wave frequency continued to get higher, and therefore the wave period became shorter, the transmitted energy dropped further along with the reflected energy. The reflected energy was less affected resulting in more energy in reflected waves than transmitted.

Figure 5.16 shows the spectral analysis of a test with characteristics  $H_s = 0.15$  m,  $T_p = 2.56$  s and  $\theta_w = 30^\circ$ . The  $T_p$  parameter of this test represented wave of the lowest frequency tested. The peak incident energy was around the peak frequency of the test, along with the peak transmitted energy. For lower frequencies, where the

FIGURE 5.17: Spectral analysis of  $H_s = 0.07$  m,  $T_p = 1.28$ s,  $\theta_w = 30^\circ$ 

waves were longest, the transmitted energy was almost equal to the incident energy, meaning little was being reflected or was absorbed. As the waves shortened and approached model frequency the transmitted energy reduced at a faster rate than the incident energy resulting in energy absorbed by the device. As the frequency continued to increase past the model frequency the reflected energy approached the incident energy again resulting in little energy being absorbed.

Figure 5.17 shows the spectral analysis of a test with characteristics  $H_s = 0.07$  m,  $T_p = 1.28$  s and  $\theta_w = 60^\circ$ . The  $T_p$  parameter of this test closely aligned with the  $T_p$  of the wavelength of the model when  $\theta_w = 60^\circ$ , 1.36 s compared to 1.28 s, shown by the vertical lines. This was similar to the test shown in Figure 5.15, however at a lower  $H_s$ , showing the difference between the two  $H_s$  values. The test with lower  $H_s$  followed the same trend as the larger  $H_s$  test in that the incident, reflected and absorbed energy all peaked around the test frequency. The transmitted energy was relatively constant for the frequency region where the incident energy was at its peak. This was slightly different to the trend for the larger  $H_s$  value, which dropped slightly when above model frequency.

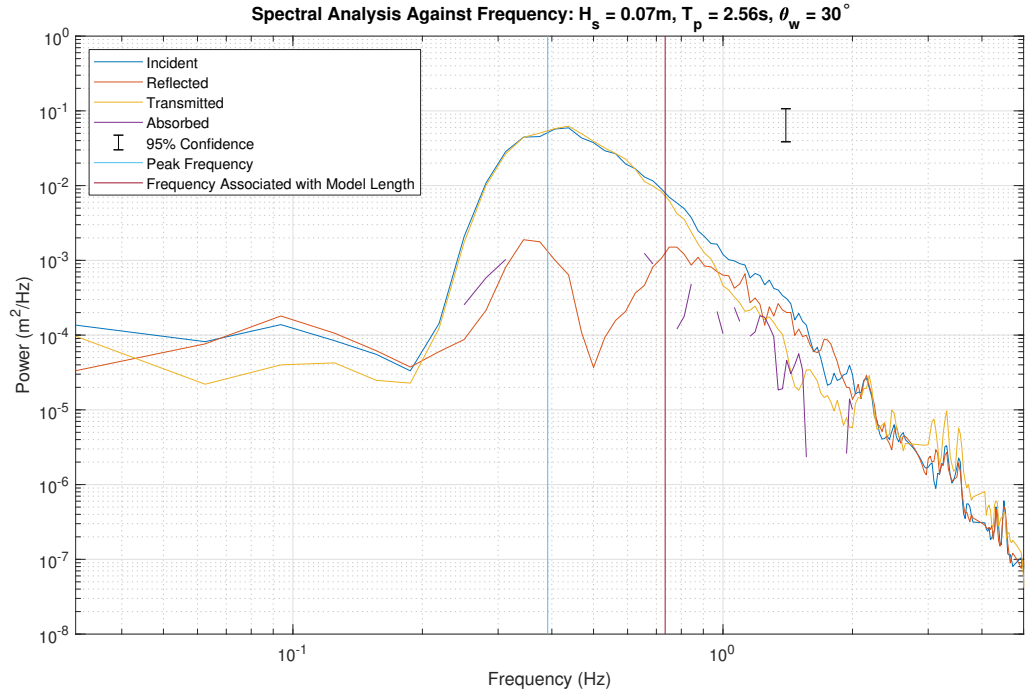
FIGURE 5.18: Spectral analysis of  $H_s = 0.07$  m,  $T_p = 2.56$  s,  $\theta_w = 30^\circ$ 

Figure 5.18 shows the spectral analysis of a test with characteristics  $H_s = 0.07$  m,  $T_p = 2.56$  s and  $\theta_w = 30^\circ$ . This is similar to the test shown in Figure 5.3, however at a lower  $H_s$ , showing the difference between the two  $H_s$  values. In the same fashion as the spectra with  $T_p = 1.28$  s, the two spectra of  $T_p = 2.37$  s showed the same trend and the change in  $H_s$  value merely altered the absolute values of the spectra. The transmitted energy was almost equal to the incident energy at lower frequencies and it began to drop faster than the incident energy when the wave frequency approached the peak test frequency, before the reflected energy rose to meet the incident energy spectra. This combination resulted in very few areas where there was energy absorbed.

### 5.2.2 Energy Coefficients

Using the spectral data from each test a total for reflected, transmitted and absorbed energy was calculated over the course of a complete test. This was then converted

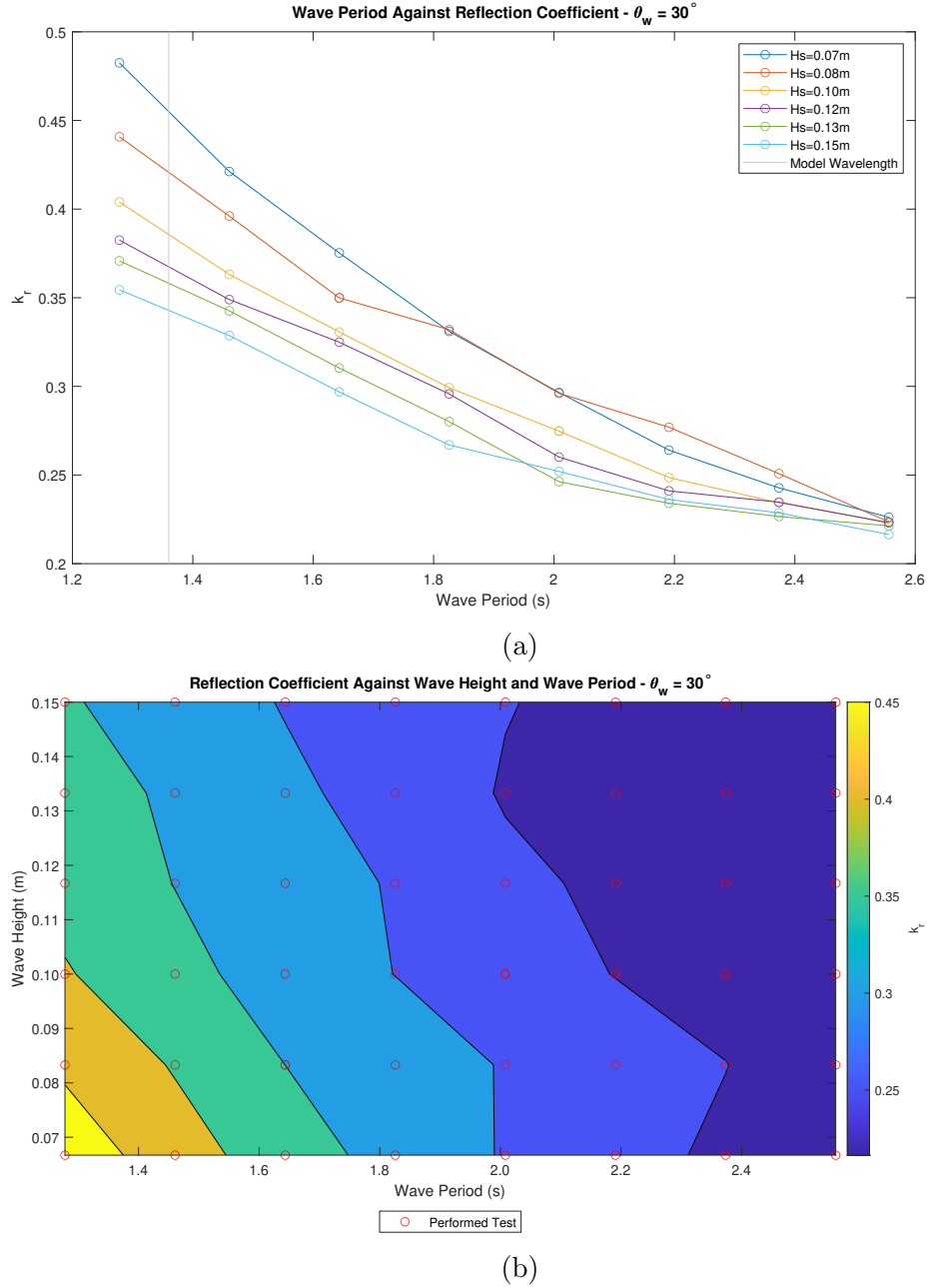


FIGURE 5.19:  $k_r$  as a function of  $T_p$ , (a), and as a contour plot against  $H_s$  and  $T_p$ , (b) for  $\theta_w = 30^\circ$

to a coefficient representing each as a fraction of the incident energy available to the test and plotted grouped by tests with the same  $T_p$  or  $H_s$  value. The coefficients  $k_r$ ,  $k_t$  and  $k_a$  are defined in Section 4.5.

Figure 5.19 shows the reflection coefficient,  $k_r$ , as a function of  $T_p$ , (a), and  $k_r$  as a contour plot against  $H_s$  and  $T_p$ , (b). While  $k_r$  started high, increasing  $T_p$  is shown

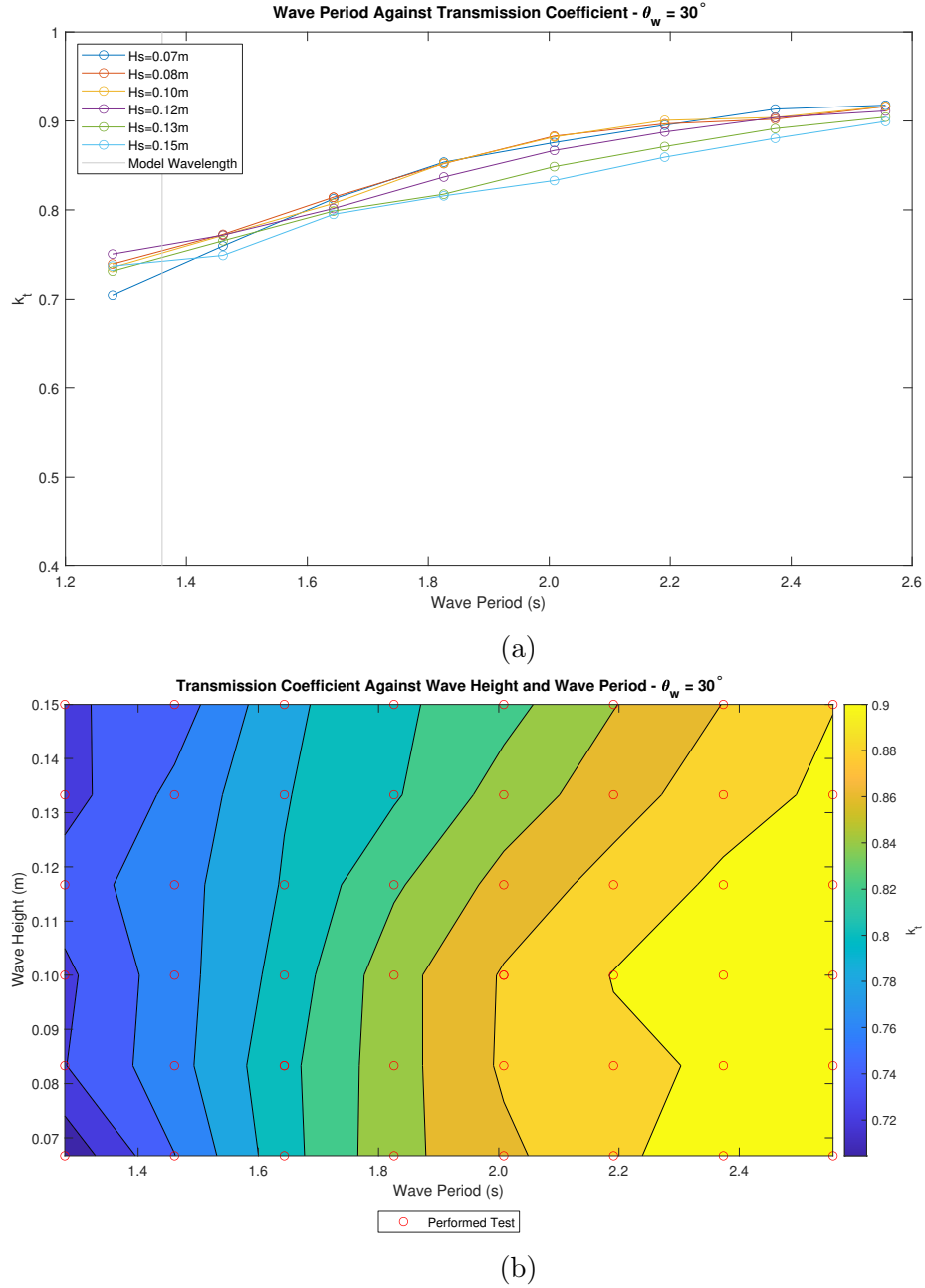


FIGURE 5.20:  $k_t$  as a function of  $T_p$ , (a), and as a contour plot against  $H_s$  and  $T_p$ , (b) for  $\theta_w = 30^\circ$

to reduce  $k_r$  values. At higher  $T_p$  values the data points were closely grouped, confirming that  $H_s$  had little effect at higher  $T_p$ . The region of highest  $k_r$  is once again where the wave conditions have the lowest  $H_s$  and  $T_p$  values. It was observed that  $k_r$  is generally lower for the  $30^\circ$  tests compared to the  $60^\circ$  tests. This was likely due to an increased amount of reflections in the wedge of the device itself redistributing energy.

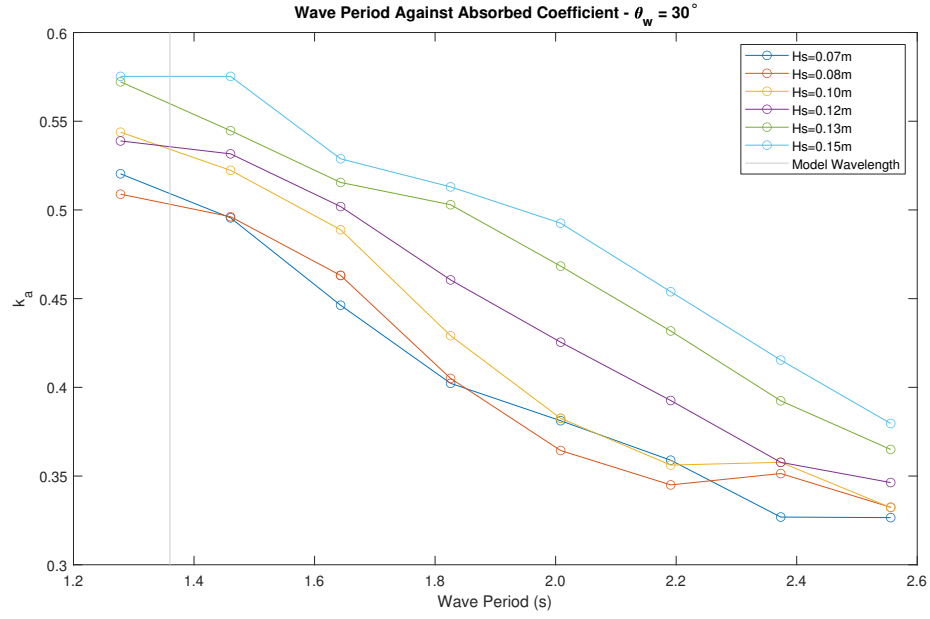


Figure 5.20 shows the transmission coefficient,  $k_t$ , as a function of  $T_p$ , (a), and  $k_t$  as a contour plot against  $H_s$  and  $T_p$ , (b). When grouped by  $T_p$  the  $k_t$  value was consistently high over the range of  $H_s$  tested. When the data was grouped by  $H_s$  the  $k_t$  value started low with low  $T_p$  and increased as the  $T_p$  also increased. The  $k_t$  was largely unaffected by  $H_s$ , instead increasing with  $T_p$ . The contour plot shows the highest region of transmission was where  $T_p$  was high and  $H_s$  was low, although for all the tests the  $k_t$  was 0.7 or higher. The behaviour observed is similar to that of the behaviour at a wedge angle of  $60^\circ$ , Figure 5.7, where at wave periods with wavelengths longer than that of the model length  $k_t$  was high and  $H_s$  had little effect on it.

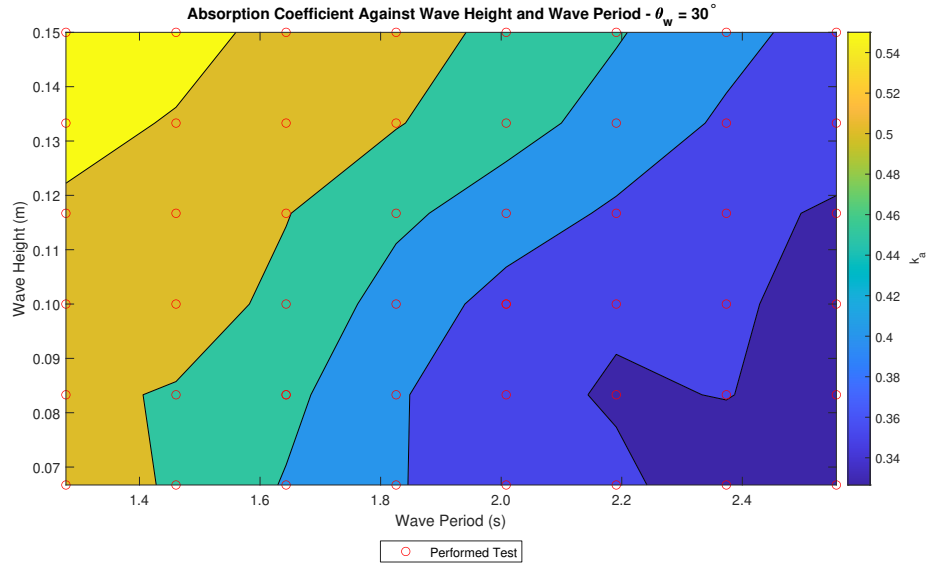
Figure 5.21 shows the absorption coefficient,  $k_a$ , as a function of  $T_p$ , (a), and  $k_a$  as a contour plot against  $H_s$  and  $T_p$ , (b). When grouped by  $T_p$  increasing the  $H_s$  generally also increases the  $k_a$ . When grouped by  $H_s$  the peak  $k_a$  of most groups is at 1.09 s rather than 1.28 s as observed when considering absolute energy values, however in the higher  $H_s$  groups the  $k_a$  value for 1.28 s is close to the peak value at 1.09 s.

Figure 5.22 shows the energy captured and recorded as it passed through the flowmeters in the WaveCat hull. Due to the narrower wedge angle the WaveCat had fewer tests in which overtopping occurred. Similar to Figure 5.9, the overtopping occurred in high  $H_s$  and low  $T_p$  tests. The tests closest to the model frequency resulted in the greatest overtopping.

Figure 5.23 shows the CWR as a contour plot against  $T_p$  and  $H_s$ . The device had the greatest CWR of 5.4% in the test where the power generated was highest, as shown in Figure 5.22. The test that performed best was  $H_s = 0.15$  m and  $T_p = 1.46$  s, which captured around 0.08 m of the incident wave front.



(a)



(b)

FIGURE 5.21:  $k_a$  as a function of  $T_p$ , (a), and as a contour plot against  $H_s$  and  $T_p$ , (b) for  $\theta_w = 30^\circ$

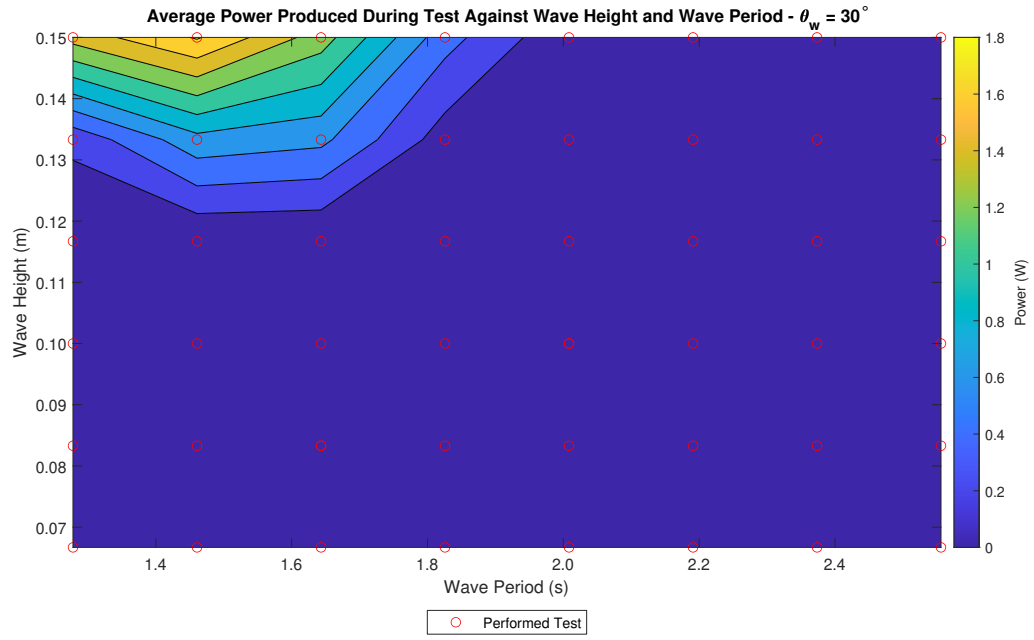


FIGURE 5.22: Energy captured against  $H_s$  and  $T_p$  for  $\theta_w = 30^\circ$

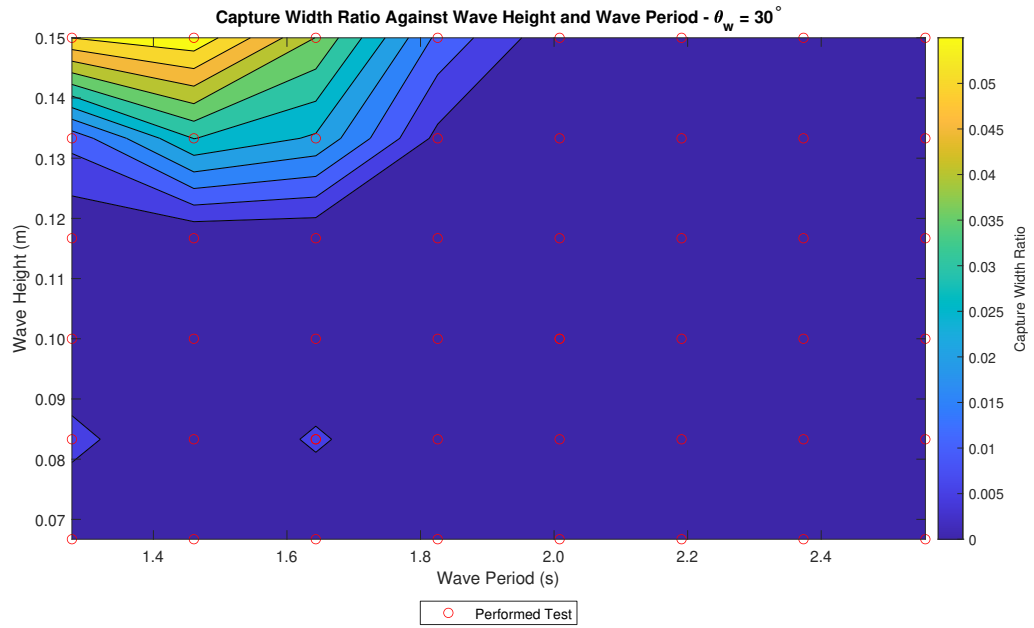


FIGURE 5.23: Contour plot of Capture Width Ratio (CWR) against  $H_s$  and  $T_p$

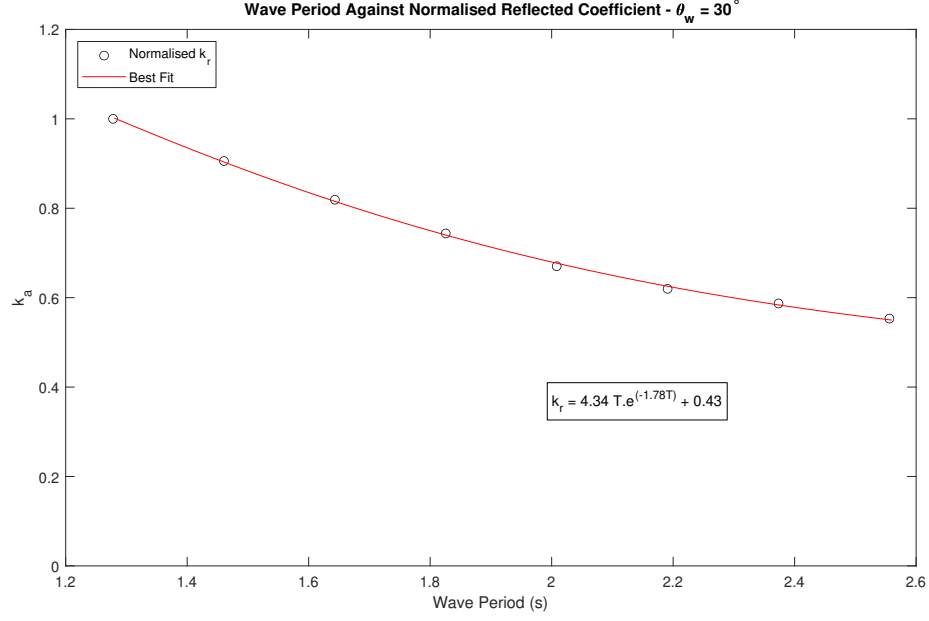
### 5.2.3 Generalised Coefficients

The coefficients  $k_r$ ,  $k_t$  and  $k_a$  shown in Section 5.2.2 were dependent on both  $H_s$  and  $T_p$ . Generalised equations for the respective coefficients were calculated into which the  $H_s$  and  $T_p$  test parameters could be input to receive a coefficient output, as described in Section 5.1.3.

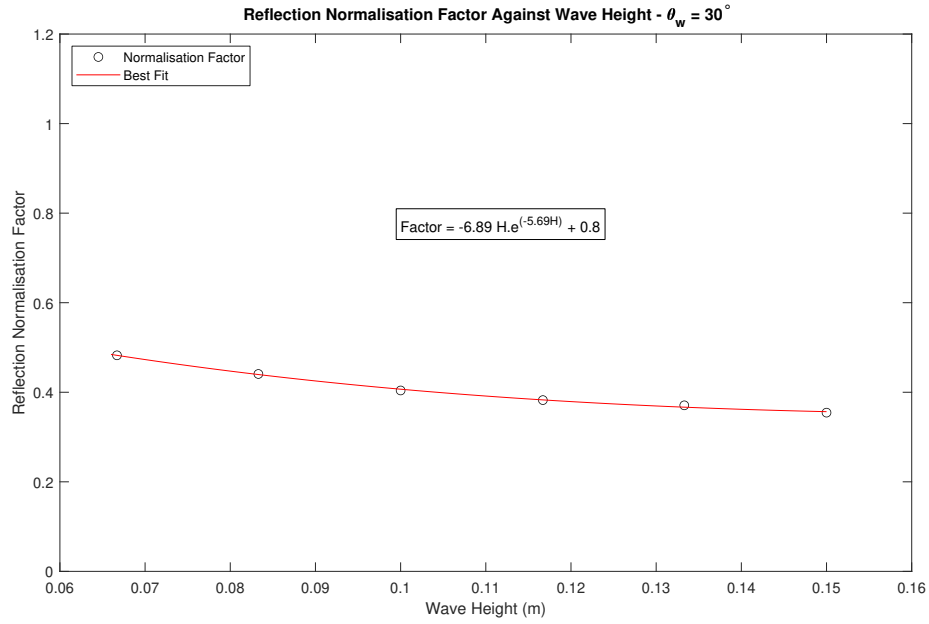
Figure 5.24 shows the two equations to reconstruct  $k_r$  from  $T_p$ , Figure 5.24a, and  $H_s$ , Figure 5.24b. The results show that increased  $T_p$  reduced  $k_r$ , and increased  $H_s$  also slightly reduced the normalisation factor.

Figure 5.25 shows the two equations to reconstruct  $k_t$  from  $T_p$ , Figure 5.25a, and  $H_s$ , Figure 5.25b. The results show that increased  $T_p$  increased  $k_t$ . From the graph showing the  $H_s$  relationship the normalisation factor was largely independent of  $H_s$  as it was flat, showing  $k_t$  for the  $30^\circ$  configuration was not dependent on  $H_s$ .

Figure 5.26 shows the two equations to reconstruct  $k_a$  from  $T_p$ , Figure 5.26a, and  $H_s$ , Figure 5.26b. The results show that increased  $T_p$  decreased  $k_a$ , and increased  $H_s$  increased the normalisation factor by a small amount, in agreement with the RAO values.

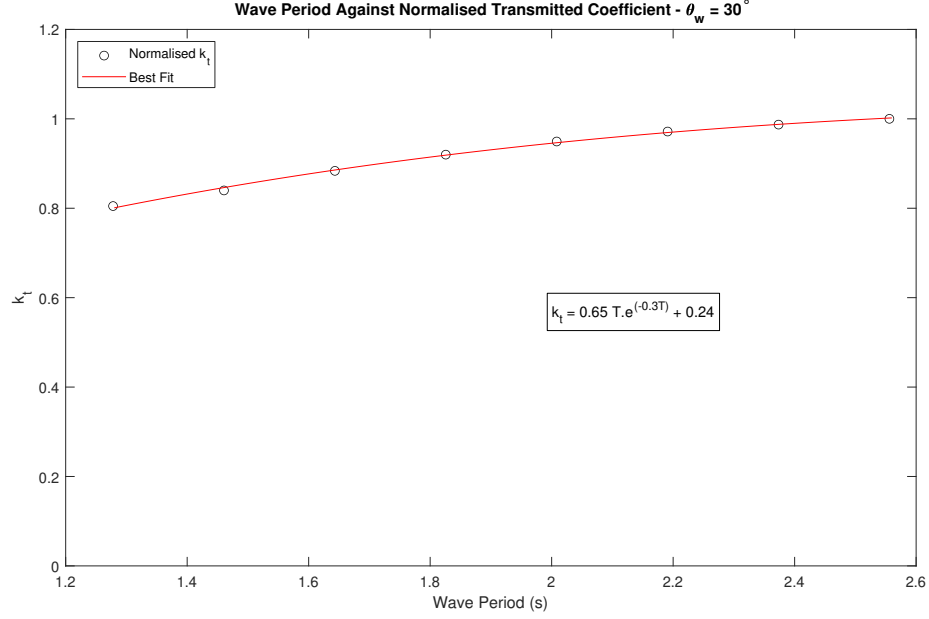


(a) Generalised normalised  $k_r$  coefficient graph against wave period for  $\theta_w = 30^\circ$ .  $R^2 = 99.9\%$

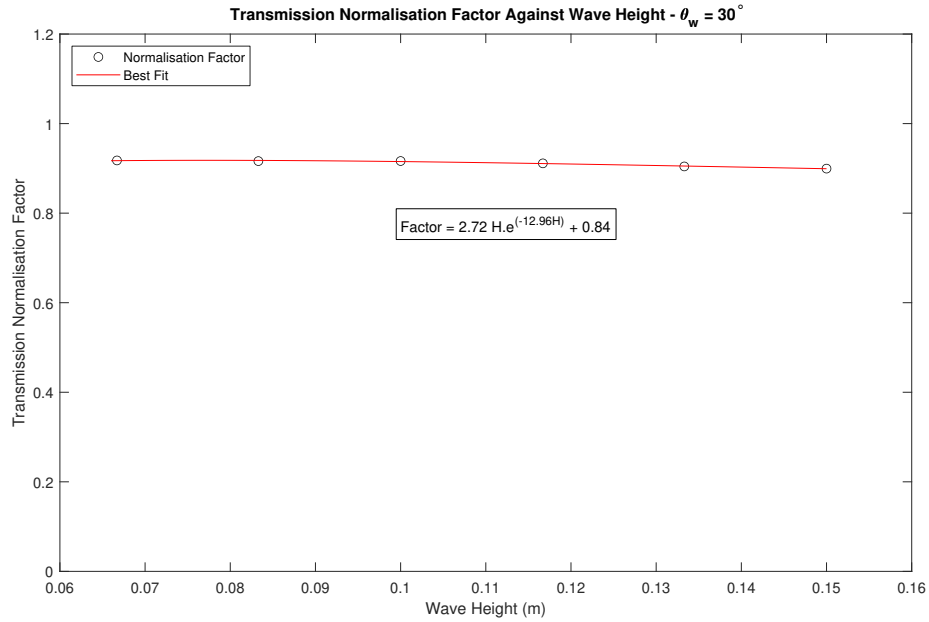


(b) Normalisation factor to obtain  $k_r$  against  $H_s$  for  $\theta_w = 30^\circ$ .  $R^2 = 99.5\%$

FIGURE 5.24: Equations to reconstruct  $k_r$  for  $\theta_w = 30^\circ$ , showing (a) generalised coefficient against  $T_p$ , and (b) normalisation coefficient against  $H_s$

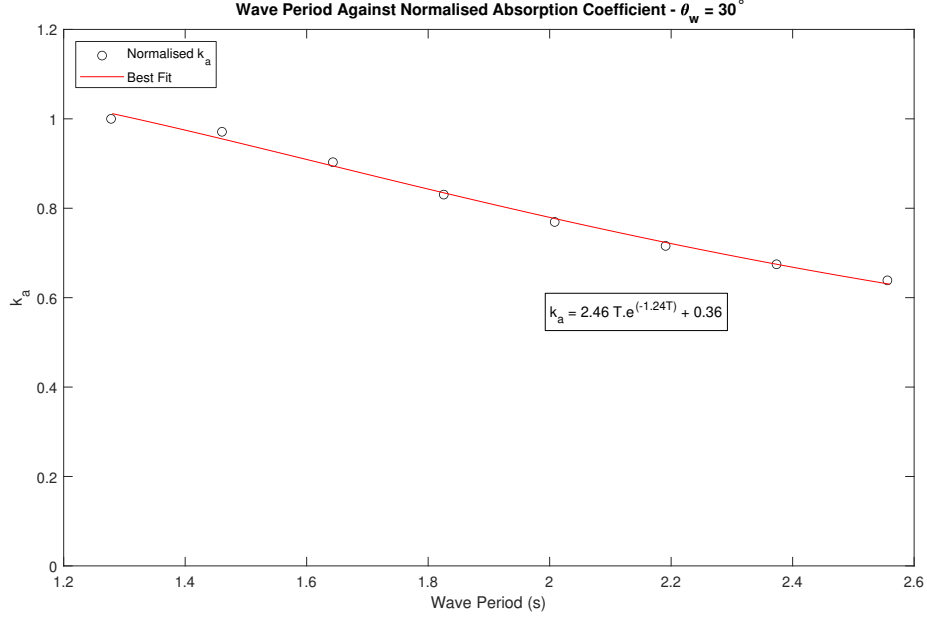


(a) Generalised normalised  $k_t$  coefficient graph against wave period for  $\theta_w = 30^\circ$ .  $R^2 = 99.7\%$

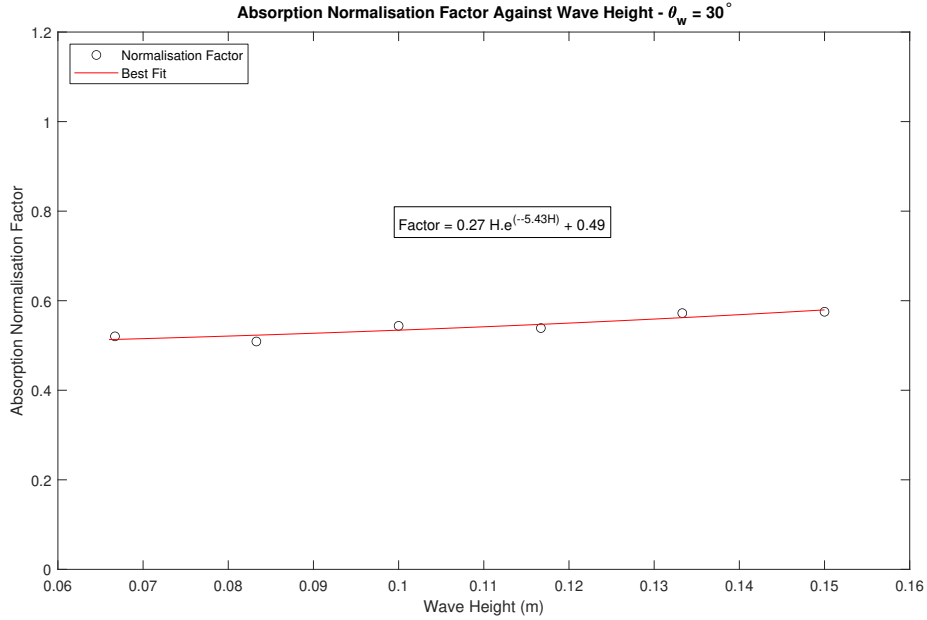


(b) Normalisation factor to obtain  $k_t$  against  $H_s$  for  $\theta_w = 30^\circ$ .  $R^2 = 97.0\%$

FIGURE 5.25: Equations to reconstruct  $k_t$  for  $\theta_w = 30^\circ$ , showing (a) generalised coefficient against  $T_p$ , and (b) normalisation coefficient against  $H_s$



(a) Generalised normalised  $k_a$  coefficient graph against wave period for  $\theta_w = 30^\circ$ .  $R^2 = 99.3\%$



(b) Normalisation factor to obtain  $k_a$  against  $H_s$  for  $\theta_w = 30^\circ$ .  $R^2 = 75.5\%$

FIGURE 5.26: Equations to reconstruct  $k_a$  for  $\theta_w = 30^\circ$ , showing (a) generalised coefficient against  $T_p$ , and (b) normalisation coefficient against  $H_s$

### 5.3 Comparison of $\theta_w$

Two wedge angles were tested in this thesis,  $60^\circ$  and  $30^\circ$ . It was anticipated that the smaller wedge angle, when the WaveCat was closer to being closed and in a survival state, would be used in cases where wave height was high and thus tests with the same height would show the  $30^\circ$  able to absorb less than the  $60^\circ$  tests.

Reflection, transmission and absorption coefficients were compared for  $\theta_w = 60^\circ$  and  $\theta_w = 30^\circ$  between two sets of tests of the same parameters. The first set of parameters were  $H_s = 0.07$  m for the range of periods tested for each wedge angle, this is equivalent to 2.00 m at full scale. The second comparison sweep used  $H_s = 0.12$  m, equivalent to 3.50 m at full scale. The  $60^\circ$  tests had a  $T_p$  range of 0.91 s to 2.37 s, representing 5 s to 13 s at full scale whereas the  $30^\circ$  tests used the range 1.28 s to 2.56 s, representing 7 s to 14 s at full scale.

Figure 5.27 shows  $k_r$  for tests of  $H_s = 0.07$  m and 0.12 m for all periods tested for both  $\theta_w = 60^\circ$  and  $30^\circ$ . Tests marked with the same colour represented tests with the same  $H_s$ , square markers represented  $60^\circ$  tests and circle markers represented  $30^\circ$ .

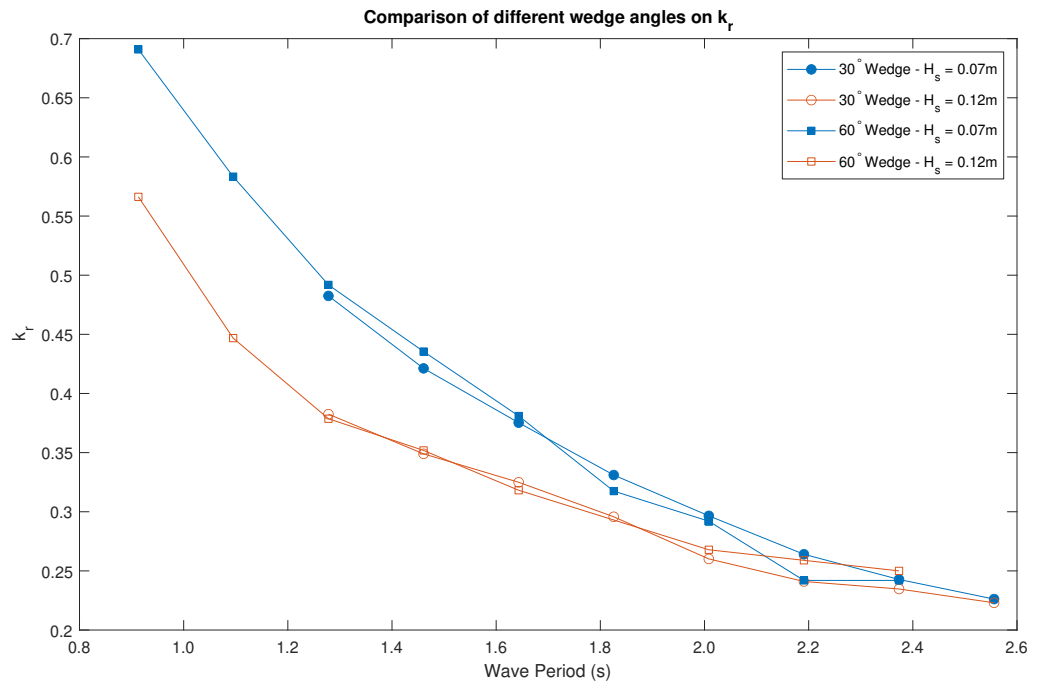
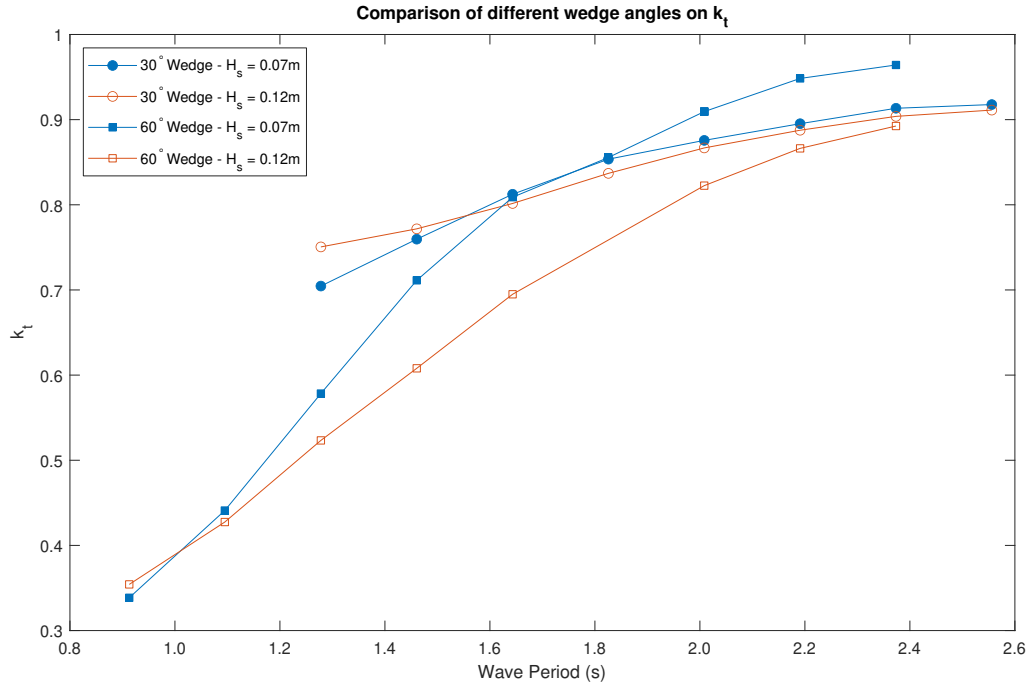


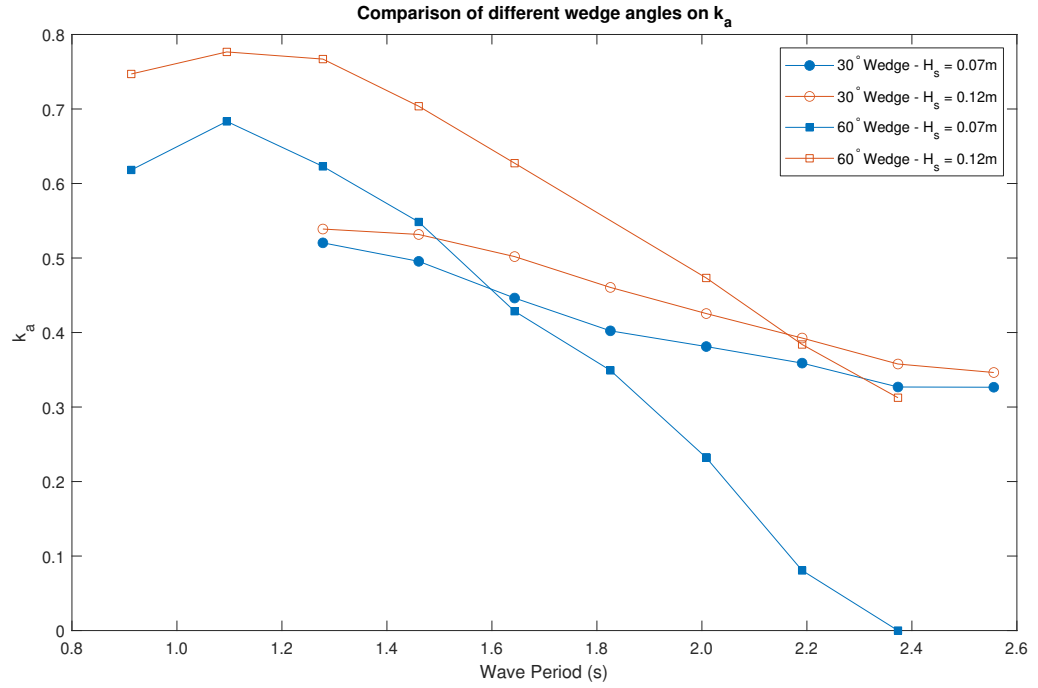
FIGURE 5.27: Comparison of  $k_r$  for  $\theta_w = 60^\circ$  and  $\theta_w = 30^\circ$



FIGURE 5.28: Comparison of  $k_t$  for  $\theta_w = 60^\circ$  and  $\theta_w = 30^\circ$ 

The graph showed that  $\theta_w$  made little difference for tests of the same conditions, as expected as reflection is largely based on the structure of the device, which was the same for both sets of tests. For both  $\theta_w$  values the  $k_r$  started high with low  $T_p$  and reduced as  $T_p$  increased. This was likely due to the freeboard of the device as it was kept constant during the tests.  $k_r$  was shown to be similar between wedge angles tested in the original prototype model which also kept freeboard the same between angles (Fernández et al., 2012a). Small variations in the tank and the position of the WaveCat during the tests likely contributed to the variability in the data.

Figure 5.28 shows  $k_t$  for tests of  $H_s = 0.07\text{ m}$  and  $0.12\text{ m}$  for all periods tested for both  $\theta_w = 60^\circ$  and  $30^\circ$ . Tests marked with the same colour represented tests with the same  $H_s$ , square markers represented  $60^\circ$  tests and circle markers represented  $30^\circ$ . The graph showed that  $\theta_w$  made a larger difference than that of Figure 5.27. The tests performed at  $\theta_w = 60^\circ$  had a larger range of  $k_t$  values over the tested periods compared to those of  $\theta_w = 30^\circ$ . The  $\theta_w = 30^\circ$  were also similar to each other, despite the  $H_s$  difference whereas the  $\theta_w = 60^\circ$  showed a separation of the trend once  $T_p$  exceeded the model frequency,  $1.28\text{ s}$  for  $\theta_w = 60^\circ$ . The wider wedge

FIGURE 5.29: Comparison of  $k_a$  for  $\theta_w = 60^\circ$  and  $\theta_w = 30^\circ$ 

angle made the transmission of the device more sensitive to wave period and wave height.

Figure 5.29 shows  $k_a$  for tests of  $H_s = 0.07$  m and  $0.12$  m for all periods tested for both  $\theta_w = 60^\circ$  and  $30^\circ$ . Tests marked with the same colour represented tests with the same  $H_s$ , square markers represented  $60^\circ$  tests and circle markers represented  $30^\circ$ . The graph showed that at lower  $T_p$  the  $\theta_w = 60^\circ$  tests absorbed a greater proportion of energy than  $\theta_w = 30^\circ$ . At higher  $T_p$  the tests with  $\theta_w = 30^\circ$  absorbed a higher proportion of energy. The test period at which the regimes changed depended on the  $H_s$ . For higher  $H_s$  tests the  $\theta_w = 60^\circ$  remained more effective until higher  $T_p$  tests, and conversely the  $\theta_w = 30^\circ$  configuration became more effective at lower  $T_p$  when combined with lower  $H_s$ . Reducing the wedge angle made the device less sensitive to wave height and wave period.

During the  $30^\circ$  model tests it was observed that the model was capable of collecting and exhausting water at higher wave heights than that of the  $60^\circ$  tests without negative effects. Tests were performed up to  $H_s = 0.15$  m for  $\theta_w = 30^\circ$ . Figure 5.22 showed that compared to the  $60^\circ$  model, Figure 5.9, the  $30^\circ$  has a smaller region in

which water is able to overtop the model and pass through the flowmeters. This was expected as the model was closer to survival mode and should have been less effective in comparable wave conditions. It also showed that for the tests in which the  $60^\circ$  configuration performed best the  $30^\circ$  did not overtop and generated no power, again to be expected for a configuration closer to survival mode. This was likely due to the  $\theta_w = 60^\circ$  tests having a larger wedge width, enabling the device to access more wave front compared to the  $30^\circ$  tests.

The results show that the device can be tuned to wave conditions while still maintaining the ability to capture and generate power by adjusting the wedge angle, as the  $60^\circ$  configuration shows a larger range for  $k_a$  than the  $30^\circ$  configuration. The reflection and transmission coefficients were shown to depend on  $H_s$  and  $T_p$  more than the wedge angle of the device, Figures 5.27 and 5.28. In smaller wave conditions the model can open the wedge to enable overtopping at lower wave heights. The exact configuration characteristics need to be examined and optimised however, as Fernández et al. (2012a) showed that opening the wedge angle to  $90^\circ$  was detrimental to the ability of the WaveCat to generate power during the concept tests.

In order to inform the understanding of the discussion, observations from experiments are presented here in the context of the WaveCat.

Figure 5.30 shows the expected motion response during waves of different lengths. When the waves are short it is expected that the device will have low responses, as the device is longer than the wavelength and will be under the action of multiple peaks and troughs at once. When the wavelength is larger than the device length then it will pitch the greatest amount, as the device will be subject to one peak and trough and thus be at the steepest condition in which it could rotate. Increasing the wavelength from then on will slowly reduce the pitch as the waves become less steep. Wave height increase will provide an amplification to the motions.

Figures 5.31 and 5.32 show how the incident waves behave differently between the two wedge angle configurations tested. The  $60^\circ$  configuration shows the waves entering the wedge and reflecting normally from the second interaction returning along

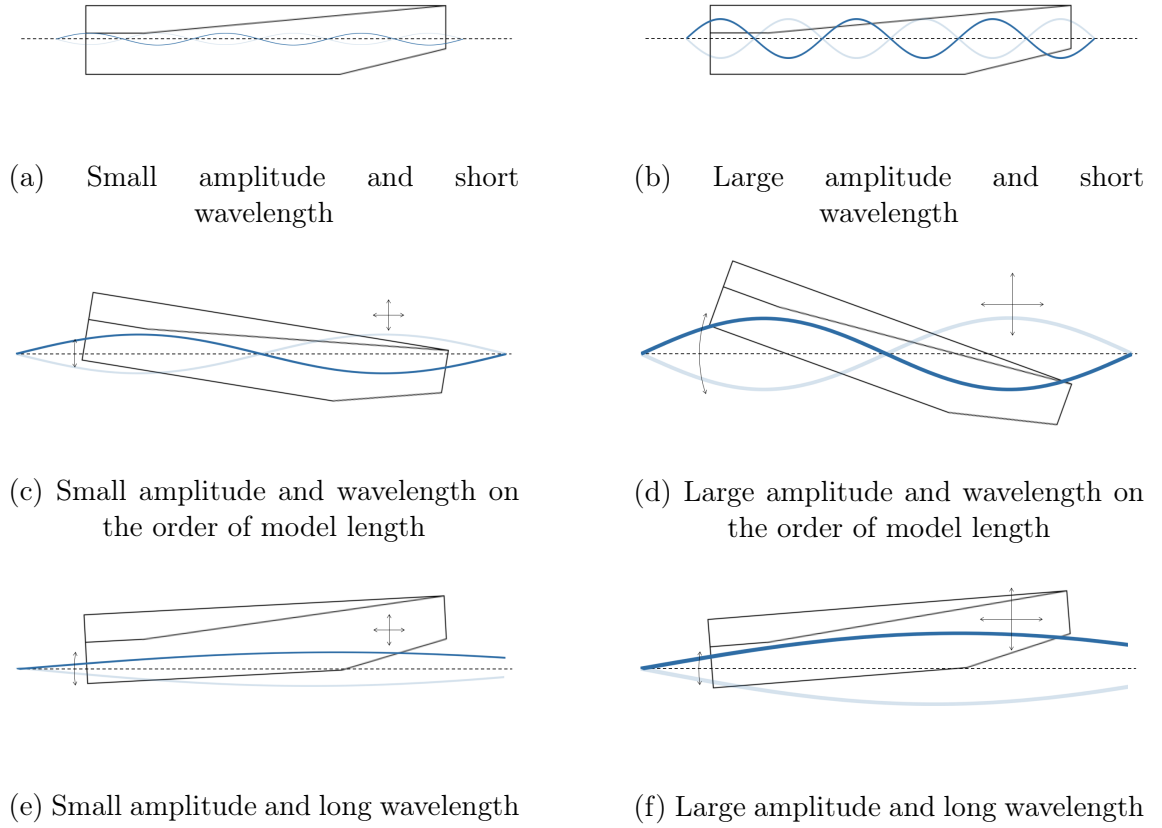


FIGURE 5.30: Anticipated WaveCat response to variations of wave steepness and amplitude

the path of the subsequent incident waves. This can setup standing waves in the wedge of the device with potential constructive interference enhancing overtopping. As the device is symmetrical the waves will also be functioning in the same manner on the opposite side of the device.

The  $30^\circ$  configuration shows the waves entering the wedge and being subject to several reflections before exiting on the opposite side of the device to entry. With the initial shallow incident angle there is potential for edge waves to be present along the inner edge of the device which may constructively interfere with subsequent waves.

With both wedge angles there is the possibility for resonance to effect the motion of the device at particular wave periods. It is predicted that with certain wedge angles and certain wave periods the wave heights will be magnified such that significant

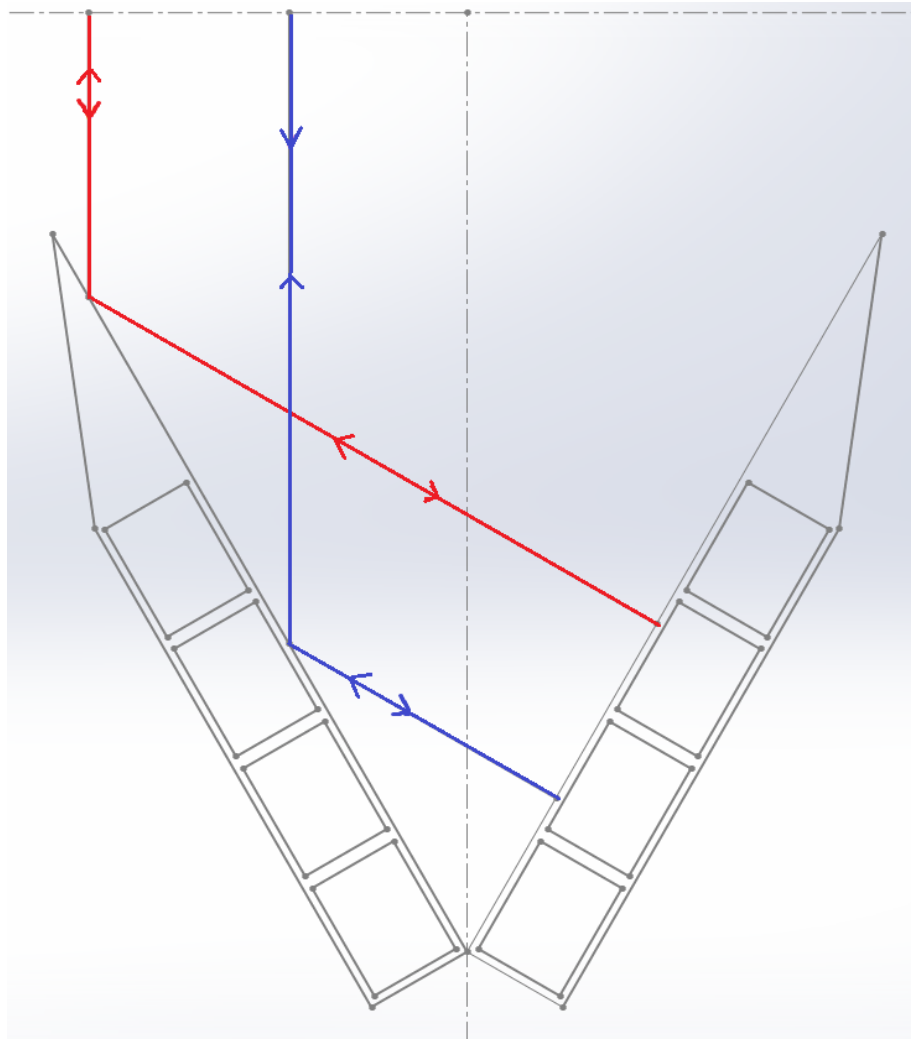


FIGURE 5.31: Wave ray trace of the 60° model configuration

overtopping will occur, and this investigation should form further testing objectives of the device.

## 5.4 Comparison with Other Devices

### 5.4.1 Device Coefficients

Fernández et al. (2012a) tested the initial laboratory model at 1:30 scale and measured reflection and transmission coefficients for two combinations of wave characteristics. The model was tested over a range of wedge angles, 30°, 45°, 60° and 90°

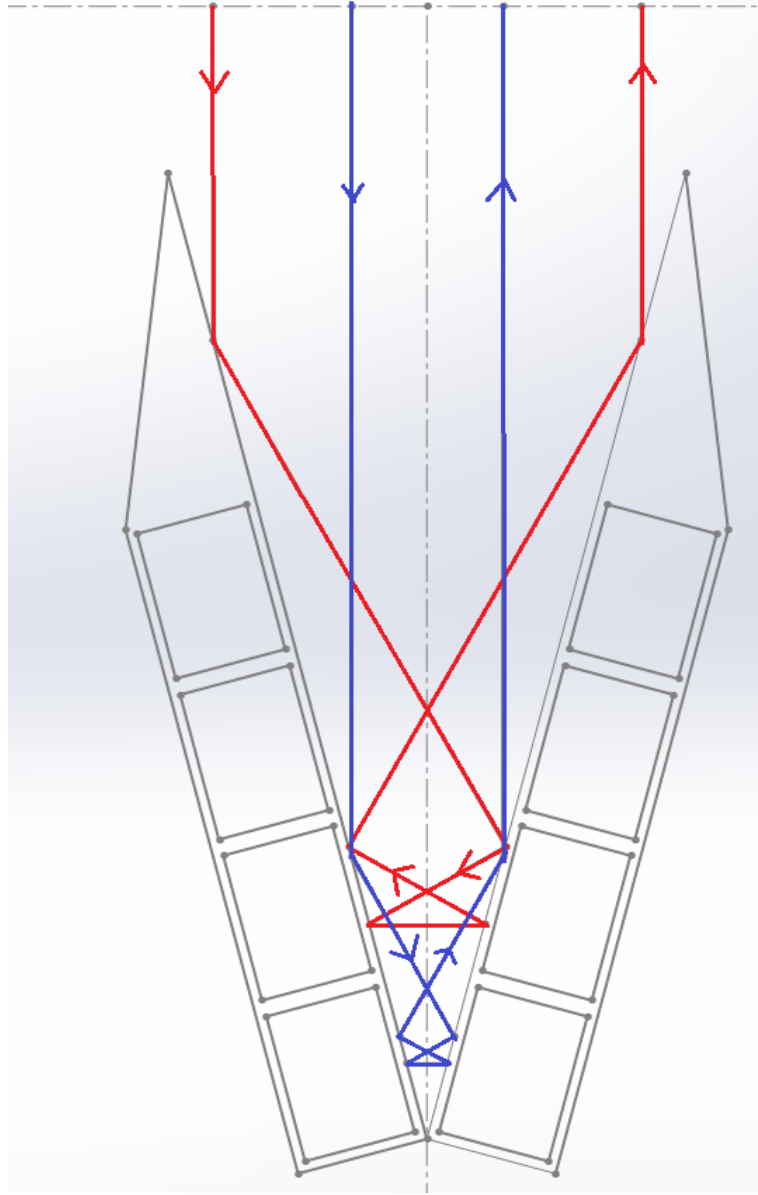


FIGURE 5.32: Wave ray trace of the 30° model configuration

for waves of  $H_s = 2.50$  m and  $T_p = 11$  s, and  $H_s = 3.00$  m and  $T_p = 12$  s at full scale. At model scale Case 1 represents  $H_s = 0.08$  m and  $T_p = 1.83$  s and Case 2 represents  $H_s = 0.1$  m and  $T_p = 2.01$  s. While the test conditions were similar, the tests presented in this study used Bretschneider spectra and the concept tests used JONSWAP spectra, resulting in a greater frequency bandwidth in the random sea spectrum. The concept also used significantly lower freeboard, 0.04 m compared to 0.2 m in the presented study, but had the overtopping tanks situated lower in the hull reducing the potential head. The scaling factor was the same between studies.

The 60° tests resulted in  $k_r$  of 0.421 and 0.431 for wave cases of  $H_s = 2.50$  m and  $T_p = 11$  s and  $H_s = 3.00$  m and  $T_p = 12$  s respectively. For the model presented in this thesis the  $k_r$  was 0.291 and 0.250 respectively, shown in Figure 5.6a, lower than that of the initial model tests. For the 30° the  $k_r$  determined by Fernández et al. (2012a) was 0.425 and 0.438 respectively, compared with 0.296 and 0.249 respectively for the model presented in this thesis in Figure 5.19a.

The transmission coefficient was also calculated for the same tests with the initial concept model having a  $k_t$  of 0.507 and 0.760 for the 60° tests respectively and 0.806 and 0.777 for the 30° tests respectively. The model presented in this thesis had  $k_t$  of 0.869 and 0.898 for the equivalent 60° tests and 0.882 and 0.900 for the equivalent 30° tests.

In all the comparable wave conditions and wedge angles the new model reflects less of the incident wave energy compared to the initial concept model, whilst maintaining the lack of change when altering the wedge angle between 60° and 30°. The transmission of the new model is higher, and where the initial concept tests showed the wedge angle making a difference between  $k_t$  for the smaller waves tested the new model does not. By applying Equation 4.30 to the  $k_r$  and  $k_t$  values given by Fernández et al. (2012a) the resultant  $k_a$  values are 0.752 for the test of  $H_s = 2.50$  m and  $T_p = 11$  s and 0.486 for the test of  $H_s = 3.00$  m and  $T_p = 12$  s. The  $k_a$  values presented in this thesis in Figure 5.8a for the equivalent tests are 0.341 and 0.302 respectively. For the 30° tests the initial concept model had  $k_a$  values of 0.412 and 0.452 for the respective cases compared to 0.364 and 0.356 for the presented model.

The main cause of the differences in the two models is that the concept model used a much lower freeboard compared to the model presented in this study. The new model, however, represents an improvement over the concept as significant overtopping occurred for tests at a  $H_s$  of 2.00 m at full scale, whereas the initial concept model only reported significant overtopping at  $H_s$  of 2.50 m and higher. In addition, while the presented model produced power of a similar magnitude as that of the initial concept model, it did so during tests with lower  $k_a$  values, showing a

higher efficiency in the system. This is likely due to the increased head in the device, as the tanks were situated higher in the model.

Nørgaard and Andersen (2012) performed physical model experiments on the Wave Dragon WEC at 1:51.8 scale to validate a Boundary Element Method (BEM) model and to determine, amongst other objectives, the wave transmission of the device. It was shown that  $k_t$  for tests with relative freeboard  $(\frac{R_c}{H_s}) = 0.9$  is related to wave period through the equation

$$k_t = -0.087T_p + 0.82 \quad (5.2)$$

in the range when  $l/\lambda_p$  is between 0.9 and 1.2 for the Wave Dragon. During tests for the WaveCat the tests performed at  $T_p = 1.28$  s fall into this range defined by Nørgaard and Andersen (2012).  $l$  is the effective length of the model, 2.62 m at  $60^\circ$  and 2.91 m at  $30^\circ$ , and the wavelength for the 1.28 s  $T_p$  test is 2.56 m giving ratios of 1.02 and 0.90 respectively. The tests at  $\theta_w = 60^\circ$  have a higher  $R_c$  of 1.7 than Wave Dragon,  $H_s = 0.12$  m with a freeboard of 0.2 m, and resulted in a  $k_t$  of 0.523. The tests at  $\theta_w = 30^\circ$  used  $\frac{R_c}{H_s} = 1.33$ , as the  $H_s$  was 0.15 m, higher than the  $60^\circ$  case. This resulted in a  $k_t$  of 0.737. The Wave Dragon would have achieved a  $k_t$  of 0.708 using Equation 5.2. The trend of the WaveCat results show increasing the wave height for the same period to achieve a similar  $R_c$  would likely reduce  $k_t$  even further, as smaller  $H_s$  and thus higher  $R_c$  increased  $k_t$ , as shown in Figures 5.7a and 5.20a for  $60^\circ$  and  $30^\circ$  respectively.

### 5.4.2 Power Generation

Fernández et al. (2012a) showed that for a 1:30 scale model of the initial concept of the WaveCat it is capable of overtopping, thus collecting water which can be used to generate power. The amount of water in the reservoirs was measured then pumped out to mimic the device exhausting the water through turbines and a power implied from the amount of water collected. The model presented in this paper



collected water in overtopping tanks before releasing it through a flowmeter in the base of the hull to take advantage of the fact the water is stored above water level and better mimic final operational processes. The power generated by the original concept model (Fernández et al., 2012a) is scaled up to full scale, and for a  $\theta_w = 60^\circ$  model configuration, during tests of  $H_s = 2.50$  m and  $T_p = 11$  s, at full scale an estimated 11.74 kW of power was generated. For tests of  $H_s = 3.00$  m and  $T_p = 12$  s an estimated 43.08 kW was generated. For the same wave characteristics, but model configuration of  $\theta_w = 30^\circ$ , the estimated generated power was 17.42 kW and 26.35 kW.

When scaling up the model presented in this thesis for the equivalent tests with  $\theta_w = 60^\circ$  the new version of the WaveCat produces 37.90 kW for the test with lower period and 35.39 kW in the test with higher period. When at  $\theta_w = 30^\circ$  the new model does not generate power from the comparable waves. This is likely due to the fact that the freeboard for the new model tests was substantially higher than that of the concept tests, 0.2 m compared to a minimum of 0.04 m in the concept model at the aft most reservoir. The new model, however, represents an improvement over the concept as significant overtopping occurred for the  $60^\circ$  tests at a  $H_s$  of 0.07 m, or 2.00 m at full scale, whereas the initial concept model only reported significant overtopping at  $H_s$  of 2.50 m and higher. This is likely due to the initial concept model operating in regions where the model does not capture as much water. Limited conditions were tested during the concept trials, with  $H_s$  between 0.07 m and 0.1 m and  $T_p$  between 1.83 s and 2.20 s. Therefore the region at which the updated version performs best was not tested at concept level. The overtopping chambers in the updated version of the WaveCat were also larger, representing a greater proportion of the models length.

In addition, while the presented model produced power of a similar magnitude at  $60^\circ$  as that of the initial concept model, it did so with less energy available after reflection and transmission coefficients were taken into account. This is likely due to a larger head present in the updated model, as the overtopping tanks were situated higher up on the model, which itself had a larger freeboard.

CWR, calculated using Equations 2.17 and 2.18, is used to compare devices of differing dimensions by comparing the amount of power the device captures from the amount of wave front that is acting on the device.

At this stage of development the WaveCat has a CWR of 1.5% in the most efficient 60° tests, at  $H_s$  of 0.08 m and  $T_p$  of 1.09 s producing approximately 0.2 W. During the most efficient 30° tests the CWR was 5.4%, at  $H_s$  of 0.15 m and  $T_p$  of 1.46 s producing approximately 1.4 W. Babarit (2015) compiled a database of known CWR values primarily from experimental results, with additional field measurements also considered. The Wave Dragon achieved CWRs between 21% and 27% depending on the device dimensions and resource. Other OWECS, such as SSG, show a CWR of 23%, the Power Pyramid 12% and the Sucking Sea Shaft 3%. Fixed OWSCs have the highest average CWR with 37%, OWCs have a mean CWR of 29%, OWECS have a mean of 17% and heaving devices have 16%. Individual devices within each category show large variations however, evidenced by large variations in the CWR in each sub-category. The WaveCat is towards the lower end of the OWECS category, however it still merits development as it is very early in development and requires significant further optimisation, primarily in the power conversion system and overtopping mechanisms. It is already showing CWR values close to that of the Sucking Sea Shaft.

Typically the Wave Dragon overtopping rates are presented as a dimensionless overtopping flow volume. The WaveCat overtopping volumes can be converted to dimensionless overtopping flow volume using the equation presented in Equation 2.19. For the best performing wave conditions,  $H_s = 0.12$  m and  $T_p = 1.09$  s at 60°, the WaveCat achieves a dimensionless overtopping flow rate ( $Q_N$ ) of  $2.8 \times 10^{-4}$ . The wave conditions result in  $\frac{R_c}{H_s} = 1.7$  for which the Wave Dragon was experiencing  $Q_N \approx 1 \times 10^{-2}$  as per Tedd et al. (2006). Kofoed (2002) identified that device specific additional factors can be added to the above equation that account for device characteristics such as, but not limited to, crest freeboard, draft of the device and slope shape. The result for Tedd et al. (2006) above incorporates the draft factor,  $\lambda_{dr}$ , shown in Equation 2.21.  $\lambda_{dr}$  for the WaveCat test equates to 0.166 with the

TABLE 5.1: Properties of the WaveCat scaled from 1:30 to 1:1

Property	WaveCat Scale (1:S)		Scaling Law	Scaling Factor (S)	Unit
	1:30	1:1			
Length	3	90	$S^1$	30	m
Width (individual hull)	0.4	12	$S^1$	30	m
Draft	0.2	6	$S^1$	30	m
Deployment Depth	2	60	$S^1$	30	m
Displacement	0.57	15390	$S^3$	27000	t
Freeboard	0.2	6	$S^1$	30	m
Power Generated	-	-	$S^{3.5}$	147885	W
RAOs	-	-	$S^0$	1	-

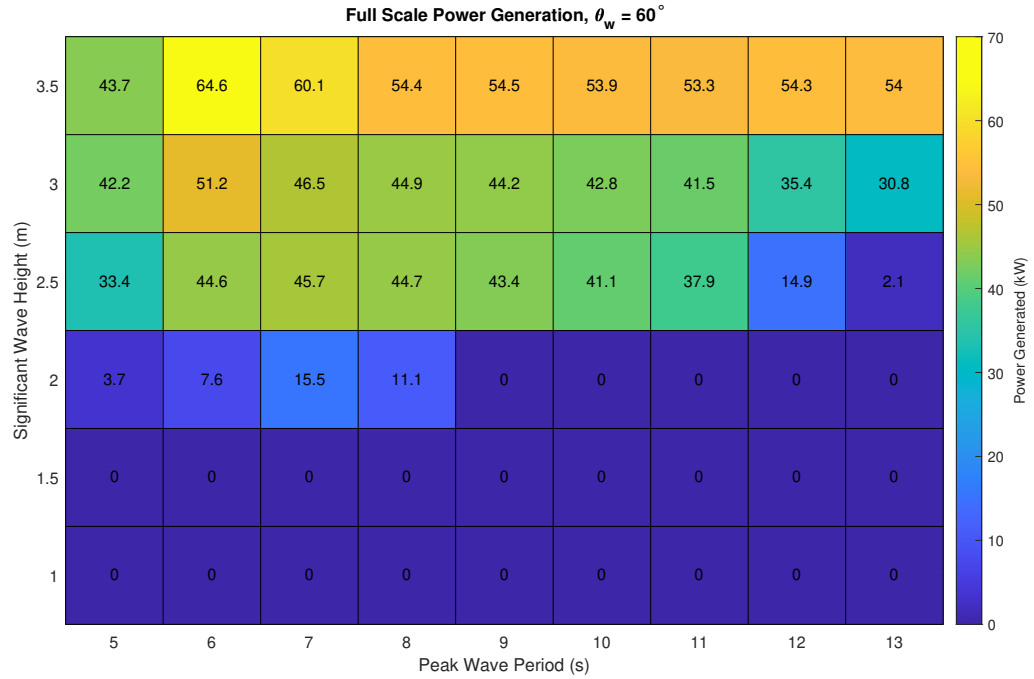
conditions mentioned above, raising  $Q_N$  to  $1.7 \times 10^{-3}$ . The draft factor for the Wave Dragon was based on the 1:4.5 prototype tests at Nisum Bredning which has a water depth of 6 m, shallower than the tested conditions of the WaveCat, thus the Wave Dragon has a larger  $\Lambda_{dr}$  factor allowing greater access to energy in the waves.

While this value of  $Q_N$  is lower than that of Wave Dragon, the Wave Dragon is further along the technology readiness chain and has had optimisation work performed to focus and increase overtopping volumes, an avenue of future research identified for the WaveCat.

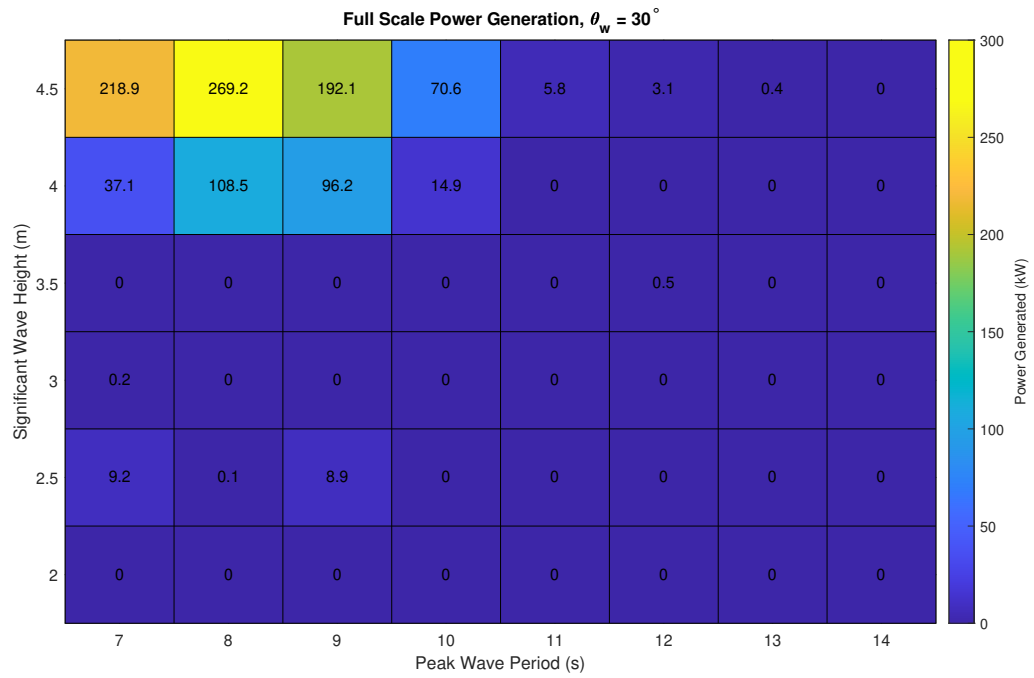
## 5.5 Full Scale WaveCat

To easily compare the WaveCat to other devices the model characteristics can be scaled back to full scale, as shown in Table 5.1 (Iglesias et al., 2011). Compared to a 4 MW version of the Wave Dragon, the WaveCat is smaller and lighter, 90 m in length compared to 150 m and 15,390 t compared to 22,000 t.

Conditions of  $H_s = 3.50$  m and  $T_p = 6$  s, and  $H_s$  of 4.50 m and  $T_p$  of 8 s, representing the best performing  $60^\circ$  and  $30^\circ$  cases for the WaveCat, would generate an estimated 64.6 kW and 270 kW respectively. The estimated power generation was used over the CWR for this comparison as this model experienced greater overtopping than



(a) Full scale power output for  $60^\circ$  configuration



(b) Full scale power output for  $30^\circ$  configuration

FIGURE 5.33: Power output of  $60^\circ$  and  $30^\circ$  configurations scaled up to full scale

could be handled by the tanks, resulting in excess energy overflowing and returning to the tank without being captured.

Based on the power matrix the Wave Dragon prototype generates 1,450 kW and 3,220 kW respectively (Silva et al., 2013; Kofoed et al., 2006) at these conditions. The SSG, for the same conditions, generates 5,348 kW and 12,860 kW respectively (Silva et al., 2013; Vicinanza et al., 2012). In the conditions described both devices are operating away from conditions that generate their maximum power in the matrix, suggesting they are better suited to different conditions to the WaveCat. For both devices they generate more power in longer period waves. The WaveCat has yet to undergo optimisation on the design to the level the Wave Dragon and SSG have had, and is suggested as a next step from this research programme. The Wave Dragon is also larger than the WaveCat, with an arm width of 237 m compared to 90 m for the WaveCat at  $60^\circ$ , thus it is capable of capturing a larger wave front.

For the best performing conditions for the WaveCat, described above, the Pelamis generated 354 kW and 628 kW respectively (Silva et al., 2013; Henderson, 2006). The trends observed in the Pelamis power matrix show similar trends to the WaveCat in that the best power generation occurs at low wave periods and high wave heights.

For the conditions described the AquaBuOY generated 54 kW and 122 kW respectively (Silva et al., 2013; Weinstein et al., 2004). While this is less than the WaveCat, the overall size of the AquaBuOY is much smaller, on the order of 5 m in diameter compared to a 90 m WaveCat. The AquaBuOY also shows the highest power returns in short period waves with high heights.

Compared to OWSCs, the Oyster and WaveRoller, for the same conditions, the Oyster produced 271 kW and 290 kW respectively (Silva et al., 2013; Whittaker et al., 2007). The Oyster power matrix shows that waves of low period and high height produce the highest power generation. While the WaveRoller has a normalised power matrix, so absolute values are unknown, the trends are observed to be the same (Mäki et al., 2014). Both devices, however, are much smaller than the WaveCat and seabed mounted in the nearshore, whereas WaveCat is floating offshore.

Limited power matrices are available for the Pico power plant (Monk et al., 2013) and the OE Buoy (Lavelle and Kofoed, 2011), but these do not contain the specific conditions above. The trends in the power can still be observed. The Pico power plant shows the highest power generation in the lowest wave periods observed, but generates less power when the wave height is too large. The OE Buoy also shows the largest power generation in lower period waves but shows a steady increase in power as wave height is increased. Both devices are OWC devices, but the OE Buoy is floating whereas the Pico power plant is shore mounted.

# Chapter 6

## Responses in Regular and Random Waves

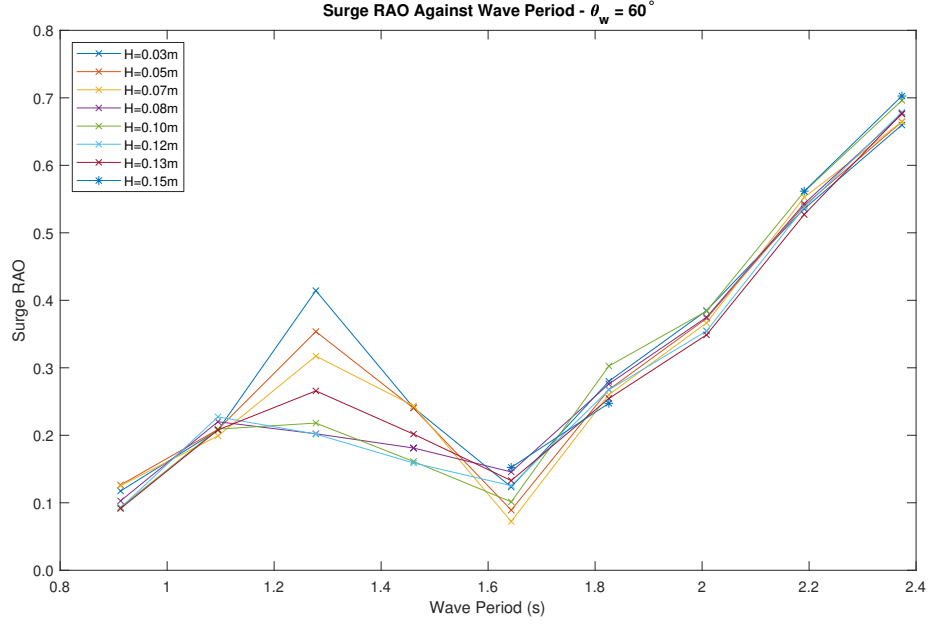
In this Chapter the device responses to the wave field are shown. The responses were measured for the WaveCat in both  $60^\circ$  and  $30^\circ$  wedge angles for all 6DOF motions and the RAOs were calculated through the response of the device to incoming regular waves, with the method described in greater detail in Chapter 4.

RAOs were defined as the relationship between the response of the device in a fixed translation or rotation and the wave height, as described in Section 4.7.

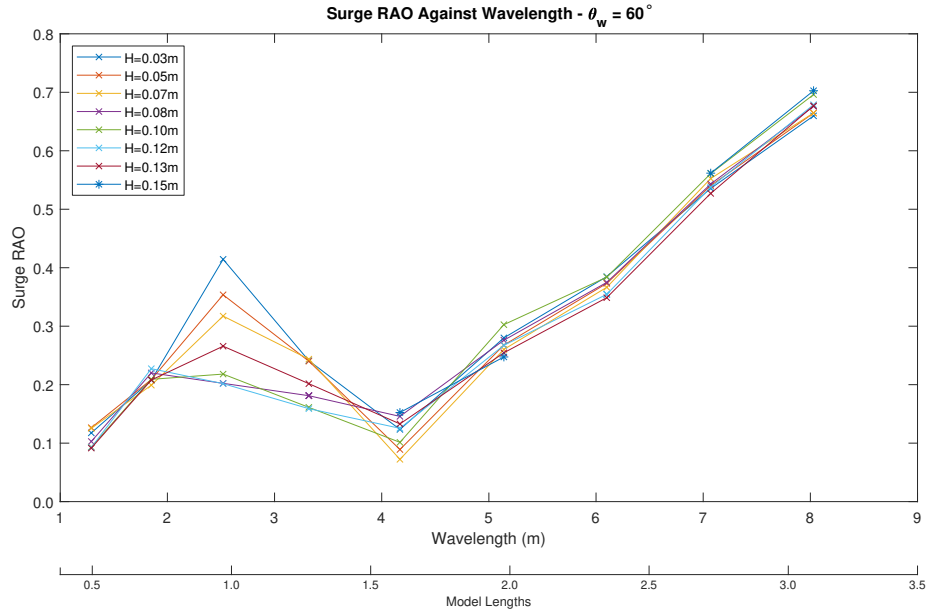
### 6.1 $60^\circ$ Wedge Angle

#### 6.1.1 Response Amplitude Operators

Figure 6.1 shows the surge RAO in regular waves for  $\theta_w = 60^\circ$  against wave period, Figure 6.1a, and against wavelength, Figure 6.1b. In general, the RAO became wave height independent at wave periods above 1.64 s and at 1.09 s and below, shown in Figure 6.1a. When the wave period was around the model wavelength, as shown



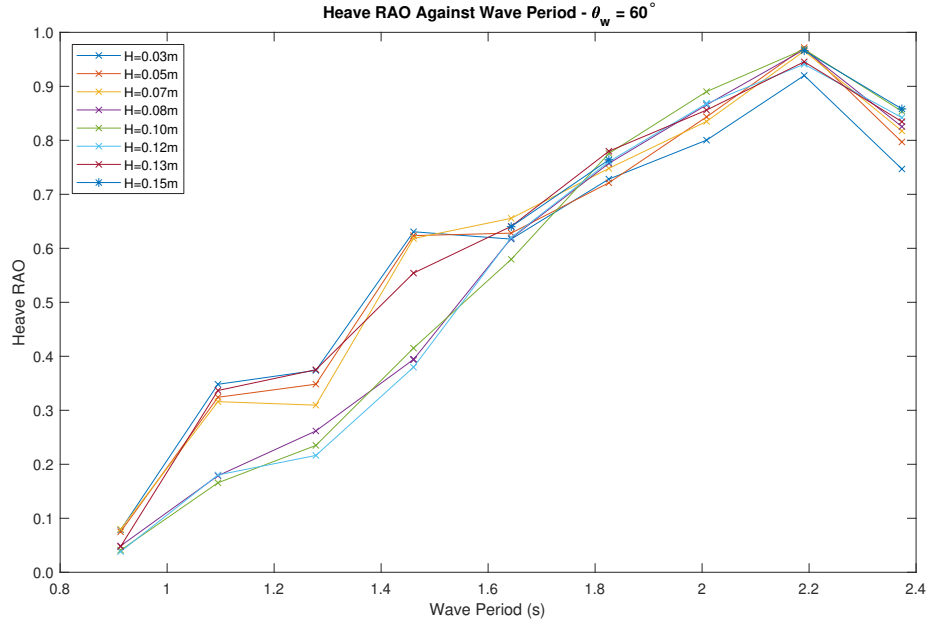
(a) Surge RAO against wave period for  $\theta_w = 60^\circ$



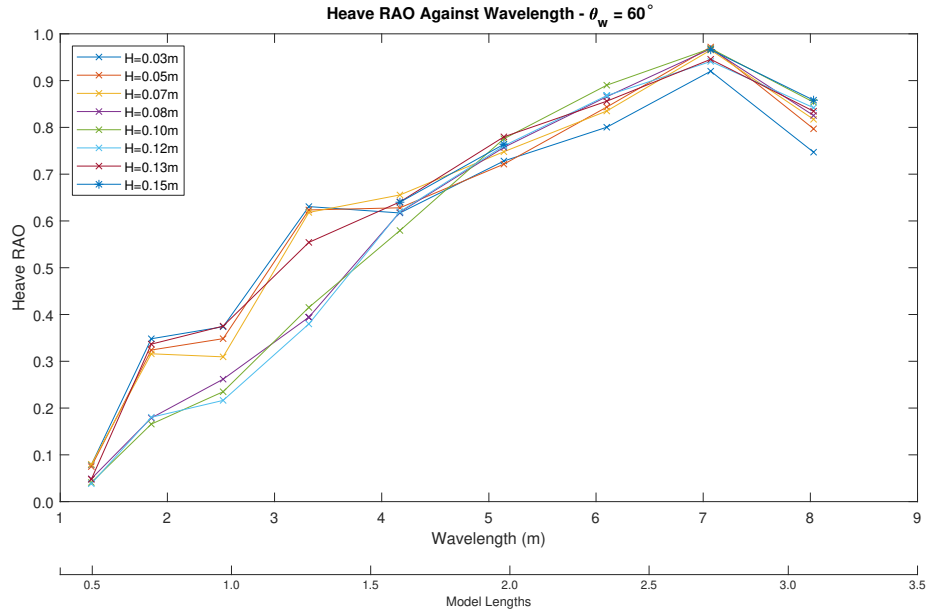
(b) Surge RAO against wavelength and model length for  $\theta_w = 60^\circ$

FIGURE 6.1: Surge RAO against wave period, wavelength and model length for  $\theta_w = 60^\circ$





(a) Heave RAO against wave period for  $\theta_w = 60^\circ$



(b) Heave RAO against wavelength and model length for  $\theta_w = 60^\circ$

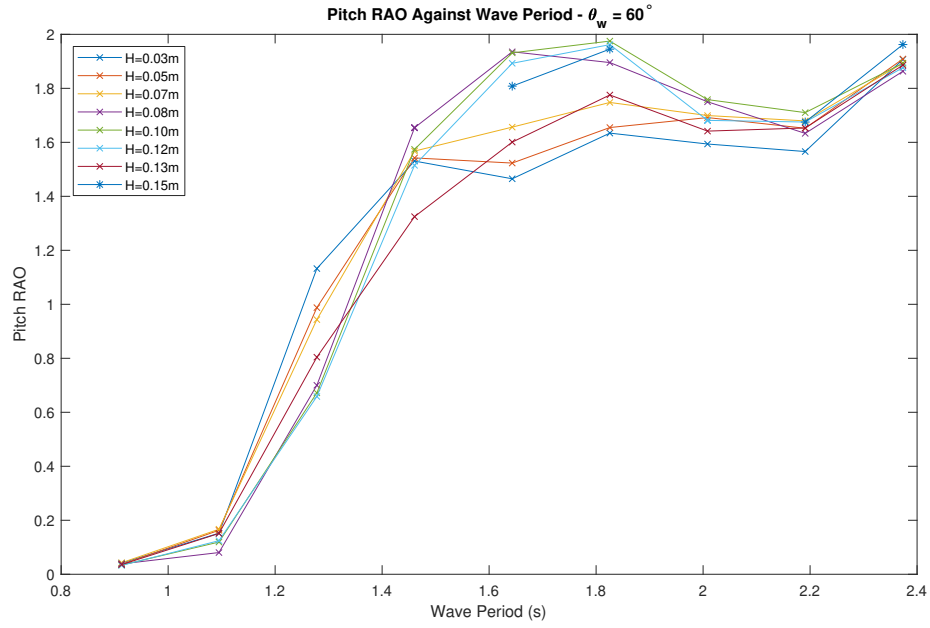
FIGURE 6.2: Heave RAO against wave period, wavelength and model length for  $\theta_w = 60^\circ$

in Figure 6.1b, the RAO became dependent on wave height as well as wave period suggesting a resonant response around the model wavelength.

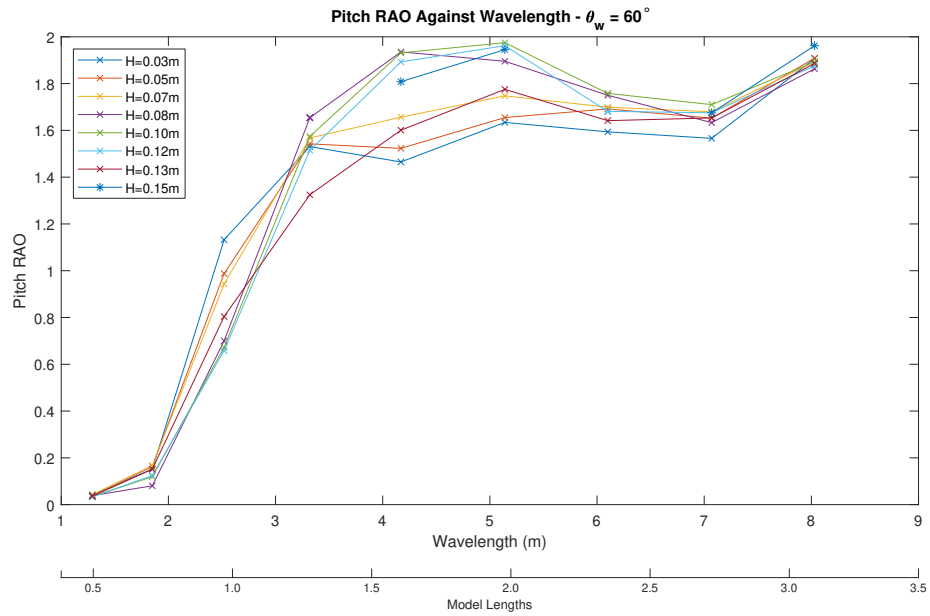
Figure 6.2 shows the heave RAO in regular waves for  $\theta_w = 60^\circ$  against wave period, Figure 6.2a, and against wavelength, Figure 6.2b. Above a wave period of 1.64 s the RAO became wave height independent, and reached an RAO of close to 1 at a

period of 2.20 s. Below wave periods of 1.64 s the RAO split into two regimes. The smallest waves of 0.05 m and less, along with the largest waves tested of 0.12 m, showed higher heave RAOs than the tests performed between 0.07 m and 0.1 m. When compared to wavelength the regime with the largest response showed a dip when the model wavelength was approximately equal to the wavelength of the tests,, before rising when the wavelength became larger than the model length.

Figure 6.3 shows the pitch RAO for  $\theta_w = 60^\circ$  against wave period, Figure 6.3a, and against wavelength, Figure 6.3b. Figure 6.3a shows that when  $T_p$  was low the pitch RAO was also low, however the pitch RAO quickly rose when  $T_p$  rose too. There was a slight dip in pitch RAO towards higher  $T_p$  tests before it rose again. When comparing the pitch RAO to wavelength, Figure 6.3b, it is shown that the rise in pitch RAO happened when the wavelength became longer than one model length, and peaked at two model lengths before dipping at higher wavelengths. Wave height had little effect on the RAO as the lines for each test are close to each other.



(a) Pitch RAO against wave period for  $\theta_w = 60^\circ$



(b) Pitch RAO against wavelength and model length for  $\theta_w = 60^\circ$

FIGURE 6.3: Pitch RAO against wave period, wavelength and model length for  $\theta_w = 60^\circ$

### 6.1.2 Responses to Random Waves

The responses to the primary degrees of freedom of the device in random waves were also measured. Heave, surge and pitch spectra were plotted with respect to frequency along with the incident wave surface elevation spectrum from Section 5.1.1.

Figure 6.4 shows the response spectra as functions of frequency along with the incident wave spectrum of a test with  $H_s = 0.12$  m and  $T_p = 1.28$  s. In this test the incident wave peak period was very close to that of the model period. The surge and heave both exhibited high responses when the wave frequency was above that of the frequency associated with waves of model length. The pitch response had a broader peak that extended either side of the model frequency.

Figure 6.5 shows the response spectra as functions of frequency along with the incident wave spectrum of a test with  $H_s = 0.12$  m and  $T_p = 0.91$  s. In this test the incident wave peak period was lower than the model period. The surge showed a high, narrow response when the wave frequency was around that of the frequency associated with waves of model length. The pitch and heave responses exhibited

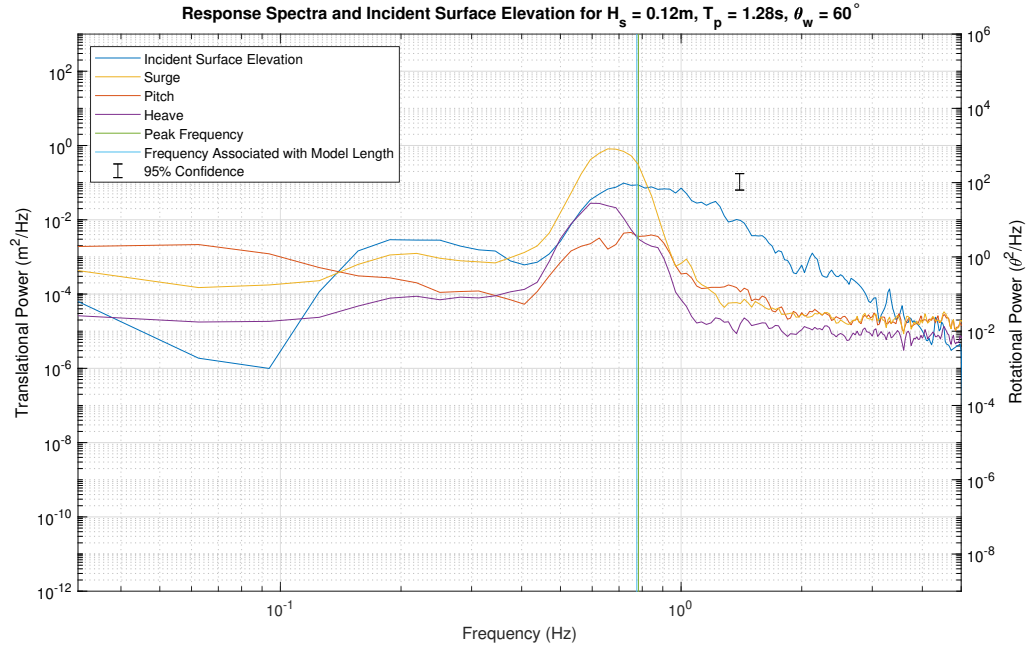


FIGURE 6.4: Spectral analysis of responses to random waves of  $H_s = 0.12$  m,  $T_p = 1.28$  s,  $\theta_w = 60^\circ$ . Incident wave spectrum is shown in blue. Surge, pitch and heave response spectra are shown in orange, yellow and purple respectively

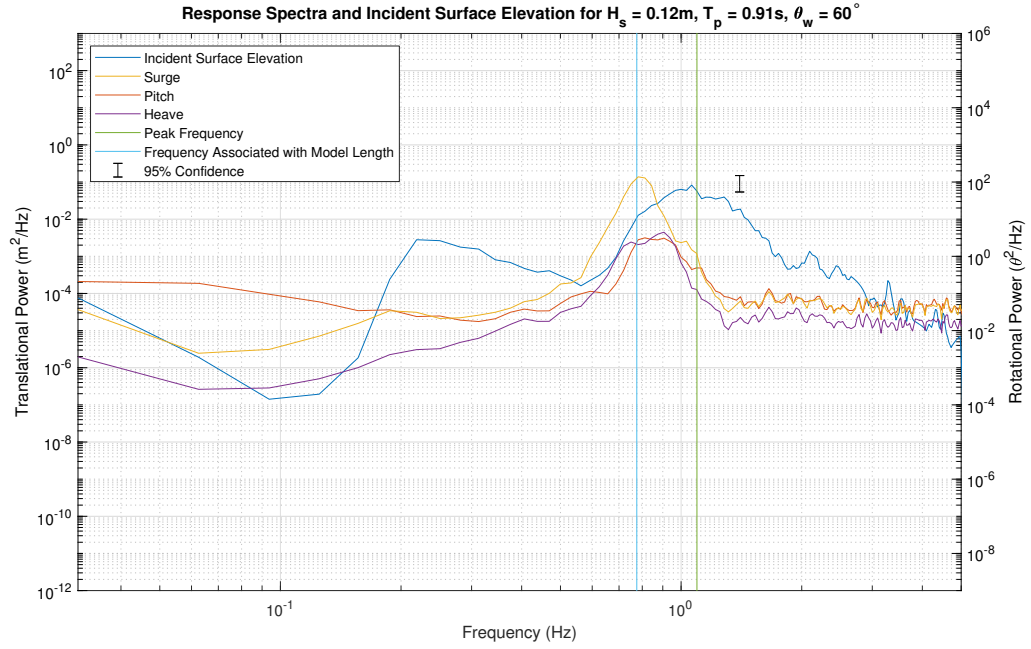


FIGURE 6.5: Spectral analysis of responses to random waves of  $H_s = 0.12$  m,  $T_p = 0.91$  s,  $\theta_w = 60^\circ$ . Incident wave spectrum is shown in blue. Surge, pitch and heave response spectra are shown in orange, yellow and purple respectively

broader peaks that extended either side of the model frequency. All three responses dropped as frequency increased.

Figure 6.6 shows the response spectra as functions of frequency along with the incident wave spectrum of a test with  $H_s = 0.12$  m and  $T_p = 2.37$  s. In this test the incident wave peak frequency was much lower than the model frequency. All three motions showed high responses at low frequency. The surge response continued at a similarly high response level until the wave frequency was higher than that of the model frequency before dropping. Conversely, the heave and pitch both peaked around the peak test frequency but dropped before the model frequency was reached.

Figure 6.7 shows the response spectra as functions of frequency along with the incident wave spectrum of a test with  $H_s = 0.08$  m and  $T_p = 0.91$  s. In this test the incident wave peak period was lower than the model period, the same as Figure 6.5 but with a lower  $H_s$ . The responses were similar to that of the test with the higher  $H_s$ . The surge showed high, narrow response when the wave frequency was around that of the frequency associated with waves of the model length. The pitch and heave

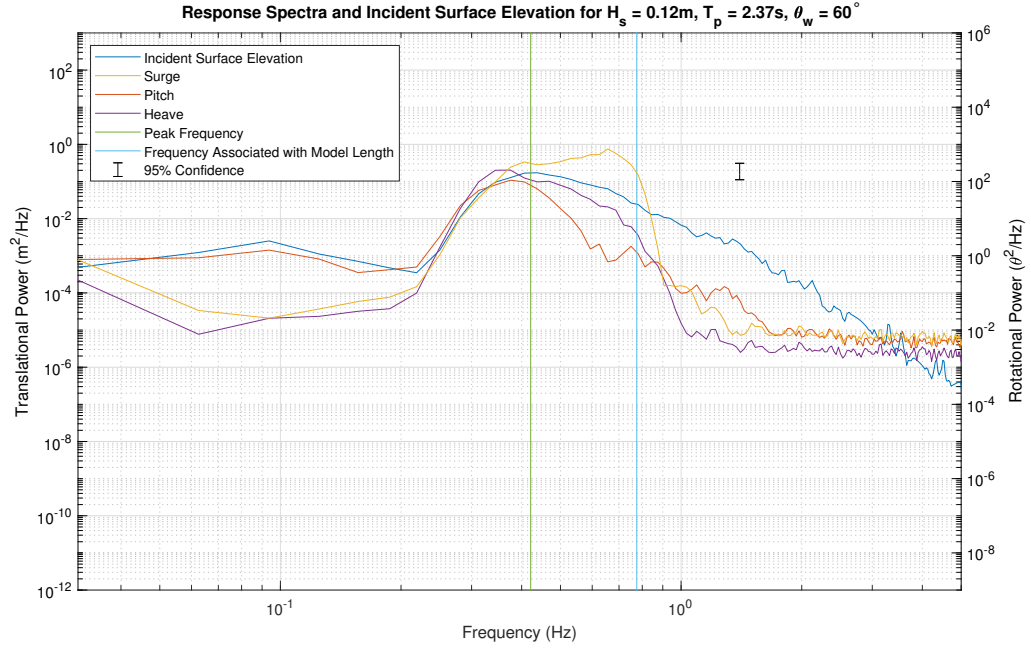


FIGURE 6.6: Spectral analysis of responses to random waves of  $H_s = 0.12$  m,  $T_p = 2.37$  s,  $\theta_w = 60^\circ$ . Incident wave spectrum is shown in blue. Surge, pitch and heave response spectra are shown in orange, yellow and purple respectively

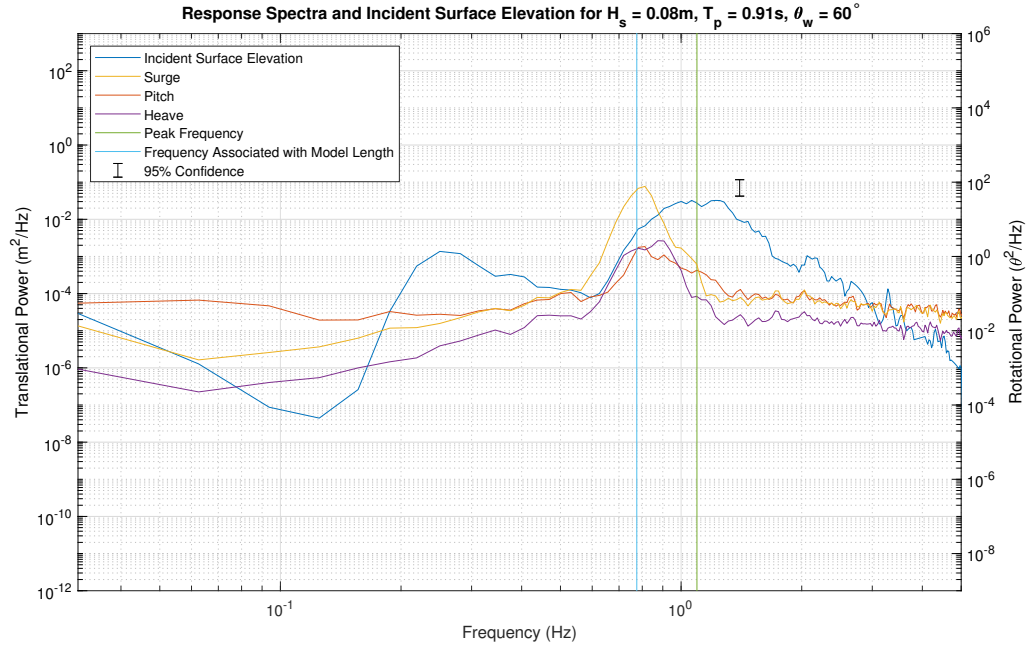


FIGURE 6.7: Spectral analysis of responses to random waves of  $H_s = 0.08$  m,  $T_p = 0.91$  s,  $\theta_w = 60^\circ$ . Incident wave spectrum is shown in blue. Surge, pitch and heave response spectra are shown in orange, yellow and purple respectively

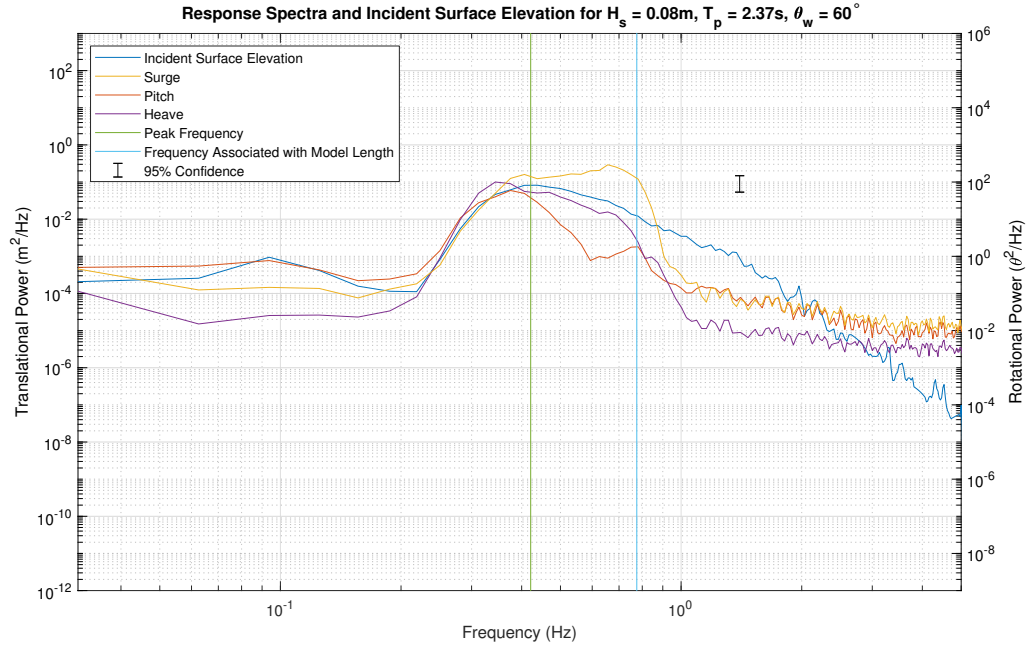


FIGURE 6.8: Spectral analysis of responses to random waves of  $H_s = 0.08$  m,  $T_p = 2.37$  s,  $\theta_w = 60^\circ$ . Incident wave spectrum is shown in blue. Surge, pitch and heave response spectra are shown in orange, yellow and purple respectively

responses show broader peaks that extended either side of the model frequency. All three responses dropped as frequency increased.

Figure 6.8 shows the response spectra as functions of frequency along with the incident wave spectrum of a test with  $H_s = 0.08$  m and  $T_p = 2.37$  s. In this test the incident wave peak frequency is much lower than the model frequency, the same as Figure 6.6 but with a lower  $H_s$ . In a similar manner to the test with the higher  $H_s$ , all three motions showed high responses when the frequency was low. The surge response continued at a similarly high response level until the wave frequency was higher than that of the model frequency before dropping. Conversely, the heave and pitch both peaked around the peak test frequency but dropped before the model frequency was reached.

The power contained in the spectra of surge, pitch and heave was calculated using Equation 4.21 and normalised for each response. Scatter plots of the normalised response compared to the wave conditions were produced.

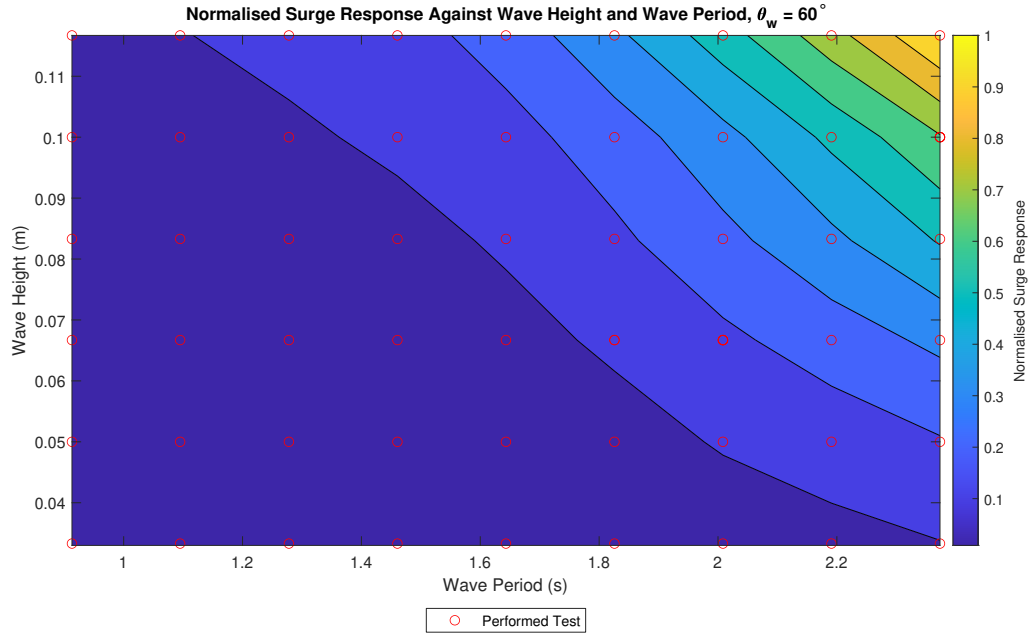


FIGURE 6.9: Scatter plot of normalised surge response against random wave conditions for  $\theta_w = 60^\circ$  model configuration

Figure 6.9 shows the scatter plot of normalised surge response against  $H_s$  and  $T_p$ . The surge response was highest when both  $H_s$  and  $T_p$  were high. The surge response was lowest when the  $H_s$  and  $T_p$  were both low.

Figure 6.10 shows the scatter plot of normalised pitch response against  $H_s$  and  $T_p$ . The pitch response was highest when  $H_s$  was high, but only when the  $T_p$  was above that of the model period. The pitch response was low when  $T_p$  was low, regardless of  $H_s$ , and also low when  $H_s$  was low.

Figure 6.11 shows the scatter plot of normalised heave response against  $H_s$  and  $T_p$ . The heave response was highest when both  $H_s$  and  $T_p$  were high. The heave response was lowest when the  $H_s$  and  $T_p$  were both low.



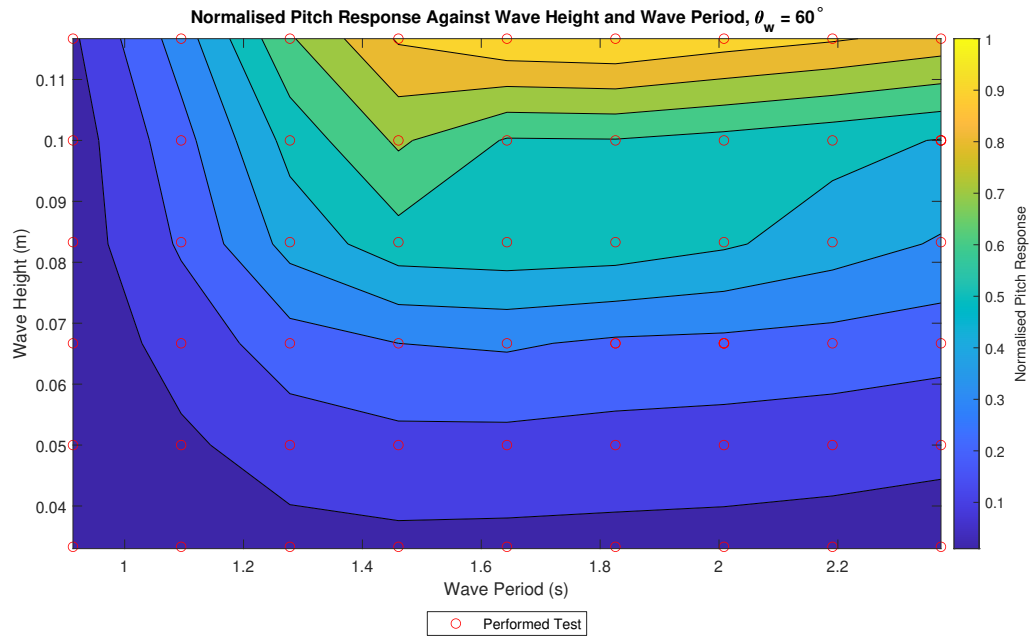


FIGURE 6.10: Scatter plot of normalised pitch response against random wave conditions for  $\theta_w = 60^\circ$  model configuration

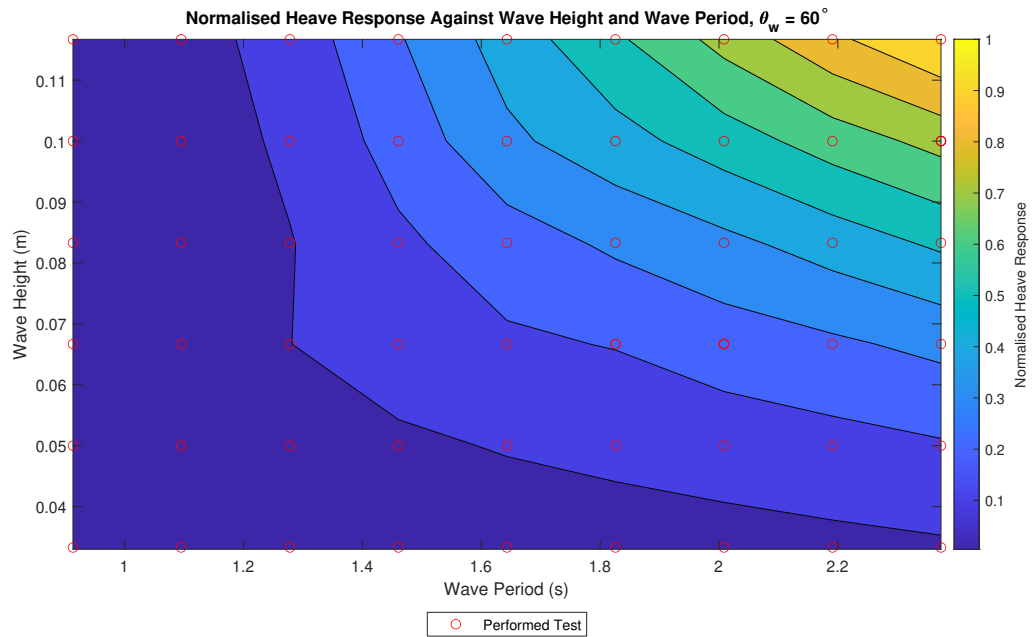


FIGURE 6.11: Scatter plot of normalised heave response against random wave conditions for  $\theta_w = 60^\circ$  model configuration

## 6.2 30° Wedge Angle

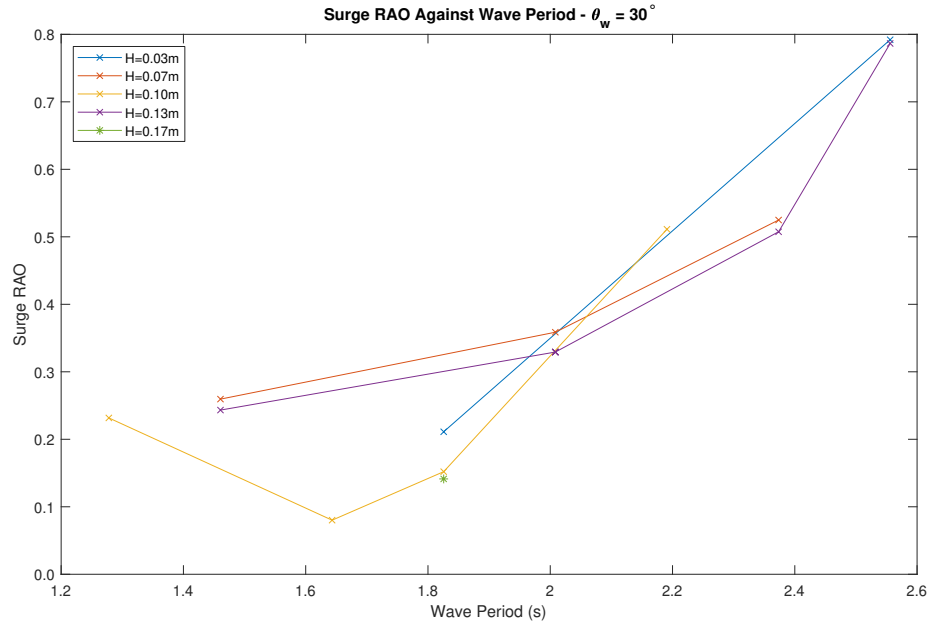
### 6.2.1 Response Amplitude Operators

Figure 6.12 shows the surge RAO to regular waves for  $\theta_w = 30^\circ$  against wave period, Figure 6.12a, and against wavelength, Figure 6.12b. Figure 6.12a shows that the lowest RAO occurred at  $T_p = 1.64$  s. When wave period was lower than this the RAO was larger, additionally, when the wave period was larger than 1.64 s the RAO was again larger. Figure 6.12b shows the RAO as a function of wavelength, with the lowest RAOs occurring around wavelengths approximately equal to model length and increased at lower and higher wavelengths.

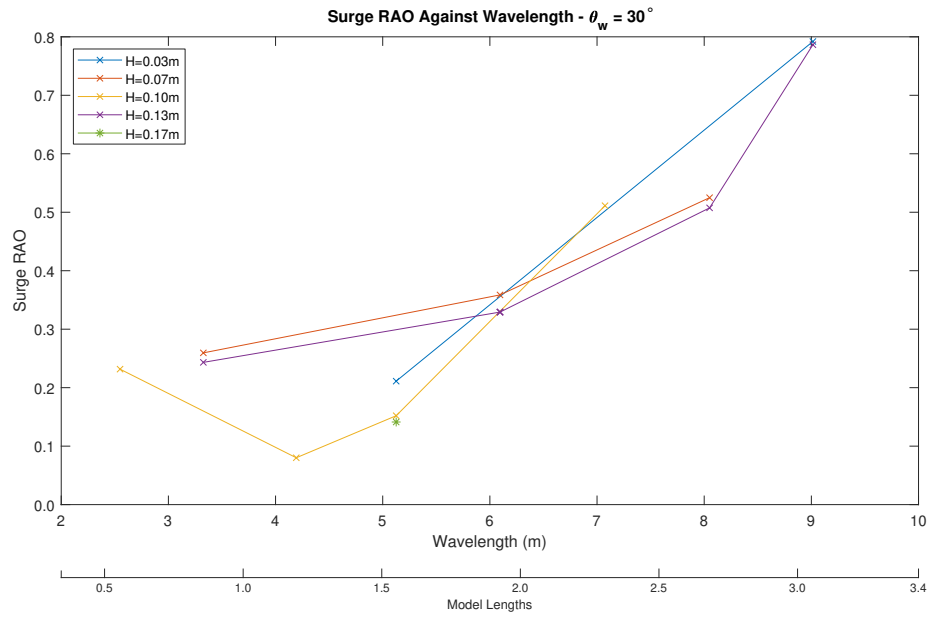
Figure 6.13 shows the heave RAO to regular waves for  $\theta_w = 30^\circ$  against wave period, Figure 6.13a, and against wavelength, Figure 6.13b. Figures 6.13a and 6.13b show that the lowest RAO occurred when the wave period was also low. The heave RAO was highest at periods of 2.19 s and 2.37 s before becoming slightly lower at the highest tested period of 2.55 s. The RAO showed little variation with wave height, as expected.

Figure 6.14 shows the pitch response to regular waves for  $\theta_w = 30^\circ$  against wave period, Figure 6.14a, and against wavelength, Figure 6.14b. Figures 6.14a and B.11b show that in general a lower wave period, and thus wavelength, resulted in a higher pitch response. The exception was at the lowest tested period, where the wavelength was approximately equal to the model length. When the wave height was increased the pitch response also increased.

Figure 6.15 shows the pitch RAO for  $\theta_w = 30^\circ$  against wave period, Figure 6.15a, and against wavelength, Figure 6.15b. Figure 6.15a shows that when  $T_p$  was low the pitch RAO was also low, however the pitch RAO quickly rose when  $T_p$  increased. There was a slight dip in pitch RAO the higher  $T_p$  became before it rose again.

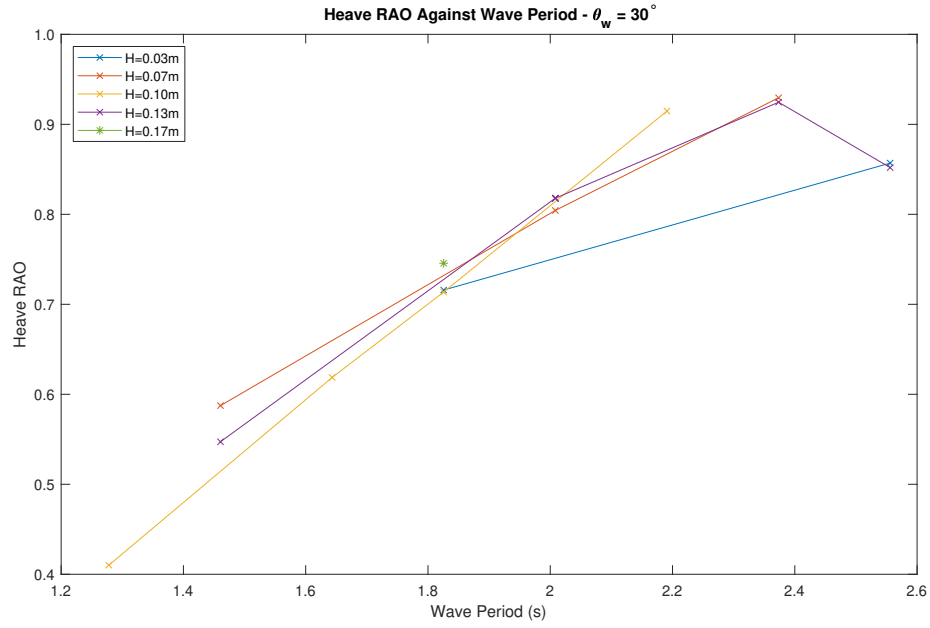


(a) Surge RAO against wave period for  $\theta_w = 30^\circ$

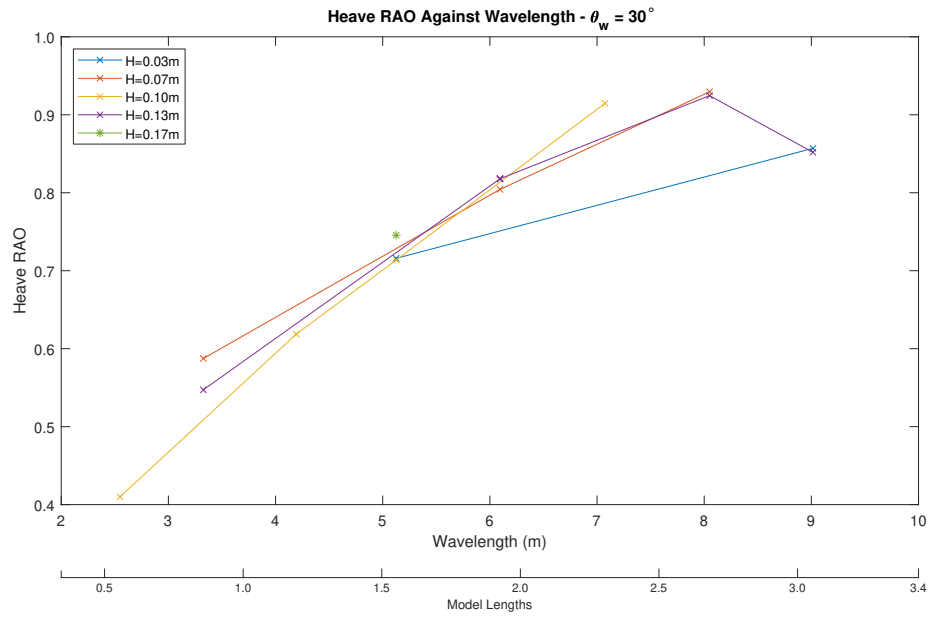


(b) Surge RAO against wavelength and model length for  $\theta_w = 30^\circ$

FIGURE 6.12: Surge RAO against wave period, wavelength and model length for  $\theta_w = 30^\circ$

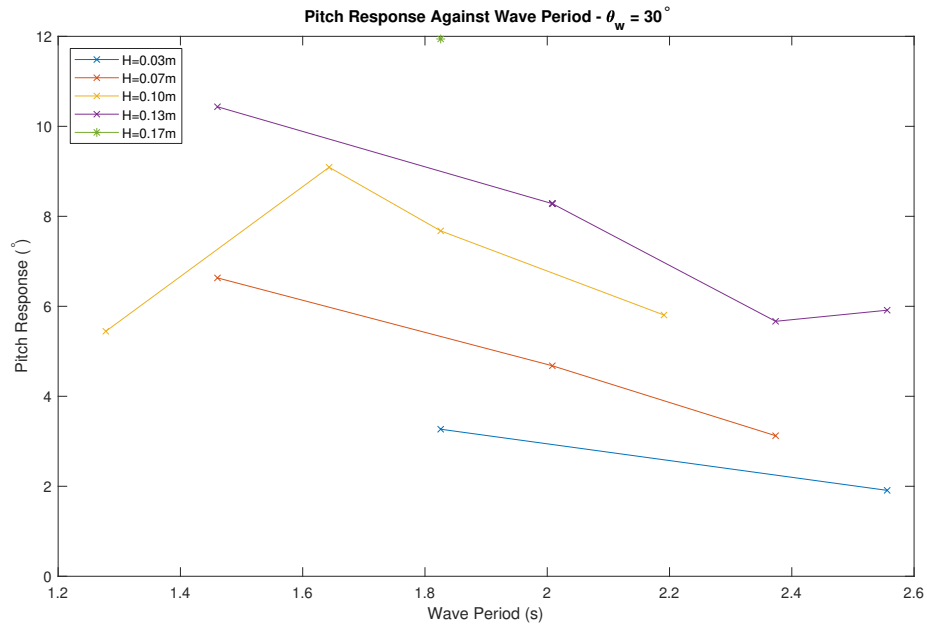


(a) Heave RAO against wave period for  $\theta_w = 30^\circ$

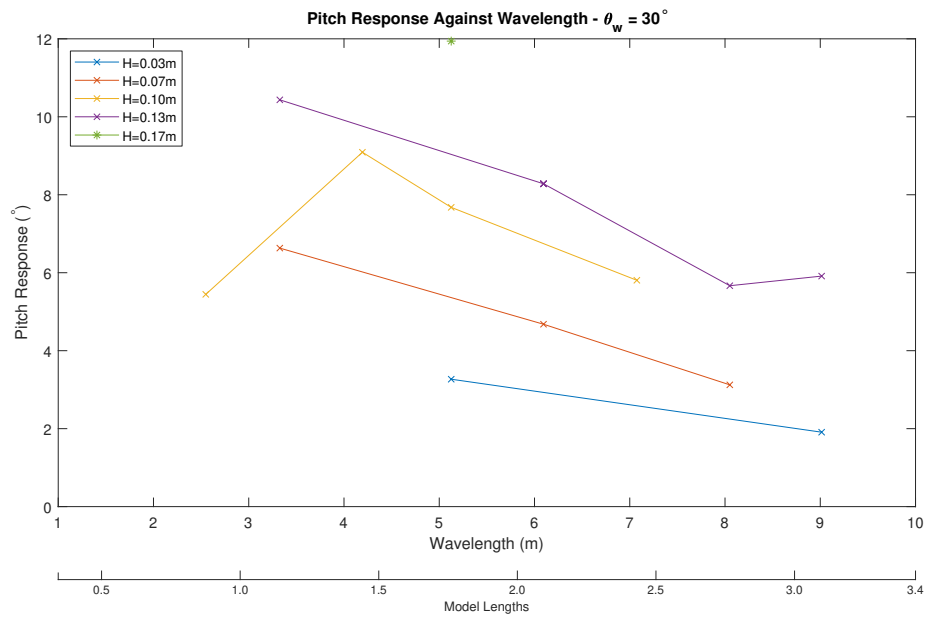


(b) Heave RAO against wavelength and model length for  $\theta_w = 30^\circ$

FIGURE 6.13: Heave RAO against wave period, wavelength and model length for  $\theta_w = 30^\circ$

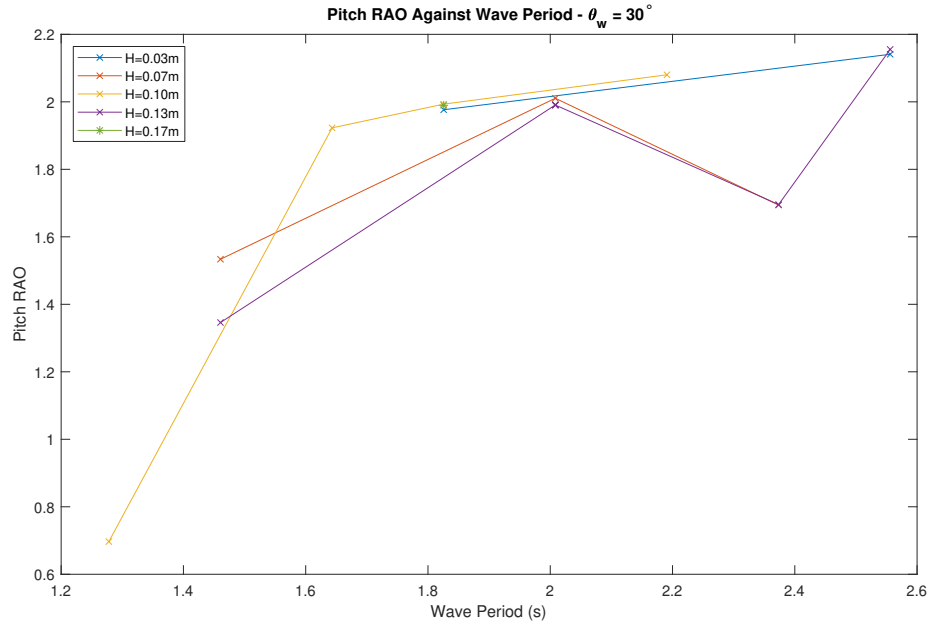


(a) Pitch response against wave period for  $\theta_w = 30^\circ$

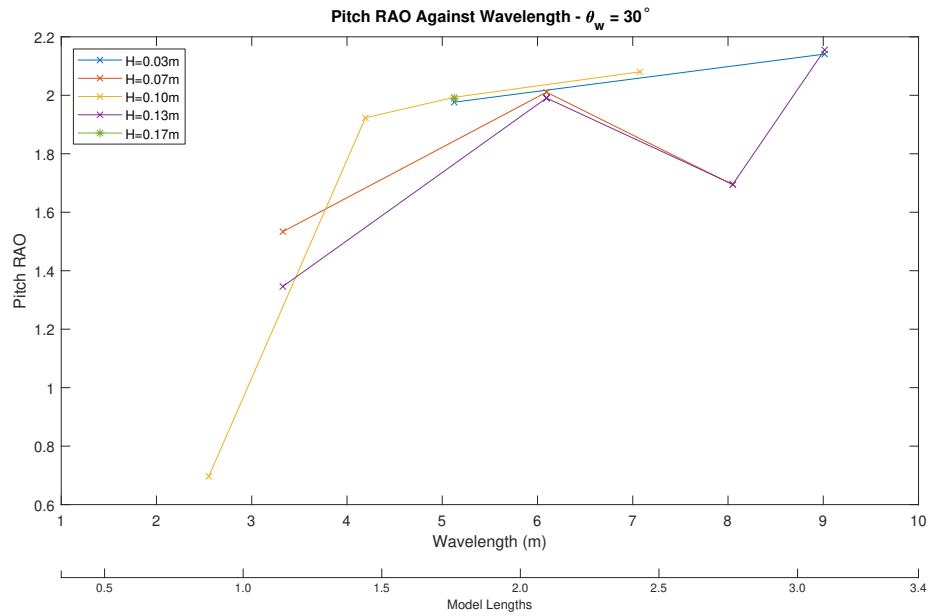


(b) Pitch response against wavelength and model length for  $\theta_w = 30^\circ$

FIGURE 6.14: Pitch response against wave period, wavelength and model length for  $\theta_w = 30^\circ$



(a) Pitch RAO against wave period for  $\theta_w = 30^\circ$



(b) Pitch RAO against wavelength and model length for  $\theta_w = 30^\circ$

FIGURE 6.15: Pitch RAO against wave period, wavelength and model length for  $\theta_w = 30^\circ$

When comparing the pitch RAO to wavelength, Figure 6.15b, it is shown that the rise in pitch RAO happened when the wavelength became longer than one model length, peaked at two model lengths and dipped at higher wavelengths.

## 6.2.2 Responses to Random Waves

The responses to the primary degrees of freedom of the device in random waves were also measured. Heave, surge and pitch spectra were plotted with respect to frequency along with the incident wave surface elevation spectrum from Section 5.2.1.

Figure 6.16 shows the response spectra as functions of frequency along with the incident wave spectrum of a test with  $H_s = 0.15$  m and  $T_p = 1.46$  s, this was the tested period closest to that of the period associated with the model length. Surge and heave peaked when frequency was just lower than the test frequency. Pitch peaked around the model and test frequency and had a second peak after a dip when the frequency was lower than that of the model frequency.

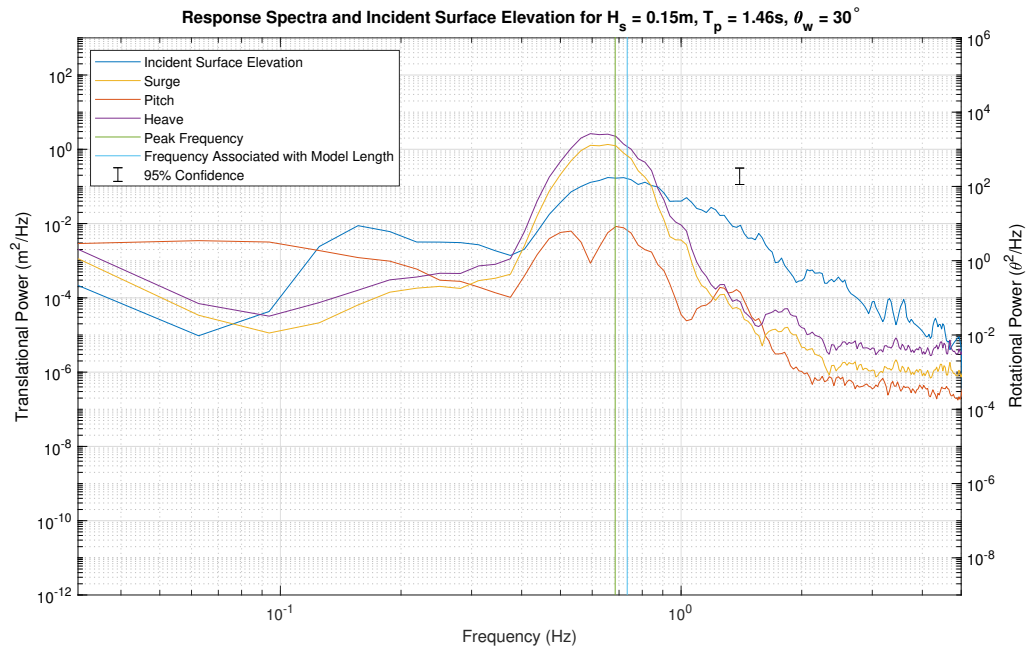


FIGURE 6.16: Spectral analysis of responses to random waves of  $H_s = 0.15$  m,  $T_p = 1.46$  s,  $\theta_w = 30^\circ$ . Incident wave spectrum is shown in blue. Surge, pitch and heave response spectra are shown in orange, yellow and purple respectively

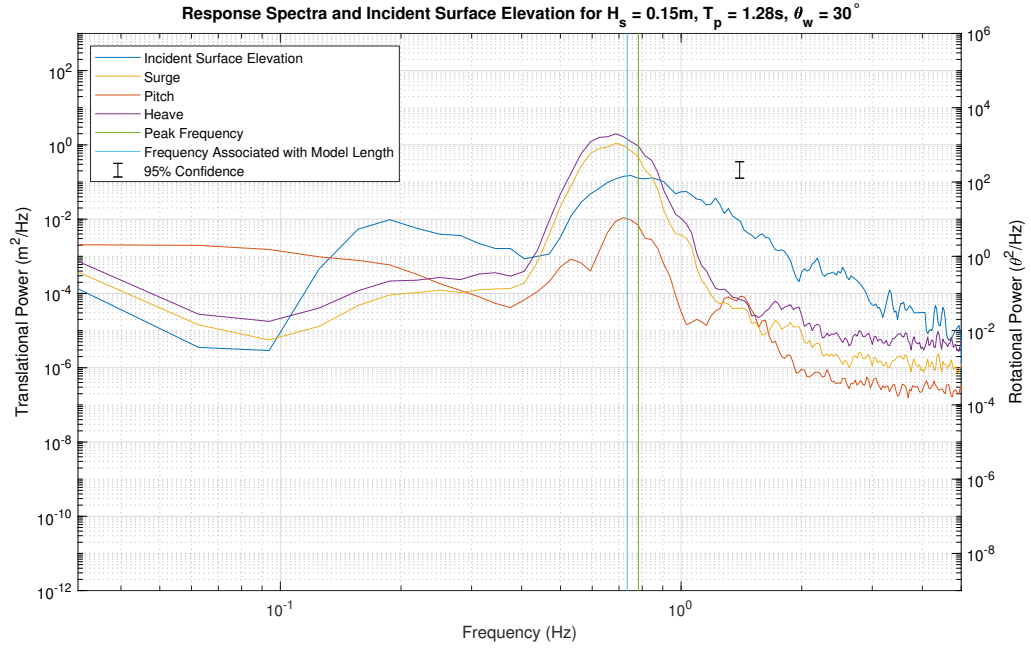


FIGURE 6.17: Spectral analysis of responses to random waves of  $H_s = 0.15$  m,  $T_p = 1.28$  s,  $\theta_w = 30^\circ$ . Incident wave spectrum is shown in blue. Surge, pitch and heave response spectra are shown in orange, yellow and purple respectively

Figure 6.17 shows the response spectra as functions of frequency along with the incident wave spectrum of a test with  $H_s = 0.15$  m and  $T_p = 1.28$  s, this was the tested period close to that of the period associated with the model length and the lowest tested at  $\theta_w = 30^\circ$ . The surge and heave responses peaked just below the tested frequency, and pitch peaked at the tested frequency before also dropping as the frequency increased.

Figure 6.18 shows the response spectra as functions of frequency along with the incident wave spectrum of a test with  $H_s = 0.15$  m and  $T_p = 2.56$  s. This test represents the highest period tested for  $\theta_w = 30^\circ$ . The surge and heave responses reached their highest response level at a frequency just below that of the test frequency. They maintained that level of response until the frequency associated with the model length was reached, at which point the responses fell. The pitch response also peaked just lower than the test frequency, however it then dropped when the frequency was between that of the peak frequency and the frequency associated with the model length. When the frequency approached the model frequency the pitch showed a smaller secondary peak in response.



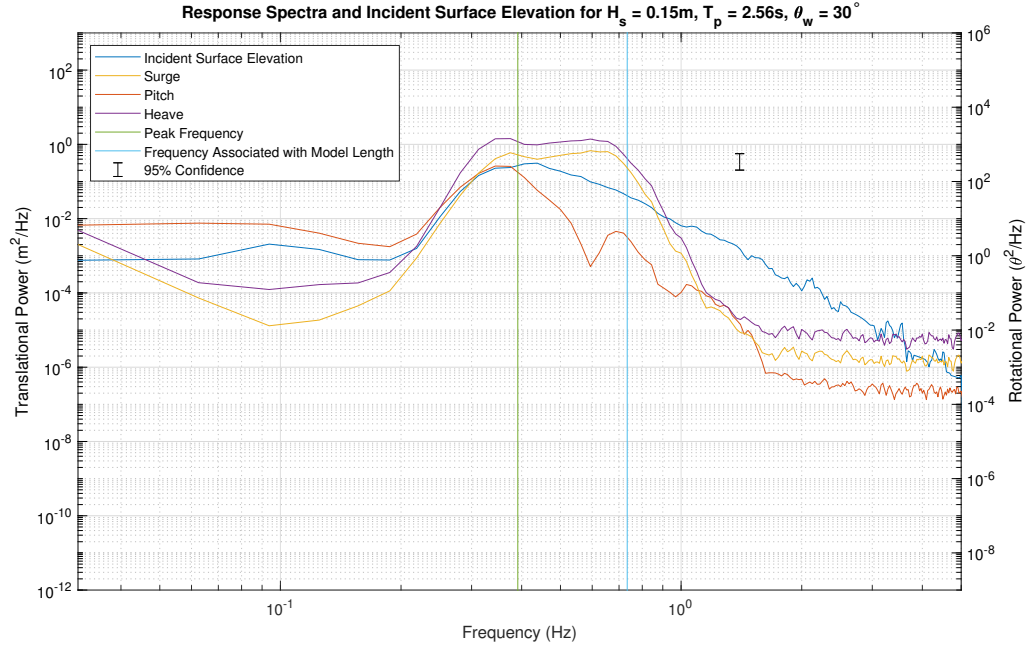


FIGURE 6.18: Spectral analysis of responses to random waves of  $H_s = 0.15$  m,  $T_p = 2.56$  s,  $\theta_w = 30^\circ$ . Incident wave spectrum is shown in blue. Surge, pitch and heave response spectra are shown in orange, yellow and purple respectively

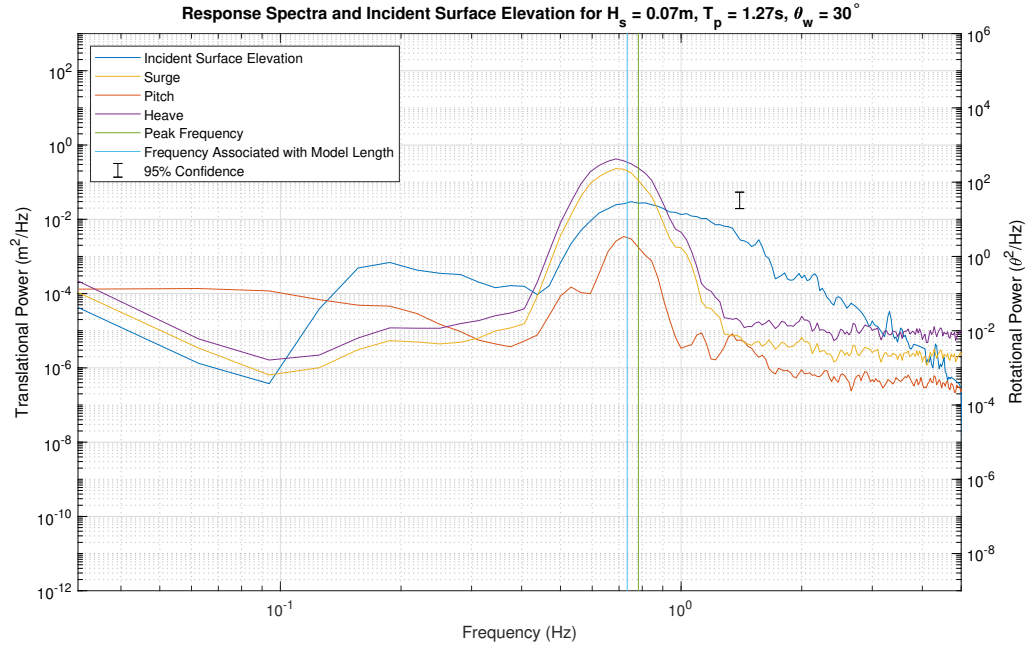


FIGURE 6.19: Spectral analysis of responses to random waves of  $H_s = 0.07$  m,  $T_p = 1.28$  s,  $\theta_w = 30^\circ$ . Incident wave spectrum is shown in blue. Surge, pitch and heave response spectra are shown in orange, yellow and purple respectively

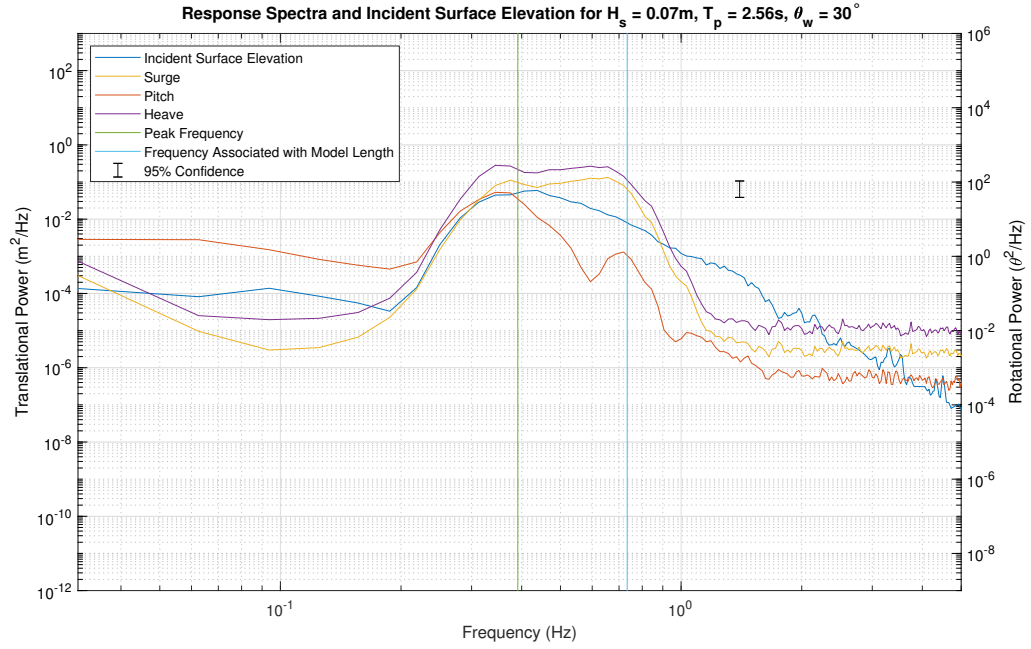


FIGURE 6.20: Spectral analysis of responses to random waves of  $H_s = 0.07$  m,  $T_p = 2.56$  s,  $\theta_w = 30^\circ$ . Incident wave spectrum is shown in blue. Surge, pitch and heave response spectra are shown in orange, yellow and purple respectively

Figure 6.19 shows the response spectra as functions of frequency along with the incident wave spectrum of a test with  $H_s = 0.07$  m and  $T_p = 1.28$  s. This was the same period as Figure 6.17 but with a lower wave height. The trends shown in the test with higher wave height were also present in this test. The surge and heave responses peaked just below the tested frequency, and pitch peaked at the tested frequency before also dropping as the frequency increased.

Figure 6.20 shows the response spectra as functions of frequency along with the incident wave spectrum of a test with  $H_s = 0.07$  m and  $T_p = 2.56$  s. This was the same period as Figure 6.18 but with a lower wave height. The trends shown at the higher wave height were followed in the test with the lower wave height. The surge and heave were approximately constant between peak frequency and model frequency and the pitch showed a peak at peak test frequency, a smaller secondary peak at model frequency and a dip in between.

The variance of surge, pitch and heave was calculated using Equation 4.23 and normalised for each response. Scatter plots of the normalised response compared to the wave conditions were produced.

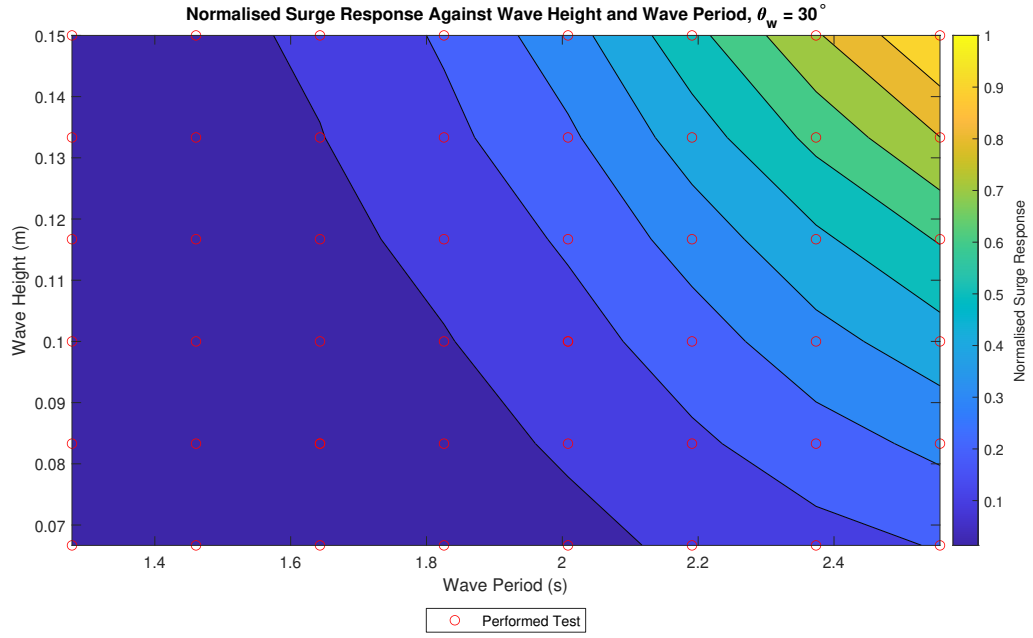


FIGURE 6.21: Scatter plot of normalised surge response against random wave conditions for  $\theta_w = 30^\circ$  model configuration

Figure 6.21 shows the scatter plot of normalised surge response against  $H_s$  and  $T_p$ . The surge response was highest when both  $H_s$  and  $T_p$  were high. The surge response was lowest when the  $H_s$  and  $T_p$  were both low.

Figure 6.22 shows the scatter plot of normalised pitch response against  $H_s$  and  $T_p$ . The pitch response was highest when  $H_s$  was high, but only when the  $T_p$  was above that of the model period. The pitch response was low when  $T_p$  was low, regardless of the  $H_s$ , and also low when  $H_s$  was low.

Figure 6.23 shows the scatter plot of normalised heave response against  $H_s$  and  $T_p$ . The heave response was highest when both  $H_s$  and  $T_p$  were high. The heave response was lowest when the  $H_s$  and  $T_p$  were both low.

### 6.3 Comparison of $\theta_w$

Changing the wedge angle between  $60^\circ$  and  $30^\circ$  altered the device profile in the water and thus altered the response to the incident waves. Primarily, the length of the model relative to the wave direction was longer when the wedge angle was smaller,

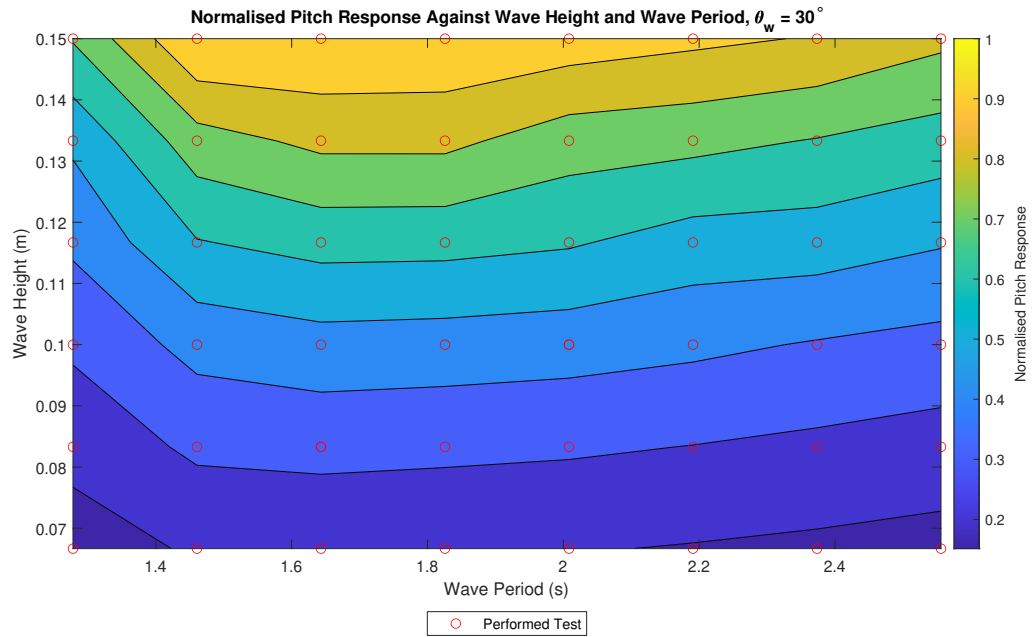


FIGURE 6.22: Scatter plot of normalised pitch response against random wave conditions for  $\theta_w = 30^\circ$  model configuration

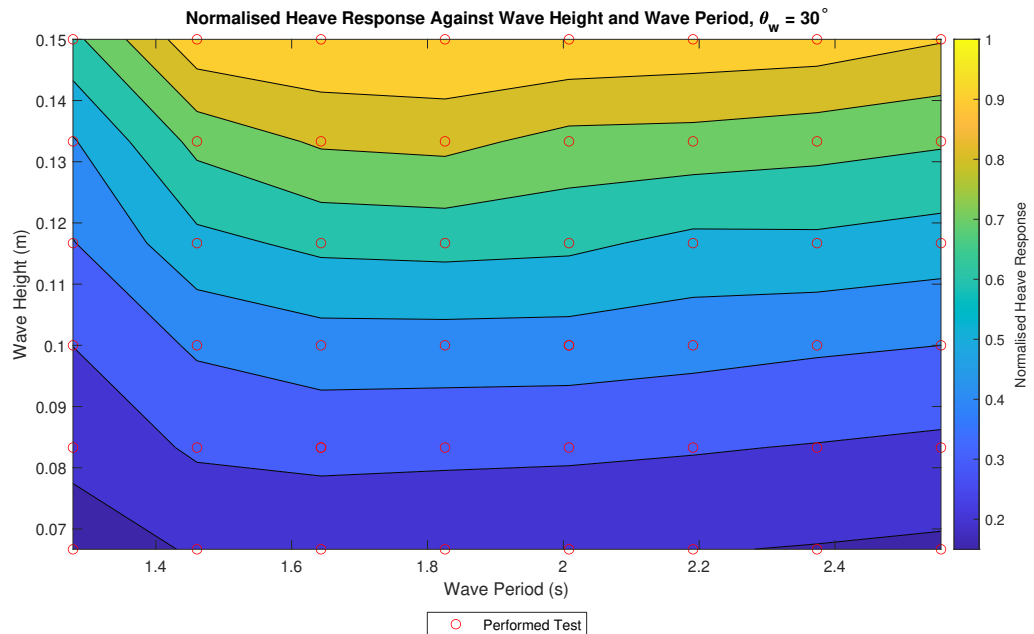


FIGURE 6.23: Scatter plot of normalised heave response against random wave conditions for  $\theta_w = 30^\circ$  model configuration

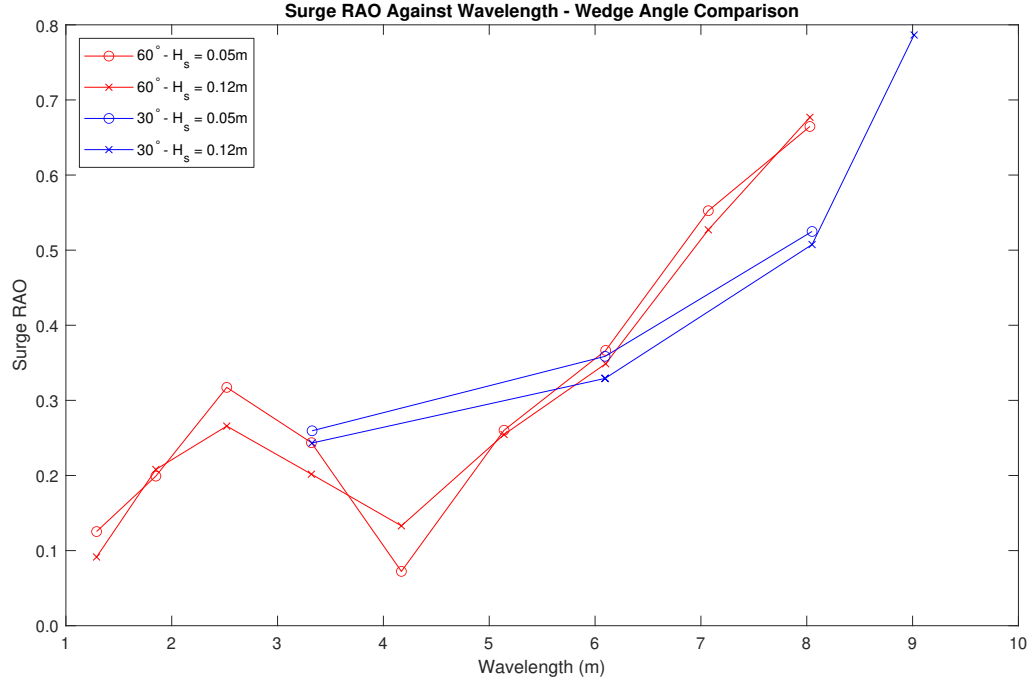


FIGURE 6.24: Comparison of surge RAOs for 60° and 30° conditions

as shown in Equation 4.1. This meant that waves of the same period have different model length per wavelength values between wedge angles.

The surge RAO shows a similar trend between 60° and 30° tests, plotted together in Figure 6.24. Both configurations showed higher surge RAO as wavelength increased. Both configurations were mostly independent of wave height, as the data points were very close together between wave heights. Further testing of the 30° configuration is needed to observe whether it matched the 60° trends at lower wavelengths.

The pitch RAO, shown in Figure 6.25, shows tests with a low  $H_s$  and a high  $H_s$  for both 60° and 30° wedge angles. The peak in pitch was at a higher wavelength for the 30° configuration than that of the 60° configuration. This was likely due to the effective length of the model being longer for 30° tests meaning the model wavelength was longer. Further testing of the 30° configuration is needed to observe whether it matched the 60° trends at lower wavelengths.

The heave RAO shows similar trends between 60° and 30° tests as well, plotted together in Figure 6.26. The heave started low for both cases before rising steadily to their maximum values when the wavelength was approximately three model lengths.

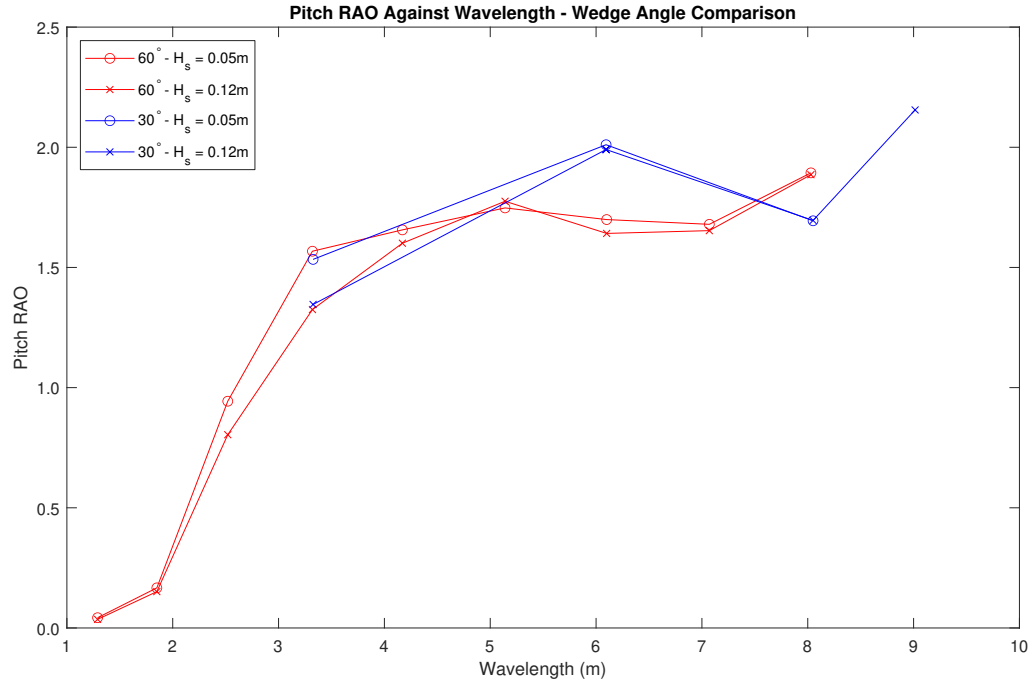


FIGURE 6.25: Comparison of Pitch responses for 60° and 30° conditions

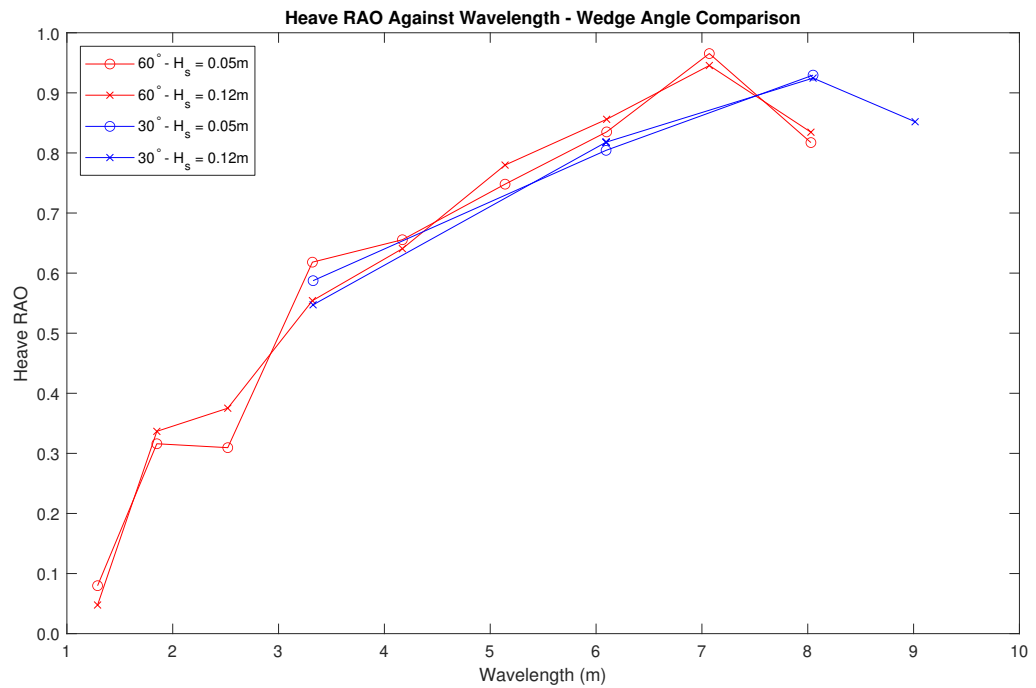


FIGURE 6.26: Comparison of heave RAOs for 60° and 30° conditions

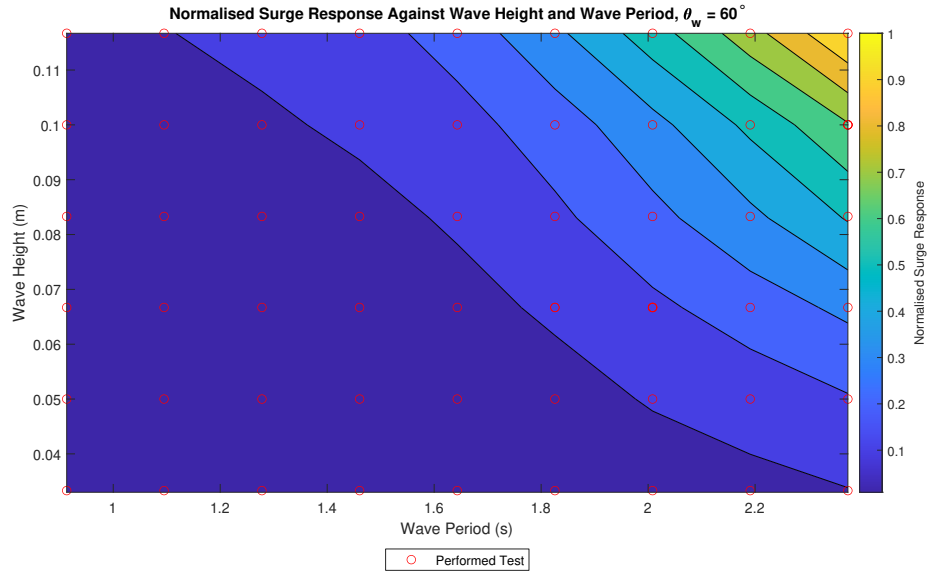
Both configurations then showed a small drop in heave at the tests performed where the wavelength was above three model lengths. The 60° configuration showed a sharper drop at higher wave periods compared to the 30° configuration, whereas at lower wave periods the two trends were very similar.

The comparisons show that further testing of the 30° configuration at low wave periods would be useful to confirm whether it followed the trend for the 60° configuration. Overall wedge angle difference has the effect of moving the peak in heave and pitch to a longer wavelength to compensate for a longer effective model length.

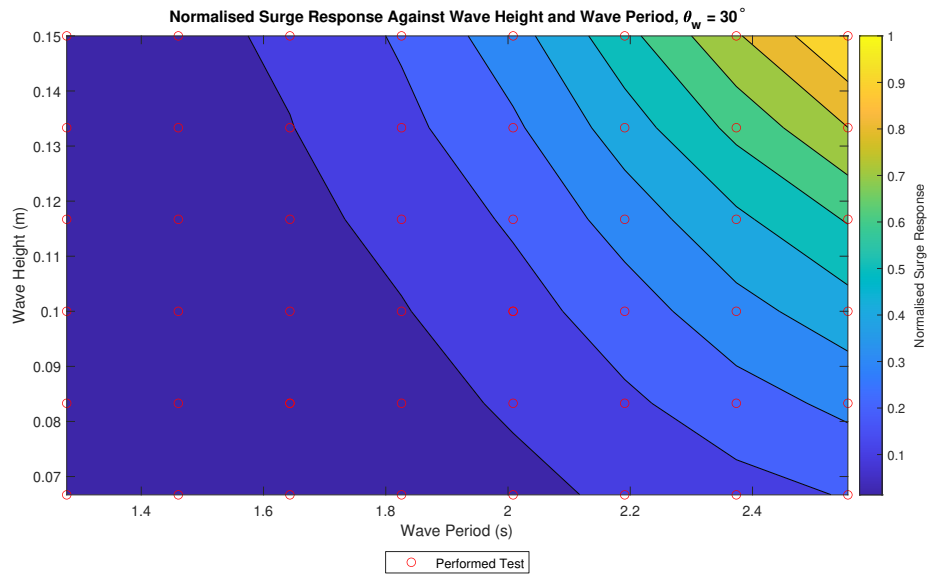
The surge response of the device to random waves was also similar between configurations, as shown in Figure 6.27, with both configurations showing the highest response when wave height and wave period were also highest. The 60° configuration retained a slightly higher surge response as wave period became lower compared to the 30° configuration. This was likely due to a wider angle causing a smaller change in the effective length of model compared to the wavelength.

The pitch response to random waves was also similar between configurations, as shown in Figure 6.28. Both configurations showed the highest response in the tests where  $T_p$  was over 1.46 s. At wave periods higher than this value the response was approximately constant with wave height, showing a regime change from period dependent to height dependent. It is shown that for the 60° configuration the pitch response was low when the wave period was low. It is recommended to perform further tests on the 30° configuration at low wave periods to determine whether the 30° configuration also experienced this reduction in pitch response at low wave period.

The heave responses between configurations were different, as shown in Figure 6.29. For the 60° configuration the heave response followed the same trend as the surge response, the highest heave response was in the test with the highest wave height and wave period. The 30° configuration however, showed the heave response resembles the pitch response more closely. It had the highest response when the wave period was representative of waves that were longer than one model length, and at wave



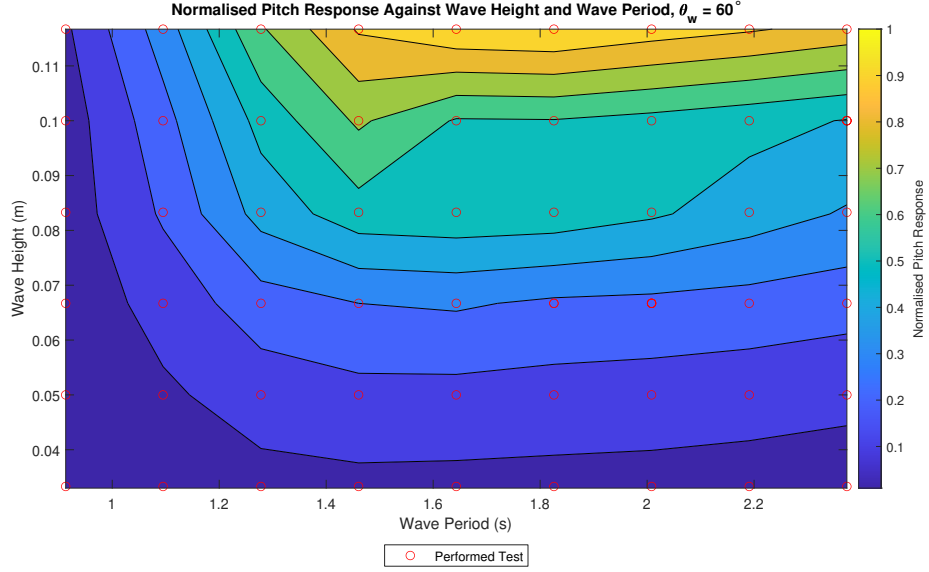
(a) Normalised surge response  $H_s$  and  $T_p$  for  $\theta_w = 60^\circ$  (repeated from page 161)



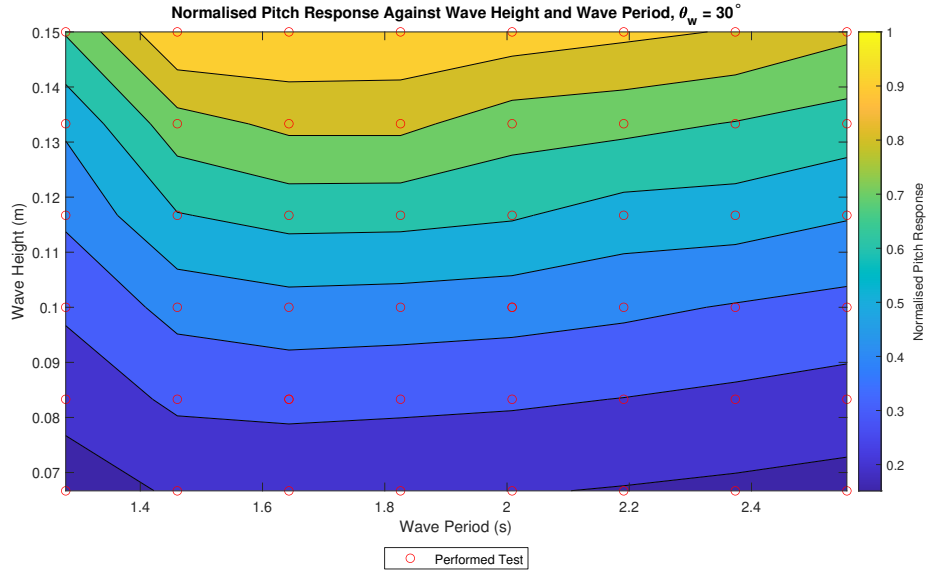
(b) Normalised surge response  $H_s$  and  $T_p$  for  $\theta_w = 30^\circ$  (repeated from page 172)

FIGURE 6.27: Scatter plots of normalised surge responses to random waves of  $60^\circ$  configuration, above, and  $30^\circ$  configuration, below



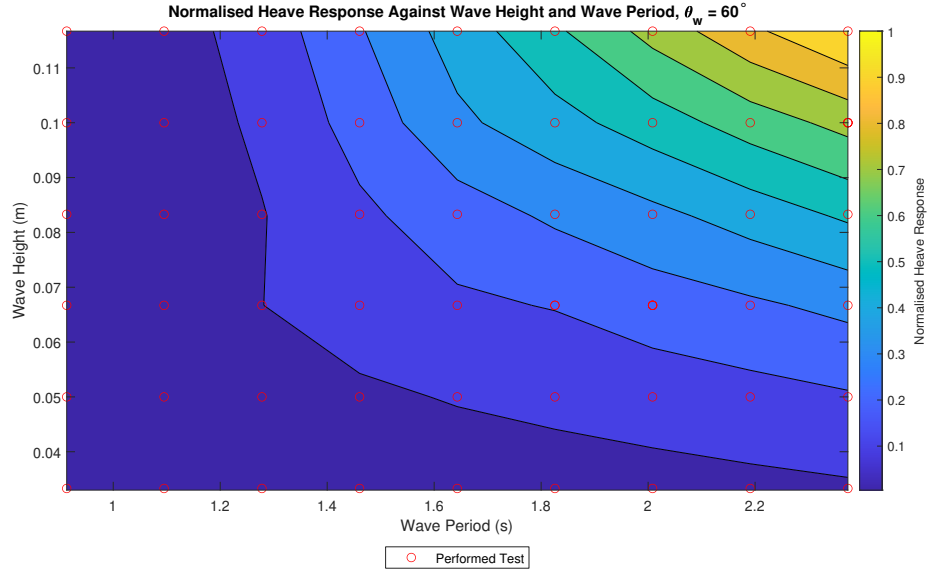


(a) Normalised pitch response against  $H_s$  and  $T_p$  for  $\theta_w = 60^\circ$  (repeated from page 162)

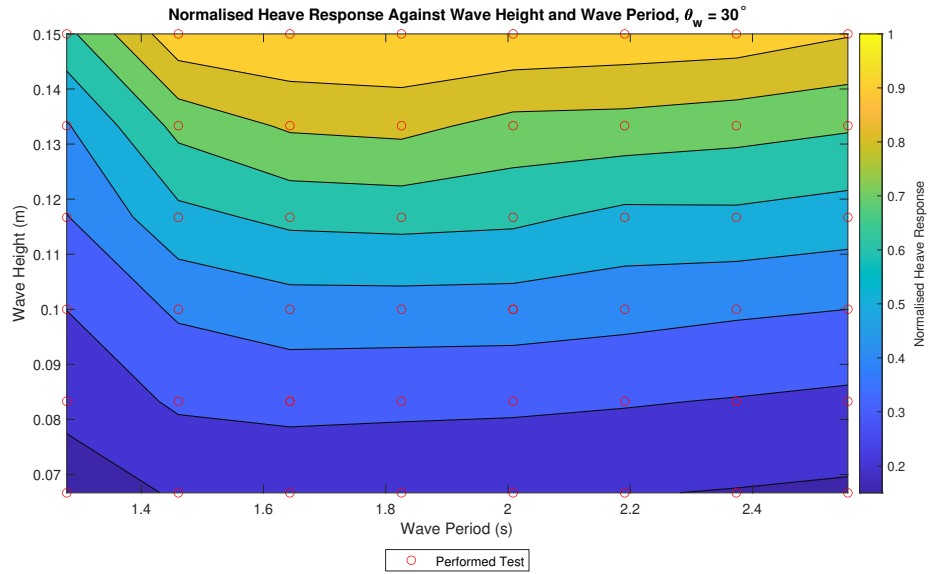


(b) Normalised pitch response against  $H_s$  and  $T_p$  for  $\theta_w = 30^\circ$  (repeated from page 173)

FIGURE 6.28: Scatter plots of normalised pitch responses to random waves of  $60^\circ$  configuration, above, and  $30^\circ$  configuration, below



(a) Normalised heave response against  $H_s$  and  $T_p$  for  $\theta_w = 60^\circ$  (repeated from page 162)



(b) Normalised heave response against  $H_s$  and  $T_p$  for  $\theta_w = 30^\circ$  (repeated from page 173)

FIGURE 6.29: Scatter plots of normalised heave responses to random waves of  $60^\circ$  configuration, above, and  $30^\circ$  configuration, below

periods above this value the response was more wave height dependent than wave period dependent.

The random wave responses generally followed the trends shown in the device responses to regular waves, however there were small differences in the heave response for the 30° configuration. This was likely due to the random waves being made up of a combination of frequencies that interacted with each other in the wedge, whereas the regular waves are one frequency with limited interaction.

## 6.4 Comparison to Other Devices

Nielsen and Kofoed (1997) showed the heave RAO of the basin section of the Wave Dragon between wave periods of 5 s and 19 s calculated through numerical modelling. The heave RAO compares similarly to the WaveCat, shown in Figure 6.2, in that both devices show a low RAO at small periods, on the order of 0.2. The Wave Dragon heave RAO rose to 1 at wave periods of 15 s and above, where the WaveCat reached a heave RAO of approximately 1 at a wave period of 12 s when scaled up to full scale.

Martinelli and Frigaard (1999) showed that by allowing the Wave Dragon model to freely float the overtopping discharge compared to a fixed model was reduced by up to 50%. The tests showed that the movement should be minimised to make the reduction as small as possible. However, tests on the Power Pyramid (Kofoed et al., 2002) showed little to no reduction in the overtopping discharge of a floating model compared to fixed tests. This suggests that the reduction due to movement is dependant on the device structure itself.

The WaveCat experiences the most overtopping discharge when the wave period is low, and the wave height is high. The conditions in which it is most effective correspond to conditions in which the device shows smaller response to incoming wave excitation. This implies that the behaviour of the WaveCat in its current form is more similar to that of the Wave Dragon than that of the Power Pyramid.

Interaction between waves of different frequencies must be considered however, as the WaveCat and Wave Dragon are redirecting waves towards overtopping chambers there is potential for constructive interference between waves of different speeds.

From the conclusions drawn by Martinelli and Frigaard (1999) subsequent versions of the Wave Dragon attempted to reduce motions, as shown in Hald and Lynggaard (2001), which also increased the overtopping volumes. This was achieved by adding ballast and increasing mooring forces.

Future iterations of the WaveCat development can focus on optimising motion to improve overtopping volumes, this could be achieved by adding more ballast thus lowering the device and in turn reducing freeboard. Another method to reduce motions for the WaveCat would be to make the device longer relative to the incident waves, the results presented in this thesis show that when the wavelength of the waves are less than the length of the model the motions are greatly reduced.

# Chapter 7

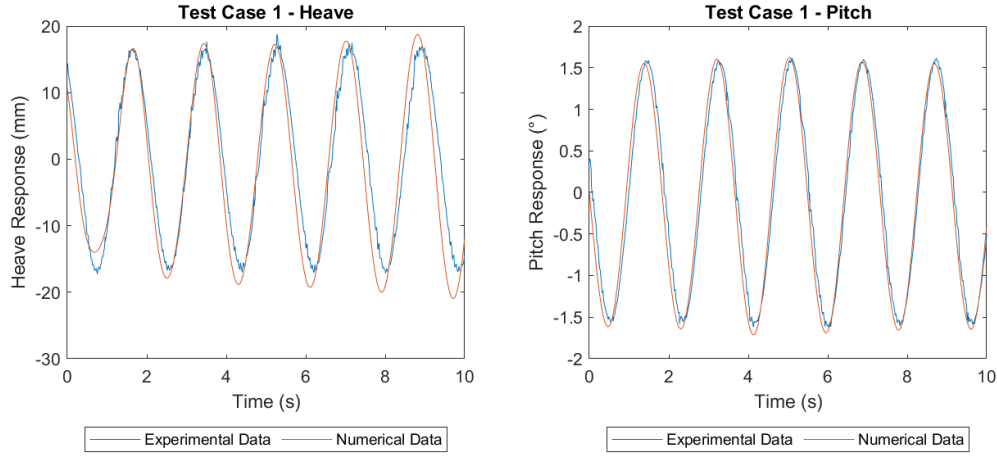
## Numerical Modelling Results

### 7.1 Introduction

The STAR-CCM+ simulations for the WaveCat output time series of pitch and heave, which were then compared to experimental model results during matching input conditions as a measure of how well the numerical model reproduces to physical modelling.

Numerical model results here are used to illustrate both the similarity with physical models, and also some of the shortcomings. This may be useful for developers in scaling up the models, and for exploring different wave conditions or model configurations when physical modelling is not available or parameters are difficult to measure experimentally.

Test conditions outlined in Table 3.2 were simulated and device response in y-rotation, pitch, and z-translation, heave, measured. The tests were performed on workstation PCs, the relevant hardware specifications, and subsequent test run times, are shown in Table A.15. The computational output was time adjusted to take into account differing wave generation points and compared with experimental data from tests of the same wave conditions.



(a) Experimental and numerical heave response for test case 1 (b) Experimental and numerical pitch response for test case 1

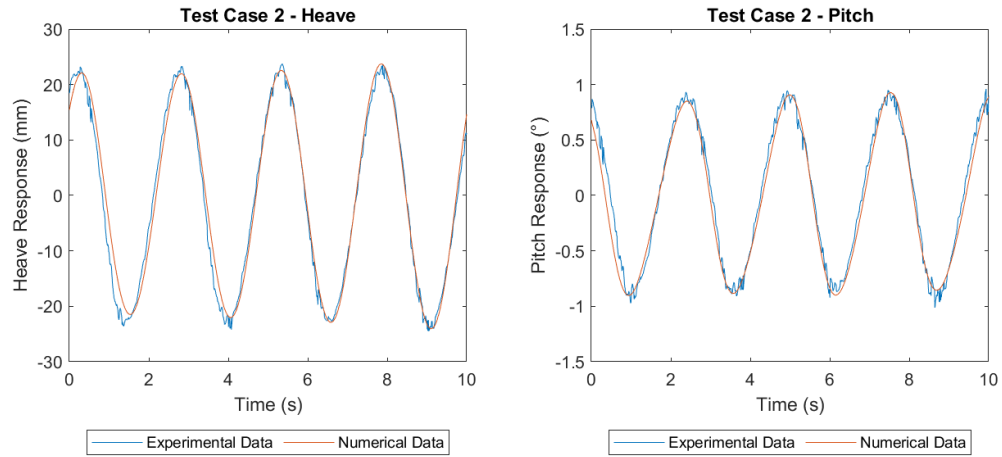
FIGURE 7.1: Experimental and numerical responses for heave and pitch under test case 1 conditions

## 7.2 Results

Figure 7.1 shows the numerical and experimental results for pitch and heave during test case 1. Figure 7.1a shows the heave results and Figure 7.1b shows the pitch results. The numerical heave closely matched the experimental heave during the tests, both showing responses of approximately 30 mm from a 50 mm incident wave. The numerical pitch also closely matched the experimental pitch, showing a response of approximately  $3^\circ$ .

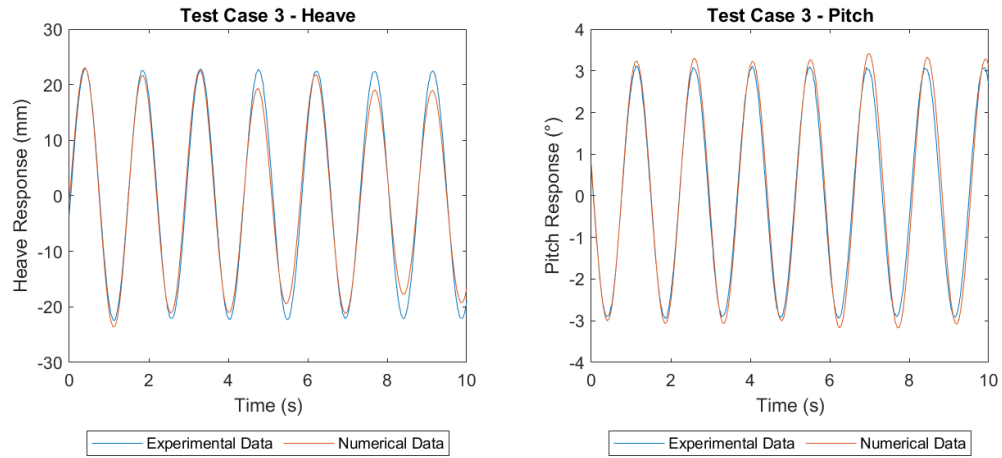
Figure 7.2 shows the numerical and experimental results for pitch and heave during test case 2. Figure 7.2a shows the heave results and Figure 7.2b shows the pitch results. The numerical heave closely matched the experimental heave during the tests, both showing responses of approximately 40 mm from a 50 mm incident wave. The numerical pitch also closely matched the experimental pitch, showing a response of approximately  $2^\circ$ .

Figure 7.3 shows the numerical and experimental results for pitch and heave during test case 3. Figure 7.3a shows the heave results and Figure 7.3b shows the pitch results. The numerical heave closely matched the experimental heave during the



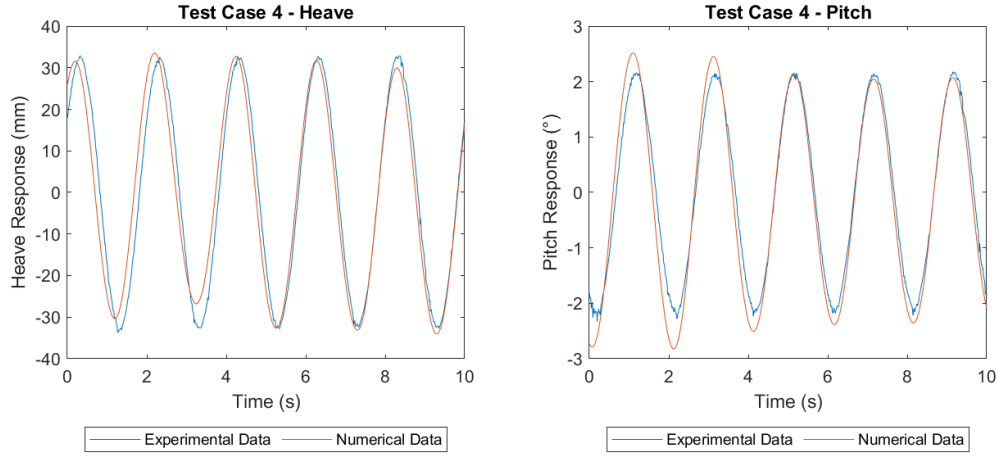
(a) Experimental and numerical heave response for test case 2 (b) Experimental and numerical pitch response for test case 2

FIGURE 7.2: Experimental and numerical responses for heave and pitch under test case 2 conditions



(a) Experimental and numerical heave response for test case 3 (b) Experimental and numerical pitch response for test case 3

FIGURE 7.3: Experimental and numerical responses for heave and pitch under test case 3 conditions



(a) Experimental and numerical heave response for test case 4 (b) Experimental and numerical pitch response for test case 4

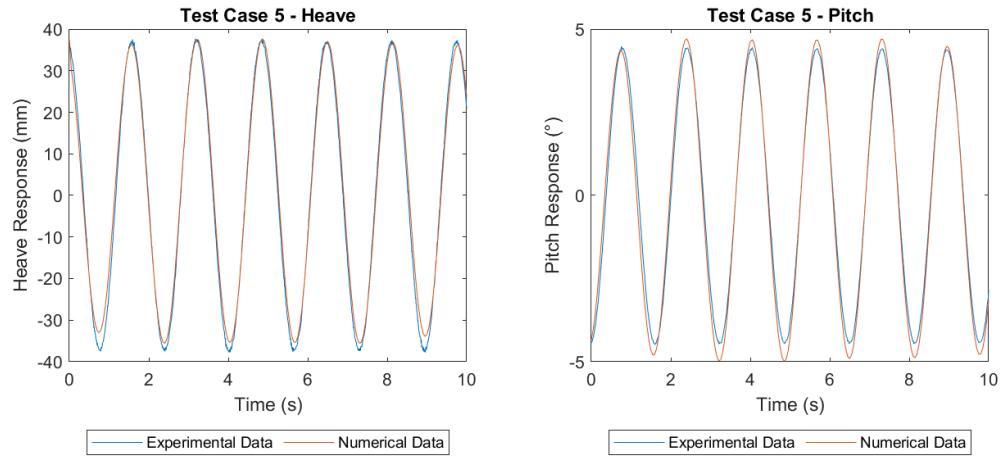
FIGURE 7.4: Experimental and numerical responses for heave and pitch under test case 4 conditions

tests, both showing responses of approximately 40 mm from a 83 mm incident wave. The numerical pitch also closely matched the experimental pitch, showing a response of approximately  $6^\circ$ .

Figure 7.4 shows the numerical and experimental results for pitch and heave during test case 4. Figure 7.4a shows the heave results and Figure 7.4b shows the pitch results. The numerical heave closely matched the experimental heave during the tests, both showing responses of approximately 60 mm from a 83 mm incident wave. The numerical pitch initially was higher than the experimental pitch but closely matched the experimental pitch by the end of the test window, showing a response of approximately  $4^\circ$ .

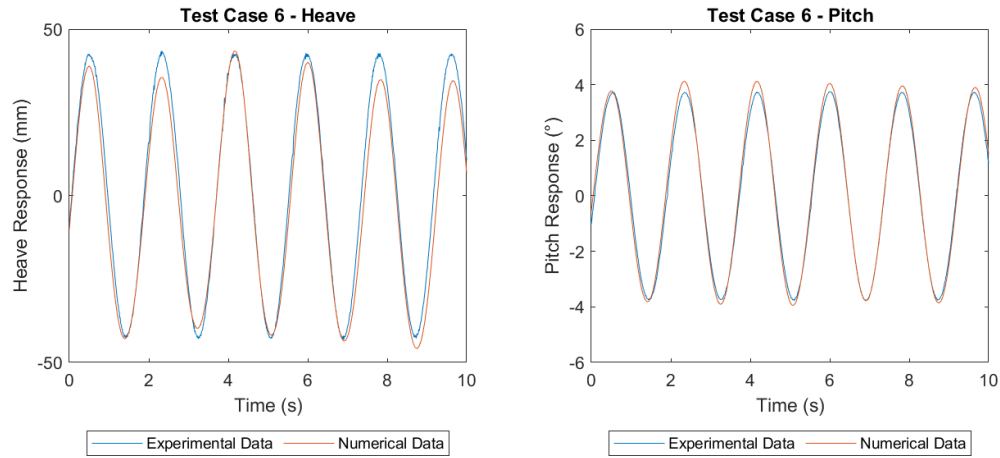
Figure 7.5 shows the numerical and experimental results for pitch and heave during test case 5. Figure 7.5a shows the heave results and Figure 7.5b shows the pitch results. The numerical heave closely matched the experimental heave during the tests, both showing responses of approximately 70 mm from a 117 mm incident wave. The numerical pitch also closely matched the experimental pitch, showing a response of approximately  $10^\circ$ .





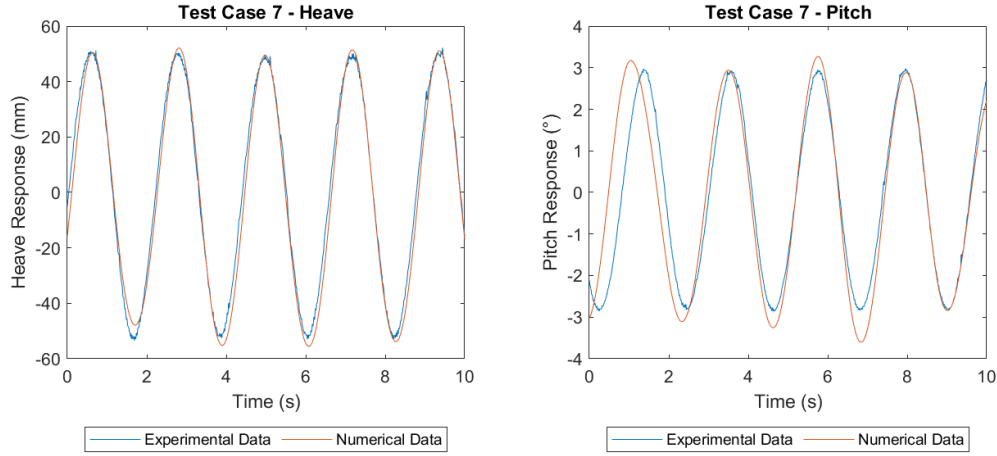
(a) Experimental and numerical heave response for test case 5  
(b) Experimental and numerical pitch response for test case 5

FIGURE 7.5: Experimental and numerical responses for heave and pitch under test case 5 conditions



(a) Experimental and numerical heave response for test case 6  
(b) Experimental and numerical pitch response for test case 6

FIGURE 7.6: Experimental and numerical responses for heave and pitch under test case 6 conditions



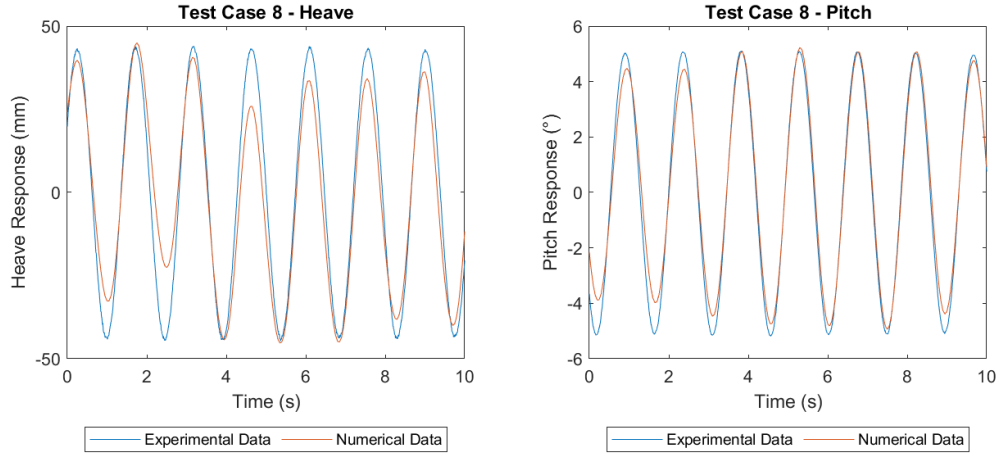
(a) Experimental and numerical heave response for test case 7 (b) Experimental and numerical pitch response for test case 7

FIGURE 7.7: Experimental and numerical responses for heave and pitch under test case 7 conditions

Figure 7.6 shows the numerical and experimental results for pitch and heave during test case 6. Figure 7.6a shows the heave results and Figure 7.6b shows the pitch results. The numerical heave closely matched the experimental heave during the tests, both showing responses of approximately 60 mm from a 117 mm incident wave. The numerical pitch also closely matched the experimental pitch, showing a response of approximately  $8^\circ$ .

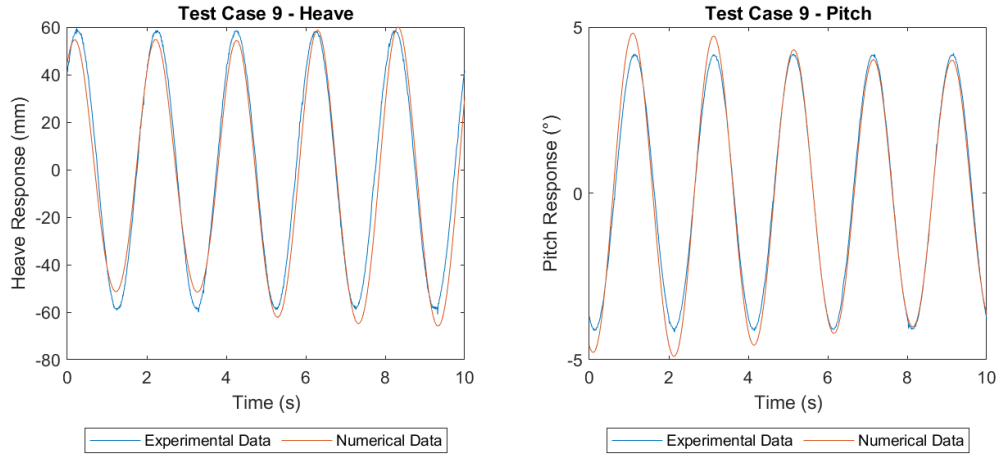
Figure 7.7 shows the numerical and experimental results for pitch and heave during test case 7. Figure 7.7a shows the heave results and Figure 7.7b shows the pitch results. The numerical heave closely matched the experimental heave during the tests, both showing responses of approximately 100 mm from a 117 mm incident wave. The numerical pitch also closely matched the experimental pitch, showing a response of approximately  $6^\circ$ .

Figure 7.8 shows the numerical and experimental results for pitch and heave during test case 8. Figure 7.8a shows the heave results and Figure 7.8b shows the pitch results. The numerical heave matched the experimental heave peak and trough during the tests, however does not exhibit a consistent regular wave, both showing maximum responses of approximately 80 mm from a 150 mm incident wave. The



(a) Experimental and numerical heave response for test case 8 (b) Experimental and numerical pitch response for test case 8

FIGURE 7.8: Experimental and numerical responses for heave and pitch under test case 8 conditions



(a) Experimental and numerical heave response for test case 9 (b) Experimental and numerical pitch response for test case 9

FIGURE 7.9: Experimental and numerical responses for heave and pitch under test case 9 conditions

numerical pitch also matched the experimental pitch, showing a response of approximately  $8^\circ$ . This response too has irregularity in the consistency of the peaks and troughs.

Figure 7.9 shows the numerical and experimental results for pitch and heave during test case 9. Figure 7.9a shows the heave results and Figure 7.9b shows the pitch

results. The numerical heave closely matched the experimental heave during the tests, both showing responses of approximately 120 mm from a 150 mm incident wave. The numerical pitch also closely matched the experimental pitch, showing a response of approximately  $9^\circ$ .

TABLE 7.1:  $R^2$  errors for heave and pitch for tested numerical cases

Test Case	$R^2$ Heave	$R^2$ Pitch
1	0.945	0.929
2	0.966	0.970
3	0.962	0.994
4	0.890	0.916
5	0.994	0.970
6	0.966	0.981
7	0.985	0.819
8	0.897	0.978
9	0.972	0.973

The  $R^2$  values for the test cases are given in Table 7.1. Both heave and pitch are reasonably well predicted, with pitch slightly more accurate apart from test case 7. This test has the second longest period tested

## 7.3 Discussion

The above numerical results typically show good similarity with the experimental results. Test cases 1 and 2, the tests with the smallest wave amplitude, show some noise on the experimental measurements for both heave and pitch likely due to the motions being small and close to the accuracy limit of Qualisys. Test cases 4, 6, 7 and 8 show small irregularities in the numerical predictions, which are likely due to the limitation on surge in the numerical model. The test cases where the  $R^2$  values are lowest tend to be those with larger periods, where the responses of the device was largest.

In general, the STAR-CCM+ model was able to replicate the experimental motion to within approximately 5 mm for heave and  $0.2^\circ$  for pitch. This shows that STAR-CCM+ is capable of replicating the physical model conditions.

# Chapter 8

## Summary, Conclusions and Recommendations

### 8.1 Summary

A 1:30 scaled physical model of the WaveCat WEC was designed, developing on previous concept work, with additional advanced control methods and a modified design. The model was tested in the COAST Laboratory Ocean Basin. The goal was to investigate the device performance and response in different wave conditions. The device performance was quantified for both random sea states and regular waves. Reflection and transmission analysis through spectral methods were used to isolate the wave conditions before and after the model to determine the interactions of the WaveCat on the wave field.

The coefficients of reflection ( $k_r$ ), transmission ( $k_t$ ) and absorption ( $k_a$ ) of the WaveCat at  $60^\circ$  and  $30^\circ$  wedge angles were quantified. The model was tested using conditions over a range of significant wave heights and peak wave periods for random waves. Significant wave heights ranged between 0.03 m and 0.12 m for  $60^\circ$  and 0.07 m to 0.15 m at  $30^\circ$  in steps of approximately 0.02 m. Peak wave periods ranged between 0.91 s to 2.37 s for  $60^\circ$  and 1.28 s to 2.56 s in steps of approximately

0.18 s for  $30^\circ$ . The motion response of the WaveCat model was also quantified under the same wave conditions to establish a connection between hydrodynamic forcing, device motion and potential for power generation.

RAOs for the model were measured under regular sinusoidal wave conditions for a range of typical operating conditions. These consisted of significant wave heights of 0.03 m to 0.15 m for  $60^\circ$  and 0.03 m to 0.17 m for  $30^\circ$  in steps of approximately 0.02 m. The peak wave period was 0.91 s to 2.37 s for  $60^\circ$  and 1.28 s to 2.56 s for  $30^\circ$  in steps of approximately 0.18 s.

The heave and pitch motion of the device was modelled in STAR-CCM+ at a  $30^\circ$  wedge angle for a selection of regular wave test cases. The experimental model in these tests was configured with covered tanks, and the numerical model was composed of a solid body in the simulations. The experimental and numerical regular waves tested were between 0.05 m and 0.15 m wave height and 1.46 s to 2.19 s in wave period. At full scale these tests represent between 1.5 m and 4.5 m in wave height and between 8 s and 12 s in wave period.

A summary of key specific results relating to the performance of the WaveCat were:

- The device absorption coefficient and expected power generation was highest during the highest  $H_s$  and lowest  $T_p$  conditions tested for both wedge angle cases.
- During the wave conditions that exhibit highest amount of power captured the device had the lowest motion responses.
- When at a  $60^\circ$  wedge angle the device generated the highest power of 0.4 W during tests of  $H_s = 0.12$  m and  $T_p = 1.09$  s. This is the equivalent of 64.6 kW at full scale conditions of  $H_s = 3.5$  m and  $T_p = 6$  s at the largest waves tested and at wavelengths shorter than that of the model length.
- The  $30^\circ$  wedge angle model did not produce power until  $H_s$  is 0.13 m or greater. This is equivalent to  $H_s = 4.0$  m at full scale.

- When at a  $30^\circ$  wedge angle the device generated the highest power of 1.8 W during tests of  $H_s = 0.15$  m and  $T_p = 1.46$  s. This is the equivalent of 269.2 kW at full scale conditions of  $H_s = 4.5$  m and  $T_p = 8$  s, at the largest waves tested and at wavelengths around that of the model length.
- The CWR of the  $60^\circ$  configuration peaked at 1.5% during tests indicating the greatest efficiency. This occurred in wave conditions of  $H_s$  of 0.08 m and  $T_p$  of 1.09 s.
- The CWR of the  $30^\circ$  configuration peaked at 5.4% during tests indicating the greatest efficiency. This occurred in wave conditions of  $H_s$  of 0.15 m and  $T_p$  of 1.46 s.
- A STAR-CCM+ model of WaveCat was developed. The model was able to predict heave and pitch motion accurately, typically within 5 mm for heave and  $0.2^\circ$  for pitch.

Further conclusions relating to the performance and behaviour of the WaveCat were identified from detailed analysis of the hydrodynamics of the device response as follows.

The reflection coefficient was highest for the WaveCat when the wave height and wave period were small, as the model was blocking the waves and they were reflecting when impinging the vertical walls of the inner edge without overtopping. At low wave periods the reflection coefficient decreased as wave height increased, at high wave periods it was less sensitive to wave height. This applied to both  $60^\circ$  and  $30^\circ$  configurations. Peak reflection for the  $60^\circ$  configuration was 0.79 and for the  $30^\circ$  configuration it was 0.48.

The transmission coefficient for the WaveCat was highest at small wave heights and large wave periods. At high wave periods the transmission coefficient decreased as wave height increased, as a greater portion of the energy was absorbed. At low wave periods it was less sensitive to wave height. This was consistent across both  $60^\circ$  and



30° configurations. Peak transmission for the 60° configuration was 0.98 and for the 30° configuration it was 0.92.

The absorption coefficient for the WaveCat was highest at high wave heights and small wave periods, where reflection and transmission were both low. It was lowest at high wave periods and low wave heights where transmission became large. This was true for both configurations tested, however the 60° case had a larger region in which the absorption was higher. Peak absorption for the 60° configuration was 0.78 and for the 30° configuration it was 0.58.

Power conversion potential was quantified through the collection of overtopping water by measuring the flow released from the tanks through exhaust pipes using flowmeters. Both configurations generated the most power in the region where absorption was highest, as indicated by the measured flow through exhaust pipes. This was expected as the regions where absorption was highest had the lowest motion responses, thus less energy was being used to move the model and was available to be captured through overtopping waves. The 60° configuration generated power when the wave height was above 0.08 m at all periods. It also generated power at wave heights of 0.07 m, and for periods between 0.91 s and 1.46 s. The 30° configuration generated power when wave height was above 0.13 m and between wave periods of 1.28 s to 1.83 s. The results were consistent with the power potential identified from the wave energy absorption analysis.

The CWR, a measure of device efficiency, of the 60° case was highest (1.5%) during conditions of  $H_s = 0.12$  m and  $T_p = 1.09$  s. At wave heights above this the device generated more power but at a lower efficiency. The CWR of the 30° configuration was highest (5.4%) during conditions of  $H_s = 0.15$  m and  $T_p = 1.46$  s. These conditions represented the highest wave height tested for the 30° configuration.

When comparing the 60° and 30° configurations the reflection, transmission and absorption coefficients were generally more sensitive to  $H_s$  and  $T_p$  than wedge angle. Small differences were observed between the  $k_r$  value for the configurations tested. Where 60° and 30° configuration tests were performed at the same parameters, the

$k_r$  was very similar for the different wedge angles (typically within 0.05 or less). The highest observed values of  $k_r$  for both configurations were at the lowest wave periods tested, and decreased as wave period increased. This was as expected as more energy was transmitted by the device.

The 60° configuration showed a greater range of  $k_t$  values between the wave periods tested. The 30° configuration showed a smaller range of  $k_t$  values across the tested wave periods that were between the minimum and maximum 60°  $k_t$  value.

For the 60° configuration the  $k_a$  peaked at 1.09 s before gradually dropping as  $T_p$  increased. At small  $H_s$  the absorption for the 60° configuration became a minimum, reaching 0 at low wave heights. For the 30° configuration  $k_a$  was less sensitive to wave height, ranging between 0.55 at low wave periods and 0.35 at high wave periods.

The surge RAO for both configurations showed that the device surged most at high wave periods. The peak RAO was 0.68 for the 60° configuration and 0.79 for the 30° configuration. The 60° tests showed that there was a small peak at low period waves, when wavelength was around one model length. It showed minima around this peak which then increased with wave period.

The 60° configuration showed low pitch RAO (0.1) at low wavelength which increased when the wavelength was greater than one model length. Both configurations showed that the pitch RAO dropped slightly when the wavelength increased, before rising again at the highest wavelengths tested. The maximum pitch RAO for the 60° configuration was 1.9 and for the 30° configuration it was 2.2.

The heave RAO for the 60° case was low at low wavelength and increased when the wavelength was greater than one model length. Both configurations showed the heave steadily increased as wavelength increased, reaching an RAO of 0.97 for the 60° case and 0.92 for the 30° case. Both configurations also showed that in the test with the highest wavelength the heave dropped slightly. This shows that efforts should be made to minimise motion in order to maximise power generation. This can be done through design or careful choice of deployment area such that the wavelengths expected are shorter than the model.

During tests with the most power generated, the  $60^\circ$  model had low surge, pitch and heave RAOs of 0.2, 0.2 and 0.3 respectively. The  $30^\circ$  model also had low surge, pitch and heave RAOs of 0.1, 2.0 and 0.6 respectively.

The STAR-CCM+ model shows that experimental model measurements were reproducible in the numerical model. Refinements to the modelling of the moorings could further improve this.

## 8.2 Conclusions

This thesis has shown development on the WaveCat design and further advanced the knowledge of the device behaviours and performance in monochromatic and random sea states. The coefficient results have shown that the device is suited to areas where the wave period is short and the wave height is large, as the absorption coefficient and estimated power generated is highest in these regions. The tests have also shown that during conditions where power extraction is highest the device motions have been small, therefore future designs of the WaveCat should aim to limit motion over a wider range of wave conditions to investigate whether this improves performance.

A set of generalised coefficients has been developed which attempts to predict the coefficients using the wave height and wave period as inputs. This will allow estimated coefficients to be generated within the experimental range tested that can be compared to other devices, both OWECs and other types. This method works best if the trends between wave condition pairs are similar.

The numerical model shows that STAR-CCM+ is suitable for modelling the motions of the device. With further refinement to better match the experimental processes parts of future experimental campaigns can instead be done numerically, which will allow an increased pace of development due to not being fully reliant on laboratory testing. This will also allow optimisation studies to be performed where the model can be fine tuned without committing experimental time to repeated model changes over similar conditions.

As the WaveCat model has been constructed as part of this thesis it will also remove some of the initial work needed to begin a new experimental campaign, allowing more time and funds to be spent upgrading the capabilities of the model, particularly those of the water release mechanisms to ensure maximum power is recorded.

Testing the device at a larger scale would be beneficial, as the results show interesting interactions in some conditions where waves are small. This would allow larger waves to be tested whilst retaining the same full scale dimensions of the conditions and model, while simultaneously moving away from the limits of the wavemakers generation capabilities. A larger model would also provide more space to develop the overtopping controls and flow measurement with a wider range of products available.

The results presented are also valuable to the WEC community as it provides real experimental data from which numerical models can be validated. This is relevant to both the device in terms of power extraction and responses, as well as the affect the device has on the wave field around it through its reflection, transmission and absorption.

The device has been shown to have the highest estimated power generation in short period high amplitude waves. The Wave Dragon shows the highest estimated power generation in regions with higher periods. The WaveCat can fill a niche of conditions where the characteristic wave period of the deployment site is shorter than the ideal wave period for the Wave Dragon and other devices and where there is no option for shore or near-shore mounted devices such as SSG and Oyster.

The conclusions presented here are not without limitations, due either to the processes involved or the characteristics of the device. The nature of physical model testing means that experiments must prioritise particular aspects of the device and the wave conditions over others. The experiments were carried out at 1:30 scale, the same scale at which Fernández et al. (2012a) and Fernández et al. (2012b) carried out the initial laboratory tests on the WaveCat. At this scale it is valid to scale the results up to full scale with Froude scaling, and indeed other models have done so for smaller scales. For example, some Wave Dragon model tests were scaled up from

1:51.8 (Parmeggiani et al., 2013), however the overtopping process is still subject to friction and surface tension forces and thus should also be validated at larger scale.

The wave conditions tested used an even spacing over a desired characteristic range throughout the tests. Wave height had a 0.5 m interval between heights and wave period had a 1 s interval between periods at full scale, approximately 0.02 m and 0.18 s at model scale of 1:30. While higher resolution could have been tested, particularly around model period, it was unknown which regions to focus on prior to the current study. It is necessary to identify these regions where higher resolution would be beneficial through a thorough sweep of the potential conditions. In the event of further testing additional conditions with 0.5 s intervals would be beneficial to test around the model period, as well as additional conditions below the smallest period tested for the 30° configuration. The results nevertheless show indicative trends across the variable space thus far, from which conclusions can be determined and areas of future focus identified.

It was observed that the model showed some low frequency oscillations in the responses, particularly in yaw and sway. These oscillations were small however, approximately 3° for yaw and 0.15 m for sway, and were likely due to the fact that the model was freely floating in the experimental area. The model was only fixed to the moorings by the bows with a slack safety line at the stern, and as such was sensitive to wave conditions. The results do show that it makes corrections throughout the test, suggesting the weather vane effect desired from the moorings was attempting to correct the movements.

Due to the shape of the device and the wedge angle of the hulls the waves that are reflected during the experiments will not return in exactly the opposite direction as shown in Figures 5.31 and 5.32. This can be beneficial however, as the waves have the opportunity to impinge more than once on the hull of WaveCat as they pass through the wedge, potentially superposing with other waves and increasing the overtopping experienced by the device. This is difficult to measure in experiments as the WaveCat itself is in motion during the tests.

During the experiments it was observed that tests with high height and low period were subject to wave breaking in the wedge of the device. While these results are still presented in this thesis it mostly affected the  $60^\circ$  tests, in which the period range tested started at 0.91 s. A key example is in Figure 5.9, in which the tests with the lower periods show less power captured compared to that of tests with higher period when the height is high, despite the highest powers observed often being in the test case with the next lowest period tested. There was still overtopping however, as the waves tested were part of a spectra with some longer period waves also present. Thus the breaking criteria of the waves at the expected deployment zone must be taken into account when determining potential power generation rates.

The wave breaking also affected the regular wave tests when the period was low and the height high. This was observed in the  $60^\circ$  tests particularly, in which a divergence of results around the low periods was found between results of increasing heights. The lower height waves should be considered more applicable than the higher height waves.

As this device is in the early stages of development there is still further optimisation work to be done. In some tests, particularly those of low period and high height, it was observed that the overtopping tanks were filling with collected water faster than could be exhausted through the flowmeters. This effectively reduced the amount of power generated from a test, as rather than pass through the flowmeters and be recorded, it overflowed the tanks and returned to the basin. This was evident when comparing the results showing the CWR, Figure 5.9, wherein the largest amounts of energy captured was in the region where the wave height was highest. This problem can be overcome in the design phase by using tanks and pipework capable of handling the expected volume of water during conditions prevalent at the deployment site. The percentage however was highest at wave heights of 0.08 m, suggesting that the higher wave heights had reached the overtopping threshold. Subsequently, when subjected to periods of high overtopping discharge during a test they were reaching the tank overspill limit and extra overtopped water was being returned to the basin.

### 8.3 Recommendations

The WaveCat is in the early stages of development and thus there are a myriad of directions in which further work can be undertaken.

The physical model experiments have been performed at 1:30 scale thus far, larger scale experiments focussing on the device operation with particular objectives on the overtopping capture and release mechanisms would greatly assist device development. Subsequent larger scale experiments could also be performed in nursery sites such as FaBTest in Cornwall. As it stands, at 1:30 scale the power is scaled by 1:147885 ( $30^{3.5}$ ) making it sensitive to small variations at 1:30 scale. By using a larger scale this sensitivity can be reduced as the scaling factor reduces.

The model characteristics themselves also should undergo thorough optimisation processes. Kofoed et al. (2006) alludes to the optimisation process that the Wave Dragon underwent as part of its development including, but not limited to; ramp shape, reflector shape, turbine power unit optimisation and mooring forces. The WaveCat should also be subjected to optimisation procedures particularly concerning the wedge angle and trim of the device and how the combination of the two affect overtopping levels and power generated. From the concept design to the updated design the structure has been modified to increase freeboard but more rigorous optimisation should be performed.

Tests with varying wedge angles can be performed. This thesis focussed on tests with  $60^\circ$  and  $30^\circ$  wedge angles, between which there were similarities, such as  $k_r$  and  $k_t$  values, but also differences, such as power generation and  $k_a$ . A sweep of wedge angles would provide for comparable data at which wedge angles the device performs better at for specified wave conditions, as it is intended the device vary the wedge angle in response to wave conditions. Tests with a wedge angle of  $0^\circ$ , in a closed survival mode, should also be performed to examine the seakeeping of the device.

The freeboard of the device was kept at a constant 200 mm during the presented experiments. The devices initial pitch can be adjusted by moving ballast location within the device body which can cause the freeboard to vary along the inner edge of the device, similar to the initial concept tests by Fernández et al. (2012a). Adding or removing ballast in total can also decrease or increase the freeboard respectively. It is anticipated that a lower freeboard will encourage overtopping and altering the freeboard variation will change the ratio of overtopping between the tanks in each hull at the cost of head.

Geometry variations to the inner edge of the WaveCat should be investigated, similar to the design of the ramp in the Wave Dragon. Adding a slope with or without curvature can encourage wave overtopping (Van der Meer et al., 2018). The impact of resonance on the design should also be investigated and either enhanced or damped by changes to the geometry of the device depending on the need.

The tested conditions were chosen to provide a sweep of conditions across a range of heights and periods. Larger waves should be tested, approaching the limits of the devices ability to collect and process the overtopping water in the reservoirs. Waves with  $H_s$  up to 8 m were tested for Pelamis and SSG, up to 7 m for Wave Dragon, 6 m for Oyster and 5.5 m for AquaBuoy. Along with this, longer and shorter period waves can be tested to increase the range of results available.

Thus far all waves have been generated to approach the device with the wave fronts parallel to the device, and as such, due to device symmetry, the overtopping has been approximately equal in each hull. By introducing oblique waves the response of the device to uneven loading can be examined. This can be in the form of enhanced motions in the roll, yaw and sway modes and different power generated between the hulls. It is expected that the greater the angle of attack the greater the reduction in overtopping volumes (Van der Meer et al., 2018).

The mooring of the device should also be examined in detail. Force transducers can be added to the system to give readings for the sweeps of wave conditions. Different types of material for the mooring can also be used to provide a restoring force when



under wave action and potentially mitigate or enhance surge response depending on desired device response to the wave conditions.

The facilities at the COAST Laboratory can also apply current and wind loading to models in the basins at a variety of angles. The combination of current, wind and wave loading should be examined to determine survivability conditions during storms. The efficacy of the device to weathervane about the mooring can also be examined when the current, wind and wave are not acting in the same direction. This will inform whether extra mooring is needed at the rear of the device (Rawson and Tupper, 2001).

The control systems of the device can be further refined with adaptive control to the wave climate. It is envisioned that a larger scale prototype would be able to adjust the wedge angle, freeboard and release rate thus a testing platform would be beneficial in a laboratory environment rather than during deployment (Lavelle and Kofoed, 2011).

The WaveCat has thus far been tested as a single entity, but could be deployed as an array of WaveCats. Inter-array spacing and positioning would need to be analysed to provide optimum power return (Rodriguez-Delgado et al., 2019; Wolgamot et al., 2012; Sharkey et al., 2013). Singular large devices such as WaveCat or Wave Dragon could be deployed to isolated populations where electricity demand is low enough to be satisfied by one device. They have the advantage of not occupying valuable near shore space, which is a premium on small islands. They can be combined with other sources of renewable energy to provide sustainable power to a community in all weather conditions (Perez-Collazo et al., 2015).

A detailed version of the model in a numerical space should be developed, as testing time is often expensive and time consuming. The existing STAR-CCM+ model can be used as the package is able to reproduce overtopping and breaking wave events (Rij et al., 2019). This will also allow many different combinations of device characteristics and wave conditions to be tested systematically without needing expensive

laboratory testing time. As always, however, experimental validation data will be required.

Overall, the WaveCat has shown the ability to capture energy over a range of wave heights and wave periods. It has the advantage of manoeuvrability and a survival mode for large wave conditions. The next stage of development is to optimise the design and onboard systems prior to large scale testing.

In summary, a newly constructed model of the WaveCat wave energy converter was tested at 1:30 model scale in the COAST Laboratory Ocean Basin. The WaveCat performed optimally in high wave height, short period seas. The RAOs and the specific frequency response for heave, surge and pitch responses to random waves showed that when the model was producing the greatest amount of power, the device responses were minimised. A numerical model was validated for the motion of the WaveCat at  $30^\circ$  wedge angle in the absence of overtopping, showing good agreement between numerical and experimental values. The findings are significant as the quantification of the device performance characteristics will further inform development of the WaveCat model. They are also of direct relevance to the wider research and industrial community interested in the performance of overtopping based wave energy converters.

# References

- ABPmer (2019). *UK Atlas of Marine Renewable Energy Gateway*. URL: <https://www.renewables-atlas.info/> (visited on 08/04/2019).
- CD-Adapco (2017). *STAR-CCM+ User Guide 12.02*.
- Allen, J., G. Iglesias, D. Greaves and J. Miles (2020). ‘Physical modelling of the effect on the wave field of the WaveCat WEC’. In: *7th PRIMaRE Conference*. Plymouth, UK.
- Allen, J., G. Iglesias, D. Greaves and J. Miles (2021). ‘Physical Modelling of the Effect on the Wave Field of the WaveCat Wave Energy Converter’. In: *Journal of Marine Science and Engineering* 9.3. DOI: 10.3390/jmse9030309.
- Allen, J., K. Sampanis, J. Wan, D. Greaves, J. Miles and G. Iglesias (2016). ‘Laboratory tests in the development of WaveCat’. In: *Sustainability (Switzerland)* 8.12. ISSN: 20711050. DOI: 10.3390/su8121339.
- Allen, J., K. Sampanis, J. Wan, J. Miles, D. Greaves and G. Iglesias (2017). ‘Laboratory tests and numerical modelling in the development of WaveCat’. In: *Proceedings of the Twelfth European Wave and Tidal Energy Conference*.
- ANSYS (n.d.). *Fluids - CFD Simulation Software | ANSYS*. URL: <http://www.ansys.com/products/fluids>.
- Astariz, S. and G. Iglesias (2015). ‘The economics of wave energy: A review’. English. In: *Renewable & Sustainable Energy Reviews* 45, pp. 397–408. DOI: 10.1016/j.rser.2015.01.061.
- Babarit, A. (2015). ‘A database of capture width ratio of wave energy converters’. English. In: *Renewable Energy* 80, pp. 610–628. DOI: 10.1016/j.renene.2015.02.049.

- Babarit, A. and G. Delhommeau (2015). ‘Theoretical and numerical aspects of the open source BEM solver NEMOH’. In: *11th European Wave and Tidal Energy Conference (EWTEC2015)*.
- Bahaj, A. (2011). ‘Generating electricity from the oceans’. In: *Renewable and Sustainable Energy Reviews* 15.7, pp. 3399–3416. ISSN: 1364-0321.
- Baquerizo, A. (1995). ‘Wave reflection at beaches. Prediction and evaluation methods’. PhD thesis. Santander, Spain.
- Barbarelli, S., M. Amelio, G. Florio and N. M. Scornaienchi (2018). ‘Study of a hydraulic system converting energy from sea waves near the coast’. In: *MATEC Web of Conferences* 240. ISSN: 2261236X. DOI: 10.1051/mateconf/201824001004.
- Barstow, S., G. Mørk, D. Mollison and J. Cruz (2008). ‘The Wave Energy Resource’. In: *Ocean Wave Energy: Current Status and Future Perspectives*. Ed. by Joao Cruz. Berlin, Heidelberg: Springer Berlin Heidelberg, pp. 93–132. ISBN: 978-3-540-74895-3. DOI: 10.1007/978-3-540-74895-3\_4. URL: [https://doi.org/10.1007/978-3-540-74895-3\\_4](https://doi.org/10.1007/978-3-540-74895-3_4).
- Beels, C., P. Troch, G. De Backer, M. Vantorre and J. De Rouck (2010a). ‘Numerical implementation and sensitivity analysis of a wave energy converter in a time-dependent mild-slope equation model’. In: *Coastal Engineering* 57.5, pp. 471–492. ISSN: 0378-3839. DOI: <https://doi.org/10.1016/j.coastaleng.2009.11.003>. URL: <https://www.sciencedirect.com/science/article/pii/S0378383909001823>.
- Beels, C., P. Troch, K. De Visch, J. P. Kofoed and G. De Backer (2010b). ‘Application of the time-dependent mild-slope equations for the simulation of wake effects in the lee of a farm of Wave Dragon wave energy converters’. English. In: *Renewable Energy* 35.8, pp. 1644–1661. DOI: 10.1016/j.renene.2009.12.001.
- Beels, C., P. Troch, J. P. Kofoed, P. Frigaard, J. V. Kringelum, P. C. Kromann, M. H. Donovan, J. De Rouck and G. De Backer (2011). ‘A methodology for production and cost assessment of a farm of wave energy converters’. English. In: *Renewable Energy* 36.12, pp. 3402–3416. DOI: 10.1016/j.renene.2011.05.019.
- Bendat, J. S. and A. G. Piersol (1986). *Random Data: Analysis and Measurement Procedures*. Vol. 150. 2, p. 566. DOI: 10.2307/2981634.

- Benek, J., J. Steger and F. C. Dougherty (July 1983). ‘A flexible grid embedding technique with application to the Euler equations’. In: *6th Computational Fluid Dynamics Conference Danvers*. Fluid Dynamics and Co-located Conferences. American Institute of Aeronautics and Astronautics. DOI: doi:10.2514/6.1983-1944. URL: <https://doi.org/10.2514/6.1983-1944>.
- Bergillos, R., C. Rodriguez-Delgado, J. Allen and G. Iglesias (2019a). ‘Wave energy converter configuration in dual wave farms’. In: *Ocean Engineering* 178, pp. 204–214. ISSN: 0029-8018. DOI: <https://doi.org/10.1016/j.oceaneng.2019.03.001>. URL: <http://www.sciencedirect.com/science/article/pii/S0029801819300939>.
- Bergillos, R., C. Rodriguez-Delgado, J. Allen and G. Iglesias (2019b). ‘Wave energy converter geometry for coastal flooding mitigation’. In: *Science of The Total Environment*. ISSN: 0048-9697. DOI: <https://doi.org/10.1016/j.scitotenv.2019.03.022>. URL: <http://www.sciencedirect.com/science/article/pii/S0048969719310009>.
- Bharath, A., I. Penesis, J. Nader and G. Macfarlane (2016). ‘Non-Linear CFD Modelling of a Submerged Sphere Wave Energy Converter’. In: *Proceedings of the 3rd Asian Wave and Tidal Energy Conference, Singapore* November, pp. 1–10.
- Boake, C. B., T. J.T. Whittaker, M. Folley and H. Ellen (2002). ‘Overview and Initial Operational Experience of the LIMPET Wave Energy Plant’. In: *Proceedings of the International Offshore and Polar Engineering Conference* 12.February 2015, pp. 586–594.
- Bombora (2020). *mWave*. URL: <https://www.bomborawave.com/mwave/> (visited on 27/01/2021).
- Brito-Melo, A., T. Hofmann, A. J. N. A. Sarmiento, A. H. Clement and G. Delhommeau (June 2001). ‘Numerical Modelling of OWC-Shoreline Devices Including the Effect of Surrounding Coastline And Non-flat Bottom’. In: *International Journal of Offshore and Polar Engineering* 11.02. ISSN: 1053-5381.
- Buccino, M., D. Salerno, D. Banfi, D. Vicinanza, J. P. Kofoed and M. Calabrese (2013). ‘Breaker types and loading characteristics at SSG’. In: *EWTEC 2013 Proceedings* January.

- Budar, K. and J. Falnes (1975). ‘A resonant point absorber of ocean-wave power’. In: *Nature* 256.5517, pp. 478–479. ISSN: 1476-4687. DOI: 10.1038/256478a0. URL: <https://doi.org/10.1038/256478a0>.
- Cahill, B. and A. W. Lewis (2014). ‘Wave period ratios and the calculation of wave power’. In: *The 2nd Marine Energy Technology Symposium*, pp. 1–10.
- Carballo, R. and G. Iglesias (2013). ‘Wave farm impact based on realistic wave-WEC interaction’. English. In: *Energy* 51, pp. 216–229. DOI: 10.1016/j.energy.2012.12.040.
- Carnegie Clean Energy (2021). *CETO Technology - Carnegie*. URL: <https://www.carnegiece.com/ceto-technology/> (visited on 20/01/2021).
- Carpintero Moreno, E. and P. Stansby (2019). ‘The 6-float wave energy converter M4: Ocean basin tests giving capture width, response and energy yield for several sites’. In: *Renewable and Sustainable Energy Reviews* 104, pp. 307–318. ISSN: 1364-0321. DOI: <https://doi.org/10.1016/j.rser.2019.01.033>. URL: <http://www.sciencedirect.com/science/article/pii/S1364032119300437>.
- Choi, J. and S. B. Yoon (2009). ‘Numerical simulations using momentum source wave-maker applied to RANS equation model’. English. In: *Coastal Engineering* 56.10, pp. 1043–1060. ISSN: 03783839. DOI: 10.1016/j.coastaleng.2009.06.009.
- COAST Laboratory (2020). *COAST Laboratory*. URL: <https://www.plymouth.ac.uk/research/institutes/marine-institute/coast-laboratory> (visited on 09/07/2020).
- Collins, K., P. Arber, D. Greaves, M. Hann, G. Iglesias, D. Simmonds, S. Stripling and A. Toffoli (Apr. 2013). *Facilitating coastal and ocean science research in the laboratory*, p. 13955.
- Collins, K., B. Howey, P. Vicente, R. Gomes, V. Harnois, M. Hann, G. Iglesias and D. Greaves (Aug. 2017). *A Physical Mooring Comparison for a Floating OWC*.
- Collins, K., G. Iglesias, D. Greaves, A. Toffoli and S. Stripling (Jan. 2014). ‘The New Coast Laboratory at Plymouth University: A World-Class Facility for Marine Energy’. In: *From Sea to Shore? Meeting the Challenges of the Sea*. Vol. 1 and 2. Conference Proceedings. ICE Publishing, pp. 1326–1335. ISBN: 978-0-7277-5975-7.

- DOI: doi:10.1680/fsts.59757.144. URL: <https://doi.org/10.1680/fsts.59757.144>.
- Cooley, J. W. and J. W. Tukey (1965). ‘An algorithm for the machine calculation of complex Fourier series’. In: *Mathematics of Computation* 19.90, pp. 297–297. ISSN: 0025-5718. DOI: 10.1090/s0025-5718-1965-0178586-1.
- Cruz, J. (2007). *Ocean wave energy: current status and future prespectives*. Springer Science & Business Media. ISBN: 3540748954.
- Davidson, J. and J. V. Ringwood (2017). ‘Mathematical modelling of mooring systems for wave energy converters - A review’. In: *Energies* 10.5. ISSN: 19961073. DOI: 10.3390/en10050666.
- Department for Business Energy & Industrial Strategy (2018). *Digest of UK energy statistics 2018*. Tech. rep. DOI: 10.1016/B978-0-444-41284-3.50010-2. arXiv: arXiv:1103.5922v2.
- Digest of UK Energy Statistics (2020). *DUKES 2020 Chapter 6: Renewable sources of energy*. Tech. rep., pp. 106–127. URL: <https://www.gov.uk/government/statistics/renewable-sources-of-energy-chapter-6-digest-of-united-kingdom-energy-statistics-dukes>.
- Dixon, S. L. and C. A. Hall (2010). ‘Chapter 9 - Hydraulic Turbines’. In: *Fluid Mechanics and Thermodynamics of Turbomachinery (Sixth Edition)*. Ed. by S L Dixon and C A Hall. Sixth Edit. Boston: Butterworth-Heinemann, pp. 303–355. ISBN: 978-1-85617-793-1. DOI: <https://doi.org/10.1016/B978-1-85617-793-1.00009-2>. URL: <http://www.sciencedirect.com/science/article/pii/B9781856177931000092>.
- EDesign (2016a). *Wave Gauges*. URL: <http://www4.edesign.co.uk/product/wavegauges/> (visited on 04/01/2022).
- EDesign (2016b). *Wave Generating Software*. URL: <http://www4.edesign.co.uk/product/wave-generating-software/> (visited on 21/10/2020).
- AW-Energy (2020). *WaveRoller - AW Energy Oy*. URL: <http://aw-energy.com/waveroller/> (visited on 03/02/2021).
- European Parliament and Council (2009). ‘Directive 2009/28/EC on the promotion of the use of energy from renewable sources’. In: *Official Journal of the European*

- Union* 140, pp. 16–62. ISSN: 02870827. DOI: 10.3000/17252555.L\_2009.140.eng. arXiv: 534.
- European Parliament and Council (2018). ‘Directive (EU) 2018/2001 of the European Parliament and of the Council of 11 December 2018 on the promotion of the use of energy from renewable sources’. In: *Official Journal of the European Union* 328, pp. 82–209.
- Falcão, A. (Jan. 2000). ‘The shoreline OWC wave power plant at the Azores’. In: *Proc. 4th European Wave Energy Conf., Aalborg, Denmark*, pp. 42–47.
- Falcão, A. F. O., A. J. N. A. Sarmiento, L. M. C. Gato and A. Brito-Melo (2020). ‘The Pico OWC wave power plant: Its lifetime from conception to closure 1986–2018’. In: *Applied Ocean Research* 98. January, p. 102104. ISSN: 01411187. DOI: 10.1016/j.apor.2020.102104. URL: <https://doi.org/10.1016/j.apor.2020.102104>.
- Falnes, J. and J. Løvseth (1991). ‘Ocean wave energy’. In: *Energy policy* 19.8, pp. 768–775. ISSN: 0301-4215.
- Fernández, H., G. Iglesias, R. Carballo, A. Castro, J. A. Fraguela, F. Taveira-Pinto and M. Sanchez (2012a). ‘The new wave energy converter WaveCat: Concept and laboratory tests’. English. In: *Marine Structures* 29.1, pp. 58–70. DOI: 10.1016/j.marstruc.2012.10.002.
- Fernández, H., G. Iglesias, R. Carballo, A. Castro, M. Sánchez and F. Taveira-Pinto (2012b). ‘Optimization of the wavecat wave energy converter’. In: *Proceedings of the Coastal Engineering Conference*.
- Flow Science Inc (2021). *FLOW - 3D / Solving the World’s Toughest CFD Problems*. URL: <https://www.flow3d.com/> (visited on 21/01/2021).
- Folley, M., R. Curran, C. Boake and T. Whittaker (Jan. 2002). ‘Performance investigations of the LIMPET counter-rotating Wells turbine’. In: *MAREC 2002, International Conference on Marine Renewable Energy - Conference Proceedings*, pp. 77–85.
- Folley, M., T. Whittaker and A. Henry (June 2007a). ‘The effect of water depth on the performance of a small surging wave energy converter’. In: *Ocean Engineering* 34, pp. 1265–1274. DOI: 10.1016/j.oceaneng.2006.05.015.



- Folley, M., T. Whittaker and M. Osterried (2004). ‘The Oscillating Wave Surge Converter’. In: *Proceedings of the International Offshore and Polar Engineering Conference* January 2004, pp. 189–193. ISSN: 10986189.
- Folley, M., T.W.T. Whittaker and J. van’t Hoff (2007b). ‘The design of small seabed-mounted bottom-hinged wave energy converters’. In: *Proceedings of the 7th European Wave and Tidal Energy Conference* September, pp. 1–10.
- Frigaard, P., J. P. Kofoed and W. Knapp (2004). ‘Wave Dragon. Wave Power Plant using Low-head Turbines.’ In: *Hidroenergia*.
- Friigo, M. and S. G. Johnson (1998). ‘FFTW : AN ADAPTIVE SOFTWARE ARCHITECTURE FOR THE FFT’. In: *Technology*, pp. 1381–1384. ISSN: 0780344286.
- Friis-Madsen, E., H. C. C. Sørensen and S. Parmeggiani (2012). ‘The development of a 1 . 5 MW Wave Dragon North Sea Demonstrator’. In: *4th International Conference on Ocean Energy*, pp. 1–5.
- Gaspar, J. F., P. K. Stansby, M. Calvário and C. Guedes Soares (2021). ‘Hydraulic Power Take-Off concept for the M4 Wave Energy Converter’. In: *Applied Ocean Research* 106.December 2020, p. 102462. ISSN: 01411187. DOI: 10.1016/j.apor.2020.102462. URL: <https://doi.org/10.1016/j.apor.2020.102462>.
- GE Renewable Energy (2021). *Haliade-X offshore wind turbine*. URL: <https://www.ge.com/renewableenergy/wind-energy/offshore-wind/haliade-x-offshore-turbine> (visited on 26/01/2021).
- Goda, Y. and T. Suzuki (1976). ‘Estimation of Incident and Reflected Waves in Random Wave Experiments’. In: *Coastal Engineering Proceedings*. Vol. 1. 15, p. 47. DOI: 10.9753/icce.v15.47.
- Götteman, M., J. Engström, M. Eriksson, M. Hann, E. Ransley, D. Greaves and M. Leijon (2015a). ‘Wave loads on a point-absorbing wave energy device in extreme waves’. In: *Proceedings of the International Offshore and Polar Engineering Conference* 2015-Janua, pp. 944–950. ISSN: 15551792.
- Götteman, M., J. Engström, M. Eriksson, M. Leijon, M. Hann, E. Ransley and D. Greaves (2015b). ‘Wave loads on a point-absorbing wave energy device in extreme waves’. In: *Journal of Ocean and Wind Energy* 2.3, pp. 176–181. ISSN: 23103604. DOI: 10.17736/jowe.2015.mkr03.

- Greaves, D. and G. Iglesias (2018). *Wave and Tidal Energy*. Wiley. ISBN: 9781119014478. URL: <https://books.google.co.uk/books?id=OKtTDwAAQBAJ>.
- Greenspan, H. P. (1956). 'The generation of edge waves by moving pressure distributions'. In: *Journal of Fluid Mechanics* 1.6, pp. 574–592. DOI: 10.1017/S002211205600038X.
- Gunn, K. and C. Stock-Williams (2012). 'Quantifying the global wave power resource'. In: *Renewable Energy* 44, pp. 296–304. ISSN: 0960-1481. DOI: <https://doi.org/10.1016/j.renene.2012.01.101>. URL: <http://www.sciencedirect.com/science/article/pii/S0960148112001310>.
- Hald, T. and J. Lynggaard (2001). *Hydraulic Model Tests on Modified Wave Dragon*.
- Hamill, L. (2011). *Understanding Hydraulics*. 3rd. Palgrave Macmillan. DOI: 10.1007/978-1-349-13296-6.
- Hann, M., D. Greaves, A. Raby and B. Howey (2018). 'Use of constrained focused waves to measure extreme loading of a taut moored floating wave energy converter'. In: *Ocean Engineering* 148, June 2017, pp. 33–42. ISSN: 00298018. DOI: 10.1016/j.oceaneng.2017.10.024. URL: <https://doi.org/10.1016/j.oceaneng.2017.10.024>.
- Harris, Robert E, Lars Johanning and Julian Wolfram (2004). 'Mooring systems for wave energy converters : A review of design issues and choices'. In: *3rd International Conference on Marine Renewable Energy* January, pp. 1–10. ISSN: 09601481. URL: [http://oreg.ca/web%7B%5C\\_%7Ddocuments/mooringsystems.pdf](http://oreg.ca/web%7B%5C_%7Ddocuments/mooringsystems.pdf).
- Hart, P. (Apr. 2012). 'Autonomous PowerBuoys Generate Power for Ocean Applications'. In: *Sea Technology* 53, pp. 10–12.
- Hattam, C., T. Hooper and N. Beaumont (2015a). *Public Perceptions of Offshore Wind Farms, The Crown Estate*, p. 50. ISBN: 9781906410667.
- Hattam, C., T. Hooper and E. Papathanasopoulou (2015b). *Understanding the Impacts of Offshore Wind Farms on Well-Being, The Crown Estate*, p. 77. ISBN: 9781906410650.
- Heath, T. (2003). 'The Construction, Commissioning and Operation of the LIMPET Wave Energy Collector'. In: *Applied Research and Technology*, pp. 1–14.

- Heath, T., T. Whittaker and C. Boake (2001). ‘The design, construction and operation of the LIMPET wave energy converter (Islay, Scotland)[Land Installed Marine Powered Energy Transformer]’. English. In: Denmark.
- Henderson, R. (Feb. 2006). ‘Design, simulation, and testing of a novel hydraulic power take-off system for the Pelamis wave energy converter’. In: *Renewable Energy* 31, pp. 271–283. DOI: 10.1016/j.renene.2005.08.021.
- Hirt, C. W. and B. D. Nichols (1981). ‘Volume of Fluid (Vof) Method for the Dynamics of Free Boundaries’. English. In: *Journal of Computational Physics* 39.1, pp. 201–225. DOI: Doi10.1016/0021-9991(81)90145-5.
- Holmes, B., J. Hurley, T. Lewis, A. J. N. A. Sarmiento, A. Brito-Melo and A. F. O. Falcão (1995). ‘1:25 scale testing of the Azores pilot plant’. In: *2nd European Wave Power Conference*. Lisbon, Portugal, pp. 148–155.
- Holthuijsen, L. H. (2007). *Wave in Oceanic and Coastal Waters*. Cambridge University Press. DOI: 10.1017/CB09780511618536.
- House of Commons (2020). *Environment Bill*. URL: <https://services.parliament.uk/bills/2019-21/environment.html>.
- Hughes, S. A. (1993). *Physical models and laboratory techniques in coastal engineering*. Vol. 7. World Scientific.
- IEA (2020a). *Renewables Information - Overview (2020 Edition)*. Tech. rep. Paris, p. 497. URL: <https://www.iea.org/reports/renewables-information-overview>.
- IEA (2020b). *World Energy Balances: Overview*. Tech. rep. URL: <https://www.iea.org/reports/world-energy-balances-overview>.
- IEA (2021). *Covid-19 impact on electricity*. Tech. rep. Paris. URL: <https://www.iea.org/reports/covid-19-impact-on-electricity>.
- Igic, P., Z. Zhou, W. Knapp, J. MacEnri, H. C. Sørensen and E. Friis-Madsen (Feb. 2011). ‘Multi-megawatt offshore wave energy converters - electrical system configuration and generator control strategy’. In: *Renewable Power Generation, IET* 5, pp. 10–17. DOI: 10.1049/iet-rpg.2009.0090.
- Iglesias, G., H. Fernández, R. Carballo, A. Castro and F. Taveira-Pinto (2011). ‘The WaveCat - Development of A New Wave Energy Converter’. In: *Proceedings of*

- the World Renewable Energy Congress*. Vol. 57, pp. 2151–2158. DOI: 10.3384/ecp110572151.
- Ingram, G. (Jan. 2009). ‘Basic Concepts in Turbomachinery’. In: p. 144. ISSN: 9788776814359.
- Isherwood, R. M. (1987). ‘Technical note: A revised parameterisation of the Jonswap spectrum’. In: *Applied Ocean Research* 9.1, pp. 47–50. ISSN: 0141-1187. DOI: [https://doi.org/10.1016/0141-1187\(87\)90030-7](https://doi.org/10.1016/0141-1187(87)90030-7). URL: <http://www.sciencedirect.com/science/article/pii/0141118787900307>.
- ITTC (2014a). ‘ITTC – Recommended Guidelines - Wave energy converter - Model test experiments 7.5-02-07-03.7 (Revision 01)’. In: *27th International Towing Tank Conference*, p. 13.
- ITTC (2014b). ‘ITTC – Recommended Procedures and Guidelines-Seakeeping Experiments’. In: *27th ITTC Seakeeping Committee*, pp. 1–22.
- Jeffrey, H., B. Jay and M. Winskel (2013). ‘Accelerating the development of marine energy: Exploring the prospects, benefits and challenges’. In: *Technological Forecasting and Social Change* 80.7, pp. 1306–1316. ISSN: 0040-1625.
- Jenkins, G. M. and D. G. Watts (1968). *Spectral Analysis and Its Application*. Holden-Day.
- Jmvolc (2006a). *Rotations*. marked as public domain, more details on Wikimedia Commons: <https://commons.wikimedia.org/wiki/Template:PD-user>. URL: <https://upload.wikimedia.org/wikipedia/commons/d/df/Rotations.png> (visited on 19/10/2020).
- Jmvolc (2006b). *Translations*. marked as public domain, more details on Wikimedia Commons: <https://commons.wikimedia.org/wiki/Template:PD-user>. URL: <https://upload.wikimedia.org/wikipedia/commons/5/59/Translations.png> (visited on 19/10/2020).
- Kaasen, K., H. Ludvigsen and K. Aas (2017). ‘Heading control of a turret-moored FPSO with and without forward thrusters’. In: *Proceedings of the Annual Offshore Technology Conference* 4, pp. 3088–3108. ISSN: 01603663. DOI: 10.4043/27794-ms.

- Kelly, J., D. O'Sullivan, W. M.D. Wright, R. Alcorn and A. W. Lewis (2014). 'Challenges and lessons learned in the deployment of an offshore oscillating water column'. In: *COMPEL - The International Journal for Computation and Mathematics in Electrical and Electronic Engineering* 33.5, pp. 1678–1704. ISSN: 03321649. DOI: 10.1108/COMPEL-09-2013-0307.
- Knapp, W., E. Holmen and R. Schilling (2000). 'Considerations for Water Turbines to be used in Wave Energy Converters'. In: *Fourth European Wave Energy Conference*.
- Kofoed, J. P. (2002). 'Wave Overtopping of Marine Structures: utilization of wave energy'. PhD thesis.
- Kofoed, J. P., P. Frigaard, E. Friis-Madsen and H. C. Sorensen (2006). 'Prototype testing of the wave energy converter wave dragon'. English. In: *Renewable Energy* 31.2, pp. 181–189. DOI: 10.1016/j.renene.2005.09.005.
- Kofoed, J. P., P. Frigaard, H. C. Sorensen and E. Friis-Madsen (2000). 'Development of the Wave Energy Converter - Wave Dragon'. In: *International Offshore and Polar Engineering Conference*. Seattle, USA.
- Kofoed, J. P., P. Frigaard, H. C. Sørensen and E. Friis-Madsen (1998). 'Wave dragon —a slack moored wave energy converter'. In: *3rd European Wave Energy Conference*.
- Kofoed, J. P., T. Hald and P. Frigaard (2002). 'Experimental Study of a Multi Level Overtopping Wave Power Device'. In: *Proceedings of the 10th Congress of International Maritime Association of the Mediterranean ( IMAM 2002 )* Imam.
- Kurniawan, A., M. Grassow and F. Ferri (Oct. 2019). 'Numerical modelling and wave tank testing of a self-reacting two-body wave energy device'. In: *Ships and Offshore Structures* 14.sup1, pp. 344–356. ISSN: 1744-5302. DOI: 10.1080/17445302.2019.1595924. URL: <https://doi.org/10.1080/17445302.2019.1595924>.
- Lavelle, J. and J. P. Kofoed (2011). 'Power Production Analysis of the OE Buoy WEC for the CORES Project'. In: *CORES EU Project, DCE Technical Report No. 119*.
- Lee, C. H. and J. N. Newman (2013). *WAMIT User Manual Version 7.0*.

- Liao, Z., N. Gai, P. Stansby and G. Li (2020). ‘Linear Non-Causal Optimal Control of an Attenuator Type Wave Energy Converter M4’. In: *IEEE Transactions on Sustainable Energy* 11.3, pp. 1278–1286. ISSN: 19493037. DOI: 10.1109/TSTE.2019.2922782.
- Lopes, M. F. P. (2011). ‘Experimental development of offshore wave energy converters’. PhD Thesis. Instituto Superior Técnico, Lisbon.
- Lucas, J., M. Livingstone, M. Vuorinen and J. Cruz (2012). ‘Development of a wave energy converter ( WEC ) design tool – application to the WaveRoller WEC including validation of numerical estimates’. In: *Proceedings of 4th International Conference on Ocean Energy*.
- Mäki, T., M. Vuorinen and T. Mucha (2014). ‘WaveRoller – One of the Leading Technologies for Wave Energy Conversion’. In: *5th International Conference on Ocean Energy* November, pp. 4–6.
- Mansard, E. P. D. and E. R. Funke (1980). ‘The measurement of incident and reflected spectra using a least squares method.’ In: *17th International Conference on Coastal Engineering*. Sydney. ISBN: 9780872622647. DOI: doi:10.1061/9780872622647.008. URL: <https://doi.org/10.1061/9780872622647.008>.
- Margheritini, L. (2009). *R&D Towards Commercialization of Sea Wave Slot Cone Generator (SSG) Overtopping Wave Energy Converter*. Aalborg.
- Margheritini, L., D. Vicinanza and P. Frigaard (2009). ‘SSG wave energy converter: Design, reliability and hydraulic performance of an innovative overtopping device’. English. In: *Renewable Energy* 34.5, pp. 1371–1380. DOI: 10.1016/j.renene.2008.09.009.
- Martinelli, L. and P. Frigaard (1999). *The Wave Dragon*. Aalborg.
- Masuda, Y. (1971). ‘Wave-Activated Generator, Int’. In: *Colloq Exposition Oceans, France, Bordeaux*.
- McNatt, J. C., A. Porter and K. Ruehl (2020). ‘Comparison of numerical methods for modeling the wave field effects generated by individual wave energy converters and multiple converter wave farms’. In: *Journal of Marine Science and Engineering* 8.3. ISSN: 20771312. DOI: 10.3390/jmse8030168.

- Mendes, A. C., F. P. Braga, L. M. A. Paredes and J. R. Chaplin (June 2017). *Performance Assessment of the Anaconda WEC in Regular Waves at 1:50 Model Scale*. DOI: 10.1115/OMAE2017-61478. URL: <https://doi.org/10.1115/OMAE2017-61478>.
- Milone Tech (2018). *Standard eTape® assembly*. URL: <https://milonetech.com/products/standard-etape-assembly> (visited on 24/04/2018).
- Monk, K., D. Conley, M. Lopes and Q. Zou (2013). ‘Pneumatic Power Regulation by Wave Forecasting and Real-Time Relief Valve Control for an OWC’. In: *10th European Wave and Tidal Energy Conference*.
- Moody, L. F. (1944). ‘Friction Factors for Pipe Flow’. In: *Transactions of the ASME* 66.8, pp. 671–684.
- Morden, D. B., E. P. Richey and D. R. Christensen (Nov. 1977). ‘Decomposition of Co-Existing Random Wave Energy’. In: *Coastal Engineering 1976*. New York, NY: American Society of Civil Engineers, pp. 846–865. ISBN: 9780872620834. DOI: 10.1061/9780872620834.049. URL: <http://ascelibrary.org/doi/10.1061/9780872620834.049>.
- Morison, J. R., J. W. Johnson and S. A. Schaaf (1950). ‘The Force Exerted by Surface Waves on Piles’. In: *Journal of Petroleum Technology* 2.05, pp. 149–154. ISSN: 0149-2136. DOI: 10.2118/950149-g.
- Munteanu, N. (2015). *Harnessing the Sea’s Wave Energy*. URL: <https://thmeaningofwater.com/2015/07/09/harnessing-the-seas-wave-energy/> (visited on 02/02/2021).
- Nielsen, A. and J. P. Kofoed (1997). ‘The Wave Dragon - evaluation of a wave energy converter by Department of Civil Engineering’. In: *Civil Engineering*.
- Nielsen, K. (2010). *Report T02-0.0 Development of Recommended Practices for Testing and Evaluating Ocean Energy Systems, OES-IA Annex II Extension*. Tech. rep. Ramboll, Denmark.
- NOAA (2019). *State of the Climate: Global Climate Report for Annual 2019*. Tech. rep.
- Nørgaard, J. H. and T. L. Andersen (2012). ‘Investigation of wave transmission from a floating wave dragon wave energy converter’. In: *Proceedings of the International Offshore and Polar Engineering Conference* 4, pp. 509–516. ISSN: 10986189.

- Nuttall, A. H. (1971). *Spectral Estimation by Means of Overlapped Fast Fourier Transform Processing of Windowed Data*. Tech. rep. No. 4169, pp. 1–40. URL: <http://oai.dtic.mil/oai/oai?verb=getRecord%7B%5C%%7D5C%7B%5C&%7DmetadataPrefix=html%7B%5C%%7D5C%7B%5C&%7Didentifier=AD0739315>.
- OceanEnergy (2020). *OE Buoy - Ocean Energy*. URL: <https://oceanenergy.ie/oe-buoy/> (visited on 03/02/2021).
- OMEGA Engineering (2018). *All Plastic Flow Sensors*. URL: <https://www.omega.co.uk/pptst/FTB600.html> (visited on 24/04/2018).
- OpenFOAM (2020). *OpenFOAM® - Official home of The Open Source Computational Fluid Dynamics (CFD) Toolbox*. URL: <https://www.openfoam.com/> (visited on 15/12/2020).
- Orcaflex (2020). *Vessel types: Conventions*. URL: <https://www.orcina.com/webhelp/OrcaFlex/Content/html/Vesseltypes,Conventions.htm%7B%5C%7DVesselTypeRotationalConventions> (visited on 03/02/2021).
- Owen, M. W. (1982). ‘The hydraulic design of sea-wall profiles.’ In:
- Ozdemir, Y. H. and B. Barlas (2017). ‘Numerical study of ship motions and added resistance in regular incident waves of KVLCC2 model’. English. In: *International Journal of Naval Architecture and Ocean Engineering* 9.2, pp. 149–159. DOI: 10.1016/j.ijnaoe.2016.09.001.
- Palha, A., L. Mendes, C. J. Fortes, A. Brito-Melo and A. Sarmiento (2010). ‘The impact of wave energy farms in the shoreline wave climate: Portuguese pilot zone case study using Pelamis energy wave devices’. In: *Renewable Energy* 35.1, pp. 62–77. ISSN: 09601481. DOI: 10.1016/j.renene.2009.05.025.
- Park, S., G. Oh, S. H. Rhee, B. Y. Koo and H. Lee (2015). ‘Full scale wake prediction of an energy saving device by using computational fluid dynamics’. English. In: *Ocean Engineering* 101, pp. 254–263. DOI: 10.1016/j.oceaneng.2015.04.005.
- Parmeggiani, S., J. P. Kofoed and E. Friis-Madsen (2013). ‘Experimental update of the overtopping model used for the wave dragon wave energy converter’. In: *Energies* 6.4, pp. 1961–1992. ISSN: 19961073. DOI: 10.3390/en6041961.



- Parmeggiani, S., A. Pecher, J. P. Kofoed and E. Friis-Madsen (2010). ‘Modelling of the Overtopping Flow on the Wave Dragon Wave Energy Converter’. In: *3rd International Conference on Ocean Energy*.
- Pecher, A., I. Le Crom, J. P. Kofoed, F. Neumann and E. De Brito Azevedo (2011). ‘Performance assessment of the Pico OWC power plant following the equimar methodology’. In: *Proceedings of the International Offshore and Polar Engineering Conference*, pp. 548–556. URL: <https://www.scopus.com/inward/record.uri?eid=2-s2.0-80052776059%7B%5C%26%7DpartnerID=40%7B%5C%26%7Dmd5=0136a894c4536f7c9abba84ac1c8fc1b>.
- Perez-Collazo, C., D. Greaves and G. Iglesias (2015). ‘A review of combined wave and offshore wind energy’. English. In: *Renewable & Sustainable Energy Reviews* 42, pp. 141–153. DOI: 10.1016/j.rser.2014.09.032.
- Qualisys (2018). *Qualisys Track Manager / Qualisys*. URL: <https://www.qualisys.com/software/qualisys-track-manager/>.
- Rafiee, A. and J. Fiévez (Sept. 2015). *Numerical Prediction of Extreme Loads on the CETO Wave Energy Converter*.
- Ransley, E. (2015). ‘Survivability of Wave Energy Converter and Mooring Coupled System using CFD’. PhD thesis. DOI: <http://hdl.handle.net/10026.1/3503>.
- Rawson, K. J. and E. C. Tupper (2001). *Basic Ship Theory*. 5th. Butterworth-Heinemann. ISBN: 0750653965. DOI: 10.1016/b978-0-7506-5398-5.x5000-6.
- Retzler, C. (2006). ‘Measurements of the slow drift dynamics of a model Pelamis wave energy converter’. In: *Renewable Energy* 31.2, pp. 257–269. ISSN: 0960-1481.
- Rij, J. van, Y. H. Yu and R. G. Coe (2018). ‘Design load analysis for wave energy converters’. In: *Proceedings of the International Conference on Offshore Mechanics and Arctic Engineering - OMAE* 10.November 2019. DOI: 10.1115/OMAE2018-78178.
- Rij, J. van, Y. H. Yu, K. Edwards and M. Mekhiche (2017a). ‘Ocean power technology design optimization’. In: *International Journal of Marine Energy* 20, pp. 97–108. ISSN: 2214-1669. DOI: <https://doi.org/10.1016/j.ijome.2017.07.010>. URL: <http://www.sciencedirect.com/science/article/pii/S2214166917300656>.

- Rij, J. van, Y. H. Yu and Y. Guo (2017b). ‘Structural loads analysis for wave energy converters’. In: *Proceedings of the International Conference on Offshore Mechanics and Arctic Engineering - OMAE* 10.July. DOI: 10.1115/OMAE2017-62139.
- Rij, J. van, Y. H. Yu, Y. Guo and R. G. Coe (2019). ‘A wave energy converter design load case study’. In: *Journal of Marine Science and Engineering* 7.8, pp. 1–22. ISSN: 20771312. DOI: 10.3390/jmse7080250.
- Rodriguez-Delgado, C., R. J. Bergillos and G. Iglesias (2019). ‘Dual wave farms and coastline dynamics: The role of inter-device spacing’. In: *Science of The Total Environment* 646, pp. 1241–1252. ISSN: 0048-9697. DOI: <https://doi.org/10.1016/j.scitotenv.2018.07.110>. URL: <http://www.sciencedirect.com/science/article/pii/S0048969718325932>.
- Ross, D. (1995). *Power from sea waves*. Oxford: Oxford University Press.
- Rourke, F. O., F. Boyle and A. Reynolds (2009). ‘Renewable energy resources and technologies applicable to Ireland’. In: *Renewable and Sustainable Energy Reviews* 13.8, pp. 1975–1984. ISSN: 13640321. DOI: 10.1016/j.rser.2009.01.014.
- Salter, S. H. (1974). ‘Wave power’. In: *Nature* 249.5459, pp. 720–724. ISSN: 1476-4687. DOI: 10.1038/249720a0. URL: <https://doi.org/10.1038/249720a0>.
- Sandberg, A. B., E. Klementsén, G. Muller, A. de Andres and J. Maillet (2016). ‘Critical factors influencing viability of wave energy converters in off-grid luxury resorts and small utilities’. In: *Sustainability (Switzerland)* 8.12, pp. 1–22. ISSN: 20711050. DOI: 10.3390/su8121274.
- Sarmiento, A. J. N. A. (1993). ‘Model-test optimization of an OWC wave power plant’. In: *International Journal of Offshore and Polar Engineering* 3.1, pp. 66–72.
- Schreck, E., M. Peric and D. Snyder (2012). ‘Overset Grid Technology in STAR-CCM+: Methodology and Applications’. In: *11th Symposium on Overset Composite Grids and Solution Technology*. URL: [http://2012.oversetgridsymposium.org/assets/pdf/presentations/2%7B%5C\\_%7D3/Overset%7B%5C\\_%7DSchreck%7B%5C\\_%7DPeric%7B%5C\\_%7DSnyder.pdf](http://2012.oversetgridsymposium.org/assets/pdf/presentations/2%7B%5C_%7D3/Overset%7B%5C_%7DSchreck%7B%5C_%7DPeric%7B%5C_%7DSnyder.pdf).
- Schroeder, G. (2011). *HyPower*. Tech. rep. URL: [https://voith.com/corp-en/HyPower%7B%5C\\_%7D20%7B%5C\\_%7Dfinal.pdf](https://voith.com/corp-en/HyPower%7B%5C_%7D20%7B%5C_%7Dfinal.pdf).

- Scottish Government (2019). *Draft Sectoral Marine Plan for Offshore Wind Energy (2019)*. December, pp. 1–74. ISBN: 9781839603747. URL: [http://marine.gov.scot/sites/default/files/draft%7B%5C\\_%7Dsectoral%7B%5C\\_%7Dmarine%7B%5C\\_%7Dplan%7B%5C\\_%7Dfor%7B%5C\\_%7Doffshore%7B%5C\\_%7Dwind%7B%5C\\_%7Denergy%7B%5C\\_%7D-%7B%5C\\_%7Dconsultation%7B%5C\\_%7Devent%7B%5C\\_%7Ddetails.pdf](http://marine.gov.scot/sites/default/files/draft%7B%5C_%7Dsectoral%7B%5C_%7Dmarine%7B%5C_%7Dplan%7B%5C_%7Dfor%7B%5C_%7Doffshore%7B%5C_%7Dwind%7B%5C_%7Denergy%7B%5C_%7D-%7B%5C_%7Dconsultation%7B%5C_%7Devent%7B%5C_%7Ddetails.pdf).
- Sharkey, F., E. Bannon, M. Conlon and K. Gaughan (2013). ‘Maximising value of electrical networks for wave energy converter arrays’. In: *International Journal of Marine Energy* 1, pp. 55–69. DOI: 10.1016/j.ijome.2013.06.002.
- Siemens Gamesa Renewable Energy (2021). *SG 5.8-170*. URL: [siemensgamesa.com/en-int/products-and-services/onshore/wind-turbine-sg-5-8-170](https://www.siemensgamesa.com/en-int/products-and-services/onshore/wind-turbine-sg-5-8-170) (visited on 27/01/2021).
- Silva, D., E. Rusu and C. G. Soares (2013). ‘Evaluation of various technologies for wave energy conversion in the Portuguese nearshore’. In: *Energies* 6.3, pp. 1344–1364. ISSN: 19961073. DOI: 10.3390/en6031344.
- Silvester, R. (1974). *Coastal Engineering*. Coastal Engineering v. 4, pt. 1. Elsevier Scientific Publishing Company. ISBN: 9780444411013. URL: <https://books.google.co.uk/books?id=22wYAQAAIAAJ>.
- Silvester, R. (1987). ‘INFLUENCE OF OBLIQUE REFLECTION ON BREAKWATERS.’ In: *Proceedings of the Coastal Engineering Conference*. Vol. 3, pp. 2253–2267. ISBN: 0872626008. DOI: 10.1061/9780872626003.166.
- Sjolte, J. and E. Hjetland (2016). ‘Off-shore Autonomous Power Supply : Measured performance of the BOLT Lifesaver System and Future Application as a Low Observable Sensor System and Recharge Station’. In: *Marine Energy Technology Symposium*.
- Smith, J. O. (2011). *Spectral Audio Signal Processing*. W3K Publishing, pp. 1–674. ISBN: 978-0-9745607-3-1. URL: [https://ccrma.stanford.edu/%7B~%7Djos/sasp/%7B%5C\\_%7D5Cnhttp://books.w3k.org/](https://ccrma.stanford.edu/%7B~%7Djos/sasp/%7B%5C_%7D5Cnhttp://books.w3k.org/).
- Sorensen, H. C. (2006). *Sea Testing and Optimisation of Power Production on a Scale 1:4.5 Test Rig of the Offshore Wave Energy Converter Wave Dragon*. Tech. rep. Copenhagen: SPOK.

- Stansby, P. K., H. Gu, E. Carpintero Moreno and T. Stallard (Sept. 2015a). ‘Drag minimisation for high capture width with three float wave energy converter M4’. In:
- Stansby, P., E. Carpintero Moreno and T. Stallard (2017). ‘Large capacity multi-float configurations for the wave energy converter M4 using a time-domain linear diffraction model’. In: *Applied Ocean Research* 68, pp. 53–64. ISSN: 01411187. DOI: 10.1016/j.apor.2017.07.018. URL: <http://dx.doi.org/10.1016/j.apor.2017.07.018>.
- Stansby, P., E. Carpintero Moreno, T. Stallard and A. Maggi (2015b). ‘Three-float broad-band resonant line absorber with surge for wave energy conversion’. In: *Renewable Energy* 78, pp. 132–140. ISSN: 0960-1481.
- Stansby, P., E. Carpintero Moreno, T. Stallard, A. Maggi and R. Eatock Taylor (2014). ‘Wave energy conversion with high capture width by the three-float line absorber M4’. In: *Proceedings Renewable Energies Offshore, Lisbon*. URL: <https://books.google.co.uk/books?id=nNCYCgAAQBAJ%7B%5C%7Dlpg=PA393%7B%5C%7Dots=omYBWILVPk%7B%5C%7Dlr%7B%5C%7Dpg=PA393%7B%5C%7Dv=onepage%7B%5C%7Dq%7B%5C%7Df=false>.
- Stansby, P., E. C. Moreno and T. Stallard (2015c). ‘Capture width of the three-float multi-mode multi-resonance broadband wave energy line absorber M4 from laboratory studies with irregular waves of different spectral shape and directional spread’. In: *Journal of Ocean Engineering and Marine Energy* 1.3, pp. 287–298. ISSN: 21986452. DOI: 10.1007/s40722-015-0022-6. URL: <http://dx.doi.org/10.1007/s40722-015-0022-6>.
- Straume, I. (2010). *Wave energy concepts overview numbered*. URL: <https://commons.wikimedia.org/wiki/File:WECs-2020.png> (visited on 20/03/2020).
- Straume, I. (2014). *Ocean wave phases numbered*. URL: <https://upload.wikimedia.org/wikipedia/commons/3/3d/Ocean%7B%5C%7Dwave%7B%5C%7Dphases%7B%5C%7Dnumbered.png> (visited on 14/05/2020).
- Tan Loh, T., D. Greaves, T. Maki, M. Vuorinen, D. Simmonds and A. Kyte (Oct. 2016). ‘Numerical Modelling of the WaveRoller Device Using OpenFOAM’. In:

- 3rd Asian Wave and Tidal Energy Conference*, pp. 134–143. DOI: 10.3850/978-981-11-0782-5\_61.
- Tedd, J. and J. P. Kofoed (2009). ‘Measurements of overtopping flow time series on the Wave Dragon, wave energy converter’. English. In: *Renewable Energy* 34.3, pp. 711–717. DOI: 10.1016/j.renene.2008.04.036.
- Tedd, J., J. P. Kofoed, W. Knapp, E. Friis-madsen and H. C. Sørensen (2006). ‘Wave Dragon , prototype wave power production’. In: *World Renewable Energy Congress*.
- Tezdogan, T., A. Incecik and O. Turan (2016). ‘Full-scale unsteady RANS simulations of vertical ship motions in shallow water’. In: *Ocean Engineering* 123, pp. 131–145. DOI: 10.1016/j.oceaneng.2016.06.047. URL: <http://www.sciencedirect.com/science/article/pii/S0029801816302372>%20https://ac.els-cdn.com/S0029801816302372/1-s2.0-S0029801816302372-main.pdf?%7B%5C\_%7Dtid=d31376a7-7168-44cf-8c13-46b3289038a9%7B%5C%7Dacdnat=1533721889%7B%5C\_%7D96c8d84ec29bf0cb41f5181eaf21a5e3.
- The European Marine Energy Centre (2009). *Tank Testing of Wave Energy Conversion Systems*. Tech. rep.
- The Queen’s University Belfast (2002). *Islay LIMPET wave power plant*. Tech. rep. April, pp. 1–62. URL: [cordis.europa.eu/documents/documentlibrary/66628981EN6.pdf](http://cordis.europa.eu/documents/documentlibrary/66628981EN6.pdf).
- Thiébaud, F., G. Sutton and C. Johnstone (2015). ‘D2.28 Model Construction Methods’. In: *MARINET Report*.
- Thoresen, C. A. (2018). *Berthing requirements*, pp. 105–148. ISBN: 9780727760043. DOI: 10.1680/pdhbfe.63075.105.
- Thornton, E. B. and R. J. Calhoun (1972). ‘Spectral Resolution of Breakwater Reflected Waves.’ In: *ASCE J Waterw Harbors Coastal Eng Div* 98.WW4, pp. 443–460.
- Toffoli, A., T. Waseda, H. Houtani, L. Cavaleri, D. Greaves and M. Onorato (2015). ‘Rogue waves in opposing currents: An experimental study on deterministic and stochastic wave trains’. In: *Journal of Fluid Mechanics* 769.April, pp. 277–297. ISSN: 14697645. DOI: 10.1017/jfm.2015.132.

- Torre-Enciso, Y., I. Ortubia, L. I. Aguilera and J. Marqués (Jan. 2009). ‘Mutriku Wave Power Plant: From the Thinking out to the Reality’. In: *Proceedings of the 8th European Wave and Tidal Energy Conference*, pp. 319–329.
- Tucker, M. J. (1991). *Waves in Ocean Engineering: Measurement, Analysis, Interpretation*. Ellis Horwood Series in Applied Science and Industrial Techn. E. Horwood. ISBN: 9780139329555.
- UK Parliament (2021). *Environment Bill 2019-21 - UK Parliament*. URL: <https://services.parliament.uk/Bills/2019-21/environment.html> (visited on 12/01/2021).
- Van der Meer, J. W., N.W.H. Allsop, T. Bruce, J. De Rouck, A. Kortenhaus, T. Pullen, H. Schüttrumpf, P. Troch and B. Zanuttigh (2018). *EurOtop*, p. 320.
- Venugopal, V. and G. Smith (2007). ‘Wave climate investigation for an array of wave power devices’. In: *7th European Wave and Tidal Energy Conference*, pp. 1–10.
- Vicinanza, D., F. Ciardulli, M. Buccino, M. Calabrese and J. P. Kofoed (Jan. 2011). ‘Wave Loadings acting on an innovative breakwater for energy production’. In: *Journal of Coastal Research* SI 64, pp. 608–612.
- Vicinanza, D., F. Dentale, D. Salerno and M. Buccino (June 2015). *Structural Response of Seawave Slot-cone Generator (SSG) from Random Wave CFD Simulations*.
- Vicinanza, D. and P. Frigaard (2008). ‘Wave pressure acting on a seawave slot-cone generator’. English. In: *Coastal Engineering* 55.6, pp. 553–568. DOI: 10.1016/j.coastaleng.2008.02.011.
- Vicinanza, D., L. Margheritini, J. P. Kofoed and M. Buccino (2012). ‘The SSG wave energy converter: Performance, status and recent developments’. In: *Energies* 5.2, pp. 193–226. ISSN: 19961073. DOI: 10.3390/en5020193.
- Weinstein, A., G. Fredrikson, L. Claeson, J. Forsberg, M. J. Parks, K. Nielsen, M. S. Jenses, K. Zandiyeh, P. Frigaard, M. Kramer and T. L. Andersen (2003). ‘AquaBuOY-the offshore wave energy converter numerical modeling and optimization’. In: *Oceans 2003. Celebrating the Past ... Teaming Toward the Future (IEEE Cat. No.03CH37492)*. Vol. 4, 1988–1995 Vol.4. DOI: 10.1109/OCEANS.2003.178203.

- Weinstein, A., G. Fredrikson, M. J. Parks and K. Nielsen (2004). ‘AquaBuOY - The offshore wave energy converter numerical modeling and optimization’. In: *Ocean '04 - MTS/IEEE Techno-Ocean '04: Bridges across the Oceans*. Vol. 4, pp. 1854–1859. ISBN: 0780386698. DOI: 10.1109/oceans.2004.1406425.
- Welch, P. D. (1975). ‘The Use of Fast Fourier Transform for the Estimation of Power Spectra’. In: *Digital Signal Processing* 2, pp. 532–574.
- Wello Oy (2021). *The Penguin Wave Energy Converter*. URL: <https://wello.eu/the-penguin-2/> (visited on 20/01/2021).
- Whittaker, T. J. T., W. Beattie, M. Folley, C. Boake, A. Wright and M. Osterried (2004). ‘The Limpet Wave Power Project – The First Years Of Operation’. In: *Scottish Hydraulics Study Group - Seminar on the Hydraulic Aspects of Renewable Energy* 1997, pp. 1–8.
- Whittaker, T., W. Beattie and M. Folley (Jan. 2003). ‘Performance of the LIMPET wave power plant - Prediction, measurement and potential’. In: *Proceedings of the 5th European Wave Energy Conference*, pp. 97–104.
- Whittaker, T., D. Collier, M. Folley, M. Osterried and A. Henry (2007). ‘The development of Oyster - A shallow water surging wave energy converter’. In: *7th European Wave and Tidal Energy Conference* January 2017, pp. 11–14.
- Whittaker, T. and M. Folley (2012). ‘Nearshore oscillating wave surge converters and the development of Oyster’. In: *Philosophical Transactions of the Royal Society A: Mathematical, Physical and Engineering Sciences* 370.1959, pp. 345–364. ISSN: 1364503X. DOI: 10.1098/rsta.2011.0152.
- Wiegel, R.L. (1964). ‘Water Wave Equivalent of Mach-Reflection’. In: *Coastal Engineering Proceedings* 1.9, p. 6. ISSN: 0589-087X. DOI: 10.9753/icce.v9.6.
- Wiersma, B. (2016). ‘Public acceptability of offshore renewable energy in Guernsey : Using visual methods to investigate local energy deliberations’. In: January, p. 372.
- Wolgamot, H. A., P. H. Taylor and R. E. Taylor (2012). ‘The interaction factor and directionality in wave energy arrays’. English. In: *Ocean Engineering* 47, pp. 65–73. DOI: 10.1016/j.oceaneng.2012.03.017.

- Yemm, R., D. Pizer, C. Retzler and R. Henderson (2012). ‘Pelamis: Experience from concept to connection’. In: *Philosophical Transactions of the Royal Society A: Mathematical, Physical and Engineering Sciences* 370.1959, pp. 365–380. ISSN: 1364503X. DOI: 10.1098/rsta.2011.0312.
- Yuan, Z., L. Zhang, B. Zhou, P. Jin and X. Zheng (2019). ‘Analysis of the Hydrodynamic Performance of an Oyster Wave Energy Converter Using Star-CCM+’. In: *Journal of Marine Science and Application* 18.2, pp. 153–159. ISSN: 16719433. DOI: 10.1007/s11804-019-00076-8.
- Zhou, Z., R. Lewis and P. Iqbal (2009). *Wave Dragon (WD) WM Power Take Off System, Electrical system configuration, power electronics converters and generator control, Final report*. Tech. rep. Swansea: Electronics Systems Design Centre, School of Engineering, University of Swansea.



# Appendix A

## Modelling Setup

This section gives a list of WG locations, tests run for each model configuration and constants used in the analysis. The parameters shown are those entered into the wave generation software, with actual parameters measured shown in 4.7. For regular waves  $H_m$  is the wave height at model scale and  $H$  is the wave height at full scale. The model scale wave period is  $T_m$  and at full scale is  $T$ . For random waves  $H_{sm}$  is the significant wave height at model scale and  $H_s$  is the significant wave height at full scale. The model scale peak period is  $T_{pm}$  and the full scale peak period is  $T_p$ .

### A.1 Basin Repeatability

The repeatability of surface elevation was examined for both regular and random waves in the Ocean Basin.

Figure A.1 shows the repeatability of the 10 regular wave tests of  $H = 0.05$  m and  $T = 1.59$  s. One test was taken as a benchmark case and the other tests compared to the benchmark test. The surface elevation was compared for each timestep during a test, as the tests should be generating identical wave trains throughout the tests. A

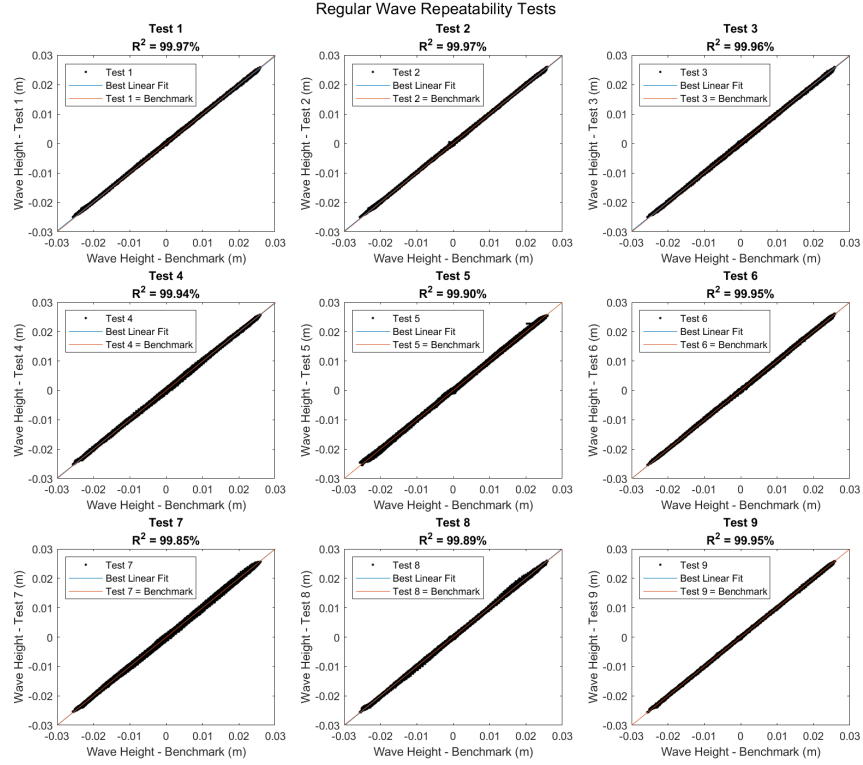


FIGURE A.1: Regular wave repeatability tests with wave conditions  $H = 0.05$  m and  $T = 1.59$  s

fit line was plotted with  $R^2$  values determined. High values between the tests show the repeatability is maintained.

Figure A.2 shows the repeatability between the three sets of random wave tests. Wave conditions  $H_s = 0.067$  m and  $T_p = 2.01$  s are shown on the top row,  $H_s = 0.1$  m and  $T_p = 2.37$  s on the middle row and  $H_s = 0.15$  m and  $T_p = 2.37$  s on the bottom row. Again, the repeatability is good, however it is lower as  $H_s$  is increased.

## A.2 Wave Synthesis Software

Figure A.3 shows the Njörðr Wave Synthesis interface for both regular, Figure A.3a, and random waves, Figure A.3b. The list of tests that have been made are shown in Area 1 and are contained within a file which was loaded into the wavemaker

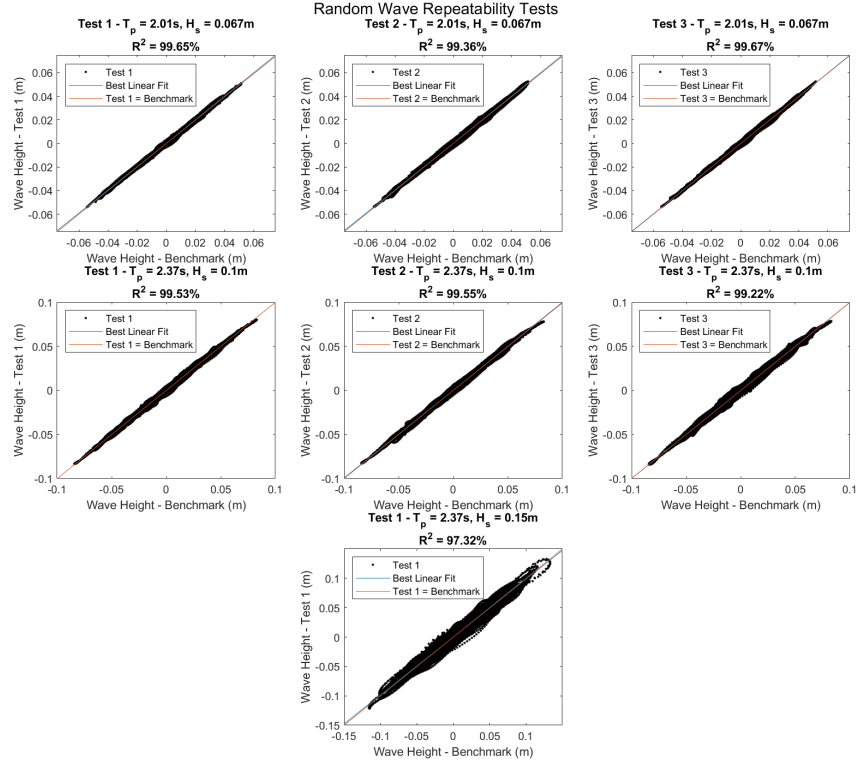
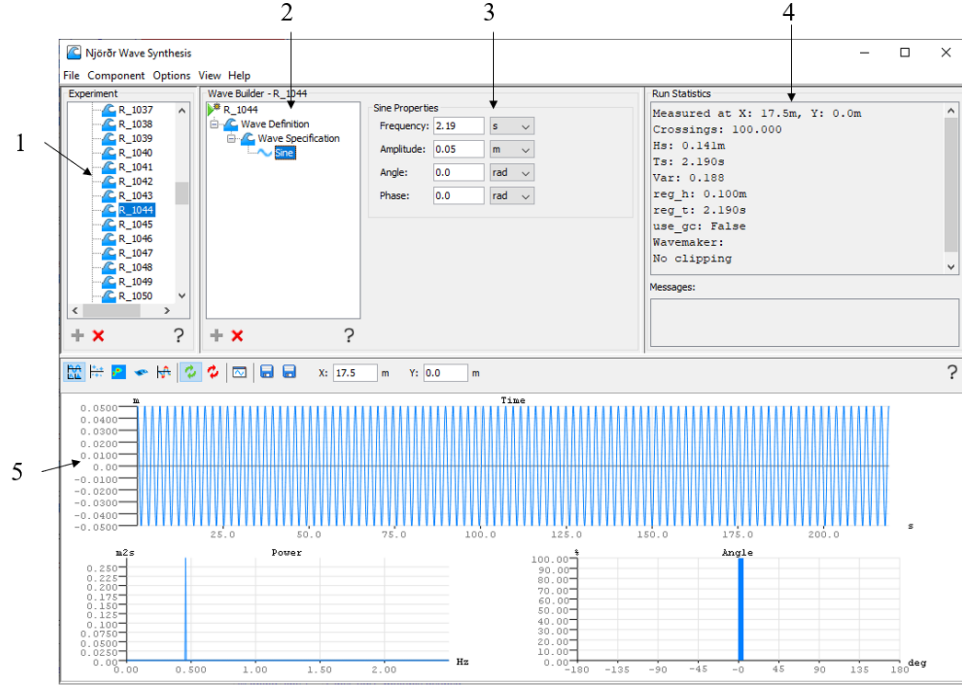
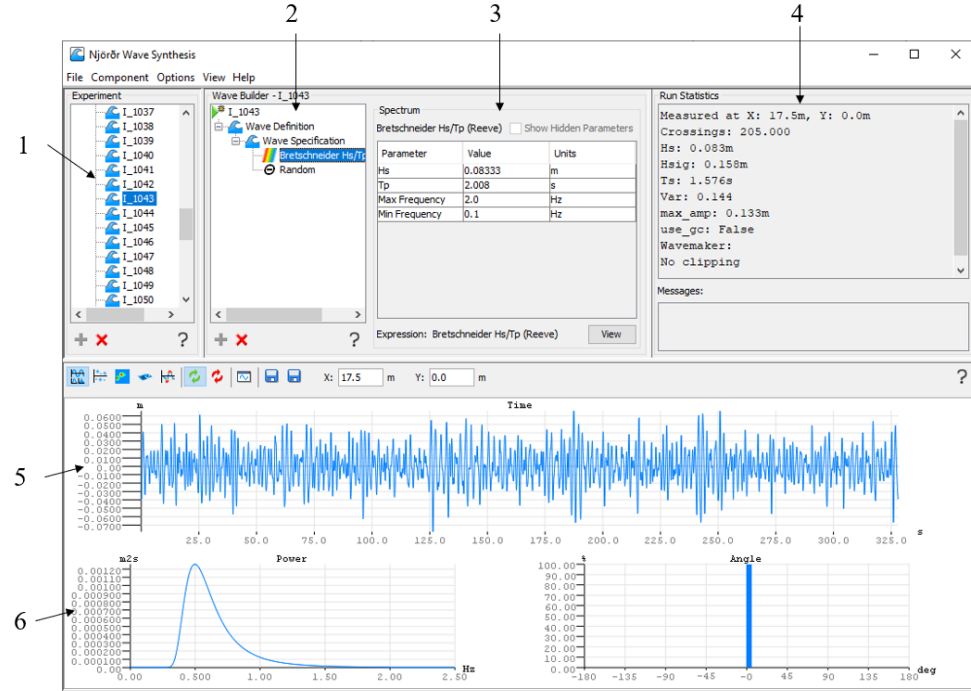


FIGURE A.2: Random wave repeatability tests with wave conditions  $H_s = 0.067$  m and  $T_p = 2.01$  s on the top row,  $H_s = 0.1$  m and  $T_p = 2.37$  s on the middle row and  $H_s = 0.15$  m and  $T_p = 2.37$  s on the bottom row

software in preparation for running the tests. Area 2 shows the type of waves of the test selected in Area 1. For regular tests a simple sine wave was used and for random waves an appropriate spectrum was used. In these tests a Bretschneider spectrum was used, with a random phase factor applied to randomly order the waves, otherwise all the waves are generated at once resulting in one large wave at the model. Area 3 shows the test specific conditions that were configurable for each test. Each level of the configuration in Area 3 has its own configurable properties, including, for example, run time and location specification. This controlled the length of the test and the location at which the generated waves had the specified properties respectively. Area 4 has a brief summary of the conditions of the test. Area 5 shows a time trace of the surface elevation the wave paddles will generate, in particular for the random waves the randomness can be seen. For random waves in



(a) Njörðr Wave Synthesis interface showing a configured regular wave test



(b) Njörðr Wave Synthesis interface showing a configured random wave test

FIGURE A.3: Njörðr Wave Synthesis interfaces showing both regular and random example tests. 1 shows the test list, 2 shows the test specification, 3 shows the test parameters, 4 shows a summary of test conditions, 5 shows the expected surface elevation and 6 shows the expected power spectrum.

Area 6 a power spectrum is also shown, allowing quick verification that the software was generating appropriate waves.

### A.3 60° Initial Regular Tests

TABLE A.1: Initial regular wave tests showing model and full scale conditions

Test Case	$H_m$ (m)	$H$ (m)	$T_m$ (s)	$T$ (s)
1	0.05	1.50	1.28	7
2	0.05	1.50	1.64	9
3	0.05	1.50	2.01	11
4	0.05	1.50	2.37	13
5	0.12	3.50	1.28	7
6	0.12	3.50	1.64	9
7	0.12	3.50	2.01	11
8	0.12	3.50	2.37	13
9	0.18	5.50	1.28	7
10	0.18	5.50	1.64	9
11	0.18	5.50	2.01	11
12	0.18	5.50	2.37	13

### A.4 60° Initial Random Tests

TABLE A.2: Initial random wave tests showing model and full scale conditions

Test Case	$H_{sm}$ (m)	$H_s$ (m)	$T_{pm}$ (s)	$T_p$ (s)
1	0.02	0.50	1.28	7
2	0.02	0.50	1.64	9
3	0.02	0.50	2.01	11
4	0.02	0.50	2.37	13
5	0.08	2.50	1.28	7
6	0.08	2.50	1.64	9
7	0.08	2.50	2.01	11
8	0.08	2.50	2.37	13
9	0.15	4.50	1.28	7
10	0.15	4.50	1.64	9
11	0.15	4.50	2.01	11
12	0.15	4.50	2.37	13

## A.5 30° Regular Wave Tests

TABLE A.3:  $\theta_w = 30^\circ$  regular wave tests showing model and full scale conditions

Test Case	$H_m$ (m)	$H$ (m)	$T_m$ (s)	$T$ (s)
1	0.02	0.50	1.83	10
2	0.02	0.50	2.56	14
3	0.05	1.50	1.46	8
4	0.05	1.50	2.01	11
5	0.05	1.50	2.37	13
6	0.08	2.50	1.28	7
7	0.08	2.50	1.64	9
8	0.08	2.50	1.83	10
9	0.08	2.50	2.19	12
10	0.12	3.50	1.46	8
11	0.12	3.50	2.01	11
12	0.12	3.50	2.01	11
13	0.12	3.50	2.01	11
14	0.12	3.50	2.01	11
15	0.12	3.50	2.37	13
16	0.12	3.50	2.56	14
17	0.15	4.50	1.83	10

## A.6 30° Random Wave Tests

TABLE A.4:  $\theta_w = 30^\circ$  random wave tests showing model and full scale conditions

Test Case	$H_{sm}$ (m)	$H_s$ (m)	$T_{pm}$ (s)	$T_p$ (s)
1	0.07	2.00	1.28	7
2	0.07	2.00	1.46	8
3	0.07	2.00	1.64	9
4	0.07	2.00	1.83	10

Test Case	$H_{sm}$ (m)	$H_s$ (m)	$T_{pm}$ (s)	$T_p$ (s)
5	0.07	2.00	2.01	11
6	0.07	2.00	2.19	12
7	0.07	2.00	2.37	13
8	0.07	2.00	2.56	14
9	0.08	2.50	1.28	7
10	0.08	2.50	1.46	8
11	0.08	2.50	1.64	9
12	0.08	2.50	1.64	9
13	0.08	2.50	1.83	10
14	0.08	2.50	2.01	11
15	0.08	2.50	2.19	12
16	0.08	2.50	2.37	13
17	0.08	2.50	2.56	14
18	0.10	3.00	1.28	7
19	0.10	3.00	1.46	8
20	0.10	3.00	1.64	9
21	0.10	3.00	1.83	10
22	0.10	3.00	2.01	11
23	0.10	3.00	2.01	11
24	0.10	3.00	2.19	12
25	0.10	3.00	2.37	13
26	0.10	3.00	2.56	14
27	0.12	3.50	1.28	7
28	0.12	3.50	1.46	8
29	0.12	3.50	1.64	9
30	0.12	3.50	1.83	10
31	0.12	3.50	2.01	11
32	0.12	3.50	2.19	12
33	0.12	3.50	2.37	13
34	0.12	3.50	2.56	14



Test Case	$H_{sm}$ (m)	$H_s$ (m)	$T_{pm}$ (s)	$T_p$ (s)
35	0.13	4.00	1.28	7
36	0.13	4.00	1.46	8
37	0.13	4.00	1.64	9
38	0.13	4.00	1.83	10
39	0.13	4.00	2.01	11
40	0.13	4.00	2.19	12
41	0.13	4.00	2.37	13
42	0.13	4.00	2.56	14
43	0.15	4.50	1.28	7
44	0.15	4.50	1.46	8
45	0.15	4.50	1.64	9
46	0.15	4.50	1.83	10
47	0.15	4.50	2.01	11
48	0.15	4.50	2.19	12
49	0.15	4.50	2.37	13
50	0.15	4.50	2.56	14

## A.7 60° Regular Wave Tests

TABLE A.5:  $\theta_w = 60^\circ$  regular wave tests showing model and full scale conditions

Test Case	$H_m$ (m)	$H$ (m)	$T_m$ (s)	$T$ (s)
1	0.03	1.00	0.91	5
2	0.03	1.00	1.10	6
3	0.03	1.00	1.28	7
4	0.03	1.00	1.46	8
5	0.03	1.00	1.64	9
6	0.03	1.00	1.83	10
7	0.03	1.00	2.01	11
8	0.03	1.00	2.19	12

Test Case	$H_m$ (m)	$H$ (m)	$T_m$ (s)	$T$ (s)
9	0.03	1.00	2.37	13
10	0.05	1.50	0.91	5
11	0.05	1.50	1.10	6
12	0.05	1.50	1.28	7
13	0.05	1.50	1.46	8
14	0.05	1.50	1.64	9
15	0.05	1.50	1.83	10
16	0.05	1.50	2.01	11
17	0.05	1.50	2.19	12
18	0.05	1.50	2.37	13
19	0.07	2.00	0.91	5
20	0.07	2.00	1.10	6
21	0.07	2.00	1.28	7
22	0.07	2.00	1.46	8
23	0.07	2.00	1.46	8
24	0.07	2.00	1.46	8
25	0.07	2.00	1.46	8
26	0.07	2.00	1.64	9
27	0.07	2.00	1.83	10
28	0.07	2.00	2.01	11
29	0.07	2.00	2.19	12
30	0.07	2.00	2.37	13
31	0.08	2.50	0.91	5
32	0.08	2.50	1.10	6
33	0.08	2.50	1.28	7
34	0.08	2.50	1.46	8
35	0.08	2.50	1.64	9
36	0.08	2.50	1.83	10
37	0.08	2.50	2.01	11
38	0.08	2.50	2.19	12

Test Case	$H_m$ (m)	$H$ (m)	$T_m$ (s)	$T$ (s)
39	0.08	2.50	2.37	13
40	0.10	3.00	0.91	5
41	0.10	3.00	1.10	6
42	0.10	3.00	1.28	7
43	0.10	3.00	1.46	8
44	0.10	3.00	1.64	9
45	0.10	3.00	1.83	10
46	0.10	3.00	2.01	11
47	0.10	3.00	2.01	11
48	0.10	3.00	2.01	11
49	0.10	3.00	2.01	11
50	0.10	3.00	2.19	12
51	0.10	3.00	2.37	13
52	0.12	3.50	0.91	5
53	0.12	3.50	1.10	6
54	0.12	3.50	1.28	7
55	0.12	3.50	1.46	8
56	0.12	3.50	1.64	9
57	0.12	3.50	1.83	10
58	0.12	3.50	2.01	11
59	0.12	3.50	2.19	12
60	0.12	3.50	2.37	13
61	0.13	4.00	1.64	9
62	0.13	4.00	1.83	10
63	0.13	4.00	2.01	11
64	0.13	4.00	2.19	12
65	0.13	4.00	2.37	13

## A.8 60° Random Wave Tests

TABLE A.6:  $\theta_w = 60^\circ$  random wave tests showing model and full scale conditions

Test Case	$H_{sm}$ (m)	$H_s$ (m)	$T_{pm}$ (s)	$T_p$ (s)
1	0.03	1.00	0.91	5
2	0.03	1.00	1.10	6
3	0.03	1.00	1.28	7
4	0.03	1.00	1.46	8
5	0.03	1.00	1.64	9
6	0.03	1.00	1.83	10
7	0.03	1.00	2.01	11
8	0.03	1.00	2.19	12
9	0.03	1.00	2.37	13
10	0.05	1.50	0.91	5
11	0.05	1.50	1.10	6
12	0.05	1.50	1.28	7
13	0.05	1.50	1.46	8
14	0.05	1.50	1.64	9
15	0.05	1.50	1.83	10
16	0.05	1.50	2.01	11
17	0.05	1.50	2.19	12
18	0.05	1.50	2.37	13
19	0.07	2.00	0.91	5
20	0.07	2.00	1.10	6
21	0.07	2.00	1.28	7
22	0.07	2.00	1.46	8
23	0.07	2.00	1.64	9
24	0.07	2.00	1.83	10
25	0.07	2.00	2.01	11
26	0.07	2.00	2.01	11
27	0.07	2.00	2.01	11

Test Case	$H_{\text{sm}}$ (m)	$H_s$ (m)	$T_{\text{pm}}$ (s)	$T_p$ (s)
28	0.07	2.00	2.01	11
29	0.07	2.00	2.19	12
30	0.07	2.00	2.37	13
31	0.08	2.50	0.91	5
32	0.08	2.50	1.10	6
33	0.08	2.50	1.28	7
34	0.08	2.50	1.46	8
35	0.08	2.50	1.64	9
36	0.08	2.50	1.83	10
37	0.08	2.50	2.01	11
38	0.08	2.50	2.19	12
39	0.08	2.50	2.37	13
40	0.10	3.00	0.91	5
41	0.10	3.00	1.10	6
42	0.10	3.00	1.28	7
43	0.10	3.00	1.46	8
44	0.10	3.00	1.64	9
45	0.10	3.00	1.83	10
46	0.10	3.00	2.01	11
47	0.10	3.00	2.19	12
48	0.10	3.00	2.37	13
49	0.10	3.00	2.37	13
50	0.10	3.00	2.37	13
51	0.10	3.00	2.37	13
52	0.12	3.50	0.91	5
53	0.12	3.50	1.10	6
54	0.12	3.50	1.28	7
55	0.12	3.50	1.46	8
56	0.12	3.50	1.64	9
57	0.12	3.50	2.01	11

Test Case	$H_{sm}$ (m)	$H_s$ (m)	$T_{pm}$ (s)	$T_p$ (s)
58	0.12	3.50	2.19	12
59	0.12	3.50	2.37	13

## A.9 WG Locations

### A.9.1 Initial 60° Tests

TABLE A.7: Wave gauge locations for 60° single device tests, positive distance from the centre line is towards the starboard of the WaveCat

Gauge Number	Distance from paddles (m)	Distance from centre line (m)
WG 1	13.16	0.00
WG 2	13.36	0.00
WG 3	13.66	0.00
WG 4	19.28	-5.07
WG 5	20.75	0.00
WG 6	20.95	0.00
WG 7	21.25	0.00

### A.9.2 30° Tests

TABLE A.8: Wave gauge locations for 30° single device tests, positive distance from the centre line is towards the starboard of the WaveCat

Gauge Number	Distance from paddles (m)	Distance from centre line (m)
WG 1	14.10	0.00
WG 2	14.30	0.00
WG 3	14.80	0.00
WG 4	19.28	-5.17
WG 5	20.88	0.00
WG 6	21.08	0.00
WG 7	21.08	0.00

### A.9.3 60° Tests

TABLE A.9: Wave gauge locations for the second set of  $\theta_w = 60^\circ$  tests, positive distance from the centre line is towards the starboard of the WaveCat

Gauge Number	Distance from paddles (m)	Distance from centre line (m)
WG 1	10.40	0.00
WG 2	10.60	0.00
WG 3	10.90	0.00
WG 4	18.15	3.07
WG 5	20.31	0.00
WG 6	20.51	0.00
WG 7	20.81	0.00

## A.10 Experimental Constants

TABLE A.10: Experimental setup comparison between experimental sessions

Property	Unit	Model Angle (°)	
		60	30
Incident WG Separation	m	[-0.5 -0.2 0.0]	[-0.5 -0.2 0.0]
Transmission WG Distance from WG 3	m	9.41	6.08
Model Distance from WG 3	m	8.00	4.48
WG 4 Location	m	[18.15, 3.92]	[19.28, 6.02]
Transmission WG Separation	m	[-0.5 -0.2 0.0]	[-0.5 -0.2 0.0]
Beach Distance from Transmission WG	m	14.19	13.62
Model Effective Length ( $l$ )	m	2.62	2.91
Model Effective Width ( $B$ )	m	3.00	1.55

Table A.10 shows the experimental measurements that influenced the analysis method and the comparison between experimental campaigns. The incident WG separation is an array of distances in the wave propagation direction of WGs 1-3 respectively, with WG 3 as the origin of the array. The transmission WG distance is the distance of WG 7 from WG 3. The model distance is the distance between the model and WG 3 at the start of each test. The WG 4 location is the coordinates of the WG located to the side of the model experimental area, relative to the basin centreline and wavemakers. The transmission WG separation is an array of distances in the wave propagation direction of WGs 5, 6 and 7, with WG 7 as the origin of the array. The beach distance is the distance between the reflecting beach at the rear of the basin and WG 16 of the transmission array. The model effective length is the length of the model accounting for the wedge angle in the wave propagation direction. The model effective width is the aperture of the model across the wave crest.



## A.11 Repeat Tests

### A.11.1 30° Regular Wave Repeat Tests

TABLE A.11:  $\theta_w = 30^\circ$  regular wave repeat tests showing model and full scale conditions

Test Case	$H_{sm}$ (m)	$H_s$ (m)	$T_{pm}$ (s)	$T_p$ (s)
1	0.12	3.50	2.01	11
2	0.12	3.50	2.01	11
3	0.12	3.50	2.01	11
4	0.12	3.50	2.01	11

### A.11.2 30° Random Wave Repeat Tests

TABLE A.12:  $\theta_w = 30^\circ$  random wave repeat tests showing model and full scale conditions

Test Case	$H_{sm}$ (m)	$H_s$ (m)	$T_{pm}$ (s)	$T_p$ (s)
1	0.083	2.50	1.64	9
2	0.083	2.50	1.64	9
3	0.100	3.00	2.01	11
4	0.100	3.00	2.01	11

### A.11.3 60° Regular Wave Repeat Tests

TABLE A.13:  $\theta_w = 60^\circ$  regular wave repeat tests showing model and full scale conditions

Test Case	$H_{sm}$ (m)	$H_s$ (m)	$T_{pm}$ (s)	$T_p$ (s)
1	0.07	2.00	1.46	8
2	0.07	2.00	1.46	8
3	0.07	2.00	1.46	8
4	0.07	2.00	1.46	8
5	0.10	3.00	2.01	11
6	0.10	3.00	2.01	11
7	0.10	3.00	2.01	11
8	0.10	3.00	2.01	11

#### A.11.4 60° Random Wave Repeat Tests

TABLE A.14:  $\theta_w = 60^\circ$  random wave repeat tests showing model and full scale conditions

TestCase	$H_{sm}$ (m)	$H_s$ (m)	$T_{pm}$ (s)	$T_p$ (s)
1	0.07	2.00	2.01	11
2	0.07	2.00	2.01	11
3	0.07	2.00	2.01	11
4	0.07	2.00	2.01	11
5	0.10	3.00	2.37	13
6	0.10	3.00	2.37	13
7	0.10	3.00	2.37	13
8	0.10	3.00	2.37	13

### A.12 Numerical Modelling Test Case Run Times

This section gives a complete list of numerical model run times and the hardware specifications each test was executed on.

TABLE A.15: The runtimes of each wave case and the hardware the test was performed on

Test Case	CPU	Clock Speed (GHz)	Threads	CPU Time (s)
1	i7-2600	3.4	6	325,550
2	i7-2600	3.4	6	319,635
3	i7-4790k	4.0	6	266,744
4	i7-4790k	4.0	6	268,156
5	i7-4790k	4.0	6	267,977
6	i7-2600	3.4	6	322,887
7	i7-4790k	4.0	6	255,195
8	i7-2600	3.4	6	331,570
9	i7-4790k	4.0	6	265,723

# Appendix B

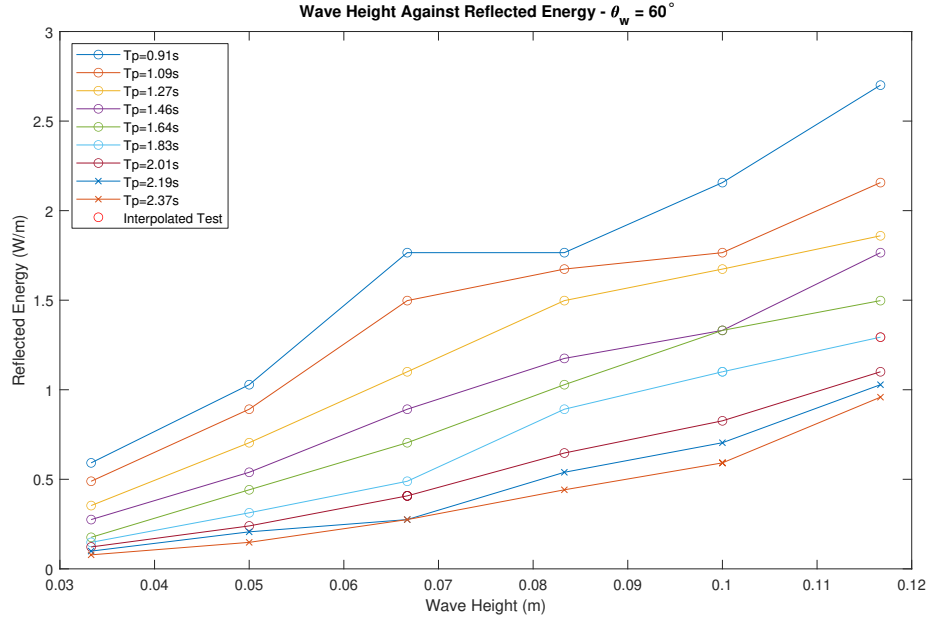
## Alternatively Displayed Results Graphs

### B.1 Reflected, Transmitted and Absorbed Energy

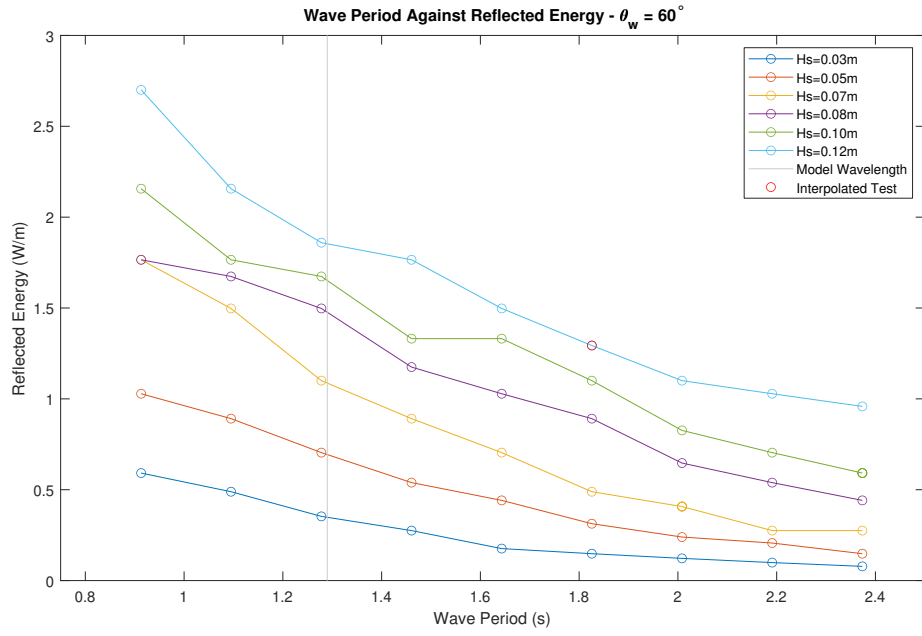
The results from Chapter 5 are presented here in alternative formats to assist with the understanding of the data.

#### B.1.1 $60^\circ$

Figure B.1 shows the reflected energy total over a test as a function of  $H_s$ , Figure B.1a, and  $T_p$ , Figure B.1b. When  $H_s$  was increased for tests of the same  $T_p$  characteristic, as shown in Figure B.1a, the amount of energy reflected over a test increased. It was also seen that increasing the  $T_p$  lowered the total amount of energy reflected over a test. When the test results were grouped by  $T_p$ , shown in Figure B.1b, it was seen that overall reflected energy was less at lower  $H_s$  tests. Also highlighted on the graph is the period associated with the wavelength of the model. This had little effect on the trend of the reflected energy total.

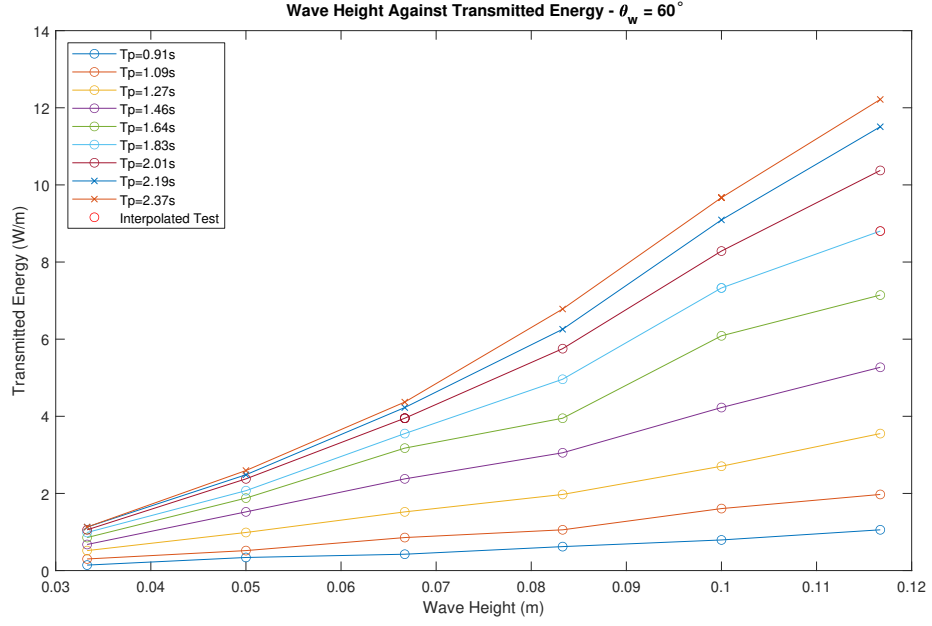


(a) Reflected energy against  $H_s$  for  $\theta_w = 60^\circ$

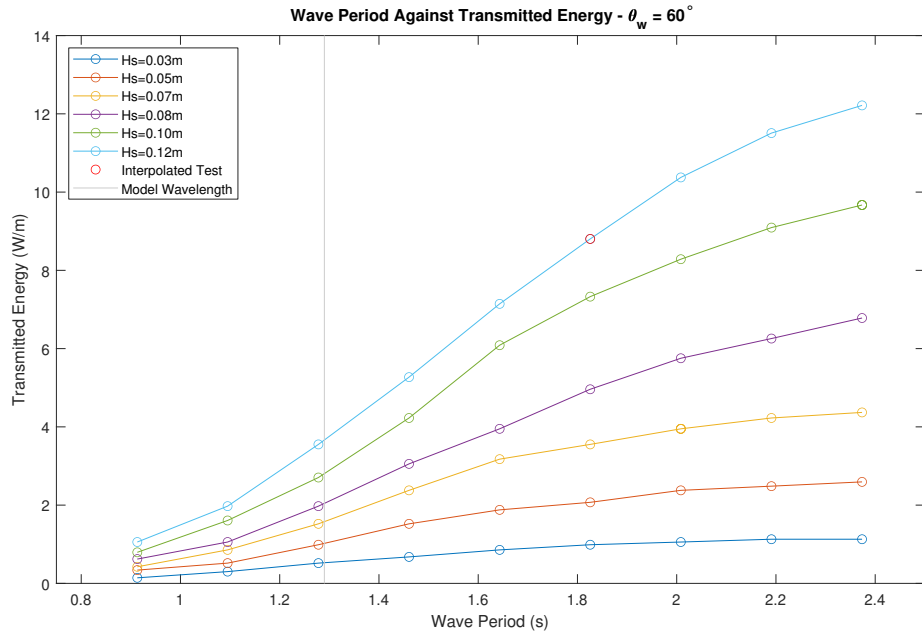


(b) Reflected energy against  $T_p$  for  $\theta_w = 60^\circ$

FIGURE B.1: Reflected energy shown as functions of (a)  $H_s$  and (b)  $T_p$  for  $\theta_w = 60^\circ$



(a) Transmitted energy grouped by  $H_s$  characteristic for  $\theta_w = 60^\circ$



(b) Transmitted energy grouped by  $T_p$  characteristic for  $\theta_w = 60^\circ$

FIGURE B.2: Transmitted energy shown as functions of (a)  $H_s$  and (b)  $T_p$  for  $\theta_w = 60^\circ$

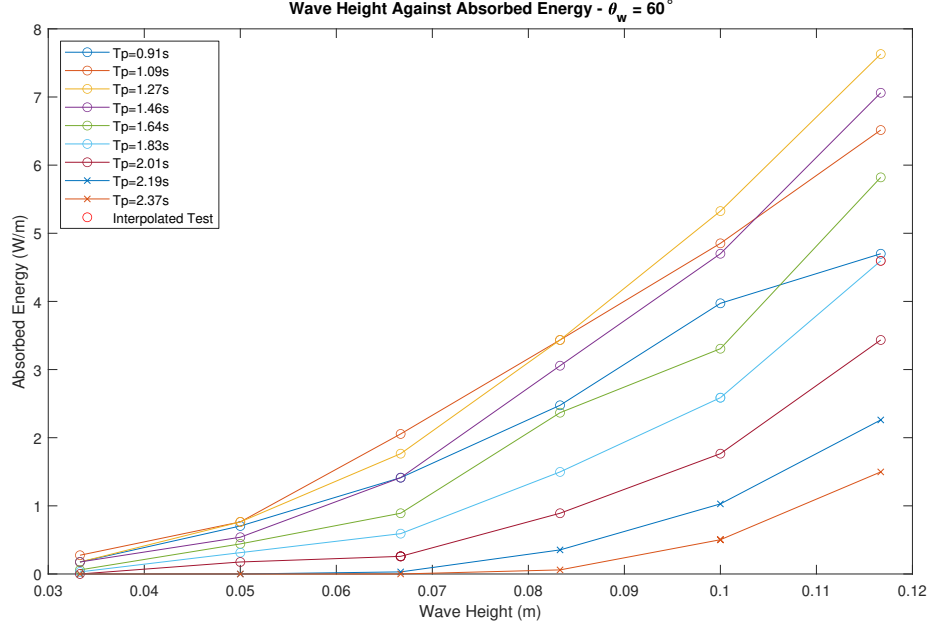
Figure B.2 shows the transmitted energy total over a test as a function of  $H_s$ , Figure B.2a, and  $T_p$ , Figure B.2b. When the data was grouped by  $T_p$  the amount of energy transmitted increased. When the data was grouped by  $H_s$  the amount of energy transmitted also increased. The WaveCat therefore transmitted the most energy when both  $H_s$  and  $T_p$  were high. If one or the other were high then the device did not transmit as much energy as when both were high. The wave period associated with the wavelength of the model, shown on Figure B.2b, had little effect on the amount of energy transmitted.

Figure B.3 shows the absorbed energy total over a test as a function of  $H_s$ , Figure B.3a, and  $T_p$ , Figure B.3b. When grouped by  $T_p$  the tests showed an increase in energy absorbed as  $H_s$  increased. However, the tests that had the largest absorbed energy were not the tests with the lowest or highest  $T_p$  characteristics, but the test with the  $T_p$  that was closest to the model frequency,  $T_p = 1.28$  s. The next highest absorbed energy totals came from the  $T_p$  tests either side of 1.28 s, 1.09 s and 1.46 s. This is clearly shown in Figure B.3b where there was a peak in the tests that had higher  $H_s$  values, however at  $H_s$  of 0.07 m the peak had moved to a lower wave period. At  $H_s$  values below that there was no peak suggesting a lack of overtopping.

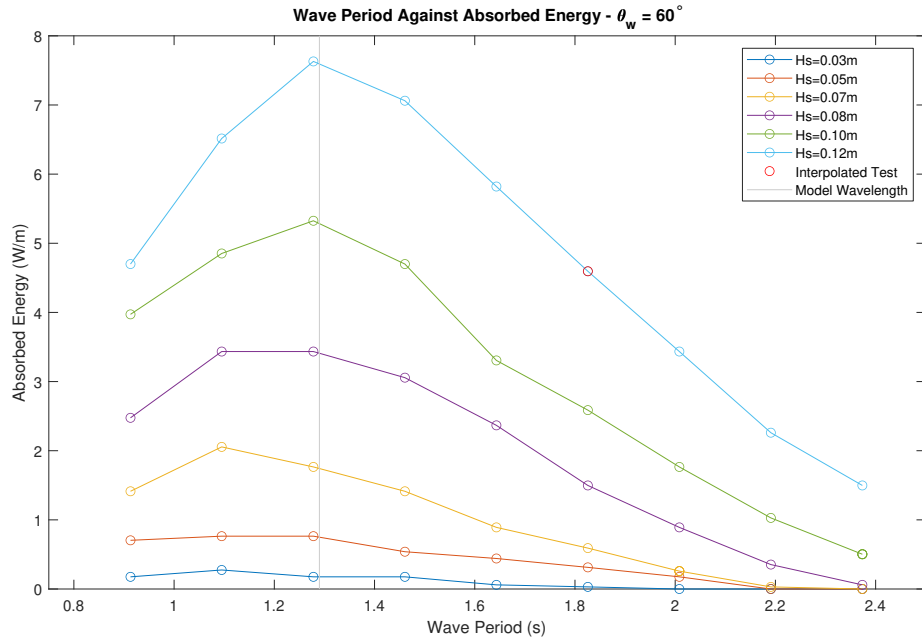
### B.1.2 30°

Figure B.4 shows the reflection energy total over a test as a function of  $H_s$ , Figure B.4a, and  $T_p$ , Figure B.4b. When increasing  $H_s$  for tests of the same  $T_p$ , as shown in Figure B.4a, the amount of energy reflected over a test increased. It was also seen that increasing the  $T_p$  lowered the total amount of energy reflected over a test. When grouping the test results by  $T_p$ , shown in Figure B.4b, it was seen that overall reflected energy was less at lower  $H_s$  tests.

Figure B.5 shows the transmitted energy total over a test as a function of  $H_s$ , Figure B.5a, and  $T_p$ , Figure B.5b. When the data was grouped by  $T_p$  the amount of energy transmitted increased. When the data was grouped by  $H_s$  the amount of energy transmitted also increased. The WaveCat therefore transmitted the most

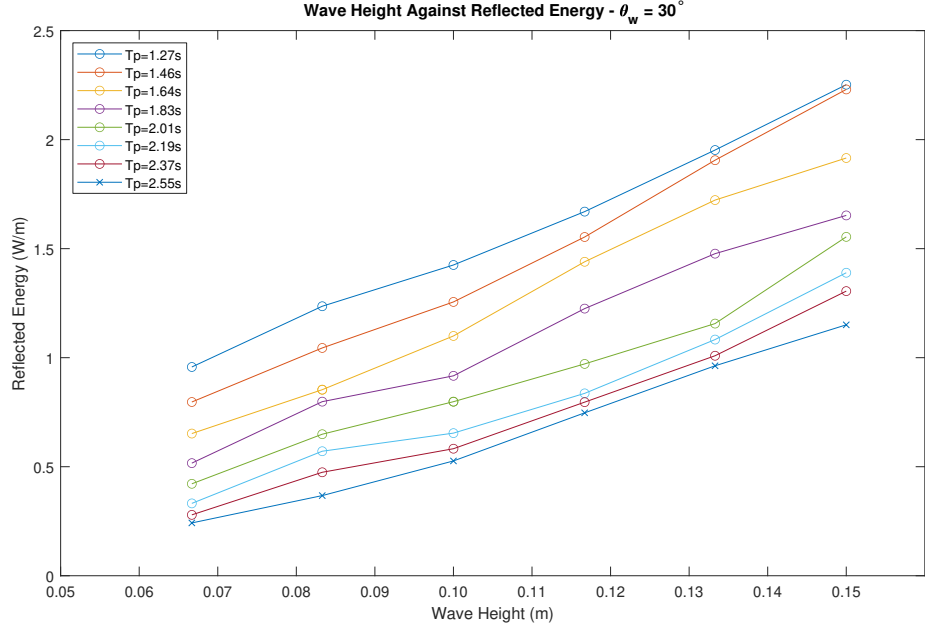


(a) Absorbed energy against  $H_s$  for  $\theta_w = 60^\circ$

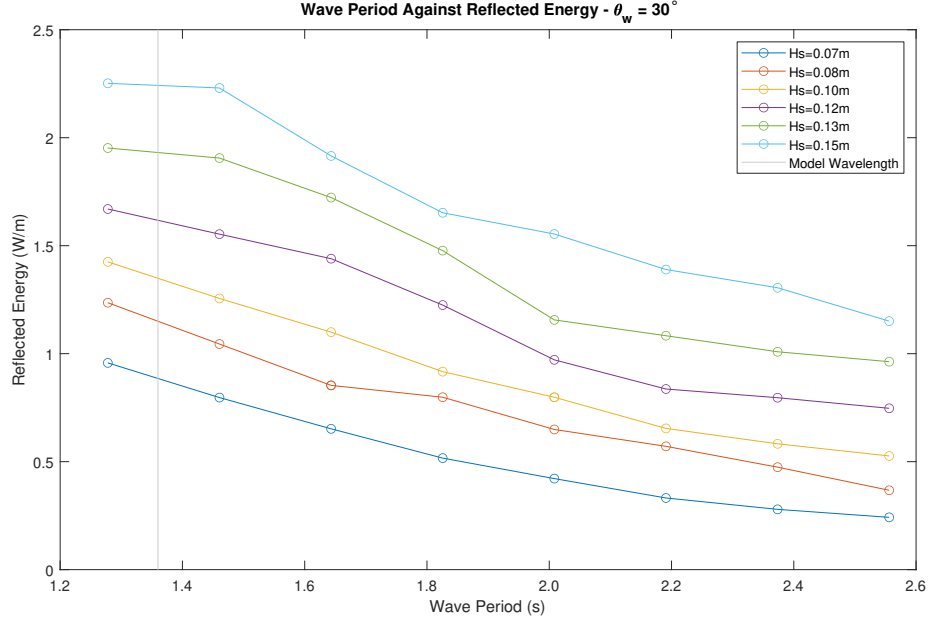


(b) Absorbed energy against  $T_p$  for  $\theta_w = 60^\circ$

FIGURE B.3: Absorbed energy shown as functions of (a)  $H_s$  and (b)  $T_p$  for  $\theta_w = 60^\circ$



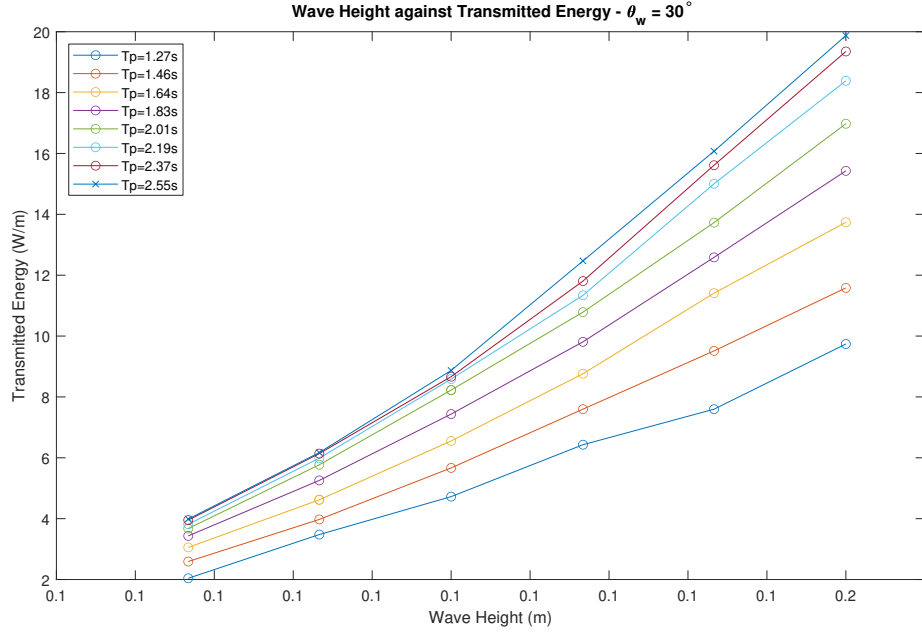
(a) Reflected energy against  $H_s$  for  $\theta_w = 30^\circ$



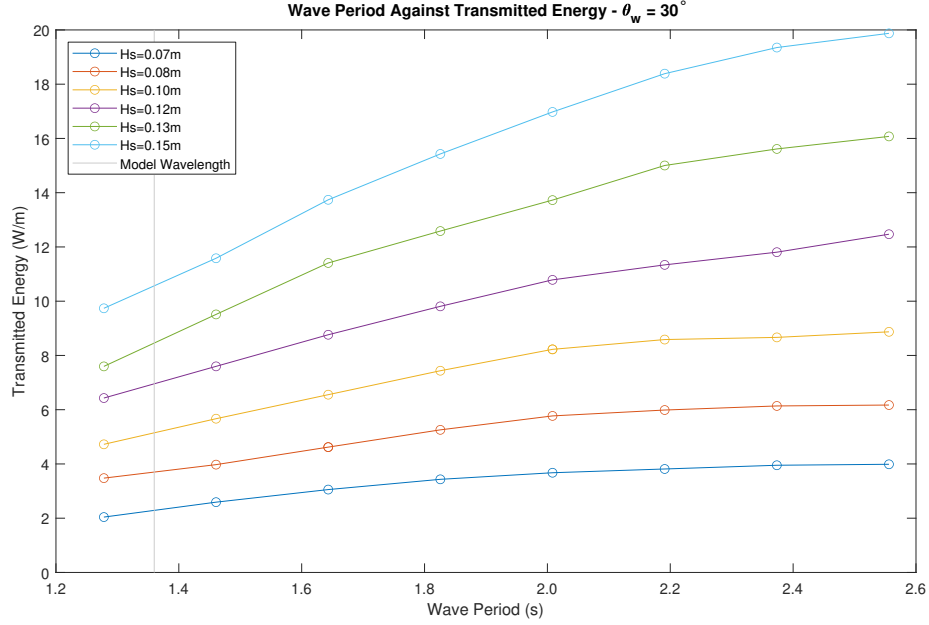
(b) Reflected energy against  $T_p$  for  $\theta_w = 30^\circ$

FIGURE B.4: Reflected energy shown as functions of  $H_s$  and  $T_p$  for  $\theta_w = 30^\circ$





(a) Transmitted energy against  $H_s$  for  $\theta_w = 30^\circ$



(b) Transmitted energy against  $T_p$  for  $\theta_w = 30^\circ$

FIGURE B.5: Transmitted energy shown as functions of  $H_s$  and  $T_p$  for  $\theta_w = 30^\circ$

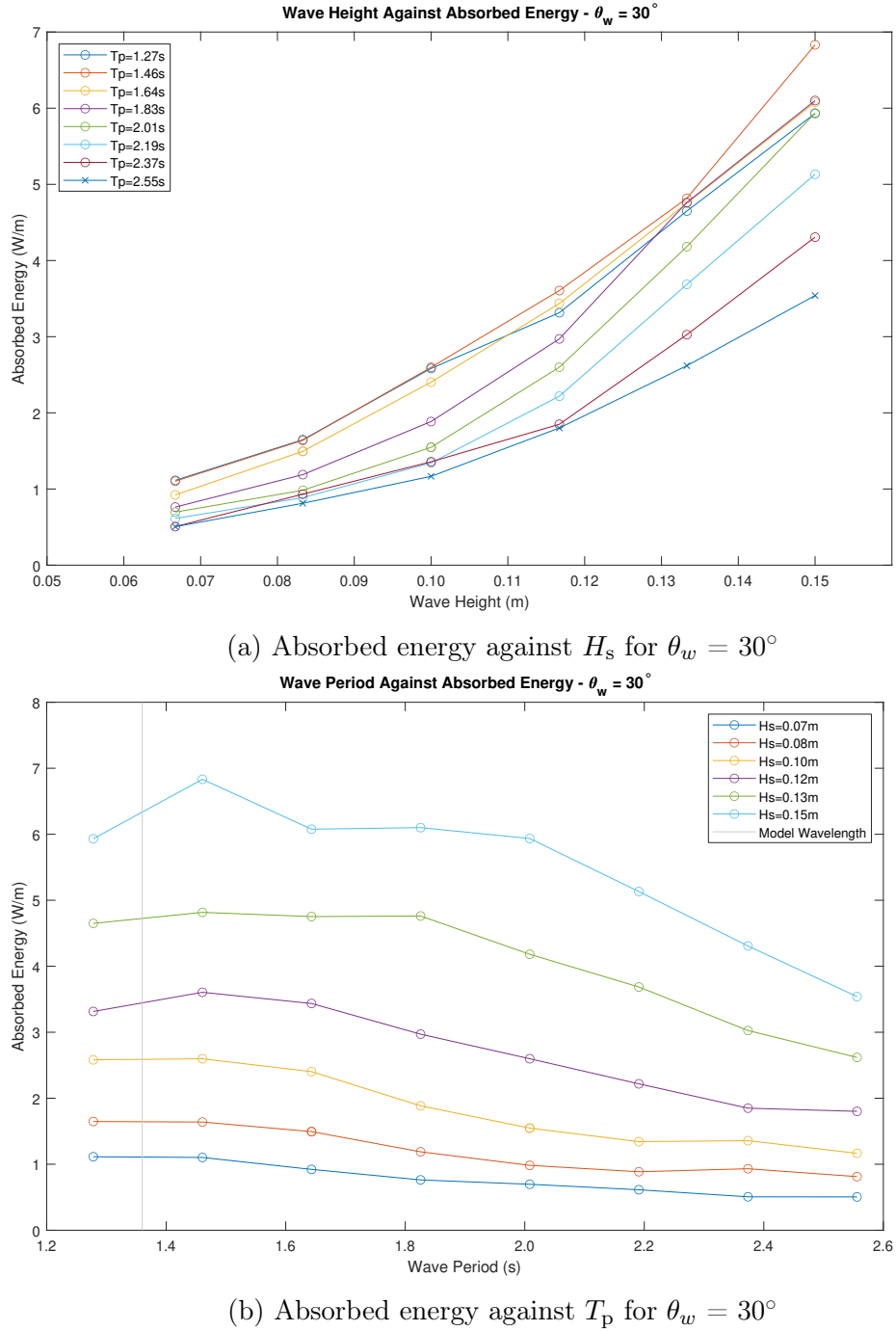


FIGURE B.6: Absorbed energy shown as functions of  $H_s$  and  $T_p$  for  $\theta_w = 30^\circ$

energy when both  $H_s$  and  $T_p$  were high, if one or the other were high then the device did not transmit as much energy as when both were high.

Figure B.6 shows the absorbed energy total over a test as a function of  $H_s$ , Figure B.6a, and  $T_p$ , Figure B.6b. When grouped by  $T_p$  the tests showed an increase in energy absorbed as  $H_s$  increased. However, the test that had the largest absorbed

energy was not the test with the lowest or highest  $T_p$  characteristic but the test with the  $T_p$  value that was closest to the model frequency,  $T_p = 1.28$  s. The next highest absorbed energy totals came from the tests with  $T_p$  either side of 1.28 s, 1.09 s and 1.46 s. This was clearly shown in Figure B.6b where there was a peak in energy in the tests that had higher  $H_s$  values. At  $H_s$  of 0.07 m the peak had moved to a lower wave period and at  $H_s$  values below that there was no peak, suggesting a lack of overtopping.

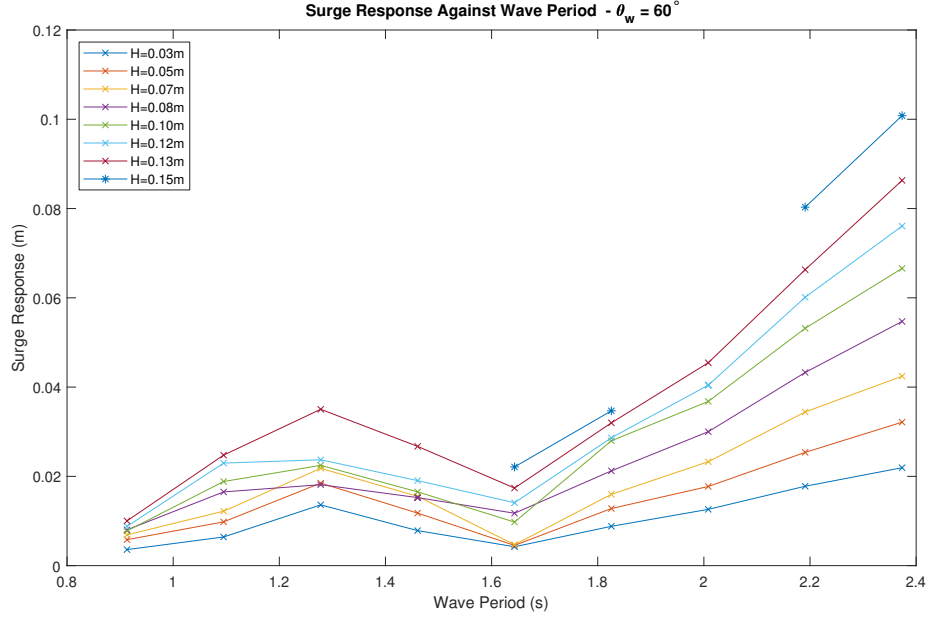
## B.2 Responses and RAOs

The results from Chapter 6 are presented here in alternative formats to assist with the understanding of the data.

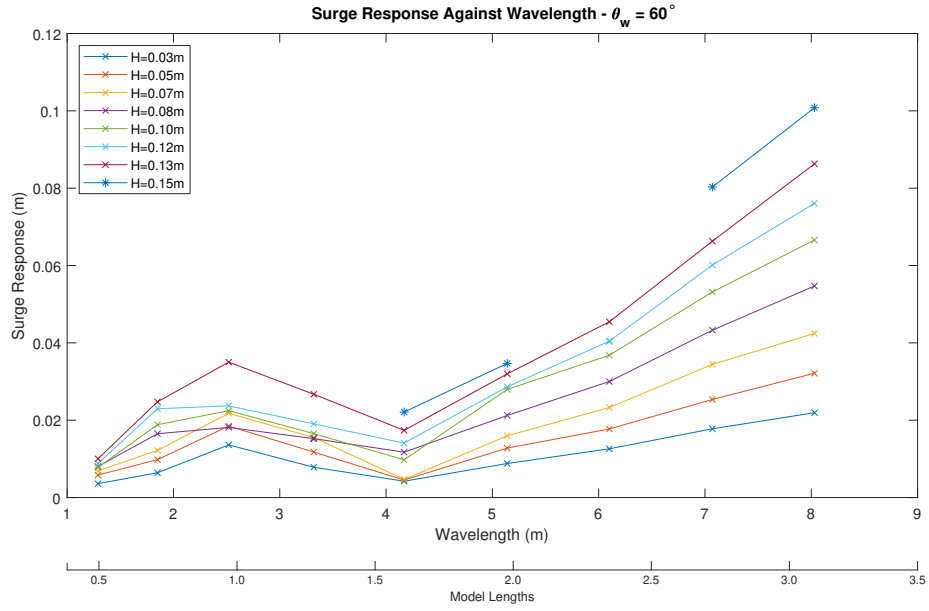
### B.2.1 $60^\circ$

Figure B.7 shows the surge response to regular waves for  $\theta_w = 60^\circ$  against wave period, Figure B.7a, and against wavelength, Figure B.7b. Figure B.7a shows that in general a lower wave period resulted in a lower surge response, however there was a peak in responses at  $T_p = 1.28$  s, before reducing again to a minimum at  $T_p = 1.64$  s, then rising when the period increased. It can be seen that as wave height increased this trend was followed by a larger response. When plotting the response against the wavelength, Figure B.7b, with the number of model lengths per wavelength also shown, the initial peak occurred at the test closest to the model wavelength, before reducing, then rising, when the wavelength was above two model wavelengths.

Figure B.8 shows the heave response to regular waves for  $\theta_w = 60^\circ$  against wave period, Figure B.8a, and against wavelength, Figure B.8b. Similar to the surge responses, the heave response was generally lower at lower wave periods before rising towards the higher wave periods. An increase in wave height increased the heave

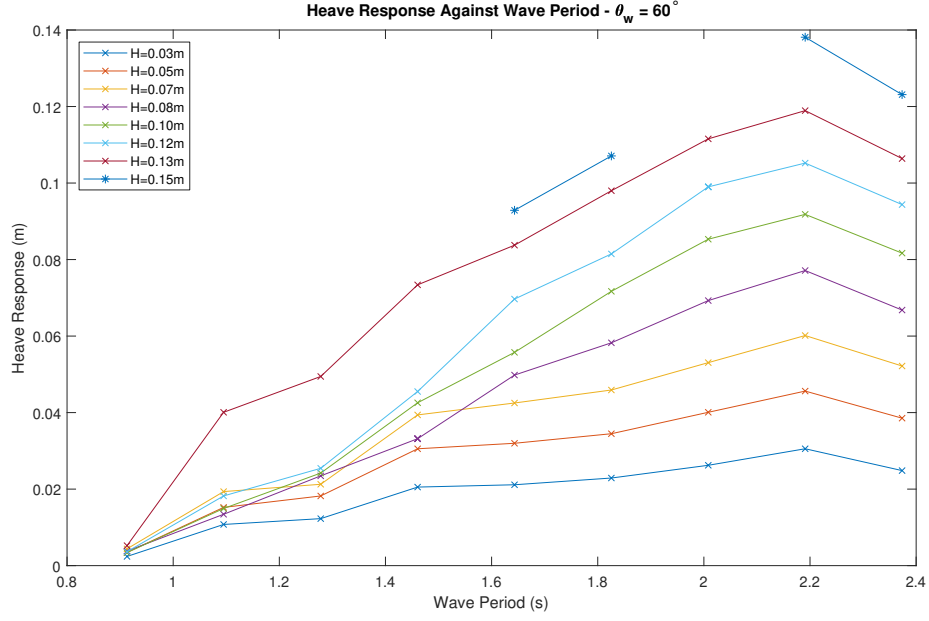


(a) Surge response against wave period for  $\theta_w = 60^\circ$

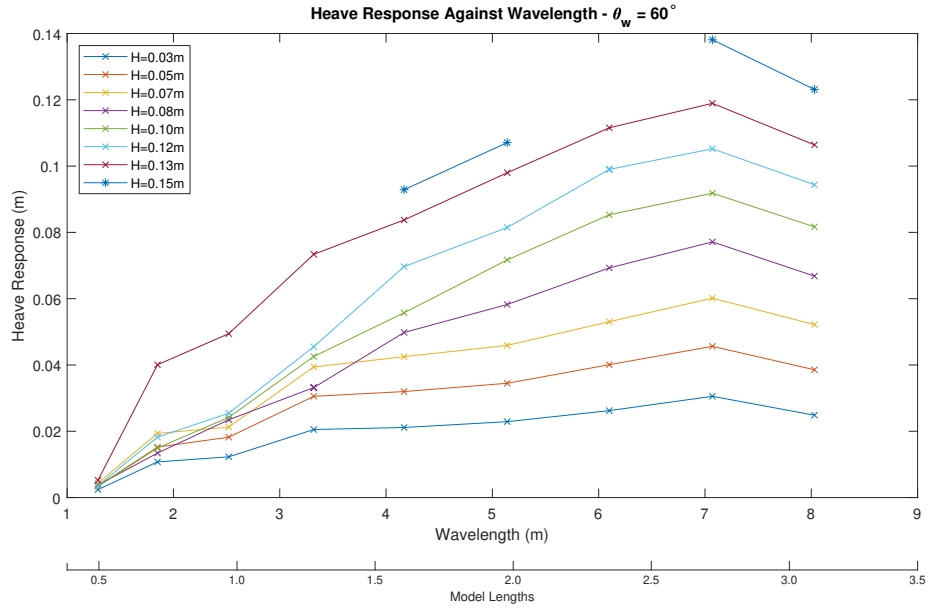


(b) Surge response against wavelength and model length for  $\theta_w = 60^\circ$

FIGURE B.7: Surge response against wave period, wavelength and model length for  $\theta_w = 60^\circ$

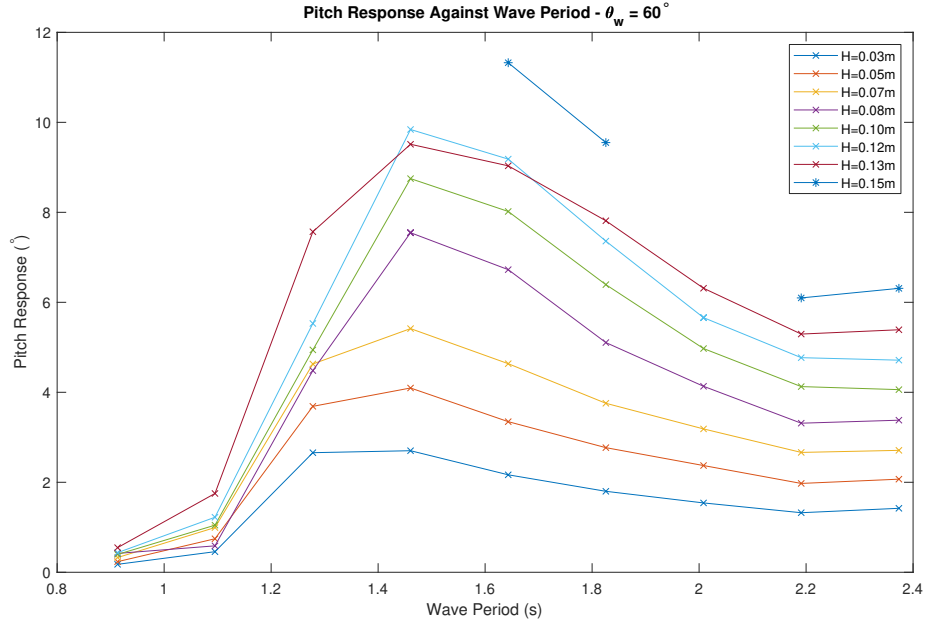


(a) Heave response against wave period for  $\theta_w = 60^\circ$

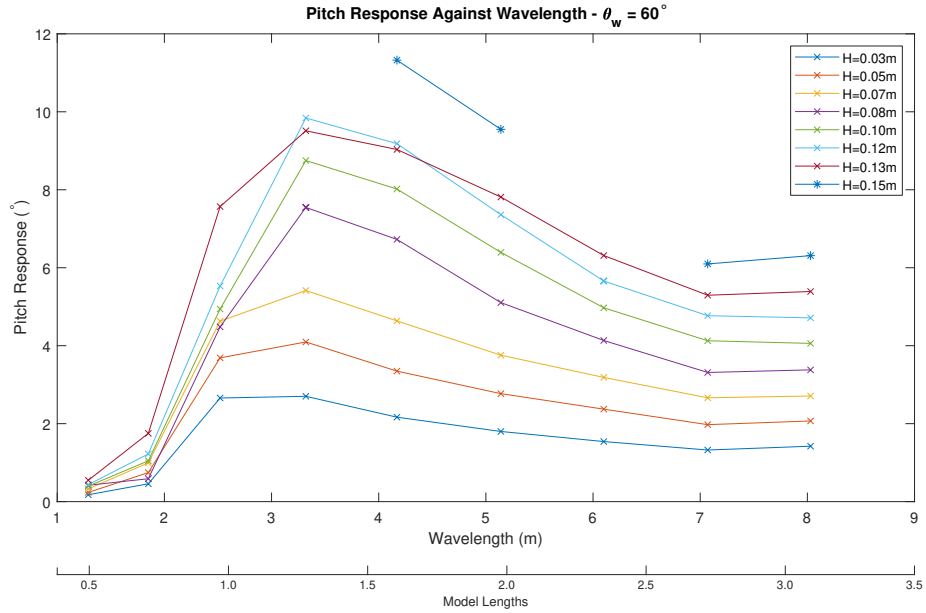


(b) Heave response against wavelength and model length for  $\theta_w = 60^\circ$

FIGURE B.8: Heave response against wave period, wavelength and model length for  $\theta_w = 60^\circ$



(a) Pitch response against wave period for  $\theta_w = 60^\circ$



(b) Pitch response against wavelength and model length for  $\theta_w = 60^\circ$

FIGURE B.9: Pitch response against wave period, wavelength and model length for  $\theta_w = 60^\circ$

response proportionally. When plotted against wavelength, Figure B.8b, the model length had little effect outside the general trend of the responses.

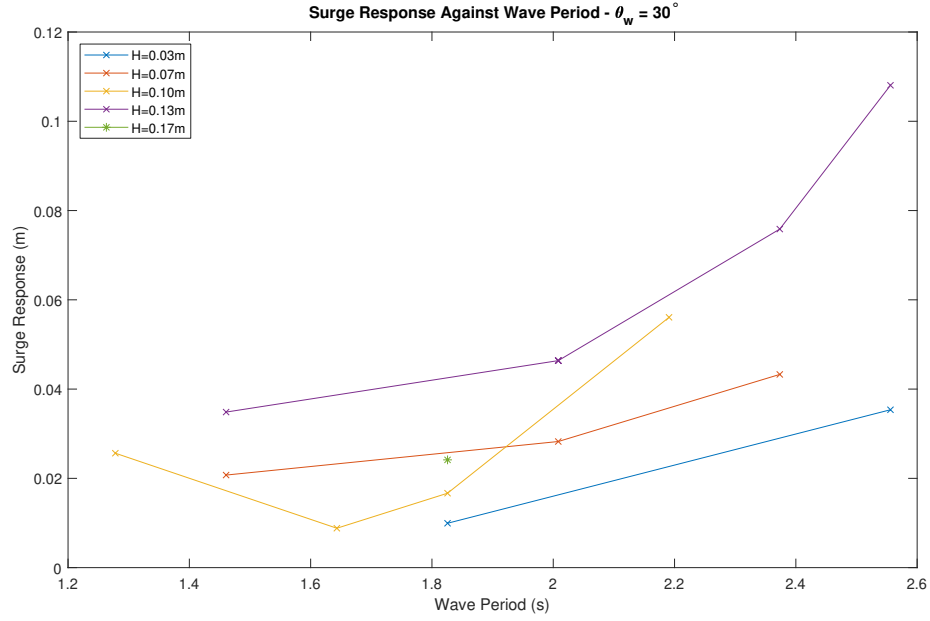
Figure B.9 shows the pitch response to regular waves for  $\theta_w = 60^\circ$  against wave period, Figure B.9a, and against wavelength, Figure B.9b. Figure B.9a shows that pitch response peaked when the wave period was 1.46 s. At periods of 1.09 s and

lower the pitch response was very low. Above the 1.46 s peak the pitch response dropped, however was still generally high. As expected, increasing wave height also increased the pitch proportionally at periods above 1.28 s, however at periods below this the wave height had minimal effect. When pitch response was viewed against wavelength, Figure B.9b, the pitch response was minimal when the wavelength was less than the model wavelength. The response then increased with model wavelength and remained high when the wavelength was above the model length.

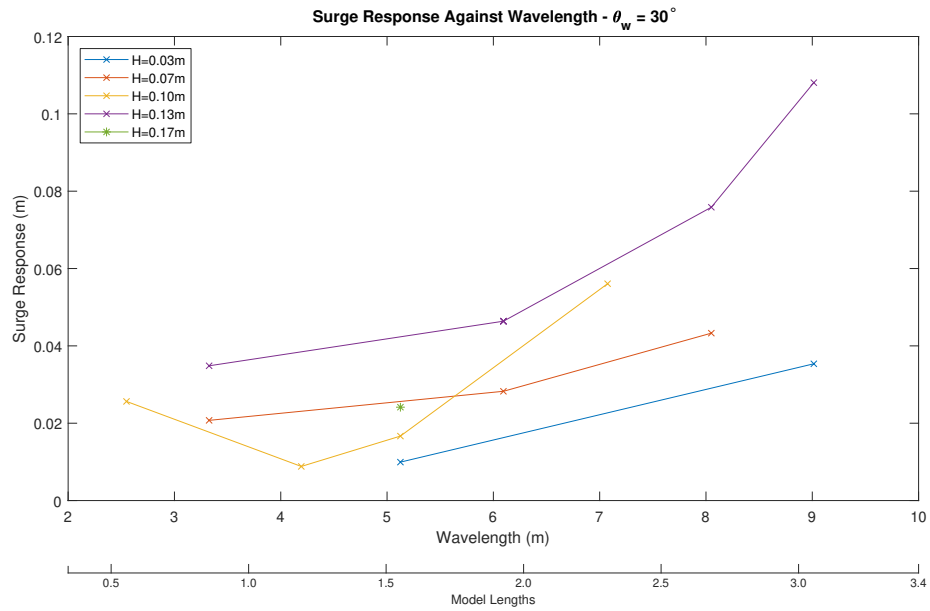
### **B.2.2 $30^\circ$**

Figure B.10 shows the surge response to regular waves for  $\theta_w = 30^\circ$  against wave period, Figure B.10a, and against wavelength, Figure B.10b. Figure B.10a shows that in general a lower wave period resulted in a lower surge response and for tests with multiple wave heights tested it can be seen that as wave height increased the response was larger. Figure B.10b shows the response as a function of wavelength, and the lowest responses occurred around wavelengths approximately equal to model length.

Figure B.11 shows the heave response to regular waves for  $\theta_w = 30^\circ$  against wave period, Figure B.11a, and against wavelength, Figure B.11b. Figures B.11a and B.11b show that in general a lower wave period, and thus wavelength, resulted in a lower heave response. When the wave height was increased the heave response also increased.



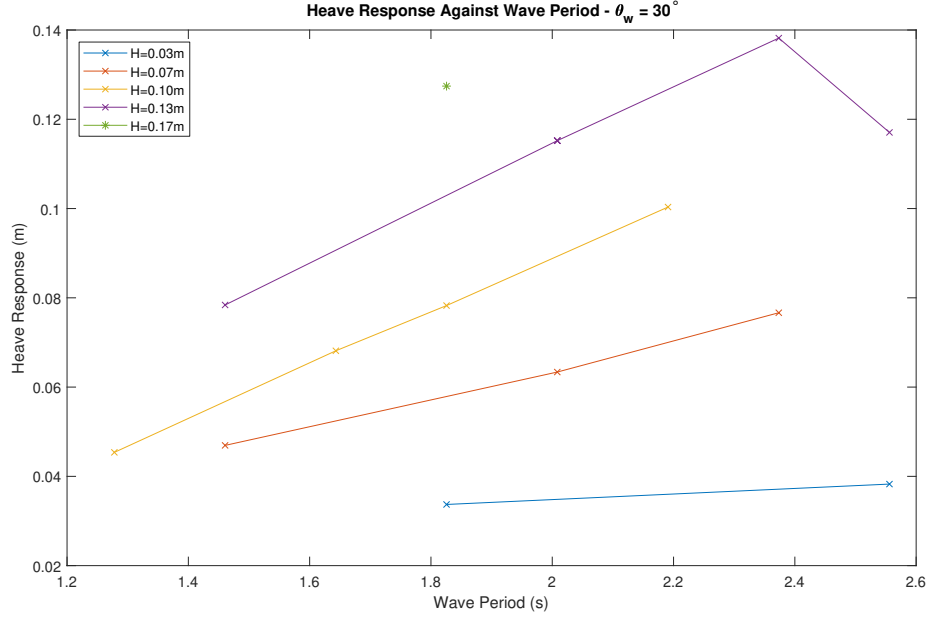
(a) Surge response against wave period for  $\theta_w = 30^\circ$



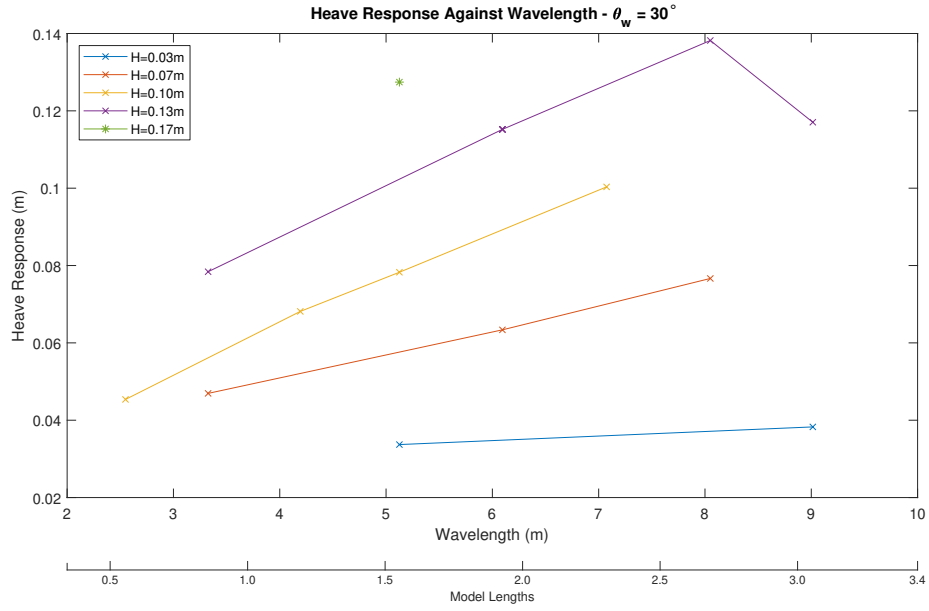
(b) Surge response against wavelength and model length for  $\theta_w = 30^\circ$

FIGURE B.10: Surge response against wave period, wavelength and model length for  $\theta_w = 30^\circ$





(a) Heave response against wave period for  $\theta_w = 30^\circ$



(b) Heave response against wavelength and model length for  $\theta_w = 30^\circ$

FIGURE B.11: Heave response against wave period, wavelength and model length for  $\theta_w = 30^\circ$